Cold Gas Dynamic Spray Impact: Metallic Bonding Pre-Requisites and Experimental Particle In-Flight Temperature Measurements

by

Aleksandra Nastic

Thesis submitted to the University of Ottawa

in conformity with the requirements for the degree of

Doctor of Philosophy in Mechanical Engineering

Ottawa-Carleton Institute for Mechanical and Aerospace Engineering

Department of Mechanical Engineering

University of Ottawa

Abstract

The impact phenomena of high velocity micron-size particles, although commonly considered and described as detrimental in numerous engineering applications, can be used in a beneficial way if properly understood and controlled. The Cold Gas Dynamic Spray (CGDS) process, known as a surface modification, repair and additive manufacturing process, relies on such high velocity impacts. In the process, solid particles are accelerated by a supersonic gas flow to velocities up to 1200 m/s and are simultaneously heated to temperatures lower than their melting point. When propelled under proper velocity and temperature, the particles can bond onto a target surface. This bonding is caused by the resulting interfacial deformation processes occurring at the contact interface. Hence, the process relies heavily on the gas/particle and particle/substrate interactions.

Although numerous experimental and/or numerical studies have been performed to describe the phenomena occurring during particle flight and impact in the CGDS process, numerous phenomena remain poorly understood. First, the effect of **substrate surface topographical condition** on the particle deformation and ability to successfully adhere, i.e. atomically and/or mechanically, has not been thoroughly investigated such that its influence is not well understood. Another aspect of the process that is generating the largest gap between experimental and numerical studies in the field is the lack of **particle in-flight temperature measurements**. Obtaining such data has proven to be technically difficult. The challenges stem from the short particle flight time, low particle temperature and small particle size preventing the use of established thermal spray pyrometry equipment. Relatedly, lack of such measurements precludes a proper experimental study of the impact related phenomena at the particle/substrate interface. As a result, **the effect of particle size dependent temperature on overall coating properties** and atomic bonding relies currently on estimates. Finally, the **effect of particle impact characteristics on interfacial phenomena,** i.e. grain size and geometry, velocity/temperature, and oxide scale thickness, on adhesion and deformation upon single particle collision has also been scarcely studied for soft particle depositions on hard substrate.

Hence, the current research work aims at studying fundamental aspects of particle/gas heat transfer and particle/substrate impact features in goals to improve the understanding of the CGDS process. Different surface preparation methods will be used to create various surface roughness and topographical features, to provide a clear understanding of the target surface state influence on coating formation and adhesion. Additionally, new equipment relying on novel technology, i.e.

high-speed IR camera, will be utilized to obtain particle in-flight temperature readings with sequence recordings. Subsequently, the experimental particle in-flight temperature readings will be used to develop a computational fluid dynamics model in goals to validate currently used Nusselt number correlations and heat transfer equations. The particle size-dependent temperature effect on the particle's elastic and plastic response to its impact with a targeted surface and its ability to successfully bond and form a coating will be studied experimentally. A thorough CFD numerical work, based on experimental findings, will be included to provide full impact characteristics (velocity, temperature, size and trajectory) of successfully deposited particles. Finally, the numerical results will be utilized in the ensuing study to correlate single particle deformation, adhesion and interfacial features to impact characteristics. A finite element model will be included to investigate the effect of particle size dependent temperature on single particle interfacial pressure, temperature and bonding ability.

Preface

The current thesis is presented as a series of articles. A statement regarding my contributions and those of the co-authors is provided in the following paragraphs.

I have co-authored (primary author) the first paper entitled "Experimental and numerical study of the influence of substrate surface preparation on adhesion mechanisms of aluminum cold spray coatings on 300M steel substrates", with Dr. Mohan Vijay, Mr. Andrew Tieu, Mr. Saeed Rahmati and Dr. Bertrand Jodoin. I have contributed directly to the presented work by producing all coatings, as well as all other experimental, characterization and numerical work. All presented results were outcomes of experiments I have conducted. I have also conducted all of the numerical work. Dr. Mohan Vijay and Mr. Andrew Tieu helped with the FPWJ equipment at their facility and allowed us to use it in our current study. Mr. Saeed Rahmati provided a numerical subroutine to implement the high strain rate Preston-Tonks-Wallace that he has developed under the supervision of Dr. Abbas Ghaei. Dr. Jodoin, my thesis supervisor, has guided me on the required tests to be performed. He also provided insights and reviewed the manuscript to ensure quality prior to submission. I am the first author of the paper as all co-authors agreed that I have been the one that has produced all the work and done all the writing, including production of figures, tables, typesetting, submission and review process, of the paper.

I have co-authored (first author) the second paper entitled "Evaluation of heat transfer transport coefficient for cold spray through computational fluid dynamics and particle in-flight temperature measurement using a high-speed IR camera" with Dr. Bertrand Jodoin. I have contributed directly to the work by producing all developed experimental and numerical work. I have produced the written document as well as all the shown figures, tables, typesetting. I have delivered the submission and the review process. Dr. Bertrand Jodoin, my thesis supervisor, guided me on the tests to be performed and has provided useful insights and has reviewed the manuscript to ensure its quality prior to the submission. I am the first author of the paper since the co-author has agreed that I have produced all experiments and numerical work and contributed the most to the technical content of the paper.

I have co-authored (leading author) the third paper entitled "Particle Temperature Effect in Cold Spray: A Study of Soft Particle Deposition on Hard Substrate", with Dr. Bertrand Jodoin, Dr. Dominique Poirier and Dr. Jean-Gabriel Legoux. I have contributed directly to this work by

producing all coatings other than the high temperature coating depositions, as we do not have access to a high pressure cold spray system, which consequently have been produced at the National Research Council Canada Industrial Materials Institute-NRC Boucherville facility with my presence. I have conducted all tests and characterizations of all produced samples. In addition, the numerical work has been completely developed and designed by me. Dr. Jodoin, my thesis supervisor, guided me on the required tests to be performed and reviewed the manuscript prior to its journal submission process. Dr. Poirier and Dr. Legoux, listed as third and fourth author, respectively, participated greatly in discussions on this subject, provided useful insights and reviewed the manuscript to ensure quality prior to its final submission. I am the first author of the paper since all the co-authors have agreed that I have contributed the most to the technical/engineering content of the paper.

I have co-authored (first author) the last paper entitled “Particle Impact Characteristics Influence on Cold Spray Bonding: Investigation of Interfacial Phenomena for Soft Particles on Hard Substrates” with Dr. Bertrand Jodoin, Dr. Jean-Gabriel-Legoux and Dr. Dominique Poirier. I have contributed directly to the presented work by producing all depositions using the low pressure cold spray system available at the University of Ottawa. All depositions produced using the high pressure cold spray system have been done at the National Research Council Canada Industrial Materials Institute-NRC Boucherville facility with my presence. In addition, I have done all the material characterization study as well as the complete numerical work. Dr. Bertrand Jodoin, my thesis supervisor, guided me on the required tests to be performed. He also provided insight and reviewed the manuscript to ensure its quality prior to submission. Both Dr. Legoux and Dr. Poirier have participated in discussions on the research, provided greatly useful insights and reviewed the manuscript prior to its submission. I am the first author of the paper as all co-authors have agreed that I have predominantly contributed to the technical/engineering content of the paper.

Acknowledgments

In this acknowledgement section I first want to thank my supervisor, Dr. Bertrand Jodoin, for his enormous support, guidance and commitment during my years of graduate studies, which have made each project enormously enjoyable. I am grateful and consider myself privileged to have had Dr. Bertrand Jodoin as a mentor and role model. Thank you again for everything!

I am also using this opportunity to thank my colleagues for making this experiencing truly pleasant. All the random talks, activities, many dinners and all the jokes we have had have made great memories! Invaluable discussions about everyone's research project have made the overall experience that much better!

Acknowledgments are due as well to the industrial partners that have given access to their equipment for the projects presented in the current thesis: Telops Inc., especially Vincent Farley, Karl-Alexandre Jahjah, Bruno Bourliaguet and Jean-Daniel Bussières, and Dr. Mohan Vijay, Mr. Andrew Tieu and Mr. Bruce Daniels, Mr. Willie Bloom and Dr. Meisheng Xu from VLN Advanced Technologies Inc. In addition, a big thanks to the technicians from the Department of Mechanical Engineering machine shop for their contribution to the projects and their amazing humour that has made every visit worth while: Paul Burberry, Stanley Weedmark and Leo Denner!.

I would also take this opportunity to thank the Ontario Graduate Scholarship (OGS), the Natural Sciences and Engineering Research council (NSERC), Fonds de Recherche du Québec-Nature et Technologies (FRQNT), Queen Elizabeth II Graduate Scholarship in Science and Technology and the Metallurgy and Materials Society program for their financial support.

Finally, a massive thanks to my family for their support and love.

Table of Contents

List of Tables

List of Figures

Table of Symbols

Symbol	Definition	Units
Supersonic flow characteristics		
ρ	Density	(kg/m^3)
c	Speed of sound	(m/s)
P	Pressure	(N/m^2)
R	Gas constant	(J/kg·K)
M	Mach number	(-)
γ	Ratio of specific heats	(-)
h	Enthalpy	(N·m)
C_p	Gas specific heat at constant pressure	(kJ/kg·K)
T	Temperature	(K)
$\dot{m}$	Mass flow rate	(kg/s)
V, v	Velocity	(m/s)
k_{st}	Material stiffness	(N/m)
A	Cross-sectional area	(m^2)
m	Mass	(kg)
Particle laden flow/Velocity		
Re_p	Relative Reynolds number	(-)
M_p	Relative Mach number	(-)
Kn_p	Knudsen number	(-)
λ	Mean free-path length of surrounding molecules	(m)
$L_{characteritic}$	Particle diameter	(m)
C_D	Drag coefficient	(-)
μ	Gas dynamic viscosity	(Pa·s)
a	Acceleration	(m/s^2)
Vol_p	Particle volume	(m^3)
Bi	Biot number	(-)
a_1, a_2, a_3	Drag coefficient constants	(-)

Symbol	Definition	Units
Particle laden flow/Temperature		
q	Total heat transfer	(kg·m^2·s^{-2})
$\bar{h}$	Convection coefficicent	(W/m^2)
A_s	Surface area	(m^2)
d_p	Particle diameter	(m)
k_g	Gas thermal conductivity	(W/m·K)
Nu	Nusselt number	(-)
Pr	Prandtl number	(-)
Nu_0	Incompressible Nusselt number	(-)
η	Dynamic viscosity	(Pa·s)
$\dot{E_{in}}$	Rate of change of internal energy	(kg·m^2·s^{-3})
$\dot{E_p}$	Rate of heat gain (or loss)	(kg·m^2·s^{-3})
t	Time	(s)
Radiation		
λ	Wavelength	(nm)
c_l	Speed of light	(m/s)
v	Frequency	(Hz)
ρ	Irradiated radiation fraction	(-)
α	Absorbed radiation fraction	(-)
τ	Transmitted irradiation	(-)
k_B, c_0, h	Constants	(…)*
I	Spectral intensity	(W/m)
E	Spectral emissivity	(J/m^2)
ε	Emissivity	(-)
θ, ϕ	Spectral emissivity directions	(°)
Ω	Solid angle light collection optics	(°)
A_e	Emitter area	(m^2)

E_p	Particle emitted infrared radiation	(W/m^2)
E_r	Emission of the surroundings	(W/m^2)
E_a	Emission of the atmosphere	(W/m^2)
Particle impact process		
E_i	Internal energy	(kg·m^2/s^2)
E_v	Viscous dissipated energy by damping	(kg·m^2/s^2)
E_f	Energy dissipated by friction	(kg·m^2/s^2)
E_k	Kinetic energy	(kg·m^2/s^2)
E_w	Work produced by external load	(kg·m^2/s^2)
E_e	Recoverable elastic strain energy	(kg·m^2/s^2)
E_p	Energy dissipated through inelastic processes	(kg·m^2/s^2)
β	Adiabacity degree	(-)
α	Thermal diffusivity	(m^2/s)
k_1	Particle-size-dependent fitting parameter	(-)
σ	Tensile strength	(-)
η	Dimensionless deposition efficiency parameter	(-)
Roughness		
R_a	Arithmetical mean surface roughness	(μm)
R_q	Root mean square roughness	(μm)
R_z	Peak to valley distance	(μm)
n	Data point	(-)
y_i	Vertical height from mean line	(μm)
R_{pi}	Peak vertical distance	(μm)
R_{vi}	Valley vertical distance	(μm)

CFD, particle/gas		
S_m	Mass added	(kg)
$\vec{F}$	External body forces	(N)
μ	Molecular viscosity	(m^2/s)
$\bar{\bar{r}}_{eff}$	Viscous stress tensor	(Pa)
S_h	Heat sources	(kg/m·s^3)
$\vec{J}_j$	Diffusion flux vector	(atoms/m^{2}s)
h	Sensible enthalpy	(J/kg)
Br	Brinkman number	(-)
α_ϵ	Inverse effect Prandtl number for ϵ	(-)
α_k	Inverse effect Prandtl number for k	(-)
G_k	Generation of turbulent kinetic energy due to mean velocity gradients	(kg/m·s^3)
G_b	Generation of turbulent kinetic energy due to buoyancy	(kg/m·s^3)
Y_M	Contribution of the fluctuating dilatation in compressible turbulence to the overall dissipation rate	(kg/m·s^3)
S_k, S_ϵ	User defined source terms	(-)
$C_{1\epsilon}, C_{2\epsilon}, C_{3\epsilon}$	Model constants	(-)
u_i	Gas velocity component in i-direction	(m/s)
x_i	Cartesian coordinate in the *i*-direction	(m)
C_v	Yakhot's formula constant	(-)
CFD solution algorithm		
L_{min}	Smallest element dimension	(μm)
c_d	Dilatation wave speed	(m/s)
λ_0, μ_0	Effective Lam's constants	(-)
M^{NJ}	Mass matrix	(kg)
P^J	Applied vector load	(N)

I^J	Internal force vector	(N)	ϵ_p	Plain strain	(µm/µm)
	Material deformation		n	Strain rate hardening constant	(-)
ϵ	Turbulent dissipation rate	(m^2/s^3)	β	High strain rate exponent	(-)
k	Turbulent kinetic energy	(m^2/s^2)	κ	Temperature dependence constant	(-)
h	Specific enthalpy	(J/kg)	γ	Strain rate dependence constant	(-)
s	Hugoniot slope	(-)	y_1	Medium strain rate constant	(-)
D	Deviatoric stress	(GPa)	y_2	Medium strain rate exponent	(-)
σ	True stress state	($kg/m{\cdot}s^2$)	M_a	Atomic mass	(kg) (Da)
D^{el}	Fourth-order elasticity tensor	(GPa)	ε^{el}	Total log elastic strain	(µm/µm)
E_H	Specific energy per unit mass	(J/kg)	E_m	Total energy per unit mass	(J/kg)
u_s, u_m	Shock speed	(m/s)	p_{bv}	Pressure stress due to bulk viscosity	(Pa)
M	Mandel stress tensor	(MPa)	Γ	Gruneisen parameter	(-)
$\boldsymbol{S}$	Deviatoric stress tensor	(GPa)	V	Volume	(m^3)
ϵ_d	Elastic deviatoric strain	(µm/µm)	p_H	Hugoniot pressure	(Pa)
σ^0	Static yield stress	(GPa)	c_0	Speed of sound in uncompressed state	(m/s)
A, B, C, J	Material parameters	(…)	$\dot{e}$	Deviatoric part of the strain rate	(1/s)
$\bar{\varepsilon}^{pl}$	Equivalent plastic strain rate	(µm/µm)	$\dot{Q}$	Heat transfer per unit mass	(J/kg)
$\hat{T}^m$	Non-dimensional temperature	(-)	$\hat{\tau}_y$	Normalized yield stress	(GPa)
$\bar{\sigma}$	Yield stress at nonzero strain rate	(GPa)	G_p	Plastic shear modulus	(GPa)
$\hat{\tau}_s$	Normalized work hardening saturation stress	(GPa)	θ	Strain hardening rate	(-)
s_0	Saturation stress at 0K	(Pa)	α	>0 material parameter	(-)

** Units are based on the calculated property*

Subscript and Superscript

Symbol	Definition
∞	Gas far field properties
b and B	Blackbody properties
c	Critical
e	Elastic
eff	Effective
g	Gas properties
m	Melting
0 and st	Gas stagnation characteristics
op	Operating
p	Plastic
r	Recovery

Abbreviations

Abbreviation	Definition	Abbreviation	Definition
BCC	Body-centered cubic	JC	Johnson-Cook
BSE	Back-scattered electron	L2F	Laser two-focus velocimetry
CCD	Charge-coupled single color	LCM	Lumped capacitance method
CFD	Computational fluid dynamics	LDV	Laser Doppler velocimetry
CGDS, CS	Cold gas dynamic spray, Cold spray	LPCS	Low pressure cold spray
CP	Commercially pure	PBI	Polybenzimidazole
CPFEM	Crystal plasticity finite element modeling	PEEQ	Equivalent plastic strain
CSM	Cold spray meter	PIV	Particle imaging velocimetry
DE	Deposition efficiency	PSV	Particle streak velocimetry
DPM	Discrete phase modeling	PTV	Particle tracking velocimetry
DPV	Doppler picture velocimetry	PTW	Preston-Tonks-Wallace
EDS	Energy-dispersive X-Ray spectroscopy	RANS	Reynold averaged Navier-Strokes
EOS	Equation of state	RSM	Reynolds stress model
FCC	Face-centered cubic	RTTC	Real time temperature calibration
FEA	Finite element analysis	SE	Secondary electron
FEM	Finite element modeling	SEM	Scanning electron microscope
FPWJ	Forced pulsed waterjet	SOD	Standoff distance
		TS	Thermal spray
HPCS	High pressure cold spray	UMAT	User material
IR	Infrared	VDW	Van der Waals

CHAPTER 1

INTRODUCTION

Establishing a proper understanding of the behavior of different materials subjected to high speed impact processes has become a leading area of research in the 21rst century (Ref 1–4). Numerous processes rely on high speed impacts to function as intended such as cold gas dynamic spray (CGDS) (Ref 5), forced pulsed waterjet (FPWJ) (Ref 6) and laser shock compression (Ref 7). Others, on the other hand, find the presence of high speed dynamic collisions detrimental to their system, such as ballistic impacts (Ref 8), cavitation erosion (Ref 9) and minute space debris attrition (Ref 10). Although proper understanding of extreme impact phenomena is essential in all these fields, numerous characteristics of the impactor material and/or resulting impacted surface features remain inappropriately characterized due to technological limitations. These challenges are associated to the short time and dimension scales ($\sim 10^{-8}$s and 1nm), and non-equilibrium regimes, i.e. high cooling rates in the order of 10^8 K/s, under which these events develop (Ref 9,11,12). To improve the knowledge of such high strain rate localized impact events, numerical models have been developed and the impactors/targeted surfaces behavior and microstructural evolution have been analysed using multi-scale methods, i.e. continuum, quasi-coarse-grained dynamics and atomistic (Ref 8,13–18). However, since these models rely primarily on experiments to validate their suitability, their accuracy in defining the high-speed impact dynamics is tied to the quality of the assumptions used in the advent of

impossible experimental measurements. The CGDS process, discovered in the 1980's, is facing such challenges despite the growing use of the process in many applications and fields.

1.1 Background

In the CGDS process, micro-particles injected in a converging/diverging nozzle and accelerated by the supersonic gas to velocities ranging between 300m/s to 1200m/s rely on the impact process resulting phenomena to adhere to a target surface. Describing the wide range of mechanical and thermodynamic conditions occurring under such loading is challenging and the induced local microstructural features are extremely difficult to segregate and observe in-situ. Under extreme dynamic loading circumstances, influenced by the particle material properties, the particle impact velocity/temperature and target surface material properties/topography, the resulting high strain-rate, pressure, and temperature cause the material to behave differently than under quasi-static conditions (Ref 2). To simplify the study of the CGDS process, i.e. from particle injection to particle deposition, the system has typically been divided in two distinct fields of study; 1) *Gas Dynamics*, relevant to the in-flight particle/gas interactions and 2) *Impact Dynamics*, pertinent to the particle/substrate deformation phenomena.

Gas dynamics perspective

The gas expansion and the presence of shock waves, in the CGDS process, induce large variations in the driving gas properties (Ref 19,20). The complex gas flow structure (inside and outside the nozzle) has been visualized using Schlieren imaging and modeled through computational fluid dynamics (CFD) simulations (Ref 19,21,22). The particle in-flight characteristics (position and velocity) have also been measured using laser-light sheet and laser two-focus velocimetry (Ref 23,24). However, the particle in-flight temperature has yet to be measured. Classical pyrometry methods providing reasonably accurate readings for temperatures above 1200°C, far above the CGDS carrier gas stagnation temperature, are unsuited for the measurement of CGDS particle in-flight temperatures (Ref 25,26). To overcome this issue, modeling has been used to predict the value of particle temperature. However, the validity of heat transfer coefficients, such as Nusselt number, and equations currently used in these CFD simulations remain to be confirmed (Ref 27–29). Since particle impact temperature affects the particle deformation behavior, its inaccurate prediction could lead to erroneous deformation prediction upon impact and consequently affect the understanding of the particle bonding process.

Impact dynamics perspective

The shock wave generated from the particle impact leads to the activation of deformation resulting in the propagation of high pressure waves. Once the local pressure exceeds the Hugoniot elastic limit, the material starts deforming plastically under the action of dislocation motion and development following the particle/substrate surface interface topography (Ref 30). Tangential velocity and friction at contact surfaces produce additional shear forces with magnitudes dependent on substrate properties and condition (Ref 31). The resulting material elastic/plastic flow propagation largely relies on the local particle temperature. Numerous plastic constitutive relations already exist, which relate solid flow parameters to physical deformation processes (Ref 14,32,33). Under the high shock loading conditions of CGDS particles, local in-situ impact phenomena occur very rapidly, and visualisation becomes difficult. In addition to the effect of particle in-flight characteristics and substrate condition on deformation and shock wave propagation, the micron-size particles microstructural features, i.e. grain size and shape, also influence the shock wave/material interactions. Powder manufacturing and processing conditions lead to specific particle microstructures, impurity levels and oxygen contents, which altogether infer mechanical properties that differ from one particle to another (Ref 34,35).

1.2 Motivation and Objectives

To date, the CGDS process has been used in a variety of fields for several different applications such as composite coatings for medical use (Ref 36,37), polymer metallization in electronics (Ref 38–46), corrosion protection of large metal deep water structures and nuclear fuel containers (Ref 47–56), restoration of aerospace parts (Ref 57,58,67,59–66), production of energetic materials (Ref 68,69), photovoltaic and photocatalytic performance in the energy industry (Ref 70,71), generation of wear resistant surfaces in automobile applications (Ref 72,73) and as an additive manufacturing process (Ref 62,74–80). The CGDS process implementation in aerospace and automotive industries has become an important way to strengthen Canada's position in the industrial field. A recent investment of 4 million CAD has been made in aim to build a network of industrial partners for a stronger Canadian value chain (Ref 81). In the US market, the CGDS repairs generate significant benefits and savings evaluated at 22.5 million USD, which are associated mainly to the reduction of magnesium production and utilization of chromated surface treatments (Ref 82). Since current technological developments rely on sustainability and performance progress, optimizing the CGDS process is crucial. To achieve an actual improvement, the gas/particle and

particle/substrate interactions must be better understood and current gaps in the process fundamental aspects must be reduced.

To this end, the current research aims at evaluating the influence of substrate surface topography on particle adhesion, to provide particle in-flight temperature measurement and consequently validate the energy transport coefficients (Nusselt) used in modeling work, to assess the influence of size-dependent particle temperature on coating and deposition characteristics and to investigate the combined effect of particle microstructure and temperature on the occurrence of metallic/atomic bonding for single CGDS particle impacts. The soft aluminum particle/hard steel substrate material combination will be utilized throughout the research. Table 1.1 summarizes the separate objectives to be covered in this thesis.

Table 1.1:Research objectives and project descriptions

Objective #	Title	Description
#1	*Substrate surface influence on bonding nature and adhesion strength*	• Surface roughness effect on particle/substrate interfacial stress, strain, contact pressure and velocity • Bonding nature/ Diffusion test • Impact requirements to enhance and induce metallic bonding/ FEM model
#2	*Particle in-flight temperature measurement/Heat transfer analysis*	• Particle/gas interactions • Particle in-flight temperature experimental measurements • CFD model for heat transfer and momentum analysis
#3	*Particle impact temperature influence on deposition and adhesion*	• CFD model of high pressure (axial injection-high temperature) and low pressure (radial injection-low particle temperature) CGDS systems • Particle in-flight characteristics statistical analysis based on flight trajectory and injection location • Particle temperature effect on impact ensuing adhesion/ coating properties
#4	*Particle impact characteristics influence on interfacial impact occurring phenomena*	• Particle characteristics influence on single particle bonding process • Particle temperature and size effect on single particle deformation • Particle interfacial features influence on bonding

1.3 Outline

The current thesis has been divided in six distinct chapters. The current **Chapter 1** has been devoted to provide a simplified overview of the relevant study background, to present the motivations that have led to the extensive numerical and experimental work and to describe the main objectives of the research.

In **Chapter 2**, a review of the CGDS process will be presented and described in terms of the current field state of knowledge. First, the gas dynamics principles will be utilized to explain the working basis of the process. Subsequently, the interaction between gas and in-flight particles will be covered through kinetics and heat transfer theories. Then, a detailed review of material deformation processes based on imparted strains, stresses and strain rates will be given. Mechanisms governing deformation will be presented based on shock wave/medium interactions, dislocation movement, multiplication and generation.

Chapter 3 will present in detail the research objectives and interests of the planned studies. It will provide to the reader a clear understanding of the current research direction.

Chapter 4 will provide the methodology and approach used in order to complete the set research objectives. The equipment and additional material will be described. The characterisation, analysis and measurement apparatus will be presented. Finally, a detailed planning of experimental and numerical steps will be given.

Chapter 5 presents the experimental and numerical results along with their discussion. Three studies have been published in peer-reviewed journals and are presented in their published form. The last work is written as an article in preparation to the submission process to a peer-reviewed journal. Each of the presented studies address different objectives presented in detail in Chapter 3. To allow the reader to easily recognize each separate work, the content of each study is introduced at the beginning of each subsection in Chapter 5.

Finally, **Chapter 6** summarizes and gathers the main conclusions from each investigation, highlighting the important results and outcomes. It also provides numerous suggestions for future work to simplify future studies on the effect of impact characteristics on the fundamental phenomena arising at the particle/substate interface.

CHAPTER 2

LITERATURE REVIEW

Review of the in-flight and impact process phenomena occurring during the CGDS is provided in this chapter. It will present findings and theories related to the current thesis topics. The review will cover the following subjects;

1. Cold gas dynamic spray historical background
2. Gas dynamics principles for converging/diverging nozzles
3. Computational fluid dynamics
4. Particle-laden flows
5. Particle velocity-temperature
6. Particle impact ensuing phenomena
7. Particle bonding
8. Particle and substrate characteristics influence on deposition
9. Finite element modeling
10. Particle microstructure

2.1 Cold Gas Dynamic Spray (CGDS) Process

2.1.1 Background

Although designed in early 19th century, it is only in 1980 that wind tunnel experiments lead to the creation and patent of a process referred to the "cold gas dynamic spray", which the working principles were based on the use of a converging/diverging nozzle (Ref 65). The CGDS process, also referred to as Cold Spray (CS), was re-discovered in the 1980's at the Institute of Theoretical and Applied Mechanics in Novosibirsk Russia (Ref 21). Its deposition and working principles have been found and revealed during the study of two-phase flow interactions (Ref 83,84). Small aluminum tracer particles have been injected in a supersonic wind tunnel and successful deposition has been discovered upon their impact with an end-plate. Alkhimov *et al.* have published results based on spatial and temporal laser diagnostic methods, i.e. laser Doppler velocimetry (LDV), laser sheet photographs and pulsed Schlieren photography, which allowed the visualisation of the particles within the flow and permitted the measurements of individual particle in-flight velocity prior and after impact (Ref 85). Figure 2.1 illustrates the influence of flow and target surface on particle trajectory and rebound velocity.

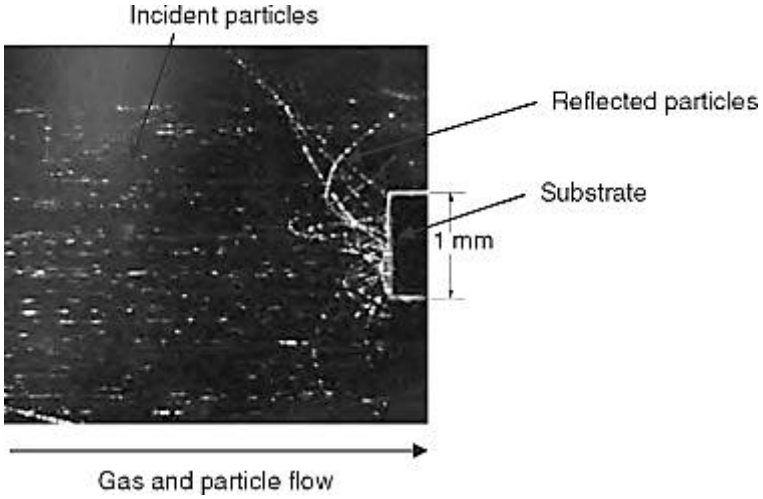

Figure 2.1: The impact process of 30-60µm Cu particles traveling at 150m/s recorded through laser sheet photography technique (Ref 83)***. (Reproduced with permission of Elsevier)***

In 1987, a pre-heating chamber was added to the original design, and in 1989, a device was designed to include separate powder and gas flow injections. Since then and after countless filed patents, the CGDS has become a commercial process used to deposit protective coating layers (Ref 52,55,86), restore components dimensional features (Ref 59,62,87), and form bulk material, i.e. additive manufacturing process (Ref 75,88). In addition, Karashin *et al.* proposed in 1996 a modified version

of the patented CGDS, in which the particles are injected into the diverging nozzle section, instead of the stagnating converging part (Ref 65).

2.1.2 Process overview

Based on Alkimov *et al.* and Karashin patents, the CGDS process is divided into two main systems based on the powder material injection location; high pressure cold spray (HPCS) and low pressure cold spray (LPCS). The former utilizes a powder injection located in the converging nozzle part, while the latter injects the powder material in the diverging nozzle section. In both systems, two gas streams enter the converging/diverging de-Laval nozzle. The first, referred to as the propulsive/carrier gas, passes through a powder feeder after which it becomes loaded with the powder feedstock material. The second stream, referred to as the driving gas, passes at high pressure through a gas heater to reach high stagnation temperature. The driving gas then accelerates as is travels through the converging/diverging nozzle to supersonic velocities, by conversion of thermal energy to kinetic energy. The general features of the HPCS system are illustrated in Figure 2.2. The powder feeder is operated at a pressure near or superior to the main gas stream local pressure at the injection point, which can reach values above 4MPa. The HPCS process design allows for powder preheating by the main gas flow in the pre-chamber section, as highlighted in Figure 2.2, prior to its acceleration after the nozzle throat.

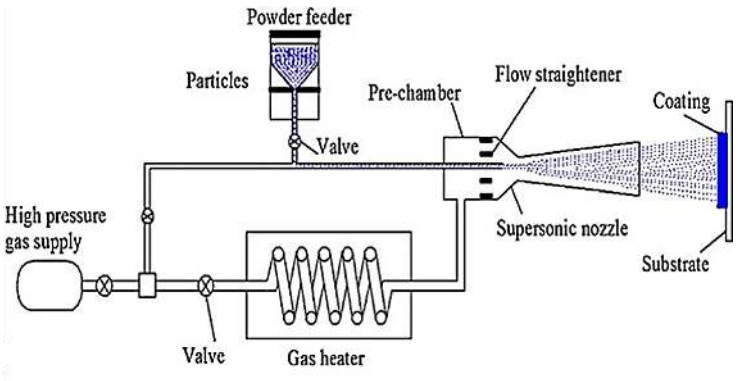

Figure 2.2: High pressure CGDS system layout with powder injection occurring upstream in the stagnating gas of the converging nozzle section (Ref 89)***. (Reproduced with permission of Elsevier)***

In Figure 2.3, illustrating the LPCS system, it is shown that the powder is injected after the throat.

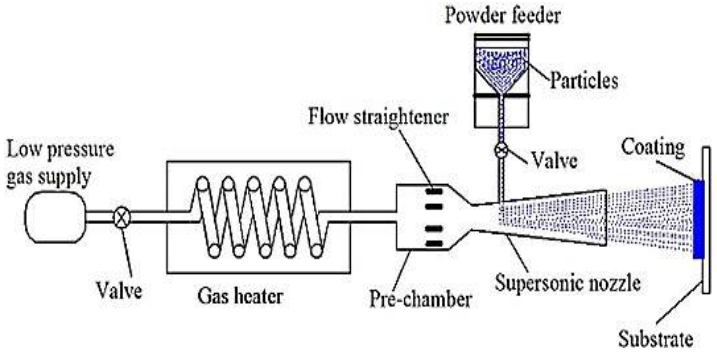

Figure 2.3: Low pressure CGDS system showing the downstream, in the supersonic flow, powder injection (Ref 90)***.***
(Reproduced with permission of Springer Nature)

In the LPCS design, the local gas pressure after the throat is restricted to normally 1.7MPa, which ensures that atmospheric pressure is enough to drive the powder material into the nozzle main gas stream. In addition, the range of nozzle expansion limits the Mach number increase at the outlet of the nozzle to usually < 3, which altogether lowers the accessible particle velocity. These features make theLPCS system more flexible and the equipment cheaper. Since the injection is made inside the supersonic gas flow, the particles accelerate at high rates immediately after entering the nozzle but at the cost of remaining at very low in-flight temperatures.

2.1.3 Other thermal spray processes

The CGDS coating deposition process belongs to the family of thermal spray processes (Ref 91,92). Its main advantages over common thermal spray methods, i.e. electricity arc spray, plasma spray and high velocity oxyfuel, is the low working carrier gas stagnation temperature and resulting solid state particle deposition, as depicted in Figure 2.4, which limit the oxidation, decomposition, formation of metastable phases, uncontrolled grain growth in powder material during their flight in the nozzle and limits the substrate surface temperature rise. Although in the 1980's, it was believed that particle melting was necessary for deposition, it was quickly found that successful particle bonding was achieved even at low temperature due to the impact resulting material characteristics that occur at the particle/substrate \contact interface. Although, it provides great control over the particle characteristics during and upon impact, low particle temperature limits the variety of materials that can be sprayed using the CGDS process to materials capable of plastic flow. It is for this reason that the process only effectively works exclusively for metals, polymers and composites where one of the components ensures proper degree of material plasticity.

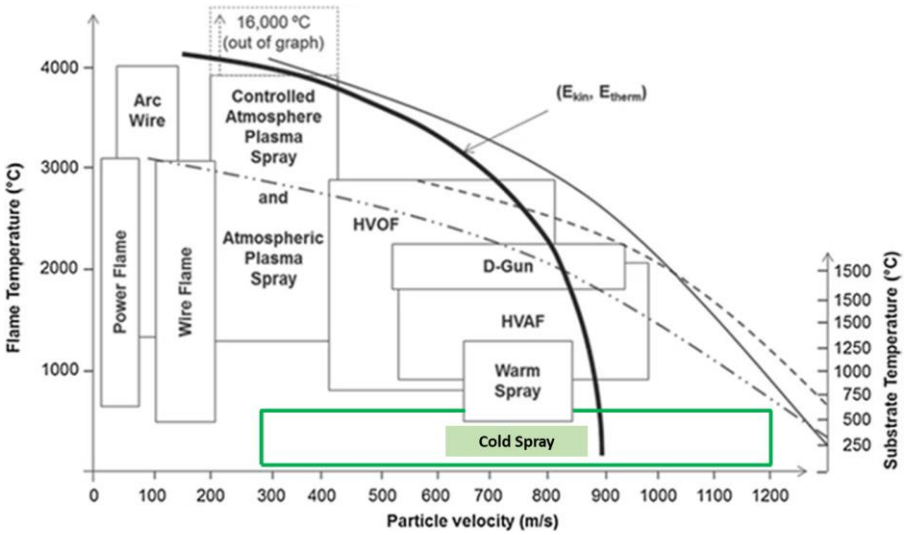

Figure 2.4: Cold spray process particle velocity, substrate temperature and working gas temperature in comparison to other important thermal spray processes (Ref 90)***. E_{kin} and E_{therm} stand for kinetic energy and thermal energy respectively. (Reproduced with permission of Springer Nature)***

To fully capture the CGDS working principles, the process can be divided in multiple segments and analysed from the perspective of gas dynamics, particle/gas interactions, particle impact and bonding mechanisms. These segments will be covered in details in the upcoming Chapter 2 sections.

2.1.4 Gas dynamic principles

The CGDS process relies on the energy imparted on the particles by the gas as they travel within the high-speed flow. Coating deposition, bonding and impact phenomena predominantly depend on particle velocity and temperature, for a given material, which renders the study of the gas stream properties important. The stored energy (enthalpy) in the high pressure and temperature flow is efficiently converted to kinetic energy using a converging/diverging nozzle with an appropriate pressure ratio between the nozzle's throat and outlet following gas dynamics principles covered in the ensuing paragraphs.

Fluids with appreciable change in density (dρ), due to a variation of pressure (dP) and temperature (dT), as a result of flow are called *compressible flows.* The rate of change of fluid density with respect to pressure can be associated to the speed of sound. Sound is described as an infinitesimal pressure wave, which creates a change in pressure, density and velocity by propagating steadily through a fluid. Its speed is defined as the distance traveled per unit time by a pressure wave that propagates through the studied fluid. By the continuity and the conservation of momentum equations across the pressure wave front, the following relations are obtained:

$$\frac{d\rho}{\rho} = \frac{dV}{c}, \qquad \textit{Eq. 1}$$

and

$$c = \sqrt{\left(\frac{\partial P}{\partial \rho}\right)_s} = \sqrt{\frac{k_{st}}{\rho}}, \qquad \textit{Eq. 2}$$

where the subscript *s* refers to a process of constant entropy as the small variation in pressure and temperature produce a nearly reversible process. The speed of sound is, thus, also defined as the square root of stiffness, k_{st}, over density, ρ, of a material or the instantaneous change in elastic stress due to the variation of density. Given that the fluid is a perfect gas and utilising the $P = \rho RT$ ideal gas law, the speed of sound of an ideal gas can be obtained through:

$$c_{gas} = \sqrt{\gamma RT}, \qquad \textit{Eq. 3}$$

where R is the gas universal constant (8.3144 J/mol·K) divided by the molecular gas weight, *W*, and γ is the ratio of specific heats, $\gamma = \frac{C_p}{C_v}$. Hence, a fluid characterized by a low speed of sound requires a low change of pressure to generate a certain change in density, which based on the previously presented relations makes that fluid more compressible than one that is described with a high speed of sound. Additionally, as described in Eq. 3, the speed of sound of an ideal gas is influenced solely by the gas temperature, *T*, and nature, γ. Such that, the higher the temperature and the specific heats ratio, the higher can the gas velocity be at the exit of the nozzle, which is desired in the CGDS process. From Table 2.1, which presents the speed of sound of common gases, it can be concluded that due to its low reactivity and abundant availability, i.e. low cost, the nitrogen gas is best suited for commercial CGDS applications.

Table 2.1: Speed of sound, c, of common gases at standard pressure and temperature.

Gases	**Speed of sound**
Carbon dioxide, CO_2	269m/s
Argon, Ar	322m/s
Air, $0.78N + 0.21O_2 + 0.093Ar + 0.0007CO_2$	346m/s
Nitrogen, N	351m/s
Helium, He	1016m/s
Hydrogen, H	1315m/s

The influence of speed of sound over the fluids compressibility and pressure pulse pattern is quantified using the Mach number:

$$M = \frac{V}{c}. \quad \textit{Eq. 4}$$

The gas flow characteristics, hence, depend on the flow velocity and the local speed of sound. The compressible effect of flows initiates at subsonic (0.3 < M < 1) speeds and fully develop at M > 1. The flow patterns and phenomena occurring in a real system comprising a compressible fluid are very complex but can be analysed and interpreted using a combination of assumptions. In such simplified analysis, the changes in flow properties are hypothesised to occur and follow:

1. *Isentropic gas flow*: Considered adiabatic and frictional effects are assumed to be small. Therefore, the flow can also be considered reversible and thus isentropic.
2. *One-dimensional gas flow*: gas properties are uniform across the perpendicular flow direction.
3. *Ideal gas*.
4. The constant-pressure ($dh = C_p dT$) and constant-volume ($du = C_v dT$) specific heats of the gas are considered constant; calorically perfect gas.

Hence, if the flow inside a converging/diverging nozzle is regarded as a control volume, which has no external source of energy or work added to it, other than the pressure and heat at the stagnation location and if heat and friction losses are negligible, then the first law of thermodynamics can be written as the stagnation enthalpy of the control volume:

$$h_0 = h + \frac{V^2}{2} = \text{constant}, \quad \textit{Eq. 5}$$

where h_0 is the enthalpy of the fluid when the velocity is equal to 0, and V is the flow velocity. The assumed constant specific heat capacity at constant pressure and the ideal gas law provide:

$$C_p = \gamma R/(\gamma - 1). \quad \textit{Eq. 6}$$

The stagnation temperature, T_0, and the mass flow rate, $\dot{m}$, of the gas are set by the user during the CGDS process. Hence, using the variables set by the user along with Eq. 6, the gas properties at any location inside the nozzle can be obtained through the following isentropic relations:

$$\frac{T_0}{T} = 1 + \frac{\gamma - 1}{2} M^2, \quad \textit{Eq. 7}$$

which clearly demonstrates the energy conversion from enthalpy to kinetic energy,

$$\frac{P_0}{P} = \left(1 + \frac{\gamma - 1}{2} M^2\right)^{\frac{\gamma}{\gamma - 1}}, \quad \textit{Eq. 8}$$

and

$$\frac{\rho_0}{\rho} = \left(1 + \frac{\gamma - 1}{2} M^2\right)^{\frac{1}{\gamma - 1}}. \qquad \textit{Eq. 9}$$

Eq. 9 shows that as the gas Mach number increases, the density is required to drastically decrease. As it will be described in a following section, this decrease in density decreases the drag force applied on the particles traveling inside the gas, which consequently reduces their velocity. Hence, expanding the gas to higher Mach numbers inside the converging/diverging nozzle may not provide higher particle velocities. For this reason, the CGDS process has been designed to work under the supersonic regime with M=2 to 3 instead of the hypersonic regime. As shown in Figure 2.5, in the incompressible regime, the enthalpy remains constant. At high flow velocities, the influence on enthalpy, therefore temperature and consequently pressure, is affected through the perfect gas law.

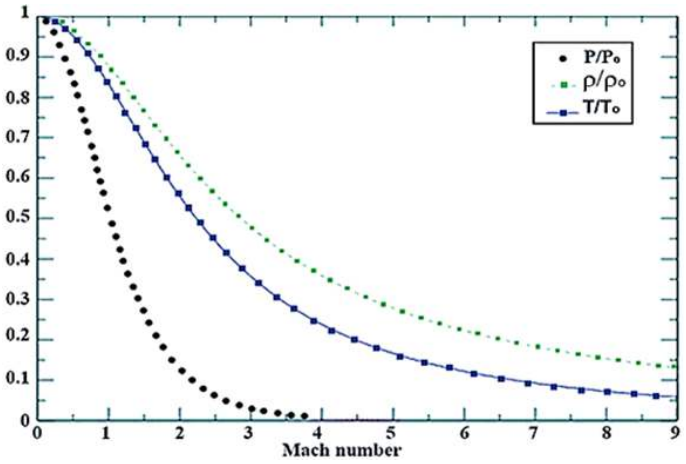

Figure 2.5: Static stagnation ratio of gas properties as a function of stream Mach number (Ref 93)***. (Reproduced with permission of Springer Nature)***

In addition to the first law of thermodynamics, the conservation of mass can also be used across the same control volume and with the relations given in Eq. 1 and Eq. 2 to yield;

$$\left.\begin{array}{c} \dot{m} = \rho V A \\ -\partial P = \rho V \partial V \\ \partial P = c^2 \partial \rho \end{array}\right\} = (1 - M^2)\frac{\partial V}{V} = -\frac{\partial A}{A} \qquad \textit{Eq. 10}$$

At M<1, reducing the cross-sectional area in the direction of the flow, $\partial A < 0$, is the sole way to induce flow acceleration ($\partial V > 0$), which is an intuitive process. With decreasing area, the velocity will keep increasing at, however, lower rate as the velocity nears the speed of sound. This decrease in rate is directly affected by the $(1 - M^2)$ term, which decreases as M increases with velocity. For M>1, Eq. 10 states that the only way to increase the gas stream velocity is by increasing the area, $\partial A > 0$. Hence, to ensure proper constant acceleration of the flow, a converging/diverging nozzle

has to be utilized, which explains its usage in the CGDS process, i.e. in the stagnating converging section of the nozzle (M<1) the area is reduced and the flow accelerated, once it crosses the throat with proper conditions, the gas will keep accelerating in the diverging portion. The condition that needs to be reached at the throat to allow proper gas acceleration throughout the nozzle is a flow with M=1.

Although the previous flow analysis process can be used for isentropic flows, there exists certain conditions of stagnation pressure and back pressure, i.e. nozzle exit pressure, that result in a non-isentropic stream and/or that do not provide proper conditions at the throat. Figure 2.6 illustrates the gas behavior for various back pressure and exit pressure ratios.

- If $\Delta P = 0$, the gas will remain static and no acceleration will be produced, i.e. no transformation from enthalpy to kinetic energy.
- As the back pressure is reduced, the flow accelerates in the direction of the nozzle exit from the converging section towards the diverging region, as similarly observed previously through Eq. 10 and area variations. If, in addition, a subsonic (M<1) condition is reached at the throat, the flow will decelerate in the diverging part of the nozzle**. (Case a)**
- Upon further decrease of the back pressure, and when a sonic (M=1) behavior is obtained at the throat, two cases can appear;
    - If the decrease in pressure is not low enough to sustain the acceleration in the nozzle diverging section, the gas will still decelerate, reconverting kinetic energy into enthalpy. **(Case b)**
    - If the exit pressure is below a critical value, i.e. below case **c** pressure, the flow will accelerate in the diverging section and a supersonic regime will be reached. However, a normal shock wave will be necessary to equalize the flow pressure with the back pressure, after which the flow velocity, temperature and density drastically decrease. The lower the exit pressure, the further downstream will this shock wave appear **(Case c)** until it reaches **Case d**.
- **Cases e and g** represent over-expanded and under-expanded flows, respectively. In the over-expanded case, the exhaust pressure is found to be lower than the registered back pressure from case **f**. A series of irreversible oblique shocks and expansion waves are then required at the exit to increase the flow pressure. On the other hand, an under-expanded flow requires additional expansion to reduce the exhaust pressure to the back pressure. Expansion waves and oblique shocks then form to ensure that the back pressure is reached.

- Finally, **Case f** represents an ideal isentropic evolution characterized by an absence of strong disturbances inside and outside the nozzle. This occurs when the gas inside the nozzle reaches exactly the back pressure once it arrives at the exit.

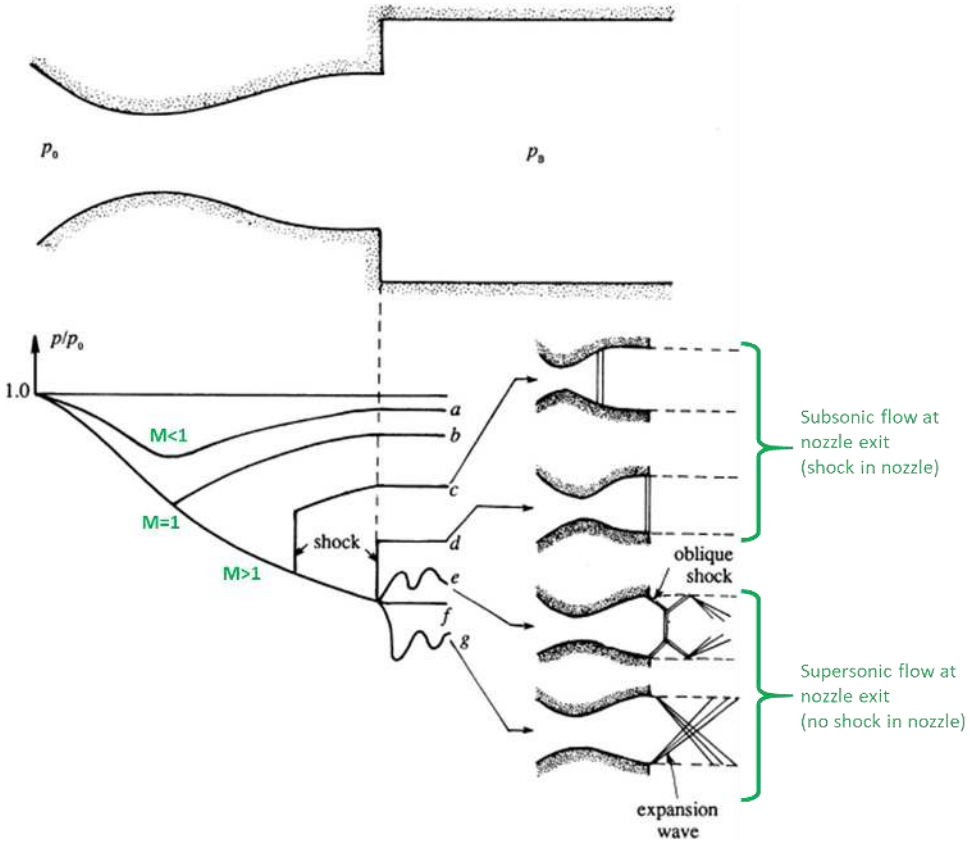

Figure 2.6: Gas flow behavior based on the stagnation and back pressure ratio. (Ref 94)***.***
(Reproduced with permission of Elsevier)

When the sonic regime is reached at the throat, the stagnation pressure, P_0, and the properties at the throat, denoted by the subscript '*', are calculated using the previously shown isentropic procedure (Eq. 7 - Eq. 9):

The temperature at the throat, T^*, is obtained by:

$$T^* = \frac{T_0}{1 + (\gamma - 1)/2}, \text{considering a } \mathrm{M}^* = 1 \text{ state,} \qquad \textit{Eq. 11}$$

then the gas velocity at the throat is given by;

$$V^* = \sqrt{\gamma R T^*}. \qquad \textit{Eq. 12}$$

Imposing a process gas flow rate allows to calculate the sonic gas density, i.e. at the throat;

$$\rho^* = \frac{m^*}{V^* A^*} \qquad \textit{Eq. 13}$$

where A^* is the cross-sectional area at the throat. In addition, using the ideal gas law, the gas pressure at the throat is obtained as follow;

$$P^* = \rho^* R\, T^* \qquad \textit{Eq. 14}$$

From the throat pressure, the stagnation pressure can be computed by;

$$P_0 = P^* \left(\frac{T_0}{T^*}\right)^{\gamma/\gamma-1} = P^* \left(1 + \frac{(\gamma-1)}{2}\right)^{\gamma/(\gamma-1)}. \qquad \textit{Eq. 15}$$

Finally, the area ratio can be related to the Mach and flow property as follow;

$$\frac{A}{A^*} = \frac{1}{M}\left[\frac{1}{(\gamma-1)}\left(1 + \frac{(\gamma+1)}{2} M^2\right)\right]^{(\gamma+1)/2(\gamma-1)}, \qquad \textit{Eq. 16}$$

which allows to predict the exit Mach number for a designed nozzle. The throat area, A^*, typically varies between 1 to 3mm in current commercial CGDS systems and its size usually depends on the maximum gas flow rate the system has been designed to handle based on the gas heater system capacity. The gas mass flow rate, constant throughout the nozzle, can be expressed as;

$$\dot{m} = \frac{A^* P_0}{\sqrt{T_0}} \sqrt{\frac{\gamma}{R}} \left(\frac{\gamma+1}{2}\right)^{\frac{-(\gamma+1)}{2(\gamma-1)}}. \qquad \textit{Eq. 17}$$

In the CGDS process, nozzles are designed to operate as close as possible to the isentropic scenario, shown in Figure 2.6 case **f**, as to avoid flow disturbances and large variations in flow properties, which can induce uncertain deposition properties. Commonly, however, for practicality reasons, a regular nozzle is used with numerous gas stagnation properties resulting in over-expanded or under-expanded regimes. Although, shocks inside the nozzle can be avoided, they cannot completely be eliminated in the CGDS spray process. After the nozzle exit and pressure readjustment processes, the supersonic gas flow is directed towards a substrate surface upon which at impact it is required to decelerate to stagnation. To successfully achieve such drastic change in velocity a bow shock is generated, as depicted in Figure 2.7, at the targeted material surface. Abrupt changes in gas properties and sudden increase in flow density in the static region affects the flow trajectory and particle in-flight properties, i.e. significant influence on smaller particles traveling with lower inertia. The strength of the bow shock increases with increasing gas velocity, which additionally limits the gas M to optimized values between 2 to 3.

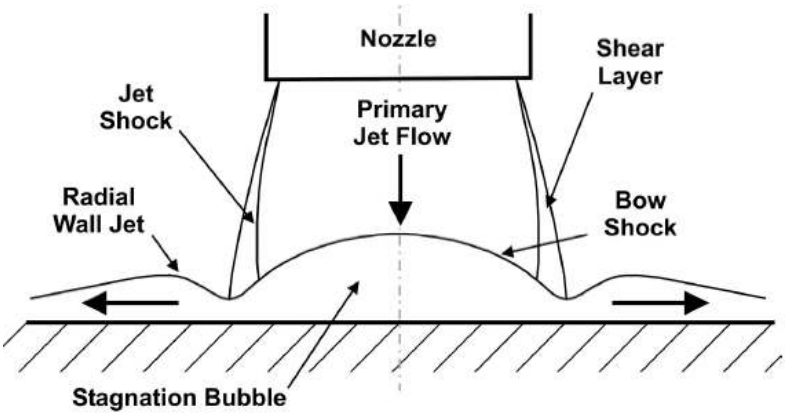

Figure 2.7: Illustration of supersonic flow impingement resulting flow features at the substrate interface. (Ref 95)**.**
(Reproduced with permission of Elsevier)

The influence of the bow shock on particle velocity can be reduced by increasing the nozzle to substrate surface distance, called the stand-off distance (SOD). The larger the SOD the smaller is the gas velocity at the impact with the substrate surface and the lesser is the bow chock energy, i.e. disappearing if high enough distance is reached. However, although the bow shock effect is diminished with SOD, particles traveling longer times within a decelerating flow, i.e. negative velocity, can also experience drastic decrease in velocity. Hence, for optimal deposition, SOD, particle size and bow shock features need to be evaluated.

The analysis presented in the current sub-section is based on isentropic assumptions. However, in reality, irreversible features in the CGDS process exist and they occur mainly due to the presence of friction, heat losses and viscous effects (Ref 96). These irreversible effects reduce the available enthalpy that is transformed to kinetic energy, consequently lowering gas velocities at exit. The boundary layer appearing at the nozzle walls can decrease the velocity of the gas up to 67% from the calculated isentropic value (Ref 97). Larger nozzles with higher area/length ratio can reduce the disturbances generated from the boundary layer and improve the flow velocity (Ref 97).

2.2 Particle-Laden Flows

The flow regimes encountered by micron-sized particles traveling in the CGDS process are such that commonly available particle heat transfer and momentum equations need to include appropriate corrections. Figure 2.8 illustrates the various flow regimes encountered by particles traveling in a rocket nozzle, which demonstrates that the use of common correlations, restricted to continuum, incompressible flow and Reynolds number below 1, is not appropriate for the analysis of supersonic micron-size particle-laden flows (Ref 10,98–100). From Figure 2.8, it is observed

that the flow regimes under which the particle travel are dependent on the particle Reynolds number, Re_p, and Mach number, M_p, defined as;

$$Re_p = \frac{\rho_g |V_g - V_p| d_p}{\mu_g} \quad \text{and} \quad M_p = \frac{|V_g - V_p|}{c}, \text{respectively,} \qquad \textit{Eq. 18}$$

where the subscripts g and p refer to the gas and particle respectively and μ is the gas dynamic viscosity. To assess the flow regimes and their deviation from the continuum approximation, the particle Knudsen number, Kn_p, is used and defined as;

$$Kn_p = \frac{\lambda}{L_{characteristic}} = \sqrt{\frac{\pi\gamma}{2}}\left(\frac{M_p}{Re_p}\right) \sim \frac{M}{Re}, \qquad \textit{Eq. 19}$$

where λ is the mean free path of molecules and $L_{characteristic}$ in the CGDS process refers to the particle diameter. The continuum criterion (molecular structure can be ignored) is followed as long as $Kn_p \ll 1$, as depicted in Figure 2.8. The fluid is considered continuous and its velocity at the particle wall is set by the no-slip condition, i.e. must be zero, as seen in the insert of Figure 2.8.

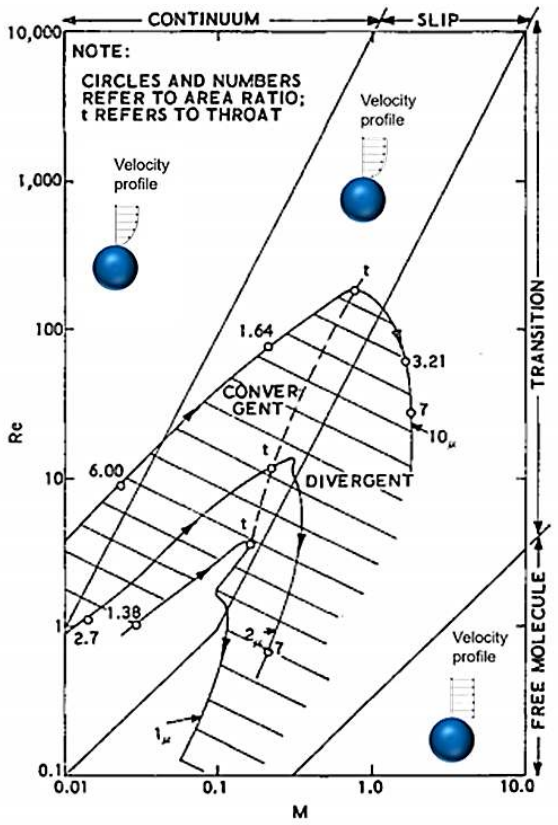

Figure 2.8: Computer calculated flow regimes encountered by particles traveling in a rocket nozzle with size ranging between 1 to 10μ. Inserts of particle velocity profile and contact surface condition (slip-no slip) for different flow regimes are included (Ref 10)***. (Reproduced with permission of AIAA)***

Based on the definition of Kn_p, at very high Reynolds numbers (Re$\gg$ 1) the flow is dominated by compressibility (M_p). At very low Reynolds number, however, rarefaction effects become dominant. In continuum, a no-slip condition can be applied at the particle/gas interface as a very large number of molecular collisions occur. With increasing Kn_p, a departure from the no-slip condition arises. When into the slip flow regime, a temperature and velocity jump is seen at the particle surface. The particle velocity profile included in the slip regime of Figure 2.8 illustrates this jump in velocity. As the Knudsen number increases to the free molecular state flow, the molecules impact and reflect from the particle's surface with negligible molecular-molecular interactions. Hence, the gas molecules arriving at the particle surface leave with full stream velocity, as depicted in the corresponding insert of Figure 2.8.

2.2.1 Flow structure characteristics

Many studies in the CGDS field utilize correlations limited to low speed and incompressible flows to describe the particle motion and occurring heat transfer processes, i.e. $C_D = f(Re_p)\ and\ Nu = f(Re_p)$, while only a limited amount of studies have included the effects of compressibility (Ref 101,102). Figure 2.9a shows that at M_p >0.6, important compressibility features start to emanate near the particle upper surface and appear as weak expansion waves followed by a lambda shock structure, as the flow becomes locally supersonic. The lambda-shock patterns lead to early flow separation. As the Mach number increases, i.e. increasing particle velocity lag, a bow shock is formed near the particle surface and the flow separation is moved further back due to the elimination of the lambda-shock pattern, as shown in Figure 2.9b. Aerodynamic/recovery heating of the particle results from the important friction and compression found near the particle surface that converts the kinetic energy of motion into heat within a thin layer surrounding the particle surface.

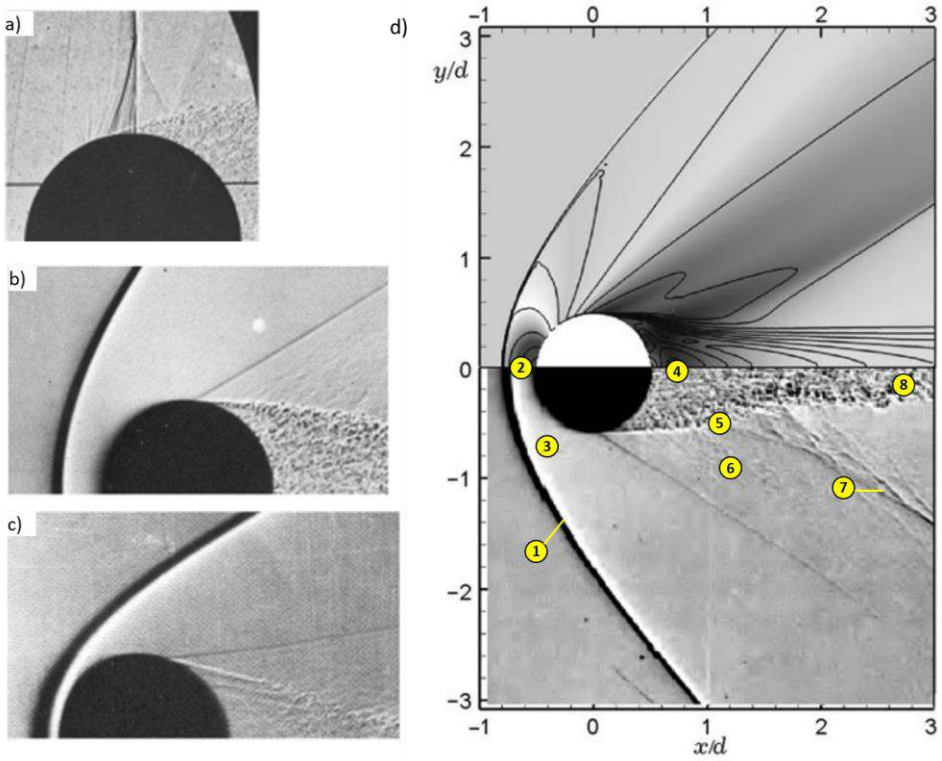

Figure 2.9: Particle with Re_p=9x10^5 at a) M_p=0.86, b) M_p=1.53 and c) M_p=3. d) Calculated Mach number field (top) and static pressure obtained with experimental measurements (Ref 103,104)***. The flow patterns shows; 1: attached bow shock, 2: subsonic region, 3: flow at M=1, 4: Recirculating zone, 5: shear flow, 6: Expanding Prandtl-Meyer, 7: Rear shock and 8: turbulent vortex. (Reproduced with permission of AIAA and Springer Nature)***

2.2.2 Particle motion

2.2.2.1 Experimental observations

The particle in-flight velocity and trajectory have been visualized and characterized using particle imaging velocimetry (PIV) (Ref 24,77,105–107), shown in Figure 2.10a, laser two-focus velocimetry (L2F) (Ref 105,108,109) and doppler picture velocimetry (DPV) (Ref 19,46,75,110–112), i.e. cold spray meter (CSM) depicted in Figure 2.10b.

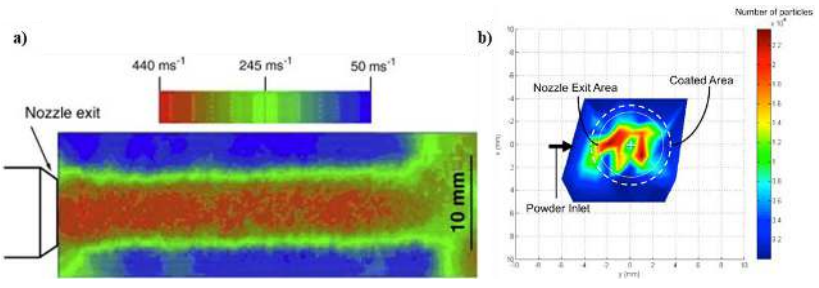

Figure 2.10:a) Particle stream velocity measured using PIV method at the nozzle exit (Ref 113) ***and b) CSM particle flow rate mapping at SOD=25mm*** (Ref 87)***. (Reproduced with permission of Elsevier)***

2.2.2.2 Empirical analysis

The particle velocity experimental measurements are used to develop analytical and numerical particle velocity models. The particulate phase in the CGDS process is commonly assumed to be sufficiently dilute to express its velocity as follow;

$$m_p a_p = C_D \rho (V - V_p)|V - V_p| \frac{A_p}{2}, \qquad \textbf{Eq. 20}$$

where m_p, a_p, C_D, v_p and A_p are the particle mass, particle acceleration, drag coefficient, particle velocity and cross-sectional area of particle, respectively. Inserting the definition of ideal gas speed of sound, $c_{gas} = \sqrt{\gamma RT}$, Mach number (Eq. 4) and using the ideal gas law, the particle acceleration can be expressed as;

$$a_p = \frac{P_0}{2RT_0}\left(1 + \frac{\gamma - 1}{2}M^2\right)^{-\frac{-1}{\gamma - 1}} \left(M \sqrt{\gamma RT_o \left(1 + \frac{\gamma - 1}{2}M^2\right)^{-1}} - V_p \right)^2 C_D \frac{A_p}{2Vol_p \rho_p}. \qquad \textbf{Eq. 21}$$

It is customary to run the CGDS process at elevated gas stagnation pressures, up to 5MPa, to maximize the gas density. However, the benefits of increased pressure level-off based on particle nature and size (Ref 114). Eq. 21 also reveals that the particle geometry and volume as well as the particle material density affect its momentum inside the gas stream.

2.2.2.3 Drag coefficient

Accurate representation of the particle drag coefficient over a wide range of flow conditions has been shown to be necessary for the calculation of particle velocity in the CGDS process, as explained in the introduction of section 2.2. Table 2.2 presents a few of the drag coefficients that have been utilised in CGDS process modeling.

Table 2.2: Drag coefficient, C_D, correlations used in CGDS process (Ref 27)***. (Only a few correlations are shown for conciseness)***

Authors	Equations	Range of applicability	Flow structure	References studies in CGDS
Crowe* (Ref 99)	$C_D = \left(C_{D(incompressible)} - 2\right)\text{x}\exp\left(-3.07\gamma^{1/2}\left(\frac{M_p}{Re_p}\right)g(Re)\right) + \frac{h(M_p)}{\gamma^{1/2}M_p}\text{x}\exp\left(\frac{-Re_p}{2M_p}\right) + 2$	$0.2 < Re_p < 100000$ $1 < M_p < 2$	Compressible	(Ref 115,116)
Morsi and Alexander (Ref 117)	$C_D = a_1 + \frac{a_2}{Re_p} + \frac{a_3}{Re_p^2}$, where $a_{1,2,3}$ are constants	$0.1 < Re_p < 50{,}000$	Incompressible	(Ref 118,119)
Clift et al. (Ref 120)	$C_D = \frac{24}{Re_p}\left(1 + 0.15Re_p^{0.687}\right) + \frac{0.42}{1 + 4.25x10^4 Re_p^{-1.16}}$	$Re_p < 300{,}000$ $M_p > 0.4$	Incompressible/ Compressible	(Ref 121,122)
Henderson** (Ref 98)	C_{D1} for $M_p \leq 1$ C_{D2} for $1 < M_p < 1.75$ C_{D3} for $M_p \geq 1.75$	Across all M_p	Compressible	(Ref 112,123)

* $g(Re) = \frac{1+Re_p(12.278+0.584Re_p)}{1+11.278Re_p}$ and $h(M_p) = \left[\frac{5.6}{(M_p+1)}\right] + 1.7\sqrt{\frac{T_p}{T}}$

** Refer to the (Ref 81) publication for details regarding the extensive equation development (C_{D1}, C_{D2} and C_{D3}) across numerous flow regimes and characteristics

2.2.3 Particle temperature

The difficulty in measuring particle temperature stems from the particle small size, high velocity and more importantly low temperature, which explains the absence of any temperature measurement in the CGDS since its invention (Ref 32,124). To determine the particle in-flight temperature within the CGDS flow, it is necessary to define an overall average particle heat transfer convection coefficient, $\bar{h}$, which accounts for all flow features surrounding the particle surface, as shown previously in Figure 2.9. The total heat transfer arising at the particle surface can be expressed as:

$$q = \bar{h}A_s(T_w - T_p) \qquad \text{with} \qquad \bar{h} = \frac{1}{A_s}\int_{A_s} h\mathrm{d}A_s, \qquad \textit{Eq. 22}$$

where A_s is the particle surface and T_w is the gas temperature in the boundary layer, i.e. wall. A dimensionless temperature gradient, the Nusselt Number, defined as;

$$\overline{Nu} = \frac{\bar{h}d_p}{k_g}\ , \quad \overline{Nu} = f(Re_p, M_p, Pr), \qquad \textit{Eq. 23}$$

where k_g is the gas thermal conductivity and d_p is the particle diameter, can be used to provide a measure of the convection heat transfer coefficient. The simplicity of the Ranz-Marshall correlation, given by Eq. 24, has been very attractive and its use, consequently, very abundant in the field:

$$Nu = 2 + 0.6Re^{0.5}Pr^{0.33}. \qquad \textit{Eq. 24}$$

However, the Ranz-Marshall correlation has been developed using droplet evaporation experiments in low Reynolds numbers (0-200) and low Mach numbers (Ref 125). Hence, it does not account, amongst many other flow features, for the effect of Mach number, compressibility and rarefaction on heat transfer, that are known to occur in supersonic particle laden flows. Other Nu correlations have been proposed in the literature, which account for the effects of Kn_p, Re_p and M_p on heating processes but the absence of particle temperature measurements in the CGDS process limits the confirmation of their accuracy and suitability in the field. Table 2.3 presents few of the proposed Nu correlations.

Table 2.3: Nusselt number correlation, Nu, used in CGDS process (Ref 27)***. (Only a few correlations are shown for conciseness)***

Authors	Equations	Range of applicability	Flow structure	References studies in CGDS
Kavanau* (Ref 126)	$Nu = \dfrac{Nu_0}{1 + 3.42 Nu_0 \dfrac{M_p}{Re_p Pr}}$	Accounts for rarefication and compressibility	Compressible and incompressible	(Ref 101)
Meingast **	$Nu = 2 + 0.4 Re_p^{0.5} Pr^{1/3} \exp(0.1 + 0.872 M_p)$	$M_p > 0.24$ $T_g > T_p$	Compressible	(Ref 101,127)
Whitaker (Ref 128)	$Nu = 2 + \left(0.4 Re_\infty^{0.5} + 0.06 Re_\infty^{2/3}\right) Pr_\infty^{0.4} \left(\dfrac{\eta_\infty}{\eta_p}\right)^{1/4}$	$3.5 \leq Re_\infty \leq 7.6\text{x}10^4$ $0.71 \leq Pr_\infty \leq 380$ $1.0 \leq \left(\dfrac{\eta_\infty}{\eta_p}\right) \leq 3.2$	Incompressible and compressible	(Ref 129)
Fiszdon et al. (Ref 130)	$Nu = 2 + 0.6 Re_\infty^{1/2} Pr_\infty^{1/3} \left(\dfrac{\rho_\infty \eta_\infty}{\rho_p \eta_p}\right)^{0.6}$	High Mach number	Compressible	(Ref 129)
Lee and Pfender (Ref 129)	$u = 2 + 0.6 Re_\infty^{1/2} Pr_\infty^{1/3} \left(\dfrac{\rho_\infty \eta_\infty}{\rho_p \eta_p}\right)^{0.6} \left(\dfrac{C_{p,\infty}}{C_{p,p}}\right)^{0.38}$	High Mach number	Compressible	(Ref 129)

* Nu_0 is the incompressible Nu number

** Original development unavailable (Ref 131)

2.2.3.1 Transient conduction

Upon particle injection in the nozzle, a transient conduction process occurs as the solid particle experiences a sudden change in thermal environment. If an overall energy balance on the entire particle is performed, the resulting balance relating the rate of heat gain (or loss), to the rate of change of internal energy, can be written as;

$$\overbrace{\bar{h}A_s(T_\infty - T_p)}^{Rate\ of\ heat\ gain\ at\ the\ surface} = \overbrace{\rho V c \frac{dT}{dt}}^{Rate\ of\ change\ of\ internal\ energy} \quad \textit{Eq. 25}$$

where $c = c_p = c_v$ is the material specific heat capacity and V is the volume. Integrating from the initial conditions leads to the following equation, which can be used to determine the time required for the particle to reach a certain temperature;

$$\frac{T_p - T_\infty}{T_0 - T_\infty} = \exp\left[-\left(\frac{hA_s}{\rho V c}\right)t\right], \quad \textit{Eq. 26}$$

where T_0 is the initial particle temperature. Provided that the particle temperature rise with time is not measurable in the CGDS process and that the particle temperature gradient, if any, is not possible to quantify, the assumption of homogeneous particle temperature can be made, under the lumped capacitance method (LCM), i.e. Biot number criterion, $Bi = \frac{hL}{k}$. However, the LCM has already been commonly used in many CGDS heat transfer studies without any proof of accuracy or applicability (Ref 32,107,114,132). If the particle temperature is assumed uniform and the LCM assumption accurate, the first law of thermodynamics yields;

$$m_p C_p \frac{dT_e}{dt} = A_{sp}\bar{h}(T_r - T_p), \quad \textit{Eq. 27}$$

where m_p, C_p, A_{sp} and T_r represent the particle mass, particle specific heat, particle surface area and the recovery temperature, respectively. The recovery temperature provides the temperature inside the boundary layer surrounding the particle during its flight in the gas stream, as discussed in section 2.2.1, and is described as;

$$T_r = T_g\left(1 + r\frac{\gamma - 1}{2}M_p^2\right), \quad \textit{Eq. 28}$$

where *r* is the recovery coefficient, generally close to 1 for gases (Ref 133,134).

2.3 Radiation Processes and Properties

To measure the particle temperature using radiation principles, the various heat fluxes that can be defined and observed at its surface must be reported. Four distinct radiation fluxes can arise and are summarized in Table 2.4, which describe the radiation over all wavelengths and in all directions.

If the radiation is incident on a *semi-transparent medium,* portion of the irradiation can be reflected (redirected with no influence on the particle, ρ), absorbed (radiation interacting with medium and increasing its internal energy, α) and transmitted (radiation crossing the medium, τ). It follows that;

$$\rho + \alpha + \tau = 1, \qquad \textit{Eq. 29}$$

where ρ is the fraction of irradiated radiation that is reflected by the particle, α represents the fraction that is absorbed and τ is the fraction of irradiation that is transmitted. If the surface is considered as *opaque*, Eq. 29 reduces to;

$$\rho + \alpha = 1. \qquad \textit{Eq. 30}$$

Table 2.4: Description of the various radiative fluxes present at the surface of an object.

Flux (W/m^2)	**Description**
Emissive power, *E*	Rate of the emitted radiation from a surface per unit area
Irradiation, *G*	Rate of the radiation that is incident on the surface per unit area (from surroundings)
Radiosity, *J*	Rate at which radiation is leaving a surface per unit area (emitted + reflected)
Net radiative flux, q''_{rad}, *J-G*	Net radiation rate leaving the analyzed surface per unit area

2.3.1 Planck distribution

A blackbody is defined as the perfect absorber and emitter and is used as a standard with which real surface radiative properties can be compared to. Planck has shown that the blackbody spectral intensity is given by;

$$I_{\lambda,b}(\lambda, T) = \frac{2hc_0^2}{\lambda^5[\exp(hc_0/\lambda k_B T) - 1]}, \qquad \textit{Eq. 31}$$

where h=6.626x10^{-34}J·s and k_B=1.381x10^{-23}J/K are the universal Planck and Boltzmann constants, respectively, c_0=2.998x10^8 m/s is the speed of light in vacuum, and T is the absolute temperature of the blackbody (K). The spectral emissivity is described as the emitted energy at the wavelength λ in the (θ, ϕ) direction per unit area normal to the defined direction. The spectral emissive power (dependence with wavelength), thus, is defined by the *Planck distribution*, or *Planck's law*, as follow for a black body (diffuse emitter, i.e. emitted radiation is independent of direction);

$$E_{\lambda,b}(\lambda, T) = \pi I_{\lambda,b}(\lambda, T) = \frac{C_1}{\lambda^5[\exp(C_2/\lambda T) - 1]}, \qquad \textit{Eq. 32}$$

where $C_1 = 2\pi hc_0^2$ and $C_2 = (hc_0/k_B)$. Figure 2.11 shows that the blackbody spectral distribution reaches a maximum for each temperature at a specific wavelength. Hence, with decreasing temperature, the radiation becomes more detectable at larger wavelengths and the emission is predominantly in the infrared region of the spectrum, shown previously in Figure 2.11, and invisible to the eye. Wien's Displacement law demonstrates;

$$\lambda_{max} T = C_3, \qquad \textit{Eq. 33}$$

where C_3=2898μm·K, which provides the wavelength at which maximum emissive power is obtained for a given temperature.

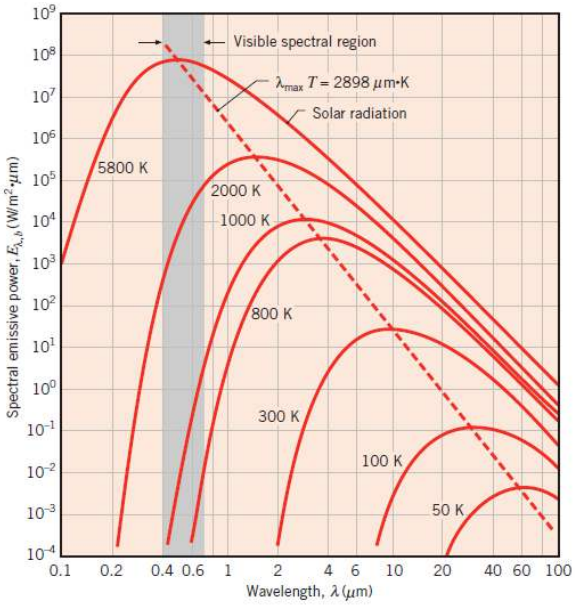

Figure 2.11: Spectral blackbody emissive power (Ref 135)***. (Reproduced with permission of John Wiley & Sons)***

However, the emission generated from real surfaces, differ from ideal blackbody behavior, as shown in Figure 2.12. The spectral radiation differs from the observed Planck distribution and the directional distribution may be different from diffuse.

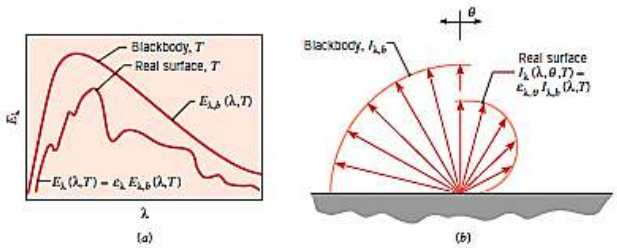

Figure 2.12: Emission of real surface in comparison to blackbody emission (Ref 135)***. a) spectral distribution and b) directional distribution features*** (Ref 135)***. (Reproduced with permission of John Wiley & Sons)***

The *total hemispherical emissivity,* can be expressed as the total emissive power of the real object, i.e. particle, over the total emissive power of a blackbody, such that;

$$\varepsilon \equiv \frac{E(T)}{E_b(T)}. \qquad \textit{Eq. 34}$$

While this form is simple, the spectral, *directional emissivity* $\varepsilon_{\lambda,\theta}(\lambda,\theta,\phi,T)$ found at a temperature T, at a wavelength, λ, and the intensity of radiation emitted in the direction θ and ϕ is expressed as;

$$\varepsilon_{\lambda,\theta}(\lambda,\theta,\phi,T) \equiv \frac{I_\lambda(\lambda,\theta,\phi,T)}{I_{\lambda,b}(\lambda,T)}. \qquad \textit{Eq. 35}$$

In many applications, however, spectral hemispherical emissivity with directional averages is used instead and often regarded as a reasonable approximation;

$$\varepsilon_\lambda(\lambda,T) \equiv \frac{E_\lambda(\lambda,T)}{E_{\lambda,b}(\lambda,T)}, \qquad \textit{Eq. 36}$$

If the emissivity of a surface is known, the spectral emissive power at any wavelength and temperature can be obtained by;

$$E_\lambda(\lambda,T) = \varepsilon_\lambda(\lambda,T)E_{\lambda,b}(\lambda,T) = \frac{C_1\varepsilon_\lambda(\lambda,T)}{\lambda^5[\exp(C_2/\lambda T)-1]}. \qquad \textit{Eq. 37}$$

For real surfaces, the spectral emissivity is expected to be dependent on wavelength, ε_λ, i.e. as spectral distribution departs from Planck distribution. The ε_λ varies with wavelength as follow;

- The ε of metal materials decreases with decreasing surface roughness, i.e. values of 0.02 can be reached for polished gold and silver.
- The presence of an oxide layer can increase ε.
- The ε of non-conductors is generally higher than for conductor materials.
- The emissivity of conductor materials increases with increasing temperature.

2.3.2 The Gray surface

A gray surface condition (independent of λ) refers to a surface in which the assumption of $\varepsilon = \alpha$, with both being independent of λ, can be made with enough validity. In practice, this assumption does not have to be accurate over the entire spectrum, but rather can be used in a concentrated region of interest in which the surface emission spectral properties are approximately constant. Figure 2.13 shows the radiation conditions in which such assumption can be made; the irradiation and surface emission are focused within a region where ε and α are approximately constant.

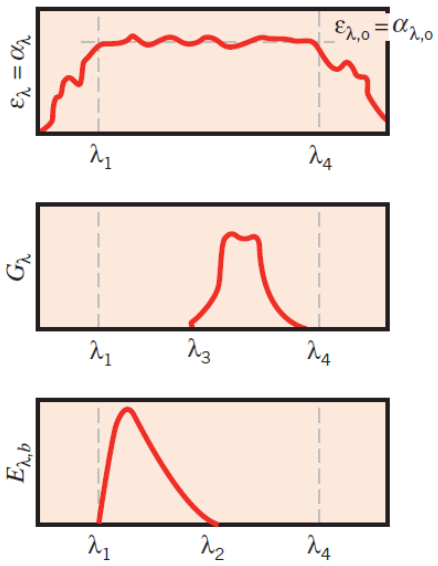

Figure 2.13: A set of conditions for which the gray body assumption can be utilized (Ref 135)***. In a spectral region with $\lambda < \lambda_1$ and $\lambda > \lambda_4$, the gray surface behavior cannot be used. (Reproduced with permission of John Wiley & Sons)***

2.3.3 In-flight particle temperature measurement in thermal spray

In thermal spray processes in general, in which the particle in-flight temperature can reach values above 1200°C, particle temperature measurements have been successfully achieved (Ref 25,26,101,136,137). Measurement techniques can be categorized as single-particle and particle-ensemble methods. The former provides individual particle temperature while the latter gives an average of a particle cluster. In addition, the particle temperature measuring systems can be distinguished by their detecting elements; (1) fiber-optic-based sensors and (2) CCD arrays (either 1D or 2D). The former provides a time-resolved measurement appearing as a pulse signal of light intensity vs time, in which the peak values of light intensity are used for pyrometry. The latter measures the light intensity averaged over the pixel's integration time and the detected intensity in a single frame, which provides spatial information as well as total intensity for pyrometry. Table 2.5 summarizes the equipment that has been utilized for in-flight particle temperature measurements in thermal spray processes.

Table 2.5: In-flight particle temperature measurement equipment. CGDS: Cold gas dynamic spray and TS: Thermal spray

Equipment	Temperature measurement	Specifications	Particle temperature studies
DPV-2000 (Tecnar Automation Ltd. St-Bruno, QC, Canada)	Two-color pyrometry, single particle method	T_p ≥1000°C V_p=5-1200m/s	CGDS: (Ref 138) No radiation signal detected TS: (Ref 139,140)
Accuraspray-g3 (TECNAR Automation Ltd., St-Bruno, QC, Canada)	Two-color pyrometry, ensemble method	T_p=1300-4000°C V_p=5-1200m/s	CGDS:N/A TS: (Ref 139)
IPP (Inflight Ltd. Co., Idaho Falls, ID, USA)	Two-color pyrometry, ensemble method	T_p=727-3272°C V_p=0.1-50m/s	CGDS:N/A TS: (Ref 141)
ThermaViz™ (Stratonics Inc. Laguna Hills, CA, USA)	Two-color pyrometry, ensemble method	T_p=1000-2500°C V_p <50m/s	CGDS: N/A TS:(Ref 142)
SprayWatch ® (Oseir Ltd., Tampere, Finland)	Two-color pyrometry	T_p=1000-4000°C V_p=1-2000m/s	CGDS: N/A TS:(Ref 143,144)
NIR Sensor (NIR Sensor, GTV Verschleiβschutz GmbH, Luckenbach, Germany)	Two-color pyrometry, single particle method	T_p=750-3000°C V_p=50-1200m/s	CGDS: N/A TS:(Ref 142)

As summarized in the table above, two-color optical pyrometers have been successfully utilised as the particles are heated to or close to melting temperatures allowing suitable detection at two selected wavelengths due to the high associated thermal emission radiation (Ref 25,26,137,145). All given radiation thermometry studies are based on Planck's law, which describes the emissive power of the radiating particle as a function of wavelength, emissivity and temperature as;

$$I_\lambda = \varepsilon_\lambda \frac{2C_1 \Delta\lambda \Omega A_e}{\lambda^5[\exp(C_2/\lambda T) - 1]}, \qquad \textit{Eq. 38}$$

where ε_λ is the spectral emissivity of the emitting surface, T is the absolute temperature and C_1 and C_2 are two Planck constants. The term A_e and Ω refer to the area of the emitter and the solid angle light collection optics, respectively. As the spectral energy is measured at two wavelengths (λ_1 and λ_2) using thermal radiance filtering, a ratio of measured radiation is obtained:

$$R = \frac{I(\lambda_1)}{I(\lambda_2)} = \left(\frac{\lambda_2}{\lambda_1}\right)^5 \frac{\varepsilon(\lambda_1) e^{C_2/\lambda_2 T} - 1}{\varepsilon(\lambda_2) e^{C_2/\lambda_1 T} - 1}. \qquad \textit{Eq. 39}$$

Since the emissivity of micron-size particles are unknown, the gray body assumption $\varepsilon(\lambda_1)/\varepsilon(\lambda_2) = 1$ is utilized and consequently the emissivity is assumed to be independent of wavelength.

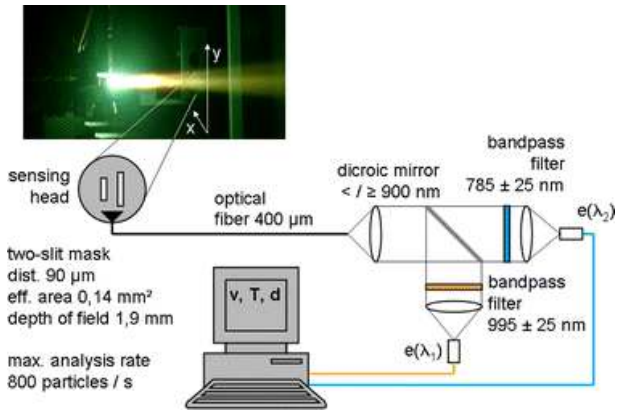

Figure 2.14: DPV-2000 diagnostic system operation principle (Ref 139)***. (Reproduced with permission of Springer Nature)***

This assumption, however, can lead to important temperature deviations. Applying Wien's approximation of Planck's law for wavelengths;

$$e^{C_2/\lambda T} \gg 1 \rightarrow e^{C_2/\lambda T} - 1 \approx e^{C_2/\lambda T}, \qquad \textit{Eq. 40}$$

the particle temperature can be obtained as follow;

$$T = \frac{C_2\left(\frac{1}{\lambda_2} - \frac{1}{\lambda_1}\right)}{\ln\left[\left(\frac{\lambda_1}{\lambda_2}\right)^5 \frac{E(\lambda_1)}{E(\lambda_2)}\right]}. \qquad \textit{Eq. 41}$$

The uncertainty in the obtained temperature value increases with temperature as the measured intensity ratio $\frac{E(\lambda_1)}{E(\lambda_2)}$ becomes less sensitive to changes in temperature according to Planck's function. Additionally, material emissivity is generally not known as it varies with surface oxide thickness and temperature. The incident power on the optical fiber is, thus, first calculated using a radiometric calibration curve, as shown in Figure 2.15a. A factor is obtained by comparing the signal received by the used blackbody, oven and a tungsten strip lamp to reach temperatures above 1000K (Ref 146), with the corresponding spectrum given by Planck's law, described by Eq. 38. The calibration curve accounts for the equipment's optical system response with wavelength.

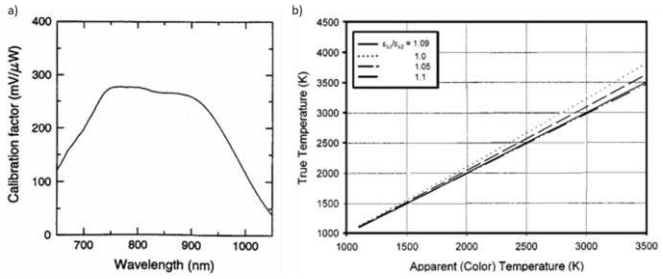

Figure 2.15: Two color pyrometer calibration curves (Ref 147)***.***

Since the tungsten lamp body used for calibration purposes does not behave as a gray body, deviations in obtained results can arise if the particle material does not behave similarly as the tungsten body, i.e. though not identical, many metals such as nickel, stainless steel and Inconel have a similar spectral ratio as tungsten at specific chosen wavelengths. The true temperature, $T_{p,x}$, of a material for which the spectral emissivity ratio differs from the one obtained in the calibration process, T_{cal}, can be obtained if the relationship between emissivity and wavelength is known, following;

$$T_{p,x} = T_{cal} + \frac{C_2\left(\frac{1}{\lambda_2} - \frac{1}{\lambda_1}\right)}{\ln\left[\frac{\varepsilon_{\lambda 1}}{\varepsilon_{\lambda 2}}\Big|_{p,x} \frac{\varepsilon_{\lambda 2}}{\varepsilon_{\lambda 1}}\Big|_{cal}\right]}. \qquad \textit{Eq. 42}$$

Figure 2.15b depicts the apparent temperature vs true temperature when the gray body assumption is used and when the instrument optics are calibrated using the tungsten source.

2.3.4 Limitations and errors

The particle thermal emission depends not only on its temperature but also on its size and emissivity. The detectors must ensure a wide dynamic range as the emission intensity is proportional to the square of the particle diameter and to the power of four of the temperature ($E \sim d^2T^4$). In two-color pyrometry, a careful selection of the two wavelength is required to avoid interference from any environmental emission, i.e. from plasma in thermal spray. As shown in Figure 2.16, emission with and without powder material needs to be conducted prior to any measurements to select the correct wavelengths that would lead to proper particle detection.

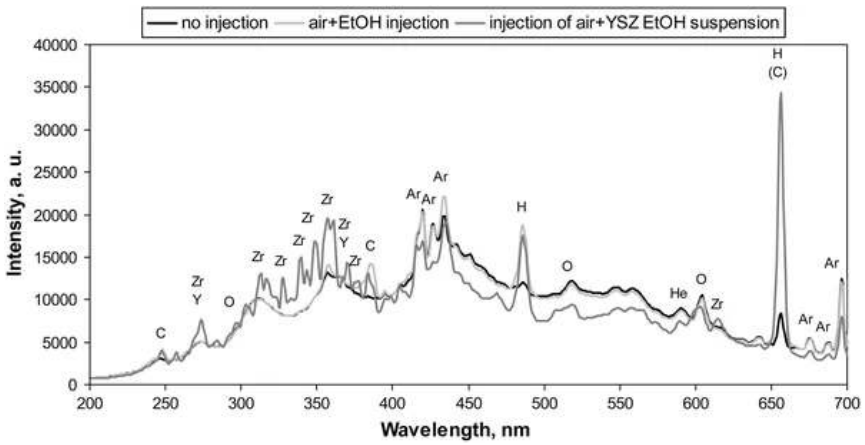

Figure 2.16: Optical emission spectra for three cases in plasma spray; (i) without any injection, (ii) ethanol and air injection and (iii) two-phase injection of air and Yttria stabilized zirconia powder in ethanol suspension (Ref 148)***. (Open access permission)***

The minimum particle emissivity for successful visualization and detection depends also on the optical arrangement, the detector sensitivity, the allowable exposure time and the background signal levels, which all have to be determined experimentally. Classical pyrometric measurements provide accurate detection of particles heated above 1200°C, which is far above the utilized CGDS stagnation temperatures. This lower limit of measurable temperature is controlled by the input signal amplitudes accepted by the analogue divider, i.e. one decade (Ref 149). The third limitation is the count rate limited to 30kHz to avoid recovery of the pulses (Ref 149). The accuracy of the set-up is, thus, dependent on the knowledge of particle emissivity and accuracy of calibration and of measurement. For the measurement of low particle temperature, i.e. low detection signals, the detectivity limit is affected by the detector and the transmission optics. The particle temperature is assumed to be accurate and measurable if the collected signal due to the thermal emission is at least three times larger than the detector noise (Ref 147,150);

$$\varepsilon\tau\Omega d^2 C_1 \frac{\lambda_1^{-5}}{\left(\exp\left(\frac{C_2}{\lambda_1}\right)-1\right)}\Delta\lambda_1 \geq 3NEP\sqrt{\Delta f}. \qquad \textit{Eq. 43}$$

where NEP is the noise equivalent power and Δf is the electrical bandwand, which for example provides a minimum required temperature of 1090°C for 50µm nickel particles.

2.4 CFD Simulation

Although the study of supersonic gas flow phenomena and particle in-flight characteristics is best analysed through experimental efforts and set-up, the relative complexity and infeasibility to capture all data significantly limits the experimental approach. As presented in the previous section, analytical solutions to various flows have been developed to predict the gas and particle properties but with the introduction of assumptions and simplifications these models might not provide accurate solutions.

2.4.1 Gas flow

Due to the presence of friction and boundary layers inside the nozzle, bow shock at the substrate surface, turbulence and outside supersonic jet, multiple publications have studied the flow characteristics deviations from the 1D calculations through computational fluid dynamics (CFD) analysis. As shown in Figure 2.17, large discrepancies between the two approach have been detected due to the assumptions utilized in the 1D isentropic analysis (Ref 100,106,112). The results show that the losses at higher operating pressure (stagnation pressure) are minimized because of decreases relative viscous forces. Figure 2.17b shows that in the isentropic flow

assumption, the flow is more efficient in converting the available energy to flow acceleration. The expected velocities must be lower than predicted by the isentropic equations due to the presence of shocks and viscous dissipations, which increase as temperature increases.

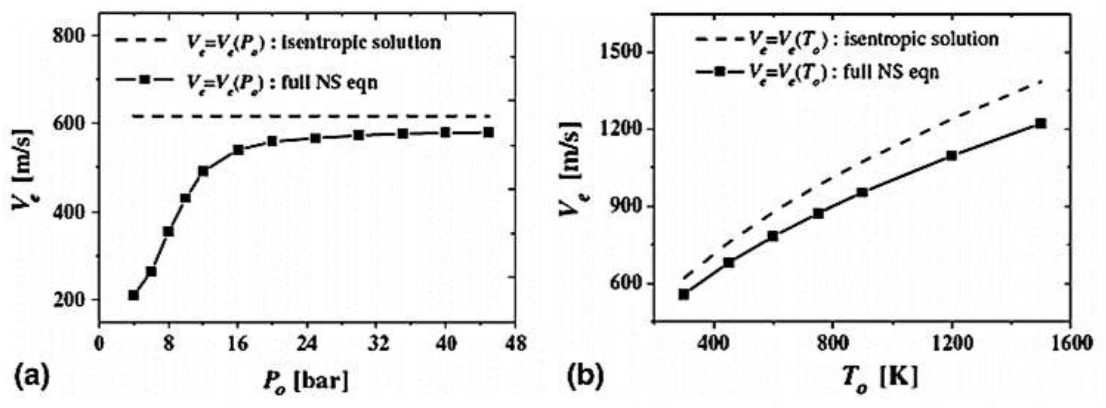

Figure 2.17: 1D isentropic analysis and CFD modeling resulting of gas flow properties (Ref 151)**. *(Reproduced with permission of Springer Nature)***

The flow definition in the CFD model is based on the Navier-Stokes equations (gives the velocity and pressure fields) set along with a turbulence model description, which altogether govern the resulting fluid properties. A total of six equation are, thus, solved in the CFD models; conservation of mass, conservation of momentum in two dimensions, conservation of energy and, an equation for the turbulence kinetic energy, k, and turbulence dissipation, ε. The mesh (small enough to resolve the size of the smallest eddies in the flow), boundary conditions, the discretization scheme, the turbulence model description and numerous other factors affect the CFD results and accuracy of the simulation (Ref 106,112,152–154). As shown in Figure 2.18, the complex supersonic flow exiting the nozzle, with the presence of a shock wave trail, is successfully modeled through CFD as attested by the included experimental Schlieren image. The turbulence model is one of the predominant factors affecting the simulation accuracy. Most of the utilized turbulence models are developed on the closure of the Reynold Averaged Navier-Stokes (RANS) equations.

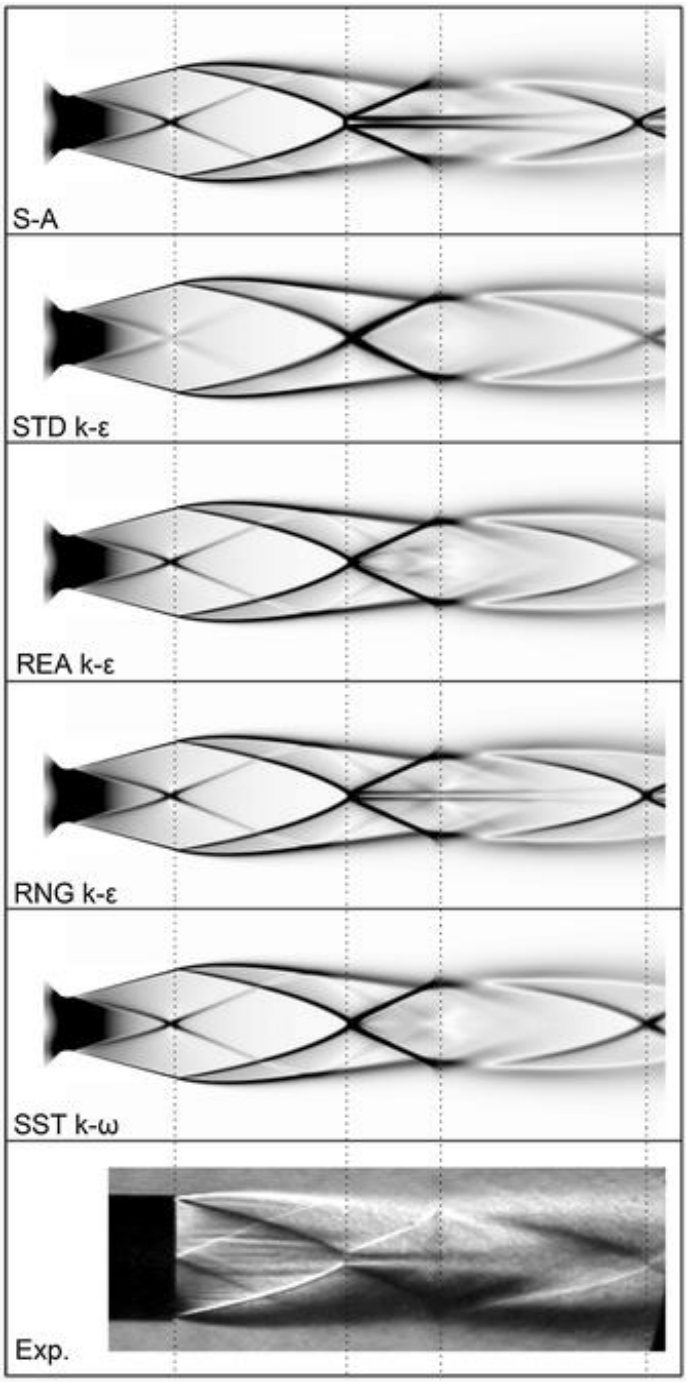

Figure 2.18: Gas flow pattern at the nozzle exit obtained using different turbulence models in CFD simulations. An experimental Schlieren image is provided for comparison purposes(Ref 27)***. (Reproduced with permission of Springer Nature)***

Table 2.6 summaries the benefits and disadvantages of numerous turbulence models in the context of supersonic flow modeling.

Table 2.6: Turbulence model benefits and disadvantages.

Turbulence model (# of equations – Model theory)	*Benefits*	*Disadvantages*	*CGDS studies*
Spalart-Allmaras (1-RANS)	- 1 equation model	- Large errors in free shear flows - Under-resolved grids and unphysical transients	(Ref 155)
Standard *k-ε (2- RANS)*	- Applicable to various flows - Simple implementation - Stable, easily converged solution	- Caution for turbulence sensitive processes. - Turbulent viscosity regarded as isotropic (Re/$\dot{\varepsilon}$ is the same in all directions.	(Ref 22)
Realizable *k-ε (2-RANs)*	- Additional transport equation - New formulation for turbulent viscosity	- Converging might be difficult compared to other simpler models	(Ref 100)
RNG *k-ε (2-RANS)*	- Improved accuracy due to additional ε equation - Higher accuracy for rapidly strained flows	- Converging might be difficult compared to other simpler models	(Ref 154,156,157)
SST *k-w (2-RANS)*	- Near wall region solved using *k-w* model - Free shear flow using *k-ε* model - Accurate prediction of complex flows	- Compressibility effect disregarded	(Ref 158)
Reynolds stress model, RSM (7-RANS)	- Accounts for non-isentropic turbulent effects -Independent Reynolds stress component solved separately	- High degree of coupling	(Ref 159,160)
Large eddy simulation, LES (…-LES)	- Large eddies solved - Small eddies accounted using sub-grid scale model	- Large computational time - Powerful computers required	N/A

2.4.2 Particle in-flight characteristics

The design of the particle-laden flow CFD model requires to first evaluate the volume fraction the particle population occupies within the flow field, which determines the severity of particles influence on flow stream properties. A one-way Lagrangian discrete phase modeling (DPM) method is used if the volume is determined as uninfluential (Ref 161,162). For dense particulate flow, i.e. large feed rates, a two-way Lagrangian method (Ref 115,162) or an Eularian DPM (Ref 100,163) are utilized although the latter is far more complex. The drag coefficient, related to both particle morphology and gas dynamics, is known to be the most influential factor in particle velocity and trajectory inside the nozzle. Its value depends on the pressure drag and friction drag, which makes the coefficient dependent on many properties and difficult to calculate as it diverges from a simple constant linear solution. Many correlations exist in the literature that provide a definition of the particle C_D (Ref 27,98,99,164), as covered in section 2.2.2.3. Due to the many interrelated factors that need to be accounted for in the drag coefficient expression, numerical methods are preferred over analytical models.

Besides the sole use of CFD in the calculation of particle in-flight characteristics, Grujicic *et al.* have also proposed an empirical model for particle velocity based on experimental and computational analysis, which has been described as;

$$V_p^{impact} = V_p^{exit} e^{-3\rho^{st}L^{st}/4\rho_p d_p}, \quad \textit{Eq. 44}$$

where

$$\rho^{st} = Re(-1.04 + 2.27M_e - 0.21M_e^2) \quad \textit{Eq. 45}$$

and

$$L^{st} = Re(0.97 - 0.02M_e) \quad 1 \leq M_e \leq 5, \quad \textit{Eq. 46}$$

for ρ^{st}, L^{st}, V_p^{impact}, V_p^{exit} and M_e being the average gas density in the stagnant zone, thickness of the stagnation region, particle velocity upon impact, particle velocity at the nozzle exit and Mach number at the exit. As shown in Figure 2.19, the particle velocity is captured more accurately using CFD modeling than empirically developed correlations as the substrate bow shock instability cannot be properly captured by simplistic analytical descriptions. In addition, irregularly shaped particles experiencing larger acceleration due to greater endured drag force can easily be modeled through CFD, while this is much more complex to account for in the empirical approach.

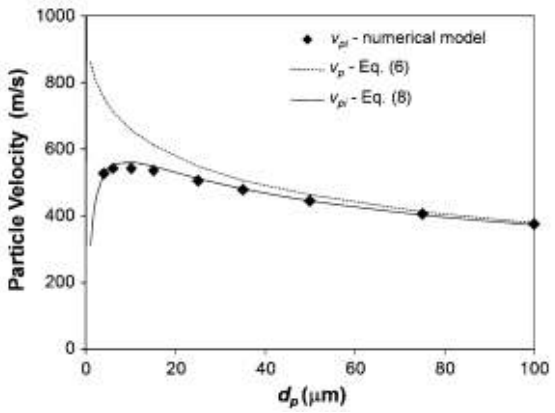

Figure 2.19: Copper particle velocity based on its diameter predicted using both CFD modeling and analytical equations (Ref 165)**.**

The particle in-flight temperature has also been simulated through CFD, as shown in Figure 2.20, utilizing the LCM and $Nu = f(Re_p)$.

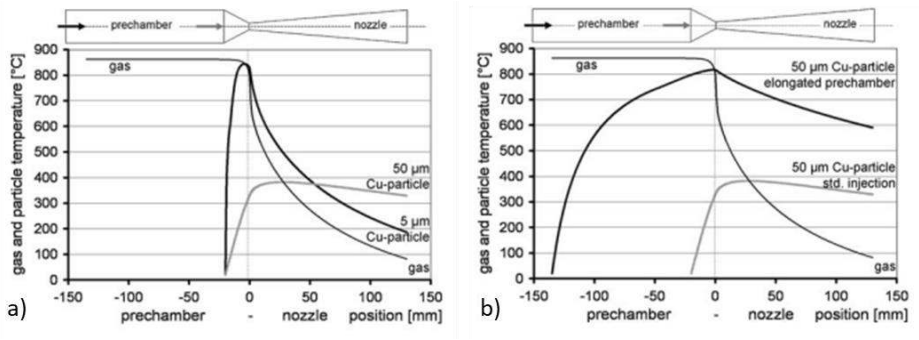

Figure 2.20: Particle in-flight temperature variation as it travels within a CGDS nozzle with an upstream injection (Ref 114). ***(Reproduced with permission of Springer Nature)***

Figure 2.20a shows that smaller particles are heated quicker and to higher values than larger particles but are also cooled rapidly in the supersonic section. This shows that larger particles can maintain their temperature over a longer traveling distance despite reaching lower temperatures. A pre-chamber can be utilized to heat large particles to the desired temperature, as shown in Figure 2.20b.

2.5 Particle Impact Process

In the CGDS impact, the system total energy is equal to the particle kinetic energy prior to its impact and the internal energy of both the substrate and particle components. Based on the energy conservation principle, the system's total energy must be constant throughout the deposition process:

$$E_{total} = E_i + E_v + E_f + E_k + E_w \quad \textbf{Eq. 47}$$

where E_i is the internal energy of the system, E_v is the viscous energy dissipated by damping mechanisms (bulk viscosity damping and material damping), E_f is the energy dissipated by friction, E_k is the kinetic energy of the system and E_w is the work produced by external load to the system. Since in the CGDS particle impact process, no external work is applied and that the E_v and E_f are negligible in comparison to the rest of the energy terms, the energy balance reduces to;

$$E_{total,CGDS} = E_i + E_k. \quad \textbf{Eq. 48}$$

The internal energy, E_i, in the CGDS impact is described as;

$$E_i = E_e + E_p \quad \textbf{Eq. 49}$$

where E_e is the recoverable elastic strain and E_p is the energy dissipated through inelastic processes such as plasticity. This energy balance definition is the base of CGDS deposition principles.

2.5.1 High strain rate deformation microstructure

The high kinetic energy stored in each particle exiting the converging/diverging nozzle generates, upon impact, extreme plastic deformation reaching strain rates up to $10^9 s^{-1}$. The plastic energy is almost fully converted into heat, i.e. 90% and more, while the remaining goes into viscoelastic deformation and elastic energy. This heat dissipation process increases locally the temperature of both the particle and substrate at the interface, which has suggested to generate localized melting, appearing as ejecta or spheroidal particles as shown in Figure 2.21a-b. The creation of intermetallic regions at the interface between two dissimilar particle/substrate materials has also been shown to occur, as seen in Figure 2.21c for copper on aluminum. Due to the limited diffusivity of copper in solid solution in aluminum, the generated layer has been associated to interfacial melting increasing the couple diffusivity at the contact surface. Although the occurrence of melting is a subject of debate, it is agreed that the highest temperature is reached in the highest deformation zone. It is within this context that Assadi *et al.* introduced the theory of adiabatic shear instability, a thermo-viscoplastic instability, to explain the localized heating processes. The concept of adiabaticity has been evaluated as valid only when the characteristic system dimension, *x*, is significantly greater than the thermal diffusion distance, i.e. $\sim\sqrt{\alpha t}$ so that the following relation prevails;

$$\frac{x^2}{\alpha t} = \beta \gg 1 \qquad and \qquad \beta \propto d_p V_p \qquad \textit{Eq. 50}$$

where α id the thermal diffusivity, t is the process time and β is a dimensionless parameter representing the degree of adiabaticity. For the same impact velocity, larger particles would tend to deform more adiabatically as the *x* parameter scales with the particle diameter, d_p, while the time scales with the ratio of d_p to impact velocity V_p.

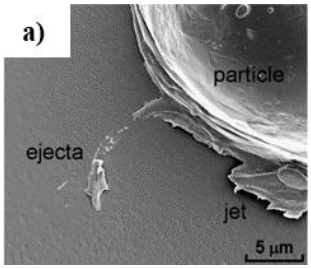

Melting-Ejecta(Ref 166)

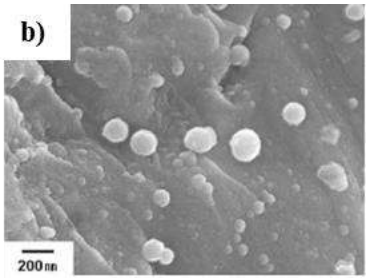

Melting-Spheroidal particles (Ref 167)

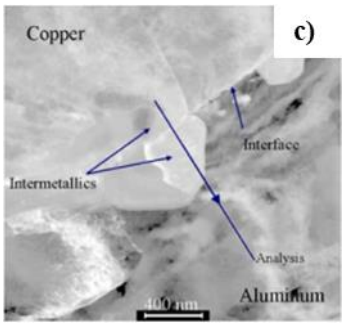

Intermetallic phases (Ref 168)

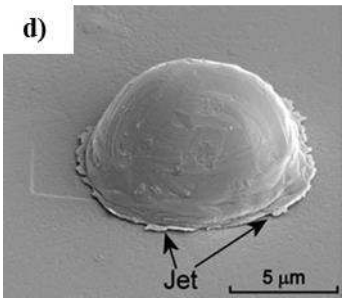

Jetting (Ref 93)

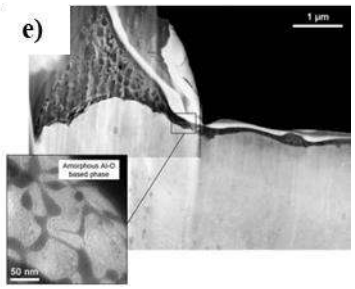

Amorphization (Ref 168)

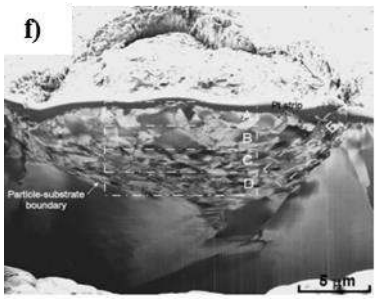

Recrystallization (Ref 169)

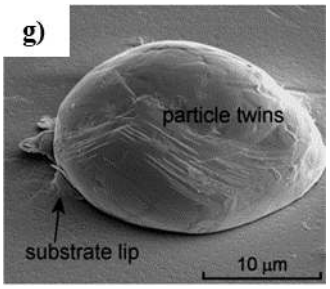

Twinning (Ref 166)

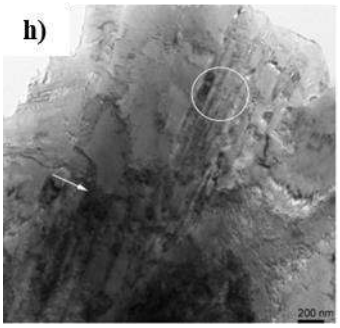

Shear band (Ref 170)

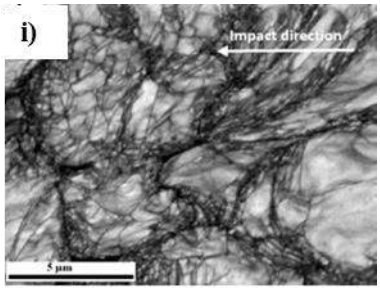

DRXee (Ref 171)

Figure 2.21: Cold spray impact induced particle microstructural features. (Reproduced with permission of Springer Nature and Elsevier)

Figure 2.22 illustrates three types of deformation behaviors based on energy dissipation mechanisms. The quasistatic (isothermal) deformation includes the dissipation of plastic energy in the form of heat exchange with the environment, which then provides a material flow stress affected only by work hardening. If the deformation process is considered adiabatic, i.e. absence of heat dissipation into the environment and the rest of the tested material, the energy dissipation generates an increase in temperature. This rise in temperature initiates thermal softening allowing material to flow under lower stresses. In the CGDS particle impact process, the heating zone is limited to areas close to the impact interface, which creates dissipation mechanisms and temperature gradients

inside the particle volume. This gradient, observed as a heterogeneity at its boundaries, can lead to localization and shear banding at a critical strain, γ_{cr}, and consequently allow the material at the interface to deform with increased softening under flow stress dropping to zero values, as illustrated in Figure 2.22.

This adiabatic shear instability deformation process has been associated to the formation of particle jetting, as shown in Figure 2.21d. The presence of adiabatic shear instability processes is, however, not necessary to generate paricle jetting (Ref 172).

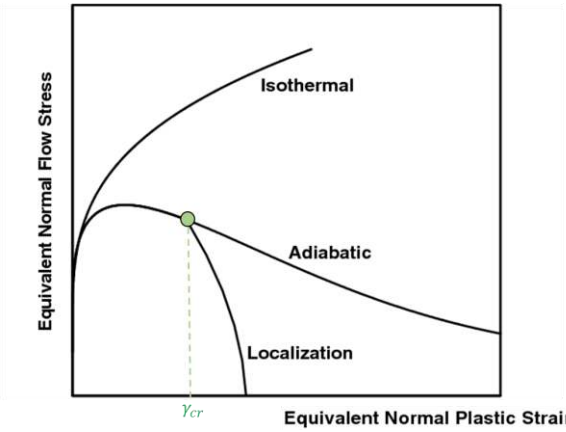

Figure 2.22: Illustration demonstrating the stress-strain variation of a typical crystalline material under isothermal, ideal adiabatic and localization conditions (Ref 173)***. (Reproduced with permission of Elsevier)***

Material jetting, in the form of localized fragmentation under a spall-like process, can also occur on a basis of hydrostatic pressure release, as shown in Figure 2.23. Initially upon impact, the particle contact edge outward velocity is faster than the shock wave velocity (I-*Attached sock*.) With time, the edge slows down enabling the pressure wave to detach (I-*Sock detachment*). Immediately after the shock detaches, a free surface is created where the pressure is necessarly zero. Adjacent to the free surface, a very large pressure exists, which induces material acceleration by pressure realease. This process generates a localized tension and material jetting, similar to the jetting occuring during adiabatic shear instability.

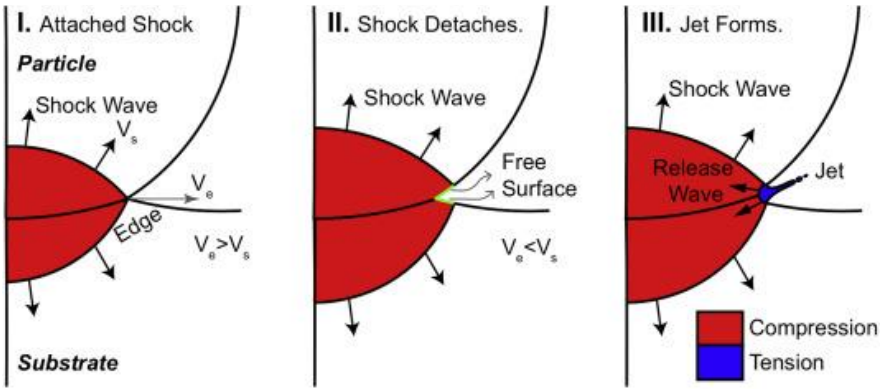

Figure 2.23: Jetting process related to pressure release in CGDS (Ref 172)***. (Reproduced with permission of Elsevier)***

In addition to the extreme material expulsion process, other strain-rate-dependent microstructural features have been detected in CGDS depositions and related to possible melting, such as amorphization (Figure 2.21e) and recrystallization (Figure 2.21f). Finally, with deformation under extreme strain rates and resulting important accumulation of dislocations, processes such as twinning (Figure 2.21g), shear banding (Figure 2.21h) and dynamic recrystallization (Figure 2.21i) can occur to accommodate further plastic deformation of the particle under the extreme loading impact process.

2.5.2 Bonding processes

Material build-up in the CGDS process relies on impact-induced features that lead to particle bonding. Numerous mechanisms have been put forward to explain particle adherence such as adiabatic shear instability, oxide layer breakup, localized melting, diffusion, interface amorphization and mechanical interlocking. In general, however, it is agreed that two type of adhesion processes exist: mechanical and metallic bonding. Other adhesion mechanisms, such as Van der Waals (VDW) and electrostatic forces are considered to have limited influence compared to the considerably stronger measured adhesion strengths in the CGDS field resulting from metallic and/or mechanical bonding. The mechanical bonding process relates to the particle mechanically/physically attaching to the deposited surface through anchoring features and interlocking processes. The interlocking bonding can result from extreme impact induced deformations leading to vortex-like interfacial structures, from surface pre-treatments generating a target surface filled with hook-like features and from strong embedment into the substrate. Figure 2.24 illustrates all three mechanical adhesion processes.

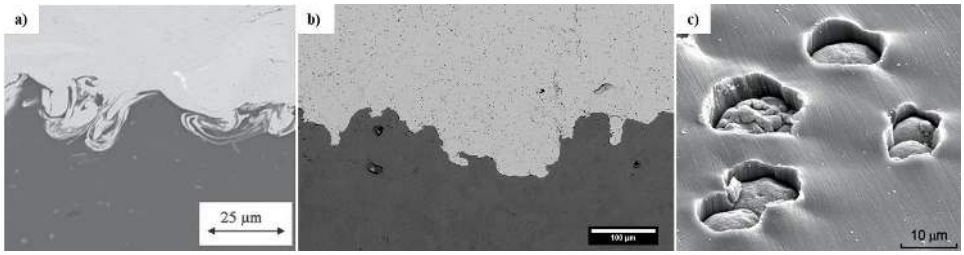

Figure 2.24: Mechanical bonding processes a) material mixing by vortex (Ref 174)***, b) anchoring to substrate topographical features generated using FPWJ and c) embedment*** (Ref 93)***. (Reproduced with permission of Springer Nature)***

The metallic bonding, on the other hand, refers to the development of atom-to-atom bonds between the particle and substrate at the contact interface. If high enough pressures are developed at the oxide-free contact zone, the valence electrons from both contacting materials can cross each other's sphere of influence, which results in the generation of a metallic bond. Outside of the sphere of influence, atoms are too far to have any repulsive or attractive interaction forces, which leads to a close contact interface deprived of metallic bonding. If atomically bonded, an equilibrium spacing, i.e. ~0.3nm, separates the atoms from both materials and the repulsive and attractive forces are balanced. The bonding energy associated to the atomic bond corresponds to the energy necessary to separate two atoms to an infinite distance. For the metallic bond comprising more than two atoms, a much more complicated state is generated in which all energy interactions provide their influence on the overall bond strength. Cold welding (CW), the simplest kind of mating process, known as solid-state pressure welding, has been extensively used to provide insight into the prerequisites for proper atom-to-atom bond generation in CGDS process. The accepted theory states that to generate a metallic bond between two surfaces, an intimate, oxide free, pressurized contact deprived of organic contaminants must exit at contact. The processes required to reach such contact surface conditions in the CGDS impact are illustrated in Figure 2.25.

The vast majority of metals have an oxide layer on their surface, (with the exception of gold), which has to consequently be broken and properly ejected in the advent of atomic bonding. Multiple studies have demonstrated that the high deformation and jetting processes are adequate to properly disrupt and extrude the native oxide layer while the working inert gas shields the contact from the atmosphere and oxidation (Ref 175–177). This hypothesis, however, is most applicable for the case of similar particle/substrate material, in which both undergo significant plastic deformation at the interface to allow such cleaning processes to evenly occur upon impact (Ref 35,178,179).

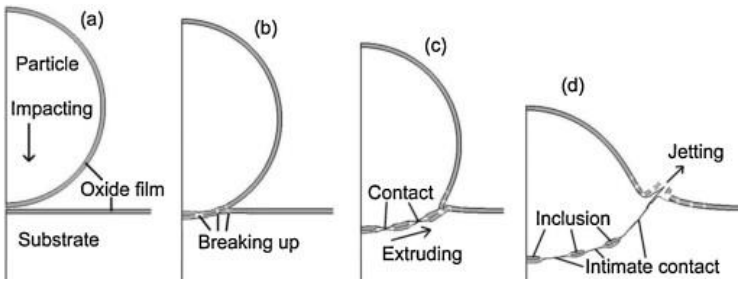

Figure 2.25: Bonding process schematic during CGDS particle impact. After high speed contact, oxide breaking and material extrusion leads to fresh metal contact surfaces (Ref 35)***. (Reproduced with permission of Elsevier)***

Xie et al. have shown that for the case of hard particle/soft substrate material combination, single particle deposition shows no presence of fresh metal-to-metal contact zones despite the large substrate plastic flow (Ref 180), as shown in Figure 2.26a. However, during complete coating deposition and upon an annealing treatment, they have shown that the interfacial oxide layer gets properly removed, which they have associated to the benefit of particle-to-particle peening processes (Ref 180), as shown in Figure 2.26b.

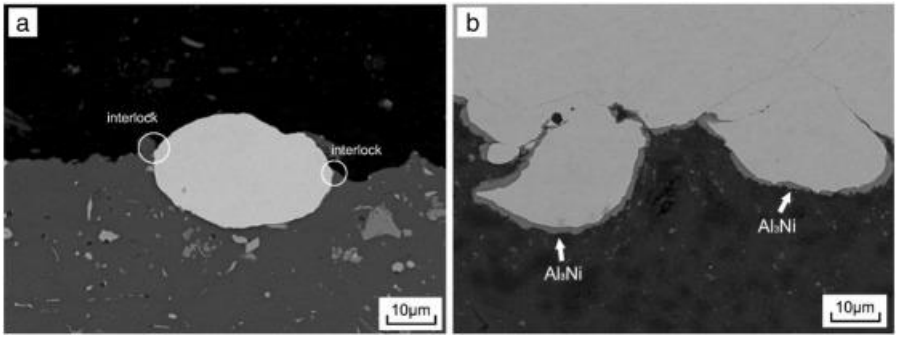

Figure 2.26: Cross section of a) single Ni particle deposition on Al substrate and b) full coating generation for the same particle/substrate combination after anneal treatment (Ref 180)***. (Reproduced with permission of Elsevier)***

The subsequent particle impacts increase substrate and deposited particle deformation leading to improved cleaning processes. Adhesion values were, however, not provided and the actual bonding nature prior to annealing was not confirmed but the requirement of material deformation, i.e. extreme plastic flow, for proper creation of fresh metal contact and eventual atomic bonding was confirmed.

2.5.3 Critical velocity

To ensure metallurgical bonding, the particles need to reach a critical velocity, V_c, as depicted in Figure 2.27. Above such value, the coating deposition efficiency (DE), described as the increase of

substrate mass gain over sprayed material mass, increases. A rapid increase in DE is achieved above V_c followed by a decay associated to erosion. Numerous equations have been developed to express the V_c dependence on material properties, particle size, particle temperature and substrate properties. Assadi *et al.* have developed the following expression to calculate the V_c (Ref 165), which has been massively used in the field:

$$V_c = k_1 \sqrt{c_p(T_m - T_p) + 16\,\frac{\sigma}{\rho_p}\left(\frac{T_m - T_p}{T_m - 293}\right)} \qquad \textit{Eq. 51}$$

where T_m is the particle melting temperature, $T_p$is the particle impact temperature, σ is the tensile strength of the particle material at 293K, k_1 is a particle-size-dependent fitting parameter, ρ_p is the density of the particle material, and c_p is the specific heat of the particle material. Eq. 51 demonstrates the importance of particle temperature in the deposition process of CGDS particles.

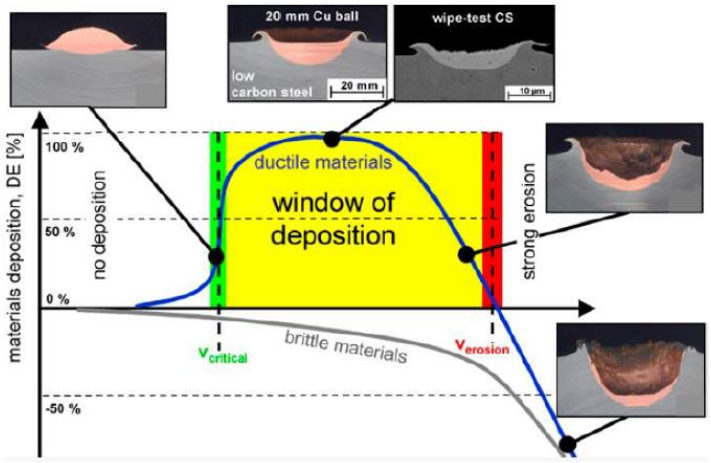

Figure 2.27: Illustration of the critical velocity concept for proper deposition (Ref 114)***. (Reproduced with permission of Springer Nature)***

In addition, it has been shown that materials with low strength and low melting point, such as copper, aluminum, nickel, tin, silver and zinc exhibit a lower V_c, as presented in Table 2.7. In addition, face-centered cubic (FCC) materials, characterized with 12 slip systems, allow larger lattice deformation, while body-centered cubic (BCC) materials require much higher V_c due to limited slip activity, as summarized in Table 2.7. Other than the influence of inherent crystal plasticity properties, the V_c also increases with decreasing particle size due to bow shock deceleration, larger oxide content (oxide film and oxide strengthening), increased cooling rates and increased strain hardening processes associated to small particles. The purity of both particle and substrate material also influences V_c; alloy content tends to reduce material deformability by

hindering dislocation motion increasing the velocity required for bonding. Hassani-Gangaraj *et al.* have shown that the V_c decreases with material decrease to oxygen affinity. Their study, in addition to showing the influence of oxide film on bonding, demonstrates that particles also require material jetting to induce close contact, i.e. the deposition of noble gold metal particle necessitated a V_c of 253m/s.

Table 2.7: *V_c dependence on material crystal structure.* (Ref 181,182)

Material	**Experimental V_c**
Tin	250-375m/s
Gold	270-625m/s
Silver	500-750m/s
Zinc	375-813m/s
Copper	470-1000m/s
Aluminum	680-1500m/s
Nickel	680-1500m/s
Titanium	750-2000m/s
Aluminum 6061	740-1750m/s

As such, in any study, reported V_c values are specific to the exact particle/substrate material properties and to date, the main factors causing discrepancies in measured V_c are the predominant inconsistencies in particle microstructure and inability to confirm the exact particle in-flight/impact temperature.

2.5.4 Effect of particle/substrate characteristics on deposition

2.5.4.1 Particle velocity

The following dimensionless parameter:

$$\eta = V/V_c, \qquad \textit{Eq. 52}$$

has been used to demonstrate that to increase DE and coating quality, one should use spray parameters that decrease V_c and/or increase the particle in-flight velocity, *V*. Increasing particle velocity leads to a rise in the systems kinetic energy and consequently allows pronounced plastic flow dissipation, jetting and local rise in temperature, all of which improve the development of successful bonding processes. Although most of the energy is dissipated through plastic flow,

recoverable elastic strain energy can lead to particle rebounding if not properly bonded to the substrate surface at impact. Consequently, one should be aware that increasing the particle velocity does also increase the recoverable strain energy (Ref 183–185), i.e. rebound from normal strain. This increase stems from the larger imparted stress at higher velocities, which increases the available recoverable elastic strain energy. However, strain-hardening, strain-rate sensitive deformation, thermal-softening and localization can complicate the calculation of the effective recoverable energy. The plastic dissipation energy also increases with particle velocity due to a rise in adiabatic heating at the interface. In addition to deformation phenomena, the increase of particle velocity, i.e. kinetic energy, increases the impact contact time (an increase from 424m/s to 515m/s increases contact time by 4ns), which may increase the number of bonded atoms at the contact area (Ref 186,187).

2.5.4.2 Particle temperature

As described in Eq. 51, the particle in-flight temperature influences the deposition process by reducing V_c. Increasing particle temperature has shown to substantially reduce the elastic strain energy and increase plastic deformation, which both improve bonding developments (Ref 184). Although there is no data on the particle temperature influence on adhesion, Schmidt et al. have shown that an increase in particle in-flight temperature increases the coating cohesive strength, which should in theory also lead to increased adhesion (Ref 188).

2.5.4.3 Substrate material

Depositing different (or similar) materials and generating a composite coating remains one of the main benefits of the CGDS process. However, the analysis becomes more complex as the density, mechanical response and heat capacity between particle and substrate start to differ. As shown in Figure 2.28, four different cases with four different bonding processes can be generated based on the material characteristics dissimilarity between particle and substrate. Differences in particle and substrate plastic deformation can lead to different thermal and kinetic surface energies and consequently to varying bonding processes.

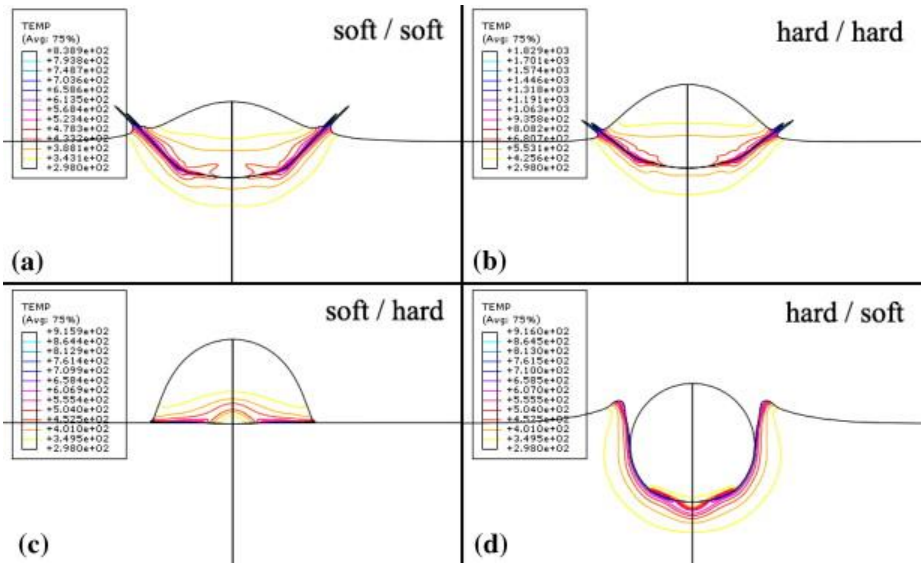

Figure 2.28: Particle/substrate material properties influence on impact development. Four possible cases exist; a) soft/soft (ex: Al particle impacting onto Al substrate at 775m/s), b) hard/hard (ex: Ti particle upon impact with Ti substrate traveling at 865m/s), c) soft/hard (ex: Al particle on mild steel substrate at 365m/s) and d) hard/soft (ex: Ti particle onto Al substrate at 655m/s) (Ref 183)***. (Reproduced with permission of Elsevier)***

Regardless of which case from Figure 2.28 is generated and which adhesion process ensues, the system dissipated energy must allow proper adhesion mechanisms to occur to avoid particle bouncing-off the substrate from the stored elastic strain energy. Bae *et al.* have shown that for dissimilar material deposition cases (hard/soft and soft/hard), the softer material deforms and heats up at extreme rates such that the critical velocity is always much lower than for similar material cases (Ref 115). Highly saturated temperature, leading to possible local melting and extremely low equivalent flow stress, has shown to result in high adhesion and low rebound energy, both beneficial to bonding processes (Ref 187).

2.5.4.4 Roughness

The particle/ surface contact area plays an important role in the adhesion process. Studies have shown that increasing the surface roughness decreases the adhesion as the crevices to particle size increase and limit proper contact area for bonding (Ref 189–191). Others have shown that increasing the roughness can increase the adhesion by providing additional mechanical anchoring to the deposited coating (Ref 192), as shown in Figure 2.29.

However, to this day, the fraction of mechanical and metallic bonding in the obtained coating adhesion strength values for different surface preparations remains unmeasured and unverified.

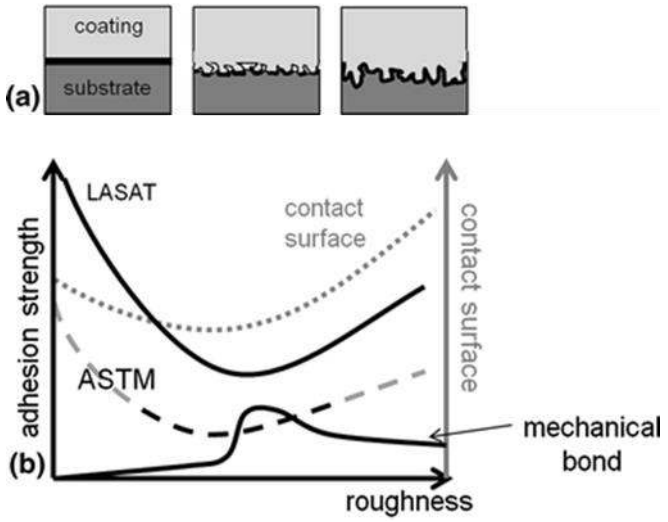

Figure 2.29: a) schematic of the substrate surface contact area and b) contact area-based adhesion strength. For substrate roughness values varying from 0.05µm to 5.53µm (Ref 193)***. (Reproduced with permission of Springer Nature)***

2.5.5 FEM simulation

2.5.5.1 General plastic flow

Since the CGDS process involves the impact of small scale particles, up to nanoscale size, and that the ensuing deformation developments occur within few nanoseconds, any in-situ experimental characterisation becomes a challenge. Over the past 20 years, finite element modeling (FEM) has become a practical tool offering the possibility to investigate the particle/substrate material behavior upon deposition by providing tools required to calculate the contact pressure at the impact interface, the elastic/plastic deformation, multi-dimensional stresses, temperatures and velocity vectors. Assadi *et al.* and Grujicic *et al.* have shown, in early 2000's using modeling, that the onset of bonding processes was related to the occurrence of adiabatic shear instability related plastic flow localized deformation, which was a breakthrough in the CGDS field. However, it is only in 2018, that through additional modeling work Hassani-Gangaraj *et al.* have instead associated the adhesion processes to hydrodynamic plasticity resulting from the interaction of strong pressure waves traveling from the impact zone towards the particle surface leading to a natural dynamic jetting effect (Ref 172). Although FEM is a great tool in the CGDS field, its accuracy heavily depends on the mechanical properties implemented in the model, which are difficult to obtain due to the high strain rate deformation the material achieves and randomness of powder microstructure.

The common experimental methods utilized to obtain material properties at high strain rate deformation are the split Hopkins pressure bar (Ref 194) and the hypervelocity impact crater

morphology (Ref 14). The Hopkins bar test particularly shows limitations as it is capable of only achieving strain rates up to 10^4 $s^{-1,}$ which is well below strain rates recorded through FEM in the CGDS impact process. In addition to the experimental testing not being perfectly suitable for the field, a large number of empirical models have been developed to allow high strain rate simulations. Figure 2.30 provides a comparison between developed empirical equations and obtained experimental material flow stress, which show that the material deformation process at extreme strain rates is best described by the Preston-Tonks-Wallace (PTW) model than others such as Johnson-Cook (JC), Voyiadjis-Abed (VA), Modified Zerilli-Armstrong (MZA), Modified Khan-Huand-Liang (MKHL) and Gao-Zhang (GZ).

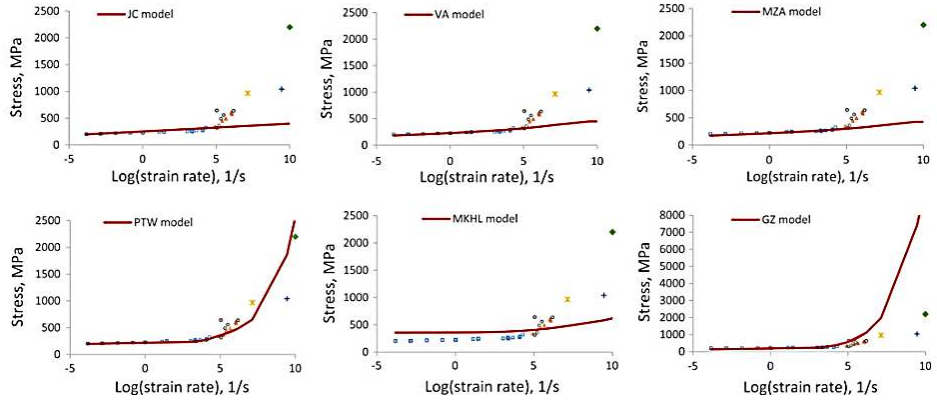

Figure 2.30: Copper deformation at various strain rates and resulting stress using different proposed models (Ref 195)***. (Reproduced with permission of Springer Nature)***

Although the suitability of the PTW to describe extreme strain rate deformations has been confirmed, its appropriateness within the CGDS particle impact has only been demonstrated through a single individual particle impact. In addition, the PTW description of the material behavior turns out to be much more complex than any other developed models. Consequently, in 2020, Chakarabarty and Song have proposed a modified simplistic Johnson-Cook model together with the inclusion of a strain gradient plasticity (SGP) prediction definition to describe the CGDS particle impact deformation processes (Ref 13). Although much simpler than the PTW development, their study still relies on tuning parameters using a single particle micrograph, as illustrated in Figure 2.31.

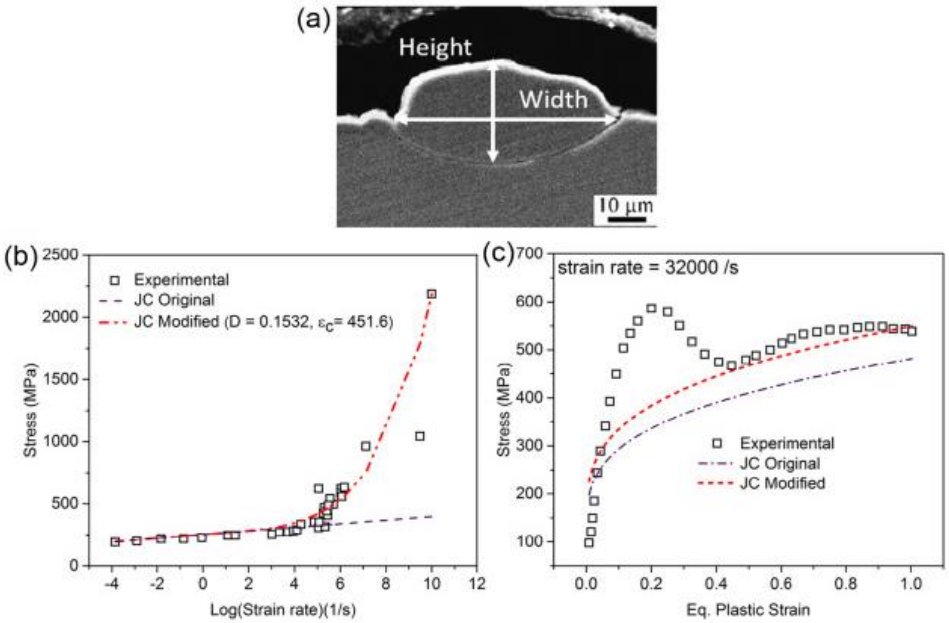

Figure 2.31: a) Copper particle travelling at 500m/s deposited using CGDS. b) stress-strain data comparison between experimental, original JC and modified JC without SGP and c) stress-PEEQ data comparison (Ref 13)***. The experimental data is obtained using a shear compression specimen test. (Reproduced with permission of Elsevier)***

2.5.5.2 Powder microstructure

A major obstacle in the CGDS process is the lack of standardized and tailored feedstock powder. The inconsistency in powder features within different powder batches and across different commercial brands have not been thoroughly studied although they have been associated to many reported results discrepancies (Ref 196–199). While most publications show the content of the starting powder utilized in their study and report variability, very few provide details about how the microstructural features would affect their results (Ref 75,200–203). Hence, a recent growing interest is the evaluation of powder microstructural features influence on their plastic deformation using numerical modeling.

Classical atomistic molecular dynamics (MD) simulations have been recently introduced to the CGDS process (Ref 18,204). In such simulations, the movement and interactions of atoms or molecules are calculated based on classical equations of motion, which allows predicting the mechanisms and kinetics of defects evolution, interaction and generation, i.e. dislocation and stacking faults, and provides information about the material state, i.e. pressure and temperature. As shown in Figure 2.32, the deformation of a 30nm particle with a single crystal composition has been modeled under impact conditions and the initial orientation influence on dislocation motion, dislocation density and final shape has been investigated (Ref 201).

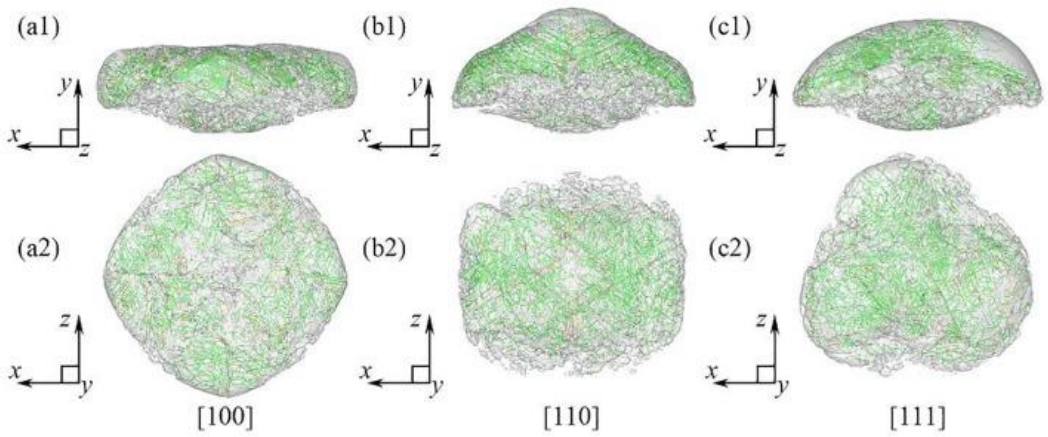

Figure 2.32: Molecular dynamics simulations studying deformation and dislocation distribution in Cu particles with crystal orientation along [100], [110] and [111] directions (from left to right). Top row shows the particle in side view while bottom row illustrates the top view (Ref 205)***. (Reproduced with permission of Elsevier)***

Although novel, the MD frame is significantly limited to length scales of a few nanometers, which is far from the dimensions of powder particles in the CGDS that span over a few hundred nanometers. This discrepancy also implicates that the grain size in the MD particles are in the range of 1nm to 6nm (Ref 16,206), which is considerably smaller than those found in the CGDS powder particles, i.e. commonly ranging between 1µm to 15µm. This dissimilarity has a crucial effect on the material microstructural evolution and response to impact as it has been demonstrated by many that the small spacing between nanograins effectively increases the pinning resistance to dislocation motion (Ref 207,208). The increased presence of grain boundaries in nanocrystalline metals readily annihilate dislocations and their stacking process within the grain interior becomes limited (Ref 209,210). Hence, the implementation of the MD simulation in a CGDS frame of work proves to be difficult. In addition to the limited dimensions, the basic concept of the MD simulation method relies on the parametrization of many terms, which are used to describe the interaction potential energy functions. The set of functions and the associated set of parameters, which are termed ‘’force field’’, are not readily available, which complicates the usage of MD in the CGDS field (Ref 211–214).

To bridge the gap between FEM and MD simulations, a quasi-coarse-grained dynamics (QCGD) method has been developed (Ref 33). The QCGD method uses representative atoms, referred to as R-atoms, to mimic the dynamics of several atoms in each volume of atomistic frame, which significantly reduces the computational time by decreasing the number of individually analysed atoms. The developed scaling relationships incorporate kinetics related to collective nucleation, evolution and interaction mechanisms of dislocations, temperature and pressure generation in

metallic materials (Ref 33). Although providing the ability to increase the analysed length scale, the collective deformation description has shown to overshoot the metal strength. Moreover, a direct comparison with experimental observations is lacking to prove the accuracy of the model and scaling process (Ref 33).

CHAPTER 3

RESEARCH OBJECTIVES

The general objective of the current research is to improve the understanding of deposition and adhesion phenomena in the CGDS process. Numerous features pertaining to the impact developments in CGDS have yet to be understood for process optimization. The lack of analysis stems mostly from the small physical and time scales at which deformation and bonding phenomena occur making any experimental in-situ observation a challenge. The current research proposes to first study ***the effect of substrate surface topography*** on pure aluminum particle deformation and bonding mechanisms upon impact on a hard steel substrate. Secondly, ***the measurement of particle in-flight temperature*** will be attempted using a newly developed commercial high-speed IR camera. The temperature data will be used to test, evaluate, and validate the accuracy of numerous Nusselt correlations utilized in the field. Subsequently, ***the effect of size dependent particle temperature on overall coating properties*** will be studied using an experimental approach involving coating generation and their property evaluation. In addition, a CFD numerical model designed using the appropriate Nusselt correlation found in the previous work will be developed. The final study will investigate the ***effect of particle impact characteristics on interfacial phenomena*** using both experimental deposition and finite element modeling of single particle impacts. The numerical approach will be used to acquire local particle/substrate interface characteristics reached upon particle collision otherwise impossible to visualize and assert. The experimental method, on the other hand, will provide evidence and support the conclusions and explanations gathered from the numerical study on bonding mechanisms and conditions.

3.1 The Effect of Substrate Surface Topography

The first objective investigates the influence of substrate topography on particle deposition and bonding nature, i.e. metallic and/or mechanical anchoring. Numerous studies have shown that substrate topography influences DE, i.e. first deposited layer, and adhesion. However, conducted experiments have been limited to arithmetic average surface roughness, R_a, of 10µm and/or to interfacial particle/substrate investigations, which do not provide any detail on the resulting bonding nature (Ref 191,192,215,216).

3.1.1 Substrate surface preparation methods

Three separate surface preparation procedures will be used and tested; polishing, grit blasting and FPWJ roughening, to allow a complete study across a wide range of surface roughness. The use of FPWJ to produce low R_a will allow to investigate the effects, if any, of grit embedment on overall coating adhesion detected in common grit blasting methods.

3.1.2 Adhesion nature evaluation

The coatings adhesion strengths will be evaluated on each surface preparation process following the ASTMC633 standard (Ref 217). A heat treatment will be applied on the produced coatings to initiate the growth of an intermetallic phase at the coating/substrate interface. The locations at which the intermetallic phases are detected will be used to reveal the position of fresh metal contact zones and provide information on the surface profile required to induce proper material deformation and oxide layer removal necessary for metallic bonding (Ref 215,218). In addition, numerical modeling of the coating adhesion test will be performed. The coating/substrate interface profile after CGDS deposition will be scanned using an optical microscope and data transferred in the FEM model (Ref 219). The simulation will model the quasi-static pull test for each coating to assess the fraction of the measured adhesion strength that can be attributed to the mechanical anchoring process.

The high speed particle impact will also be modeled through FEM to study the effects of surface roughness on resulting particle and substrate material deformation. As depicted in Figure 3.1, an impact on four different surface profiles will be studied and their influence on local interfacial variables, i.e. temperature, contact pressure, velocity vector and high equivalent plastic strain (PEEQ), reached in the particle and substrate material will be evaluated. The obtained values will be associated to the impact ability to generate metallurgical bonding at the contact interface (Ref 166,167,220).

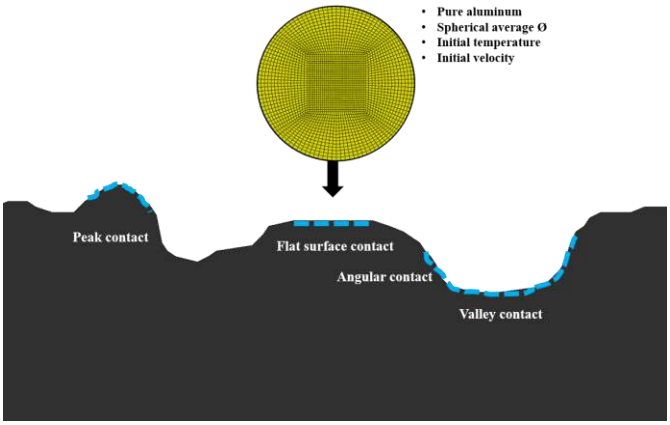

Figure 3.1: Numerical simulation of particle impact on four different substrate surface profiles (peak, valley, flat and angular contact).

3.2 Measurement of Particle in-Flight Temperature

A high speed mid-wave infrared camera (FAST M2k, Telops, QC, CA) will be utilized to measure the particle's in-flight temperature (Ref 221). Figure 3.2 illustrates the experimental set-up that will be utilized.

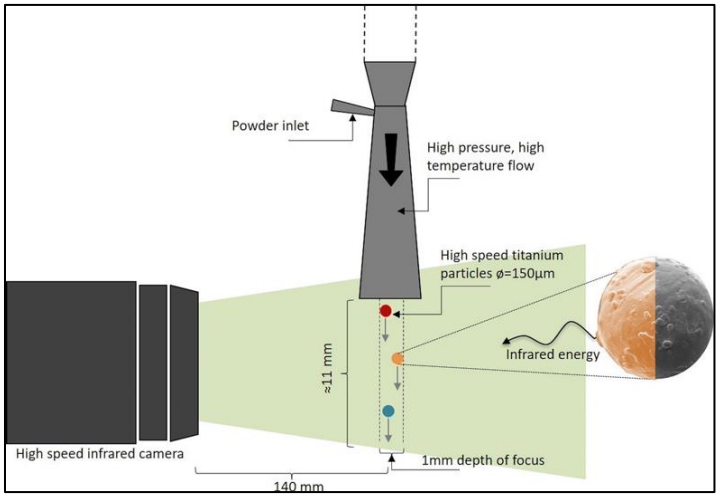

Figure 3.2: Temperature measurement using a high-speed infrared mid-wave camera during the CGDS process.

The CGDS gas stagnation parameters will be adjusted to ensure proper particle heating and acceleration at the nozzle exit.

3.2.1 Experimental particle velocity measurement

Although various techniques and equipment have been utilized to measure the particle velocity at the exit of the CGDS nozzle, the current study will use particle streak velocimetry (PSV) and particle tracking velocimetry (PTV) methods (Ref 25,105). The former process will use the particle streak length, i.e. generated from the utilised exposure time, from the obtained IR camera images, while the latter will utilize the particle position and travel time between two sequential frames.

3.2.2 Heat transfer and momentum exchange analysis

Following the measurement of particle in-flight temperature, a CFD study will be performed using ANSYS Fluent® and compared with the obtained particle velocity and temperature measurements. A one-way coupled Lagrangian scheme along with a RSM turbulence model will be utilized to track the particle trajectory, to model the particle/gas interactions and to predict the particulate phase in-flight characteristics (Ref 115,155,161,162). Numerous drag coefficient correlations will be tested to ensure proper particle motion description. The main goal of the numerical analysis, however, remains to test and validate which of the utilized Nusselt number correlations provides the most accurate definition of particle/gas heat transfer process occurring in the CGDS process.

3.3 Effect of Size-Dependent Particle Temperature on Overall Coating Properties

The influence of particle size dependent impact temperature on the adhesion, deposition and impact on previously bonded particulate phase, i.e. in-situ peening, will be studied in the present work.

3.3.1 Particle size dependent impact temperature

The first objective will be to generate depositions of particles with varying temperatures travelling at the same velocities using both low and high pressure cold spray systems. The stagnation pressure and temperature parameters will be investigated and obtained velocities at the nozzle exit will be measured. Once the CGDS process parameters are found, coatings will be generated on polished and grit blasted samples. Three sets of spherical feedstock powder with distinct and narrow size distributions will be used to ensure proper incorporation of the particle size effect.

3.3.2 Impact temperature influence on coating properties

The effect of impact temperature on powder deposition efficiency will be investigated. The mass gain will be measured during coating deposition to obtain the overall coating deposition efficiency. The effect of impact temperature on coating adhesion will then be studied, following the ASTM-C066 standard. Generated coatings will be machined to appropriate thickness and pulled to measure their adhesion/cohesion strength. The obtained values will be compared to the results obtained in the study presented in section 3.1 as to investigate the influence of temperature and size on the particle infiltration and mechanical anchoring on grit blasted samples. The coatings will also be investigated under the SEM to qualitatively describe the temperature effect on particle deformation. Finally, bend-to-break tests will be produced, following similar steps as presented in the ASTM-D4145-10 standard (Ref 222), to study the particle size dependent temperature apparent toughness, crack propagation mechanisms and fish scale processes. The objective of these experimental tests are to investigate the particle collision characteristics effects on metallic bonding processes (adhesion and cohesion) and the phenomena leading to coating attachment.

3.3.3 CFD modeling for particle trajectory and impact characteristics

As the measurement of particle temperature under high parameters, i.e. high speed, and of typical CGDS particle size, i.e. 30 to 70µm, might not be possible without extensive experimental testing, the developed numerical heat transfer model in the study presented in section 3.2 will be utilized instead. Thus, both low and high pressure CGDS systems will be modeled using ANSYS Fluent® CFD software in goals to retrieve the particle temperature at impact for all generated depositions. The flow structures, particle size influence on powder stream trajectory and impact characteristics will be studied. In addition to the main goal, the results and CFD analysis obtained from the current work will provide a clear understanding of the major differences between both CGDS systems and their individual inherent advantages. Finally, experimentally measured deposition efficiencies will be used to numerically acquire the full impact characteristics of depositing particles.

3.4 Effect of Particle Impact Characteristics on Interfacial Phenomena

The objective of the current investigation will be to study the effect of particle size and temperature on the deformation and interfacial bonding phenomena of single particle deposition.

3.4.1 Single particle deposition and characterization

Isolated single pure aluminum particle depositions will be generated using both high and low pressure CGDS systems at the parameters set in the previous study. Particles of spherical geometry will be utilized to reduce the effect of powder irregularities and satellite presence on deposition. The objective is to fully characterize the interfacial phenomena occurring at impact for both adhered and rebounded particles. The deposited single particles will be pulled using a local adhesion test process to reveal the particle/substrate interfacial state and presence of metallic bonding, i.e. atomically bonded zones will be identified using cup-and-cone features and/or protruding material. Particles traveling below their critical velocity will be collected after rebound using carbon tape near the CGDS gun trajectory.

3.4.2 Numerical simulation of single impact

The differences in deposition and bonding processes will be explained using FEM. Similarly as for the study presented in section 3.1.2, the commercial software package Abaqus/Explicit will be used to model single particles with varying impact characteristics. The characteristics obtained in section 3.3.3 will be utilized. Analysis of the obtained results will consist of investigating the interfacial temperature, pressure and oxide layer removal. In addition, the influence of local contact pressure on melting temperature and melt propagation process at the impact interface will be described in goals to understands its influence on particle bonding.

CHAPTER 4

RESEARCH APPROACH METHOD AND EQUIPMENT

The current chapter presents the experimental approach that will be used. More specifically, it provides the description of the equipment and apparatus that will be utilized. In addition, the numerical models, i.e. computational fluid dynamics simulation and finite element models, chosen to analyse the particle/gas and particle/substrate interface phenomena will be described and explained.

4.1 Feedstock and Substrate

The current sub-section describes the powder feedstock and substrate material that will be used to achieve the objectives presented in Chapter 3.

4.1.1 Powder material

Figure 4.1 presents the powder feedstock that will be sprayed. The teardrop shaped pure aluminum powder, shown in Figure 4.1a, which has been manufactured via gas atomization, has a chemical composition of 99.8% Al. The pure aluminum powders depicted in Figure 4.1b, with a 99.99% Al elemental composition, have been manufactured by Equispheres®, which generates spherical particles eliminating any geometrical effects related to irregular powder shape. As this powder will be used to study the particle size influence on deposition, three specific size distributions will be sprayed. All three size sets are shown in Figure 4.1b. The last powder that will be studied is a gas atomized spherical commercially pure (CP) titanium powder shown in Figure 4.1c. The CP Ti powder will be sieved using an in-house tap-sieve shaker unit (W.S. TYLER Ro-Tap Sieve Shaker, OH, USA) with proper woven sieve mesh cylinders to separate and recover all particles above 125μm of diameter, which will facilitate individual particle tracking processes during the particle temperature measurement tests.

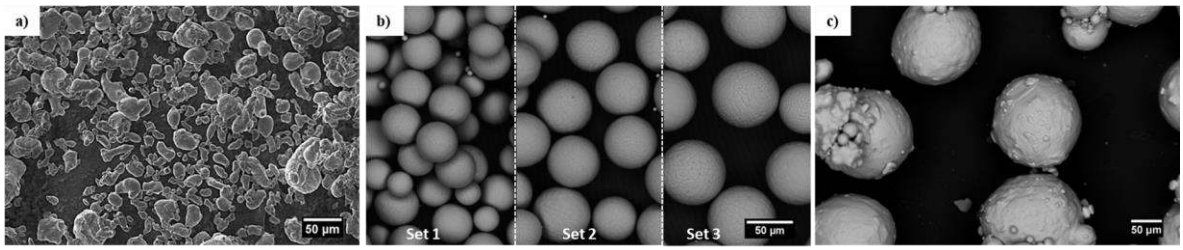

Figure 4.1: Powder feedstock to be sprayed in the current research. a) Irregularly shaped pure aluminum (99.8% Al, CenterLine (Windsor) Limited, Windsor, ON, Canada) b) Spherical pure aluminum (99.9% Al, Equispheres, ON, CA) and c) Spherical CP titanium with satellites (CP Ti Grade 1, Crucible Research, PA, USA).

4.1.2 Substrate

The substrate material, geometry and surface preparation prior to CS deposition are presented in the following sub-sections.

4.1.2.1 Substrate material and geometry

Steel alloys will be used as substrate material. Table 4.1 presents the chemical composition of both the vacuum arc remelted (VAR) 300M (Carpenter Technology, Mississauga, CA) and SAE1018 steels, selected specifically for the current research work.

Table 4.1: Steel alloy substrate compositions

Elements	Mn	C	S	P	Ir	Cr	Mo	Ni	Si	V	Al	Ti
300M	0.78	0.42	0.001	0.006	Bal.	0.81	0.40	1.90	1.68	0.07	0.04	0.002
SAE1018	0.70	0.15	0.02	0.03	Bal.	N/A	N/A	N/A	N/A	N/A	N/A	N/A

All substrates will be machined to a cylindrical geometry with dimension of 25.4mm diameter and 40mm height to facilitate subsequent mechanical testing, presented in section 4.4.1. The CS depositions will be made on the flat ends of the cylindrical samples.

4.1.2.2 Substrate surface preparation processes

Three different substrate surface preparation methods will be used to study the substrate topographical feature influence on coating bonding phenomena.

The first surface preparation method is the grit blasting process, commonly utilized in the CS field. A handheld gravity fed grit blasting unit will be used to this end to roughen the substrate surface. The grit will be fed through a steel nozzle and propelled using nitrogen at a pressure of 1.4MPa to 2MPa. During surface preparation, the nozzle will be held at a 45° angle and at a 50.8mm standoff distance to ensure proper surface preparation. Ferrosilicate abrasive with 20mesh size (850µm) will be utilized as the impacting medium.

The second surface treatment method is the forced pulse waterjet (FPWJ, VLN Advanced Technologies, Ottawa, CA) process, shown in Figure 4.2. The FPWJ method is equipped with a piezo-electric transducer, vibrating at a rate of 40KHz, which generates ultrasonic vibrations. These vibrations are transported to an internal nozzle assembly and the oscillatory waves are transmitted to a microtip located at the core of the nozzle generating the output flow. As the microtip vibrates, the pressurized water stream injected inside the nozzle is converted at its exit from a continuous flow to an interrupted pulsated jet. The intermittent slugs of water impart cyclic loading onto the substrate surface upon impact. In addition to the cyclic stress, a water hammer pressure is generated at the water/substrate interface during the impact process of each slug. This water hammer pressure represents the main advantage of the FPWJ process over the continuous waterjet impingement process. The resulting substrate surface cold working and erosive phenomena induced by the FPWJ are a mixed result of cavitation processes, cyclic loadings, lateral water flow and water hammer induced elastic-plastic deformation. The topographical features resulting from the FPWJ surface treatment are particular to the water/solid impingement and easily discernable from other surface treatment techniques.

Finally, the third process is polishing up to a mirror finish polish. Gradual grinding and polishing steps up to a final process using a 3µm abrasive suspensions are planned to be applied onto the substrate specimen. The polishing equipment to be used is described in more details in section 4.3.3.

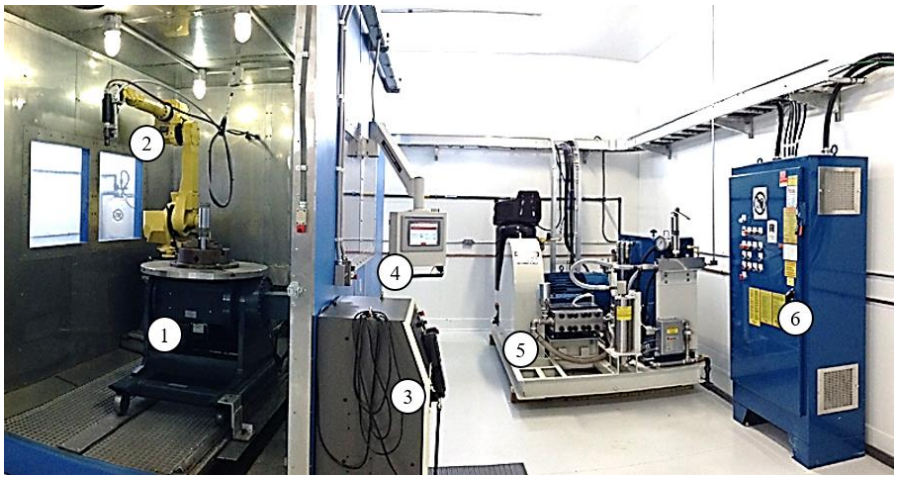

Part#	Part	Part #	Part
#1	Sample holder/table	#4	User control unit
#2	Robotic arm and nozzle assembly	#5	Pump assembly
#3	Safety unit	#6	FPWJ control unit

Figure 4.2: Forced pulsed waterjet surface preparation equipment.

4.2 Cold Spray Equipment

Two different systems have been chosen to complete the set goals of the current research; a LPCS accessible at the University of Ottawa Cold Spray Laboratory and a HPCS available at the National Research Council (NRC) – IMI , in Boucherville. Since the former is planned to be used extensively for each separate presented project, for the developing stages and proof of concept phases, it will be described and presented in much more details than the latter.

4.2.1 Low pressure cold spray system

The commercially available (SST-EP, CenterLine Limited, Windsor, ON, Canada) LPCS system that will be used is shown in Figure 4.3. The system runs using a 15kW heater which can provide a maximal temperature of 650°C and a maximal operating pressure of 3.45MPa. The carrier gas pressure is provided by an 18MPa single nitrogen bottle pack unit that holds eleven industrial high pressure nitrogen cylinders. The control unit shown in Figure 4.3a is used to set the operating pressure and temperature prior to deposition. The spray gun assembly includes the main gas heater and nozzle, as shown in Figure 4.4.

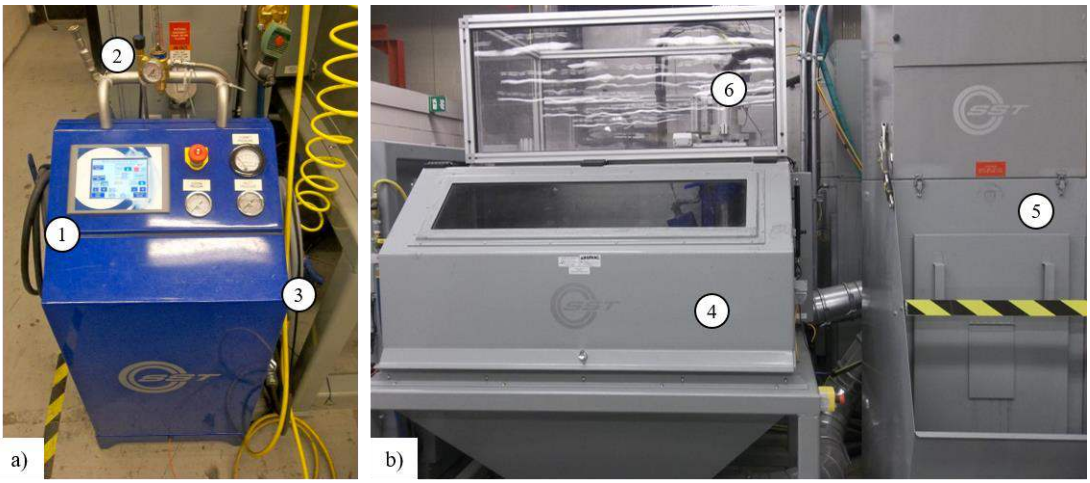

Part#	Part	Part #	Part
#1	Temperature control unit	#4	Spray chamber
#2	Powder feeder flow meter (argon)	#5	Water filtering system and HEPA filter
#3	Pressure regulator	#6	Step motor assembly

Figure 4.3: SST-EP CGDS system to be used at the University of Ottawa Cold Spray Laboratory. a) Centerline (Windsor) Ltd. SST-EP control unit and b) spray chamber and ventilation unit.

The entire assembly is mounted on a step motor controlling the acceleration, velocity and x-y displacement of the gun. The movement characteristics, i.e. velocity, acceleration, step size, number of cycles, total displacement and individual distances, are controlled by the user through PC Interface Software for X-SEL program. During spray, the samples will be enclosed in the spray chamber, shown in Figure 4.3, which is equipped with a ventilation system ensuring proper air working environment. Figure 4.4 also includes the converging/diverging nozzle at the bottom of the high pressure and temperature cylinder. Two different nozzles will be used. The pure aluminum powder will be deposited using a Centerline SST-Ultiflow polymer nozzle with a 2 mm throat diameter, 6.5 mm exit diameter and 120 mm of diverging length. The nozzle is machined out of polybenzimidazole (PBI) to avoid powder deposition at the nozzle walls during spraying at high stagnation parameters, which are planned to be used for proper deposition of coatings in the current study. To propel the CP titanium powder, a stainless steel (SS) nozzle will be utilized, which has the same dimensions as the PBI nozzle.

Part #	Part
#1	Heater, high pressure/temperature
#2	Converging and throat connection
#3	Diverging section of nozzle
#4	Powder feeding line
#5	Powder preheating inlet

Figure 4.4: Spray gun including the assembled converging/diverging nozzle.

The powder feeder, shown in Figure 4.5, main components are the powder canister, feeding wheel, the control panel and the gas carrier flow rate regulator. The canister keeps the powder away from contact with the atmosphere and allows a pressure buildup to propel the powder to the nozzle. The volumetric flow of nitrogen particle carrier gas will be set to 30SCFH for all tests, i.e. equivalent to 1.16NCMH.

Part #	Part
#1	Powder feeder canister
#2	Powder outlet
#3	Wheel speed controller

Figure 4.5: Termach powder feeder assembly.

4.2.2 High pressure cold spray system

The KINETIKS 4000 (Oerlikon Metco KINETIKS 4000, Switzerland, CH) HPCS system that will be used at the NRC facility is depicted in Figure 4.6.

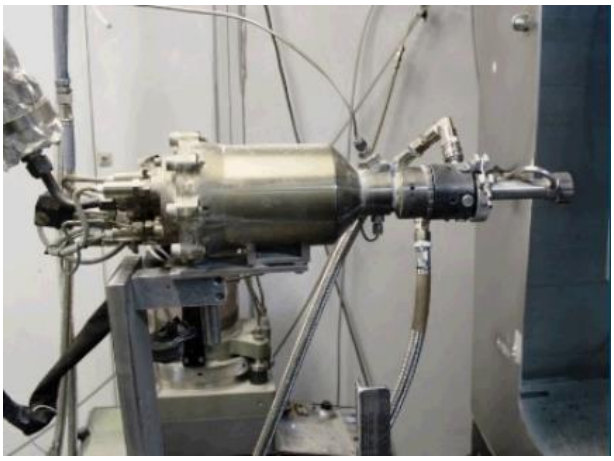

Figure 4.6: Oerlikon Metco KINETIKS 4000 cold spray system at the NRC facility.

The powder material is injected axially prior to the throat in the converging section of the setup. This powder feeding location, as mentioned in the literature, allows the powder to preheat to temperatures closer to the gas stagnation temperature. In addition, the system working parameters can reach a maximum of 800°C and 4MPa. Similarly as for the LPCS system, nitrogen will be used as the carrier and driving gas. A SiC nozzle will be used to propel the pure aluminum powder towards the substrate surface. The converging/diverging nozzle is characterized by a throat of 2.70 mm, an exit diameter of 6.96 mm and a diverging length of 132 mm. The converging section into which the powder material is injected has a length of 40 mm, i.e. no pre-chamber.

4.3 In-flight Particle Characteristics Measurements

4.3.1 High speed infrared camera

The high speed infrared camera that is planned to be used is shown in Figure 4.7. The IR camera (FAST M2K, Telops, QC, CA) is also equipped with a real time temperature calibration (RTTC) software, which facilitates its usage in dynamic environments such as in the nitrogen gas flow exiting from the converging/diverging CS nozzle. The RTTC allows the camera to be used at any recorded exposure time without the need to recalibrate the detected radiance with a high-accuracy blackbody. The working distance between the far end lens and the gas flow centre will be set to a constant distance for all experiments.

SPECIFICATIONS	FAST M2k
DETECTOR TYPE	InSb
SPECTRAL RANGE	1.5 µm to 5.5 µm
SPATIAL RESOLUTION	320 × 256 pixels
DETECTOR PITCH	30 µm
APERTURE SIZE	F/2.5
FULL FRAME RATE	1 910 Hz
MAXIMUM FRAME RATE	78 600 Hz @ 64 × 8 90 000 Hz @ 64 × 4
TYPICAL NETD	25 mK
EXPOSURE TIME	1 µs to full frame rate
LENS MOUNT	Bayonet interface

Figure 4.7: FAST M2K high speed infrared camera.

4.3.1.1 Heat transfer analysis and resulting particle temperature

The HypIR ® software, developed by Telops, will be used to analyze the saved sequences of the CGDS powder laden flow. The following analysis process will be used to calculate the particle resulting temperature.

The total infrared radiation, W_{tot}, captured by the IR detector will come from multiple sources bounded by the surrounding environment. This total radiation can be written as;

$$W_{tot} = E_p + E_r + E_a \qquad \textit{Eq. 53}$$

where E_p is the emitted infrared radiation by the in-flight particle, E_r corresponds to the emission generated by the surroundings and reflected by the particle and E_a is the emitted infrared energy by the surrounding atmosphere. The presented Eq. 53 can be rewritten as;

$$W_{tot} = \varepsilon_p \alpha_p E_p^B + \left(1 - \varepsilon_p\right)\alpha_g E_{ref}^B + (1 - \alpha_g)E_g^B \qquad \textit{Eq. 54}$$

where the subscript *p* and *g* relate to the particle and gas, respectively. The term $\alpha_g$corresponds to the gas transmittance, ε_p is the particle emissivity and E^B represents the radiation emitted towards the surrounding, i.e. from the gas or particle. The Eq. 54 is written in a simplified form, which does not take into account the dependence from T and $\tilde{\lambda}$ on the presented terms although the current study will account for them. Since the atmospheric transmittance, α_g, is approximately 90%, the E_g^B term has very little influence on the particle temperature and consequently, the atmospheric influence on the IR camera readings will be disregarded in the analysis.

Following Planck's law, the electromagnetic radiation emitted by the particle, $E_{\lambda p}$, at a specific wavelength, λ, and temperature, T, can be expressed by;

$$E_{\lambda p}(\lambda, T) = \varepsilon_{\lambda,T} \frac{C_1}{\lambda^5 \left(e^{\frac{C_2}{\lambda T}} - 1\right)} \quad \textit{Eq. 55}$$

where C_1 and C_2 correspond to the first and second radiation constants, respectively. In the current study, the utilized IR camera operates at midwave, which corresponds to wavelengths varying between λ_1 =3µm and λ_2 =5µm. The radiance emitted by the particles between these two wavelengths is calculated using an average radiance;

$$E_{mean} = \frac{1}{\lambda_2 - \lambda_1} \int_{\lambda_1}^{\lambda_2} E_{\lambda p}(\lambda, T)\, d\lambda \quad \textit{Eq. 56}$$

Since the radiance is continuous with wavelength and by applying the intermediate theorem, the emitted energy can be expressed as follow;

$$E_{mean} = E_{\tilde{\lambda}} = \varepsilon_{\tilde{\lambda},T} \frac{C_1}{\lambda^5 \left(e^{\frac{C_2}{\lambda T}} - 1\right)} \quad \textit{Eq. 57}$$

where $\tilde{\lambda}$ varies between the wavelength bounded by the used IR camera. By combining the expressions described in Eq. 54 and Eq. 57, the total infrared radiation captured from the IR camera during usage can be written as;

$$W_{total} = \varepsilon_{\tilde{\lambda},T} \frac{R}{\exp\left(\frac{B}{T_p}\right) - F} + \left(1 + \varepsilon_{\tilde{\lambda},T_p}\right) \frac{R}{\exp\left(\frac{B}{T_{ref}}\right) - F} \quad \textit{Eq. 58}$$

where R is function of the integration time and wavelength band, B is function of wavelength and F is a positive value close to 1. The particle temperature,T_p, highlighted in green in Eq. 58, will then be obtained from the total infrared radiation recorded internally by the detector.

4.3.2 Cold Spray meter (CSM)

The particle velocity will be measured experimentally using a Cold Spray Meter (Tecnar Automation Ltd. St-Bruno, QC, CA). The CSM is equipped with a continuous laser that provides a power density of 6.57 W/cm^2 and a 2.4W power at the exit of the optic fiber. The laser, characterized by a wavelength of 810 nm, features a spot size of 8mm at the 10 cm focal point. The particles traveling at high velocity are detected using their corresponding diffracted light.

4.3.3 General sample cutting, mounting and polishing

A precision saw (Secotom-10, Struers, Mississauga, CA) equipped with a silicon carbide cut-off wheel will be used to cut the samples to appropriate size for further analysis. Following the cutting

process, the samples will be mounted using a phenolic plastic powder in an automatic hot mounting press (LaboPress-3, Struers, Mississauga, CA) for samples requiring a cross-sectional analysis. The mounting process allows samples to have the appropriate cylindrical dimensions for grinding/polishing processes. For this purpose, an automatic grinder/polisher (Tegrapol, Struers, Mississauga, CA) will be used.

4.3.4 Optical microscope/ Scanning- Electron Microscope (SEM)

A digital optical microscope (VHX-2000 Keyence Corporation, Osaka, JP) will be used to obtain a general magnified image of samples cross-sections and a three-dimensional stitched image of the top surface topographical features. The microscope is equipped with a maximal magnification of 1000X, a variable depth-of-field that provides full focus for depth composition imaging and a high definition resolution allowing 54million pixels of data. The three-dimensional surfaces obtained using the digital optical microscope will be used to calculate the substrate surface roughness through a Matlab code that enables the evaluation of the arithmetical mean surface deviation (*Ra*), root mean square roughness (*Rq*) and peak to valley distance (*Rz)*. The definition of all three surface roughness descriptive parameters are given as follow;

$$R_a = \frac{1}{n}\sum_{i=1}^{n}|y_i| \qquad \textit{Eq. 59}$$

$$R_q = \sqrt{\frac{1}{n}\sum_{i=1}^{n} y_i^2} \qquad \textit{Eq. 60}$$

$$R_z = \frac{1}{n}\sum_{i=1}^{n} R_{pi} - R_{vi} \qquad \textit{Eq. 61}$$

where y_i is the vertical height from the mean line of the surface topography to the i^{th} data point for n ordered equally spaces points.

A scanning electron microscope (SEM, Oxford Instrument, EVO-MA10, Zeiss, UK) will also be utilized under secondary electron (SE) and back-scattered electron (BSE) signals to obtain specimen surface topography and elastic scattering, respectively. In addition, the energy-dispersive X-ray spectroscopy (EDS) analytical technique will be used to provide elemental atomic structure characterization. Prior to analyzing the samples mounted in phenolic plastic under the SEM, the sample surface will be coated with a thin gold conductive layer using a cold gold sputter device

(Denton Vacuum, USA). In addition to the gold layer, a copper tape will be placed from the coated surface to the metal sample holder to provide a conductive path for the electrons and avoid surface charge build-up during analysis.

4.4 Mechanical Characterization

4.4.1 Adhesion Test

The adhesion/cohesion of cold sprayed coatings will be tested according to the ASTM C633 standard. After deposition, the coatings will be faced using a lathe and machined to a uniform thickness. A thermally curing elastomeric adhesive bonding agent (FM-1000, Cytec Engineering Materials, MD, USA), with an 80 MPa bonding strength will be used to join the coated sample to a counter specimen after which the assembly will be positioned in an oven for 2 hours at 190°C. Three to six samples per sets will be tested for statistical purposes. For all tests, once the adhesive has cured, the assembled sample and counter specimen will be pulled using an Instron Universal tensile testing machine (Instron Series 420) at a rate of 0.7 mm/sec.

4.5 Other Relevant Equipment

4.5.1 Precision Balance

A precision scale for mass measurement, accurate urate to the 0.0001g, will be used to detect surface mass gain during CGDS deposition processes and calculate the deposition efficiency.

4.5.2 Profilometer

For very smooth substrate surfaces, the use of the three-dimensional stitching process to measure the roughness becomes difficult as it approaches the limit of the optical microscope. Hence, for polished surfaces a portable profilometer equipped with a 5μm diamond tip stylus (PHASE, SRG-4000, NJ, USA) will be used instead. The depth measuring tool allows detecting surface irregularities approaching the range of 0.0005μm to 16μm, which results in a display resolution of 0.001μm.

4.5.3 High temperature oven

A natural convection air oven (Carbolite PF120, Hope Valley, UK) will be used for all parts in the study requiring heating processes.

4.6 Numerical Model Structure

4.6.1 CFD/ gas and particle interaction

The following subsection covers the governing fluid flow equations and presents the computational methodology that will be used in the Computational Fluid Dynamics models.

4.6.1.1 Basic governing equations for compressible flows

The ANSYS/Fluent solver will be used to solve equations of mass, momentum and energy conservation. In ANSYS/Fluent, the compressible flow is described by standard continuity and momentum equations. The energy equation included in the solver incorporates proper coupling between the flow velocity and the static temperature. As the current study deals with compressible flows, the ideal gas law will be described as follow;

$$\rho = \frac{P_{op} + P}{\frac{R}{M_w}T} \qquad \textit{Eq. 62}$$

where ρ is the flow density, P_{op} is the operating pressure, defined as the atmospheric pressure, P is the local static pressure relative to the atmospheric pressure, R is the universal gas constant and M_w is the molecular weight. The temperature, T, is computed using the energy equation. The conservation of mass, or continuity, is written as follow;

$$\overbrace{\frac{\partial \rho}{\partial t}}^{Mass\ accumulation\ rate\ in\ CV} + \overbrace{\nabla \cdot (\rho \vec{v})}^{Net\ mass\ flux\ through\ CV} = S_m \qquad \textit{Eq. 63}$$

where the source S_m is the mass added to the gas phase from the particles injected in the flow and CV stands for control volume. In the current study, the mass added by the particulate phase has been evaluated to be too small to generate any important effect on the main flow such that the S_m term has been neglected. For 2D axisymmetric models, the conservation of mass can be written as follow;

$$2D\ axisymmetric \qquad \frac{\partial \rho}{\partial t} + \frac{\partial}{\partial x}(\rho v_x) + \frac{\partial}{\partial r}(\rho v_r) + \frac{\rho v_r}{r} = S_m \qquad \textit{Eq. 64}$$

where x is the axial coordinate, r is the radial coordinate, v_x is the axial velocity and v_r is the radial velocity. The momentum equation is written as follow;

$$\overbrace{\frac{\partial}{\partial t}(\rho \vec{v})}^{Transient} + \overbrace{\nabla \cdot (\rho \vec{v} \vec{v})}^{Convection} = \overbrace{-\nabla p}^{Pressure} + \underbrace{\nabla \cdot (\bar{\bar{\tau}})}_{Shear} + \overbrace{\rho \vec{g}}^{Body} + \underbrace{\vec{F}}_{External\ forces} \qquad \textit{Eq. 65}$$

where p is the static pressure, $\rho \vec{g}$ is the gravitational body force term, $\vec{F}$ is the external body forces (lift force, virtual mass force, external body force), the convection term expressed the change due

to the movement of the fluid element from one location to another where the flow properties are diverging, and $\bar{\bar{\tau}}$ is the stress tensor described as;

$$\bar{\bar{\tau}} = \mu\left[(\nabla\vec{v} + \nabla\vec{v}^{T}) - \frac{2}{3}\nabla\cdot\vec{v}I\right] \quad \textit{Eq. 66}$$

where μ is the molecular viscosity and I is the unit tensor. The second term on the right describes the effect of volume dilatation. In Eq. 65, the $\nabla\cdot\vec{v}$ term expresses the following;

$$\nabla\cdot\vec{v} = \frac{\partial v_x}{\partial x} + \frac{\partial v_r}{\partial r} + \frac{v_r}{r} \quad \textit{Eq. 67}$$

For 2D axisymmetric geometries, as the one used in the study described in section 3.2.2, the axial and radial momentum equations can be written as follow;

$$\frac{\partial}{\partial t}(\rho v_x) + \frac{1}{r}\frac{\partial}{\partial x}(r\rho v_x v_x) + \frac{1}{r}\frac{\partial}{\partial r}(\rho r v_r v_x) = -\frac{\partial P}{\partial x} + \frac{1}{r}\frac{\partial}{\partial x}\left[r\mu\left(2\frac{\partial v_x}{\partial x} - \frac{2}{3}(\nabla\cdot\vec{v})\right)\right] + \frac{1}{r}\frac{\partial}{\partial r}\left[r\mu\left(\frac{\partial v_x}{\partial r} + \frac{\partial v_r}{\partial x}\right)\right] + F_x \quad \textit{Eq. 68}$$

and

$$\frac{\partial}{\partial t}(\rho v_r) + \frac{1}{r}\frac{\partial}{\partial x}(r\rho v_x v_r) + \frac{1}{r}\frac{\partial}{\partial r}(\rho r v_r v_r) = -\frac{\partial P}{\partial r} + \frac{1}{r}\frac{\partial}{\partial x}\left[r\mu\left(\frac{\partial v_r}{\partial x} + \frac{\partial v_x}{\partial r}\right)\right] + \frac{1}{r}\frac{\partial}{\partial r}\left[r\mu\left(2\frac{\partial v_r}{\partial r} - \frac{2}{3}(\nabla\cdot\vec{v})\right)\right] - 2\mu\frac{v_r}{r^2} + \frac{2}{3}\frac{\mu}{r}(\nabla\cdot\vec{v}) + \rho\frac{v_z^2}{r} + F_r \quad \textit{Eq. 69}$$

The conservation of energy in the studied system is defined as;

$$\overbrace{\frac{\partial}{\partial t}(\rho E)}^{Transient} + \overbrace{\nabla\cdot\left(\vec{v}(\rho E + p)\right)}^{Convection} = -\nabla\cdot\left(\overbrace{k_{eff}\nabla T}^{Conduction} - \underbrace{\sum_j h_j\vec{J}_j}_{Species\ diffusion} + \overbrace{\left(\bar{\bar{\tau}}_{eff}\cdot\vec{v}\right)}^{Viscous\ dissipation}\right) + S_h \quad \textit{Eq. 70}$$

where k_{eff} is the effective conductivity ($k_{eff} = \left(\frac{1}{Pr}\right)C_p\mu_{eff}$) in which Pr represents the Prandtl number, and $\vec{J}_j$ is the diffusion flux of species j. The energy transfer from conduction, species diffusion, and viscous dissipation are represented by the first three terms of the right side of Eq. 70, respectively. The S_h defines the heat of chemical reaction and any volumetric heat sources, i.e. radiation source, interphase source and reaction source. In the CGDS process, the S_h has been neglected. In Eq. 70;

$$E = h - \frac{p}{\rho} + \frac{v^2}{2} \qquad \textit{Eq. 71}$$

where sensible enthalpy, h, is defined for ideal gases as follow;

$$h = \sum_j Y_j \, h_j \qquad \textit{Eq. 72}$$

and where Y_j is the mass fraction of species j and where

$$h_j = \int_{T_{ref}}^{T} C_{p,j} dT \qquad \textit{Eq. 73}$$

with T_{ref} =298.15K. In a pressure-based solver, the thermal energy generated by viscous shear in the flow is not automatically included by the solver in the conservation of energy equation, Eq. 70. Thus, the viscous heating is separately added through the viscous model and is functional when the Brinkman number, Br, approaches or exceeds unity. The Br number is defined in the solver as;

$$Br = \frac{\mu V^2}{k \Delta T} \qquad \textit{Eq. 74}$$

in which ΔT represents the temperature difference in the analysed system.

4.6.1.2 Turbulence model

Due to the small scale and high frequency in which the turbulent fluctuations appear, it is computationally too expensive to directly calculate and account for those fluctuations. To remedy this problem, governing equations can be time-averaged, ensemble-averaged or manipulated to remove the resolution of small scales. This modification in governing equations however introduces additional unknown variables, which can be solved using turbulence models. In the current research, the RNG k-ε turbulence model will be used. This model uses the two following relations;

$$\underbrace{\overbrace{\frac{\partial}{\partial t}(\rho k)}^{Rate\ of\ increase} + \overbrace{\frac{\partial}{\partial x_i}(\rho k u_i)}^{Convective\ transport} = \overbrace{\frac{\partial}{\partial x_j}\left(\alpha_k \mu_{eff} \frac{\partial k}{\partial x}\right)}^{Diffusion\ transport} - \overbrace{\widetilde{\rho\epsilon}}^{Dissipation/Destruction} - Y_M + S_k + G_k + G_b}_{Turbulent\ kinetic\ energy/Transport\ of\ k} \qquad \textit{Eq. 75}$$

and

$$\underbrace{\overbrace{\frac{\partial}{\partial t}(\rho \epsilon)}^{Rate\ of\ increase} + \overbrace{\frac{\partial}{\partial x_i}(\rho \epsilon u_i)}^{Convective\ transport} = \overbrace{\frac{\partial}{\partial x_j}\left(\alpha_\epsilon \mu_{eff} \frac{\partial \epsilon}{\partial x}\right)}^{Diffusion\ transport} + \overbrace{C_{1\epsilon}\frac{\epsilon}{k}(G_k + C_{3\epsilon}G_b)}^{Generation} - \overbrace{C_{2\epsilon}\rho\frac{\epsilon^2}{k}}^{Destruction} - R_\epsilon + S_\epsilon}_{Dissipation\ rate/Transport\ of\ \epsilon} \qquad \textit{Eq. 76}$$

where G_k and G_b are the generation of turbulent kinetic energy due to the mean velocity gradient and the buoyancy, respectively. Y_M is the contribution of the fluctuating dilatation in compressible turbulence to the overall dissipation rate, α_k and α_ϵ are the inverse effective Prandtl numbers for k and ϵ, respectively. User defined source terms can also be added and are accounted for in S_k and

S_ϵ. The terms $C_{1\epsilon}$=1.42 and $C_{2\epsilon} = 1.68$ are derived analytically using the RNG theory. In addition, the RNG theory generates a differential equation for turbulent viscosity, given as;

$$d\left(\frac{\rho^2 k}{\sqrt{\epsilon\mu}}\right) = 1.72\frac{\hat{v}}{\sqrt{\hat{v}^3 - 1 + C_v}}d\hat{v} \qquad \textit{Eq. 77}$$

where $\hat{v} = \mu_{eff}/\mu$ and $C_v \approx 100$. Eq. 77 provides the variance of the effective turbulent transport with Reynolds number, which allows increased accuracy at the CGDS nozzle near-wall regions and low Reynolds number flow.

4.6.1.3 Solution time dependence

In the current research, to capture the time dependent solutions of the Navier-Stokes equations, the Reynolds-averaged Navier-Stokes (RANS) method for turbulent flows will be utilized. The fundamental approach of the technique consists of decomposing a flow variable into a mean and fluctuating component.

4.6.1.4 Solution algorithm

4.6.1.4.1 Pressure based

A pressure-based solver will be used to calculate the flow properties in the converging/diverging nozzle system. The solver employs a method, commonly called projection method, where the constraint of mass conservation of the velocity field is generated by solving a pressure equation. The pressure equation is derived from the continuity and momentum equations such that the velocity field corrected by the pressure satisfies the continuity. Since the equations governing the flow properties are nonlinear and coupled, the solver process includes iterations in which the governing equations are solved repeatedly until a converged solution is reached. To solve, a SIMPLE segregated algorithm is used, which solves the governing equations sequentially, i.e. segregated from one another, and the individual solutions are obtained one after the other, as shown in Figure 4.8.

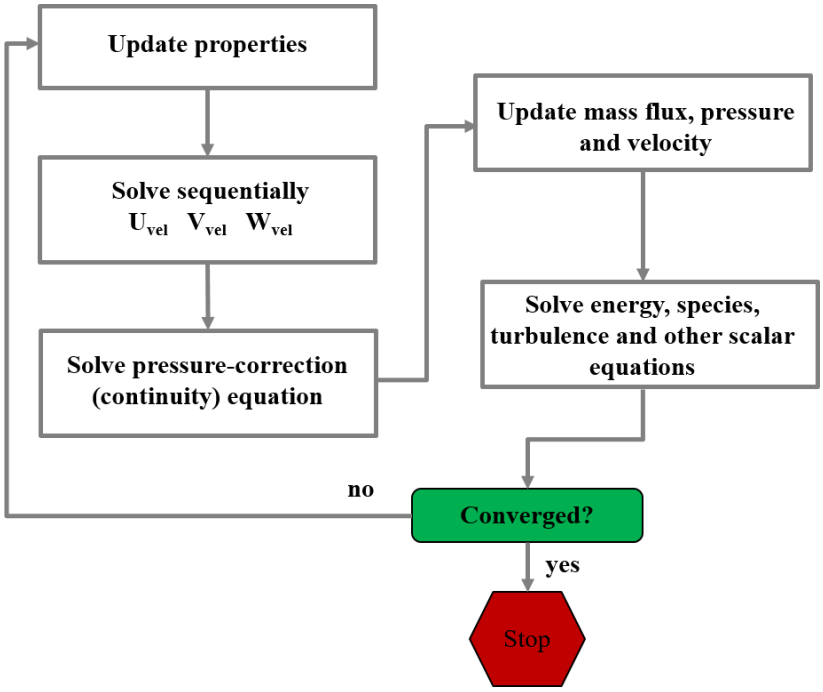

Figure 4.8: Illustration of the SIMPLE segregated algorithm approach in solving the governing flow equations.

The separate steps include the following;

1. Based on the current solution, fluid properties are updated (density, viscosity, specific heat, turbulent viscosity).
2. Momentum equations are solved sequentially using the updated values of pressure and face mass fluxes.
3. The pressure correction equation is solved with updated velocity field and mass-flux.
4. From step 3. The face mass fluxes, pressure and the velocity field are updated based on the solution of the pressure correction equation.
5. Solve equations for additional scalars such as turbulent quantities.
6. Update the source terms arising from the interaction generated between different phases (source terms in the carrier gas phase due to discrete particles).
7. Verify convergence.

4.6.1.4.2 Density based

In addition, a density based solver will also be used in the current research for the three dimensional CS flow models, described in section 3.3. The density based solver similarly to the pressure based approach utilizes a control-volume based technique, however, the governing equations (continuity, momentum and energy) are solved simultaneously rather than sequentially. The following steps, illustrated in Figure 4.9, are looped until the converging criteria is met;

1. Fluid properties updated (initialized values are used at the start of the simulation).
2. Solve the continuity, momentum and energy equations.
3. Solve equations for scalars such as turbulence using previously updates values of other variables.
4. Verify convergence.

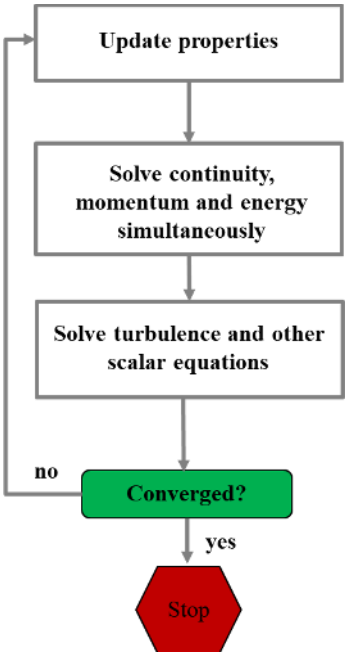

Figure 4.9: Density based solution steps.

The formulation of the solver will be implicit, which although requires more computational memory than the explicit formulation allows reaching a converged state much faster. The implicit approach solves all coupled variables (p, u, v, w, T), in all cells at the same time. Each unknown variable in a cell is computed using a relation that includes both existing and unknown values from the neighboring cells. These unknowns are thus included in more than one equation and then solved for simultaneously.

4.6.1.5 Discretization schemes

Different spatial discretization schemes will be used. A second order upwind and QUICK (Quadratic Upstream Interpolation for Convective Kinematics) schemes will be utilized for that purpose. The second order upwind will be used for the spatial discretization of the flow and turbulent properties. This scheme calculates quantities at cell faces using a multidimensional linear reconstruction approach. The QUICK discretization scheme, on the other hand, is based on a weighted average of second-order upwind and central interpolation of the studied variable.

4.6.2 FEM/Impact process and adhesion test

The explicit dynamic procedure will be used for the simulation of particle impact processes and the quasi-static adhesion testing.

4.6.2.1 Explicit dynamic analysis frame

ABAQUS/Explicit ®, commonly used to simulate the impact of CGDS particles on deformable target substrate surfaces will be used in the current research. The explicit dynamic analysis for integration uses a central-difference operator, i.e. the displacement and velocities are calculated based on known data at the start of an increment. Hence, the global mass and stiffness matrices do not need to be formed and inverted as normally completed in an implicit frame of work. The stability of the central-difference method is controlled through the selected time increment. To avoid rapidly growing errors, the time increment is chosen as the time required for a stress wave to cross the smallest element dimension in the model. Hence, this solving method is favoured in problems that include a total dynamic response time only a few orders of magnitude longer that the stability limit, such as the impact of CGDS particles for which the full analysis requires only a few nanoseconds. An approximation to the stability limit can be expressed as;

$$\Delta t \approx \frac{L_{min}}{c_d} \qquad \textit{Eq. 78}$$

where L_{min} is the smallest element dimension in the chosen meshing process and c_d is the dilatation wave speed, solely responsible for volume changes in the analyzed medium. The dilatation wave speed can be expressed in terms of λ_0 and μ_0 as;

$$c_d = \sqrt{\frac{\lambda_0 + 2\mu_0}{\rho}} \qquad \textit{Eq. 79}$$

where ρ is the material density and λ_0 and μ_0 are both effective Lam's constants defined in terms of the young's modulus, E, and Poisson's ratio, *v*. In ABAQUS/Explicit the default time incrementation scheme is set to ***fully automatic*** and is used in the current study.

The solving procedure implemented in ABAQUS software considers both the explicit integration rule and a diagonal element mass matrix. Hence the equations of motion are integrated using the central-difference integration rule as follow;

$$\dot{u}^N_{(i+\frac{1}{2})} = \dot{u}^N_{\left(i-\frac{1}{2}\right)} + \frac{\Delta t_{(i+1)} + \Delta t_{(i)}}{2} \ddot{u}^N_{(i)} \qquad \textit{Eq. 80}$$

and

$$u^N_{(i+\frac{1}{2})} = u^N_{(i)} + \Delta t_{(i+1)} \dot{u}^N_{(i+\frac{1}{2})} \qquad \textit{Eq. 81}$$

where u^N is the degree of freedom (ex: a displacement) and the subscript *i* is the increment number in the explicit dynamic step. Hence, the kinematic state of the analysed body as it advances in time is calculated with known values of $\dot{u}^N_{\left(i-\frac{1}{2}\right)}$ and $\ddot{u}^N_{(i)}$ from the previous increment. The diagonal element mass matrices, with known accelerations, are computed as follow;

$$\ddot{u}^N_{(i)} = (M^{NJ})^{-1}\left(P^J_{(i)} - I^J_{(i)}\right) \qquad \textit{Eq. 82}$$

where M^{NJ} is the mass matrix, P^J is the applied vector load and I^J is the internal force vector assembled from contributions of individual elements.

In the CGDS field, a fully coupled thermal-stress analysis is commonly used to perform calculations as the mechanical and thermal effects influence each other strongly. In the explicit frame, the heat transfer equations are integrated using the explicit forward-difference time integration.

The quasi-static adhesion tests will also be simulated using the explicit dynamic framework. Applying the explicit procedure, described above, to quasi-static problems reduces the required system resources, which decreases the simulation time.

4.6.2.2 Material properties

4.6.2.2.1 Elastic properties and shock wave influence

Following is the definition of the materials linear elastic model behavior. In the model, the total stress in the elastic region is defined using the total elastic strain;

$$\sigma = \boldsymbol{D}^{el}\varepsilon^{el} \qquad \textit{Eq. 83}$$

where σ is the true stress state, $\boldsymbol{D}^{el}$ is the fourth-order elasticity tensor and ε^{el} is the total logarithmic elastic strain (of same value than engineering strain at small deformations). The hydrodynamic stress, related to the volume changes, is determined by an equation of state. The equation for conservation of energy needs to equate the increase in internal energy per unit mass, E_m, to the rate at which work is being produced by stresses and the rate at which heat is being added, such that;

$$\overbrace{\rho\frac{\partial E_m}{\partial t}}^{Change\ of\ internal\ specific\ energy} = \overbrace{(p-p_{bv})\frac{1}{\rho}\frac{\partial \rho}{\partial t} + \boldsymbol{S}:\dot{e}}^{Rate\ of\ work\ done\ by\ stresses} + \overbrace{\rho\dot{Q}}^{Added\ heat\ rate} \qquad \textit{Eq. 84}$$

where p is the pressure stress, p_{bv} is the pressure stress due to the bulk viscosity (resistance to deformation), $\boldsymbol{S}$ is the deviatoric stress tensor, $\dot{e}$ is the deviatoric part of the strain rate and $\dot{Q}$ is the heat transfer per unit mass. The p_{bv}, however, is a default numerical effect added in FEM to smear a shock front and prevent elements from collapsing (zero volume across a single time increment)

under extreme velocity gradients. An equation of state is defined which assumes the pressure is a function of the density, ρ, and the internal energy per unit mass, E_m, such that;

$$p = f(\rho, E_m) \quad \textit{Eq. 85}$$

In high energy impacts, such as the impact generated by particles in the CGDS process, the hydrodynamic pressure is calculated using the analytical Mie-Gruneisen equation of state (EOS) instead of the linear elastic part of the stress-strain curve (Young's modulus). The Mie-Gruneisen EOS is a special form of the Gruneisen model used to describe the effect of the volume change on the vibrational properties of crystal lattice. This influence describes, in other words, the effect of a change in density on the internal material energy. The Gruneisen model provides;

$$\Gamma = V\left(\frac{dP}{dE}\right)_V \quad \textit{Eq. 86}$$

where Γ is the Gruneisen parameter, V expresses the volume, P is the pressure and E is the internal energy. With the assumption that the Gruneisen parameter, Γ, is independent of P et E, when integrated, the expression in Eq. 86, can be written as follow;

$$p - p_H = \Gamma\rho(E_m - E_H) \quad \textit{Eq. 87}$$

where p_H and E_H are the Hugoniot pressure and specific energy per unit mass at a reference state. This reference state is commonly taken from a model that expresses the pressure dependence on density and internal energy, which doesn't account for the volume change effect on lattice vibration (cold curve). For the current Mie-Gruneisen EOS case, the reference is estimated by the Hugoniot equations given by Eq. 87. In a shock compressed material, the Hugoniot equations are developed following mass, momentum and energy conservation. In a material which includes a shock wave propagation, a relative motion exists between the two that needs to be accounted for. As shown in Figure 4.10, the shock propagates at a speed, u_s, while the material compressed by the pressure behind the shock travels at another speed, u_m. The Hugoniot equations developed using a moving reference frame, i.e. the shock front, have velocities expressed as follow;

$$\begin{gathered}\text{velocity of material behind the shock} = u_s - u_m \\ \text{velocity in front of the shock} = u_s.\end{gathered} \quad \textit{Eq. 88}$$

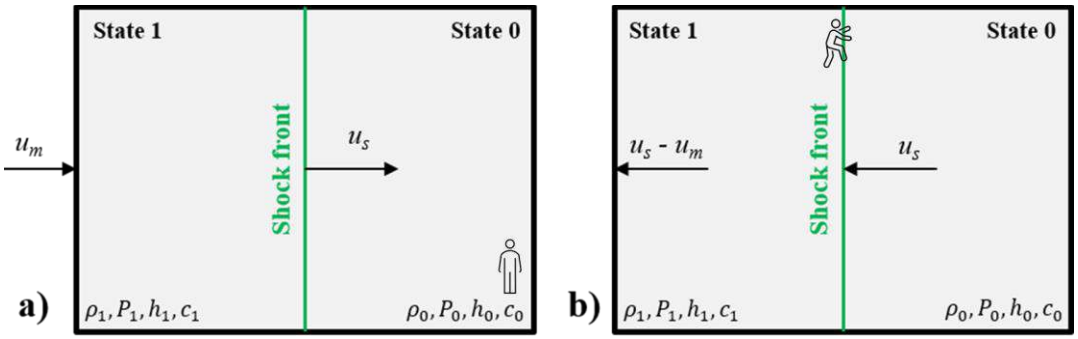

Figure 4.10: Shock wave propagation through material in a) stationary medium and b) moving frame.

Assuming a steady state and that the area before and after the shock is the same, the conservation laws utilized in the Hugoniot analysis can be expressed as follow;

Mass conservation: $$\frac{\dot{M}}{A} \equiv \rho_0 u_s = \rho_1(u_s - u_m) \quad \textit{Eq. 89}$$

Momentum conservation: $$P_1 - P_H = \rho_0 u_s u_m \equiv \frac{\dot{M}}{A}(u_m) \quad \textit{Eq. 90}$$

Energy conservation: $$\frac{\dot{M}}{A} \cdot \left[h_1 - h_0 + \frac{1}{2}(u_s - u_m)^2 - \frac{1}{2}(u_s)^2\right] = 0 \quad \textit{Eq. 91}$$
(1rst law of thermodynamics)

where $\dot{M}$ is the mass flow rate, A is the area and h is the specific enthalpy. These sets of equations are conditions on the jump in values across any shock wave and they are referred to as the Rankine-Hugoniot equations. To solve, the linear relationship between the shock and material speed used;

$$u_s = c_0 + s \cdot u_m \quad \textit{Eq. 92}$$

where c_0 is the speed of sound at an uncompressed state and s is the Hugoniot slope ($s = dU_s/dU_p$) determined by experiments. Eq. 92 states that shock wave velocity is proportional to particle velocity. At this stage, if the shock wave velocity, u_s, is known from experiments, all unknowns in Eq. 89 to Eq. 91 (u_m, P_1, ρ_1, h_1) can be determined. However, in CGDS the u_s value is not measurable, and instead the EOS is used as expressed in Eq. 85 to obtain an additional relation to Eq. 89 to Eq. 91.

Using the previous relations, the Hugoniot energy, E_H, and the Hugoniot pressure, P_H, required in the Mie-Gruneisen EOS, can be expressed as;

$$E_H = \frac{P_H\left(1-\rho_0/\rho\right)}{2\rho_0} \quad \text{(steps presented in Appendix } A\text{)} \quad \textit{Eq. 93}$$

Using the mass, momentum and experimental relationship, the Hugoniot pressure is provided by;

$$P_H = \frac{\rho_0 c_0^2 \eta}{(1-s\eta)^2} \qquad \text{(steps presented in Appendix } B\text{)} \qquad \textit{Eq. 94}$$

such that the Gruneisen ratio term, Γ, present in Eq. 86, is defined as;

$$\Gamma = \Gamma_0 \frac{\rho_0}{\rho} \qquad \textit{Eq. 95}$$

where Γ_0 is a material constant, ρ_0 is the material reference density and $\eta = \frac{\rho}{\rho_0}$. Using the Gruneisen ratio definition, the Hugoniot pressure expression and the Hugoniot energy, the Mie-Gruneisen equation, expressed by Eq. 87 can be rewritten as follow;

$$p = \frac{\rho_0 c_0^2 \eta}{(1-s\eta)^2}\left(1 - \frac{\Gamma_0 \eta}{2}\right) + \Gamma_0 \rho_0 E_m. \qquad \textit{Eq. 96}$$

The Mie-Gruneisen equation is implemented in ABAQUS, which will be used in the current study for the high speed particle impact simulation. The Γ_0, c_0, ρ_0 and s parameters are material dependent properties.

The development presented above only describes the hydrodynamic stress, i.e. stress related to volume changes. The deviatoric stress, *d*, related to the stress causing shape change, given by the following equation will be used in the current simulations;

$$\mathrm{d} = 2G_e\epsilon_d \qquad \textit{Eq. 97}$$

where G_e is the elastic shear modulus and ϵ_d is the elastic deviatoric strain.

4.6.2.2.2 Plastic properties

The plasticity model commonly used in the CGDS field is the Johnson-Cook model. It is indented for applications including kinematic hardening and important rate-dependent effects. The model uses the Mises yield surfaces, common definition of isotropic yielding, independently of the equivalent pressure stress. During isotropic hardening, the yield surface size uniformly changes in all directions such that the yielding stress increases with increasing plastic straining. The Johnson-Cook hardening model has been used by many in the field to model the particle high-rate deformation impact process. The static yield stress, σ^0, is expressed as;

$$\sigma^0 = \left[A + B\left(\bar{\varepsilon}^{pl}\right)^n\right]\left[1 - \hat{T}^m\right] \qquad \textit{Eq. 98}$$

where $\bar{\varepsilon}^{pl}$ is the equivalent plastic strain, *A, B, n* and *m* are materials parameters and $\hat{T}$ is the non-dimensional temperature defined as;

$$\hat{T} \equiv \begin{cases} 0 & for\ T < T_{transition} \\ (T - T_{transition})/(T_{melt} - T_{transition}) & for\ T_{transition} \le T \le T_{melt} \\ 1 & for\ T > T_{melt} \end{cases}$$

where T is the current temperature, T_{melt} is the melting temperature and $T_{transition}$ is the transition temperature defined as the temperature at which or below which the material has no temperature dependence on the calculation of yield stress. When $T > T_{melt}$, the material is in its melted form and will behave as a fluid such that no shear resistance will be generated and $\sigma^0 = 0$. In addition, the Johnson-Cook model also includes a strain rate dependent term, described as follow;

$$\bar{\sigma} = \sigma^0\left(\bar{\varepsilon}^{pl}, T\right)R\left(\dot{\varepsilon}^{pl}\right) \qquad \textit{Eq. 99}$$

and

$$\dot{\varepsilon}^{pl} = \dot{\varepsilon}_0 exp\left[\frac{1}{C}(R-1)\right] \qquad for\ \bar{\sigma} \geq \sigma^0 \qquad \textit{Eq. 100}$$

where $\bar{\sigma}$ is the yield stress at nonzero strain rate, $\dot{\varepsilon}^{pl}$ is the equivalent plastic strain rate, $\dot{\varepsilon}_0$ and C are material parameters measured at or below $T_{transition}$, $\sigma^0\left(\bar{\varepsilon}^{pl}, T\right)$ is the static yield stress and $R\left(\dot{\varepsilon}^{pl}\right)$ is the ratio of the yield stress at nonzero strain rate to the static yield stress, i.e $R(\dot{\varepsilon}_0 = 1.0)$. Finally, the form in which the Johnson-Cook yield stress model will be used in the current research is expressed as;

$$\sigma^0 = \overbrace{\left[A + B(\bar{\varepsilon}^{pl})^n\right]}^{Plastic\ strain\ influence} \cdot \overbrace{\left[1 + C\ln\frac{\dot{\varepsilon}^{pl}}{\dot{\varepsilon}_0}\right]}^{Strain\ rate\ effect\ (viscosity)} \cdot \overbrace{\left[1 - \hat{T}^m\right]}^{Thermal\ softening/Temperature\ effect} \qquad \textit{Eq. 101}$$

where $\bar{\sigma}$ is the yield stress at nonzero strain rate, $\dot{\varepsilon}^{pl}$ is the equivalent plastic strain rate, $\dot{\varepsilon}_0$, C are material parameters measured at or below $T_{transition}$, *A, B, n* and *m* are materials parameters, and $\hat{T}$ is the non-dimensional temperature. Many have used the previous equation to characterize the material plastic deformation. However, this model has clear limitations at very high strain rates ($> 10^7 s^{-1}$). Erroneous results have been obtained through extreme element deformation and distortion. This limitation stems from the fact that at very high strain rates, the mechanisms governing the dislocation motion transforms from thermally activated to phonon drag. To account for this change, the Preston-Tonks-Wallace (PTW) constitutive model has been used in CGDS modeling. The PTW model and material relations are not included in the ABAQUS software and will thus be added separately through a user subroutine (VUHARD). The flow stress, σ, defined by Preston et al. is given as follow;

$$\sigma = 2\left[\hat{\tau}_s + \alpha\ln\left[1 - \varphi\exp\left(-\delta - \frac{\theta\epsilon_p}{\phi\varphi}\right)\right]\right]G_p \qquad \textit{Eq. 102}$$

$$\phi = \frac{s_0 - \hat{\tau}_y}{n}, \qquad \delta = \frac{\hat{\tau}_s - \hat{\tau}_y}{\alpha}, \qquad \varphi = \exp(\delta) - 1 \qquad \textit{Eq. 103}$$

where $\hat{\tau}_s$ is the normalized work hardening saturation stress, $\hat{\tau}_y$ is the normalized yield stress, θ is the strain hardening rate, $\epsilon_p$is the plane strain, s_0 is the saturation stress at 0K and n is the strain hardening constant. The plastic shear modulus, G_p,is dependent on the temperature and is defined by the Mechanical Threshold Stress (MTS) model:

$$G_p(T) = G_0 - \frac{B}{\exp\left(\frac{J}{T}\right) - 1} \qquad \textit{Eq. 104}$$

in which G_0 is the shear modulus at 0K, B is a material constant, J is a temperature material constant and T is the corresponding node temperature. The following equations are used to determine the work hardening saturation stress, $\hat{\tau}_s$, and the yield stress, $\hat{\tau}_y$;

$$\hat{\tau}_s = \max\left\{s_0 - (s_0 - s_\infty)\mathrm{erf}\left[\kappa\hat{T}\ln\left(\frac{\gamma\dot{\xi}}{\dot{\epsilon}_p}\right)\right], s_0\left(\frac{\dot{\epsilon}_p}{\gamma\dot{\xi}}\right)^{\beta}\right\} \qquad \textit{Eq. 105}$$

$$\hat{\tau}_y = \max\left\{y_0 - (y_0 - y_\infty)\mathrm{erf}\left[\kappa\hat{T}\ln\left(\frac{\gamma\dot{\xi}}{\dot{\epsilon}_p}\right)\right], \min\left\{y_1\left(\frac{\dot{\epsilon}_p}{\gamma\dot{\xi}}\right)^{y_2}, s_0\left(\frac{\dot{\epsilon}_p}{\gamma\dot{\xi}}\right)^{\beta}\right\}\right\} \qquad \textit{Eq. 106}$$

where $\hat{T} = T/T_m$, T_m is the melting temperature, s_∞ is the saturation stress near the melting temperature, κ is the temperature dependence constant, γ is the strain rate dependence constant, $\dot{\epsilon}_p$ is the plastic strain rate, β is the high strain rate exponent, y_0 is the yield stress constant at 0K, y_∞ is the yield stress constant near melting temperature, y_1 is the medium strain rate constant and y_2 is the medium strain rate exponent. The two definitions provided in the maximum function are used for both low and high strain rate regimes. When low strain rates prevail, the first correlation in the maximum function is used, while the second is utilised when the strain rate goes above a threshold which defines the start of the dislocation drag mechanism governed dislocation movement.

The material parameter, $\dot{\xi}$, in the pervious equations is defined as follow;

$$\dot{\xi} = \frac{1}{2}\left(\frac{4\pi\rho_m}{3M_a}\right)^{1/3}\left(\frac{G_p(T)}{\rho_m}\right)^{1/2} \qquad \textit{Eq. 107}$$

where M_a is the atomic mass.

CHAPTER 5

RESEARCH PROJECTS RESULTS

This chapter presents three peer reviewed papers published in international journals relevant to the current research. Two of which have been published in the Journal of Thermal Spray Technology (*J. Therm. Spray Technol.*) and one in the Surface and Coating Technology (*Surf. Coat. Technol.*). The last study is written as a research article and will be submitted in a peer-reviewed journal. Each paper addresses one of the main research objectives presented in Chapter 3.

5.1 RESEARCH PROJECT 1

This paper studies the effect of substrate surface roughness on the impact induced interfacial properties and characteristics susceptible to generate fresh-metal contact zones, i.e. localized pressure rise and extensive material plastic flow, and subsequently metallic (atomic) bonding, i.e. localized temperature rise, large contact pressures and particle beneficial vertical momentum. The fraction and role of mechanical and metal bonding in the obtained coating adhesion strengths are characterized using FEM and experimental diffusion test, respectively. It was shown that for any increase in substrate roughness, the adhesion process shifts from a metallic bonding, on polished surface, to a mechanical anchoring process. The polished surface allows the generation of improved contact characteristics, such as temperature and contact pressure. This peer-reviewed paper addresses the objectives presented in section 3.1.

J Therm Spray Tech (2017) 26:1461–1483
DOI 10.1007/s11666-017-0602-1

PEER REVIEWED

Experimental and Numerical Study of the Influence of Substrate Surface Preparation on Adhesion Mechanisms of Aluminum Cold Spray Coatings on 300M Steel Substrates

A. Nastic[1] · M. Vijay[2] · A. Tieu[2] · S. Rahmati[3] · B. Jodoin[1]

Submitted: 2 March 2017 / in revised form: 5 July 2017 / Published online: 27 July 2017

Abstract The effect of substrate surface topography on the creation of metallurgical bonds and mechanical anchoring points has been studied for the cold spray deposition of pure aluminum on 300M steel substrate material. The coatings adhesion strength showed a significant decrease from 31.0 ± 5.7 MPa on polished substrates to 6.9 ± 2.0 MPa for substrates with roughness of 2.2 ± 0.5 µm. Strengths in the vicinity of 45 MPa were reached for coatings deposited onto forced pulsed waterjet treated surfaces with roughnesses larger than 33.8 µm. Finite element analysis has confirmed the sole presence of mechanical anchoring in coating adhesion strength for all surface treatment except polished surfaces. Grit embedment has been shown to be non-detrimental to coating adhesion for the current deposited material combination. The particle deformation process during impacts has been studied through finite element analysis using the Preston–Tonks–Wallace (PTW) constitutive model. The obtained equivalent plastic strain (PEEQ), temperature, contact pressure and velocity vector were correlated to the particle ability to form metallurgical bonds. Favorable conditions for metallurgical bonding were found to be highest for particles deposited on polished substrates, as confirmed by fracture surface analysis.

✉ A. Nastic
[redacted]

[1] uOttawa Cold Spray Laboratory, University of Ottawa, Ottawa, ON, Canada

[2] VLN Advance Technologies Inc, Ottawa, ON, Canada

[3] Isfahan University of Technology, Isfahan, Iran

Keywords adhesion strength · cold spray · finite element analysis · mechanical interlocking · metallurgical bonding · intermetallics

Introduction

Cold gas dynamic spray or cold spray (CS) coatings are used in a wide range of applications in which the coating adhesion strength is of utmost importance (Ref 1-3). In this process, the sprayed particles remain in solid state throughout their flight as their temperature is kept below melting point. Particle/substrate and particle/particle adhesion require the particles reaching an impact velocity greater than a material dependant critical velocity (Ref 4-6). For the typically sprayed materials, this critical velocity ranges from 300 to 1200 ms^{-1} (Ref 7, 8). The strong pressure field experienced by a particle at impact generates high strain rate and induces localized shear straining. The resulting adiabatic shear instability condition is characterized by a sudden local temperature increase due to plastic strain energy dissipation and as a result, the induced particle thermal softening process starts dominating over the strain hardening process. Consequently, the stress starts to drop rapidly with strain resulting in viscous-like material flow (Ref 8, 9). Any additional strain generates excessive material deformation, known as jetting, characterized by an accumulation of narrow strain bands. This extensive localized deformation causes particle surface oxide layer removal, which promotes intimate conformal contact and bonding (Ref 10-12). Computational and experimental studies have shown that since the impact process characteristic time is in the order of nanoseconds, interfacial inter-atomic diffusion has a lower and limited impact on particle/substrate bonding mechanism compared to high

pressure contact, plastic flow localization and adiabatic shear instability (Ref 12).

Through modeling, many have shown that the zone of maximum equivalent plastic strain (PEEQ), a potential precursor to metallurgical bonding, is restrained to a limited portion of the interacting surfaces (Ref 13-15). Moreover, the occurrence of localized interfacial melting can affect the nature of bonding by promoting metallurgical connectivity (Ref 16). Evidence of materials reaching locally their melting point during CS has been established through observation of microstructural features such as intermetallic formation, spherical submicron particle expulsion, particle remnants on substrate surfaces and amorphous material layer formation (Ref 17-25). However, only a limited amount of experimental observations have demonstrated the presence of metallurgical bonds at individual particle/substrate interfaces (Ref 26-29).

Many modeling studies have used the Johnson–Cook plasticity model to describe the particle deformation under impact during CS (Ref 9, 15, 30-33). While some have obtained good correlations with experimental observations, others have found limitations in the model to provide accurate high strain rate ($>10^7$ s^{-1}) particle deformation. Particularly, extreme and non-representative jetting processes were obtained at the particles periphery. Such erroneous depiction is related to incorrect material behavior description at high strain rates. An increase in yield stress with strain rate is normally observed under general strain rate deformation; however, the increase is sharply amplified for deformation rates exceeding 10^4 s^{-1}. This change is attributed to the transformation of the mechanisms governing the dislocation motion from thermally activated to phonon drag principles. Consequently, new models have been used in the CS field, which account for both mechanisms. The Preston–Tonks–Wallace (PTW) constitutive model has shown to be the most accurate (Ref 9, 14).

The influence of substrate surface preparation and roughness level prior to CS on particle/substrate bonding mechanisms has been scarcely studied (Ref 34-37). A proper identification of the contribution of metallurgical and mechanical bonding mechanisms on the overall coating adhesion strength is also lacking. It has been proposed that substrate grit blasting induces substrate surface work hardening, which potentially limits its deformation and consequent oxide removal (Ref 30). Residual grit contamination was also used to explain reduced adhesion due to the presence of micro-pores and the reduction in metal-to-metal contact regions (Ref 11). Surface roughness (topography) was also shown to improve to some extent the adhesion strength by providing the coating mechanical interlocking sites with the substrate and a larger contact area (Ref 12, 36).

The main goal of the current work is to assess the effect of substrate surface roughness on adhesion strength and provide insight on a potential transition between bonding mechanisms that might occur based on the state of the substrate surface morphology, for the case of a soft powder sprayed on a harder substrate. A soft pure aluminum powder is sprayed on a hard 300M steel substrate to characterize the individual contributions of both metallurgical and mechanical adhesion mechanisms. The effect of grit embedment on the coating adhesion strength is also evaluated. Heat treatments of the coating/substrate couple are used to enhance the formation of an intermetallic layer and assert the initial presence of metallurgical bonding in the as-sprayed conditions (Ref 38). Finite element analysis (FEA) is used to characterize the particle impact behavior on different surface profiles using the PTW model (Ref 9, 14). Finally, an FEA model simulating adhesion test is developed and used to correlate experimental and theoretical data relevant to the bonding mechanisms.

Experimental Procedures

Substrate and Feedstock Materials

Round 25.4 mm diameter 300M-VAR (vacuum arc remelting) aerospace alloy steel cylinders have been used as substrate material. Surface preparation treatments and coating depositions were made on the flat ends of the cylindrical samples. The tempered martensite microstructure had a measured Knoop hardness (Buehler Micromet 6030, IL, USA) of 310 $HK_{0.1}$ in the as received state. The chemical composition obtained through EDS analysis (wt.%) was C-0.42%, Si-1.68%, Mn-0.78%, S-0.001%, P-0.006%, Cr-0.81%, V-0.07%, Ni-1.90%, Mo-0.40%, Cu-0.08%, Ti-0.002%, Al-0.04%, Sn-0.006% and Fe-Bal.

The aluminum powder (99.8% Al, CenterLine (Windsor) Limited, Windsor, ON, Canada) is composed of distorted teardrop and oval shaped particles as shown in the scanning electron microscope (SEM) images (Oxford Instrument, EVO-MA10, Zeiss, UK) of Fig. 1. The powder particle size distribution was measured using laser diffraction (Microtrac model S3500, Montgomeryville, PA, USA) and the resulting 10th, 50th and 90th size percentile correspond to 11.3, 23.8 and 47.4 μm, respectively. The powder chemical composition, obtained through energy dispersive x-ray spectroscopy (EDS) (Oxford Instrument, EVO-MA10, Zeiss, UK), was 98.12 wt.% Al and 1.88 wt.% O.

Substrate Surface Preparation

Three different substrate surface preparation methods have been used to produce distinct surface topographies and

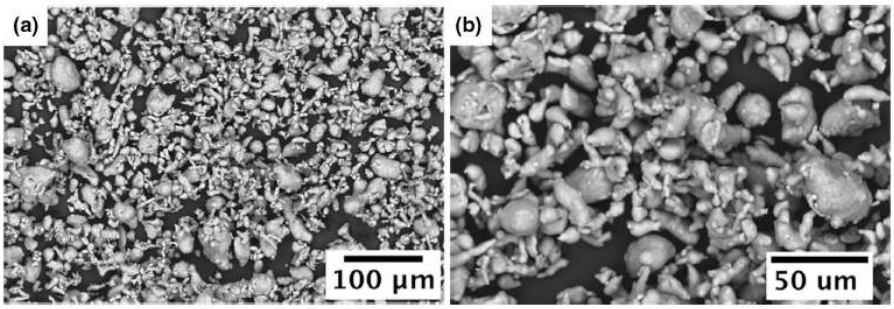

Fig. 1 Scanning electron microscope (SEM) images of as received pure aluminum feedstock powder. (a) Low magnification and (b) high magnification

arithmetic average surface roughnesses (Ra). A polishing procedure was employed to create a mirror surface finish by gradually grinding and polishing down to a final surface finish step using 3 µm abrasive suspensions. A gravity-fed grit blasting process using a 20 mesh (850 µm) ferrosilicate abrasive was also utilized at different propelling pressures at a 45° angle to roughen the substrate surfaces. Two steel nozzles with different exit diameters have been used to propel the grit medium as presented in Table 1. Moreover, to generate different roughnesses and surface topography characteristics between the grit-blasted specimens, the surface exposure time has also been varied and is expressed in terms of surface coverage, as seen in Table 1. A 100% coverage defines a single surface scan. Finally, samples were also prepared using the forced pulsed water-jet (FPWJ) process (Ref 39-41). A total of nine different surface roughnesses were produced using FPWJ in which three approximately matched surface roughnesses obtained using the grit blasting procedures. Table 2 presents FPWJ process parameters used in this study. A digital optical microscope (VHX-2000 Keyence Corporation, Osaka, Japan) was utilized to generate a 3D profile of the surface topography obtained for both the grit blasting and FPWJ methods. The resulting roughness was then calculated by analyzing the depth profile compositions through Matlab. The grit embedment percentage was measured by contrast using backscattered electron detector (BSD) images. Due to the very low substrate surface roughness of the polished samples, their arithmetic average roughnesses were measured using a portable profilometer equipped with a diamond stylus (PHASE II, SRG-4000, NJ, USA).

Table 1 Grit blasting process parameters

Operating parameters		Values
Nozzle diameter 1 (ND1)		4.8 mm
Nozzle diameter 2 (ND2)		9.3 mm
Standoff distance		25.4 mm
Blasting angle		45°
Carrier gas		Nitrogen
Sample	Grit blasting pressure, MPa	Coverage, %
GB-1 using ND2	1.4	100
GB-2 using ND2	2	400
GB-3 using ND1	2	100

Cold Spray Deposition

A commercially available (SST-EP, CenterLine (Windsor) Limited (Windsor, ON, Canada)) CS system has been used to produce pure aluminum coatings. To prevent nozzle

Table 2 FPWJ process parameters

Operating parameters	Values
Nozzle diameter	1.4 mm
Standoff distance	28.6 mm
Water pressure	69 MPa
Step index	0.1 mm/pass
Amplitude	85%
Pulse frequency	40,000 Hz
Sample	FPWJ nozzle velocity, mm/s
FPWJ-1	325
FPWJ-2	250
FPWJ-3	200
FPWJ-4	175
FPWJ-5	150
FPWJ-6	100
FPWJ-7	75
FPWJ-8	50
FPWJ-9	25

clogging, a polymer nozzle with a 2.0 mm throat diameter, 6.4 mm exit diameter and a diverging length of 126 mm has been used. Prior to the deposition process, all samples have been cleaned and degreased in an ethanol ultrasonic bath. The spray parameters are presented in Table 3. Prior to the deposition process, all substrate surfaces were pre-heated by running the CS gun over their surface without feedstock powder and using a gas temperature of 500 °C, in order to help induce softening of the substrate surface and consequently promote the oxide layer removal process through deformation during impact (Ref 42-45). For consistency purposes, each individually sprayed sample was thermally insulated from the surrounding using a high-temperature polybenzimidazole holder. For microstructural analysis, the aluminum coatings have been etched using Keller's reagent. The coatings porosity was evaluated through image analysis. Multiple coating cross sections were analyzed using ImageJ through a contrast process generated from the chosen representative threshold value.

Adhesion Strength Evaluation

The adhesion test specimens were machined and tested according to the ASTM-C633 standard (Ref 46) for coating adhesion/cohesion strength evaluation. A thermally curing elastomeric adhesive bonding agent, FM-1000 (Cytec Engineering Materials, MD, USA), with a bonding strength of 80 MPa was used to hold the coated sample to the counter specimen. All coatings were machined down to 800 µm total thickness prior to testing. Three samples per surface preparation were tested.

Post Heat Treatment Procedure

Experimental observation and characterization of metallurgical bonding at particle/substrate interface is hard to assess and presents a wide range of challenges (Ref 47-49). Multiple authors have used scanning and transmission electron microscopy to report metallurgical bonding. However, only very local conclusions were conveyed at single particle boundaries, providing limited insight of the overall coating bonding. The current approach is based on the growth of intermetallics by inter-diffusion. Since rapid inter-diffusion occurs at bonded regions and at oxide-free metal surfaces, the amount of intermetallic phases present at the heat-treated interface can be used to qualitatively determine the extent of original metallurgical bonding and thus the impact of surface roughness on the creation of metallurgical bonds (Ref 38). To assess the formation of aluminum-iron intermetallics at the coating/substrate interface, a dedicated set of sprayed samples has been produced and heat-treated after the deposition. The heat treatments were produced for coatings sprayed on four different surface roughnesses generated using polishing, grit blasting and FPWJ. Separate heat treatments were performed at 600 °C for 10 min, 35 min and 1 h in an air furnace for each sample roughness. The samples were cooled in air at room temperature.

Table 3 Cold spray deposition parameters

Parameters	Values
Gas temperature during preheat	500 °C
Gas temperature during deposition	300 °C
Gas pressure	3.4 MPa
Gas nature	Nitrogen
Traverse speed	20 mm/s
Feed rate	21 g/min
Standoff distance	15 mm
Step size	1 mm/pass
Number of passes	1

Numerical Model

ABAQUS/Explicit, a commercial Finite Element Analysis (FEA) software, was used to simulate individual particle impact on different substrate surface features. An FEA analysis was also conducted to estimate the purely mechanical portion of the adhesion strength of coatings deposited on all FPWJ-treated samples. The substrate 2D profile (cross section) for each set of roughness was recorded using images from the optical microscope and transferred to ABAQUS through x–y coordinates conversion using ImageJ software.

Particle Impact Simulation

To reduce computational time, a 2D Lagrangian formulation model was used to simulate the particles deformation behavior during impact. Each substrate was partitioned into sections characterized by fine meshing in the region of impact and coarse meshing elsewhere. The meshing for both particles and substrates consisted of quadratic 4-node-coupled temperature-displacement elements (CPE4RT). The mesh size for the particles was set to 1/50 the powder average size (Ref 50). A fixed boundary and x-symmetric conditions were applied at the bottom and on the sides of the substrates, respectively. The tangential interaction behavior was described by a general contact condition with a friction coefficient of 0.5 (Ref 14, 51). A hard contact pressure-overclosure was set for the normal behavior characteristic. The aluminum powder was assumed to be a perfect sphere of 30 µm diameter. The initial particle and substrate temperatures were set to 348 and 398 K, respectively, based on values found in the literature (Ref

Table 4 General materials properties (Ref 74)

Properties	Pure aluminum	Steel 4340
Density (ρ_0), kg/m^3	2700	7800
Specific heat (C_p), J/kg K	910	475
Thermal conductivity (κ), W/mk	237	445
Melting temperature (T_m), K	934	1793

Table 5 Elastic response properties (Ref 75)

Properties	Pure aluminum	Steel 4340
Shear modulus (G), GPa	26	74
Grüneisen's constant (Γ_0)	2.14	1.69
Speed of sound (c_0), m/s	5292	3935
Hugoniot slope (s)	1.4	1.58

14, 47, 52, 53). The pure aluminum particle traveling velocity was set to 500 m/s (Ref 14, 54). The density, specific heat and thermal conductivity of both materials as used in the model are listed in Table 4. Due to the lack of information in the literature on the 300M steel material temperature and strain rate-dependent Johnson–Cook properties, mechanical properties of stainless steel 4340 have been used instead due to the similar carbon content and subsequent properties.

Material Elastic Response Properties The hydrodynamic and deviatoric stresses, both subsets of a given stress sensor, have been defined in the simulation as follow:

The hydrodynamic stress, related to volume changes, was modeled using the Mie-Grüneisen equation of state (EOS) through the linear $U_s - U_p$ Hugoniot form given by:

$$p = \frac{\rho_0 c_0^2 \eta}{(1 - s\eta)^2}\left(1 - \frac{\Gamma_0 \eta}{2}\right) + \Gamma_0 \rho_0 E_m \quad \text{(Eq 1)}$$

$$\eta = 1 - \frac{\rho_0}{\rho} \quad \text{(Eq 2)}$$

where p is the hydrodynamic stress, ρ_0 is the initial density, c_0 is the material speed of sound, Γ_0 is the Grüneisen's constant, E_m is the internal energy per unit mass, ρ is the density, and s is the Hugoniot slope coefficient.

The deviatoric stress, related to shape changes and defined as the stress left after subtracting the hydrodynamic stress, has been approximated by the following linear elastic model:

$$d = 2G_e\varepsilon_s \quad \text{(Eq 3)}$$

where d is the resulting deviatoric stress, G_e is the elastic shear modulus, and ε_s is the elastic deviatoric strain. The elastic properties defined in the simulation for both studied materials are summarized in Table 5.

Material Plastic Response Properties The high strain rate (up to 10^{11} s^{-1}) model developed by Preston–Tonks–Wallace has been used to describe the particle plastic deformation during impact (Ref 9). The flow stress σ, which is based on the dislocation motion during plastic deformation, is written as follow:

$$\sigma = 2\left[\hat{\tau}_s + \alpha ln\left[1 - \varphi exp\left(-\delta - \frac{\theta \varepsilon_p}{\alpha\varphi}\right)\right]\right]G_p \quad \text{(Eq 4)}$$

$$\alpha = \frac{s_0 - \hat{\tau}_y}{p} \quad \text{(Eq 5)}$$

$$\delta = \frac{\hat{\tau}_s - \hat{\tau}_y}{\alpha} \quad \text{(Eq 6)}$$

$$\varphi = \exp(\delta) - 1 \quad \text{(Eq 7)}$$

where $\hat{\tau}_s$ is the normalized work-hardening saturation stress, θ is the strain hardening rate, ε_p is the equivalent plastic strain, s_0 is the saturation stress at 0 K, $\hat{\tau}_y$ is the normalized yield stress, and p is the strain hardening constant. The plastic shear modulus G_p is a function of temperature and material density and is defined by the mechanical threshold stress (MTS) model as follow (Ref 9, 14, 55):

$$G_p(T) = G_0 - \frac{D}{\exp\left(\frac{T_0}{T}\right) - 1} \quad \text{(Eq 8)}$$

where G_0 is the shear modulus at 0 K, D is a material constant, T_0 is a temperature material constant, and T is the node temperature.

The plastic deformation process at low strain rates is governed by thermal activation, while at high strain rates it is controlled by dislocation drag mechanisms, also known as Wallace's theory of overdriven shocks (Ref 56). The maximum (high strain rates) and minimum (low strain rates) of the work-hardening saturation stress ($\hat{\tau}_s$) and yield stress ($\hat{\tau}_y$) are defined as follow:

$$\hat{\tau}_s = \max\left\{s_0 - (s_0 - s_\infty)\mathrm{erf}\left[\kappa\hat{T}\ln\left(\frac{\gamma\dot{\xi}}{\dot{\varepsilon}_p}\right)\right], s_0\left(\frac{\dot{\varepsilon}_p}{\gamma\dot{\xi}}\right)^{\beta}\right\} \quad \text{(Eq 9)}$$

$$\hat{\tau}_y = \max\left\{\begin{array}{l} y_0 - (y_0 - y_\infty)\mathrm{erf}\left[\kappa\hat{T}\ln\left(\frac{\gamma\dot{\xi}}{\dot{\varepsilon}_p}\right)\right], \\ \min\left\{y_1\left(\left(\frac{\dot{\varepsilon}_p}{\gamma\dot{\xi}}\right)^{y_2}\right), s_0\left(\frac{\dot{\varepsilon}_p}{\gamma\dot{\xi}}\right)^{\beta}\right\} \end{array}\right\} \quad \text{(Eq 10)}$$

where $\hat{T} = T/T_m$, T_m is the melting temperature, s_∞ is the saturation stress close to the melting temperature, κ is the temperature dependence constant, γ is the strain rate

dependence constant, $\dot{\varepsilon}_p$ is the plastic strain rate, β is the high strain rate exponent, y_0 is the yield stress at 0 K, y_∞ is the yield stress constant near melting temperature, y_1 is the medium strain rate constant,y_2 is the medium strain rate exponent, and $\dot{\xi}$ is defined as:

$$\dot{\xi} = \frac{1}{2}\left(\frac{4\pi\rho}{3M}\right)^{1/3}\left(\frac{G_p(T)}{\rho}\right)^{1/2} \quad \text{(Eq 11)}$$

with M being the atomic mass. Neither the PTW nor the MTS relations are included in ABAQUS and were consequently integrated through a user subroutine (VUHARD).

Due to the substrate limited deformation, the Johnson–Cook (JC) model was used to describe its behavior under impact. This model is very simple and able to predict accurately material deformation at low strain rates (Ref 9), which is why it is used in this study to describe the plastic behavior of the substrate material only. The model considers the separate effect of plastic strain, strain rate and temperature on the material flow stress and its equation is given by:

$$\sigma = \underbrace{\left[A + B\varepsilon_p^n\right]}_{\text{Strain hardening}} \underbrace{\left[1 + C\ln\left(\frac{\dot{\varepsilon}_p}{\dot{\varepsilon}_{ref}}\right)\right]}_{\text{Strain rate (viscosity) effect}} \underbrace{\left[1 - \left(\frac{T - T_{ref}}{T_m - T_{ref}}\right)^m\right]}_{\text{Thermal softening effect}} \quad \text{(Eq 12)}$$

where A, B, n, C and m are material constants determined from flow stress data, ε_p is the equivalent plastic strain, $\dot{\varepsilon}_p$ is the plastic strain rate, $\dot{\varepsilon}_{ref}$ is the strain rate at which the material constants are obtained, T_m is the melting temperature, T_{ref} is the transition temperature, and T is the absolute temperature. Table 6 summarizes the mechanical and thermal properties of both materials used in the particle impact simulation.

Table 6 PTW (Ref 56, 76) and JC material properties (Ref 13, 77, 78)

Properties	Values
PTW parameter-pure aluminum	
Strain rate dependence constant (γ)	0.0001
Strain hardening rate (θ)	0.0529
Strain hardening constant (p)	3
Yield stress constant at 0 K (y_0)	0.00942
Yield stress constant at melting (y_∞)	0.00566
Medium strain rate constant (y_1)	0.00354
Medium strain rate constant (y_2)	0.50
High strain rate exponent (β)	0.23
Saturation stress at 0 K (s_0)	0.032
Saturation stress at melting (s_∞)	0.00791
Temperature dependence constant (κ)	0.494
Atomic mass (M), kg/atom	4.48×10^{-26}
Shear modulus at 0 K (G_0), GPa	28.8
Material constant (D), GPa	3.44
Temperature material constant (T_0), K	215

Properties	Steel 4340	Pure aluminum
JC parameters		
A, MPa	792	148.4
B, MPa	510	345.5
C	0.014	0.001
n	0.26	0.183
m	1.03	0.895
Reference strain rate, $\dot{\varepsilon}_{ref}$	1	1

Adhesion Strength Simulation

To assess the distinct contribution of metallurgical and mechanical bonding on the overall coating adhesion strength for the various substrate roughnesses, a 2D FEA Langragian model has been used (Ref 57). The substrate/coating size (thickness) was set to approximately 10 times the peak to valley distance of the equivalent roughness for all tested substrates in order to avoid the influence of stress concentration for the determination of the overall average stress. A quadratic element shape with a 4-node plane strain (CPE4R) meshing was used. The boundary conditions were set to fixed at the bottom of the substrate, x-symmetric on the side walls and a uniform velocity of 0.02 mm/s (as per the ASTM-C633 standard) at the top of the coating. Figure 2 illustrates the simulation concept and provides details of the included features.

A general uniform friction coefficient of 0.5 was applied at all contacting surfaces (Ref 51). Both the coating and substrate were set at room temperature. The Johnson–Cook model was used to describe the material flow process of both materials during the adhesion test (properties are presented in Table 6). The substrate roughness profiles integrated into the simulations have been transferred in the same way as for the particle impact simulation. To properly capture the anchoring regions, cross-sectional images taken at a magnification of 400X have been used for substrates with average roughness higher than 40 µm, 500X for roughness between 10 and 40 µm and at 1000X for surfaces with roughness lower than 10 µm. These magnifications were taken based on visual inspection to increase surface coverage while keeping good interface representation. The final coating adhesion strength was obtained by averaging the vertical stress (S22) in the elements located at the bottom of the substrate for each simulation. In total five surface profiles per substrate roughness have been

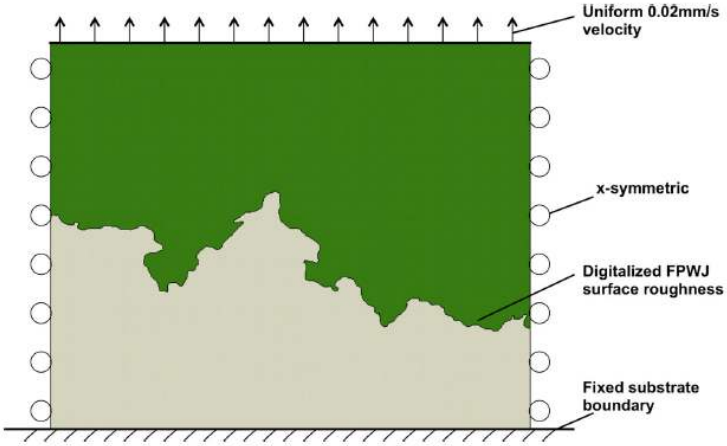

Fig. 2 Adhesion strength simulation illustration for a FPWJ surface profile

analyzed and the obtained average stress was selected as the resulting simulated coating adhesion strength.

Results and Discussion

Substrates Surface and Coatings Characterization

The resulting substrates surface topography obtained using all three surface preparation methods are shown in Fig. 3, with their corresponding average surface roughness (Ra). A surface roughness of 0.2 ± 0.1 µm is obtained after polishing. Low substrate roughnesses were obtained using both the abrasive blasting and FPWJ processes and varied from 2.0 ± 0.3 to 6.1 ± 0.8 µm and 2.2 ± 0.5 to 5.2 ± 0.9 µm, respectively. The grit blasting process modifies the surface primarily through erosion by surface shearing during grit impact, which leaves grit like marks at the surface. The FPWJ process, however, alters the surface by plastic deformation without significant material loss at high gun speeds and by localized erosion at low gun speeds. The high surface roughnesses were obtained using only FPWJ (as grit blasting was found to be limited to surface roughnesses around 7 µm), which varied from 15.8 ± 1.6 µm up to 84.9 ± 6.4 µm. In the FPWJ process, the surface damage by microfracture through erosion gradually increases with processing time (low gun speed). As the surface gets rougher, more fluid penetrates through the created cavities, which forms micro-jets and increased localized material fracture. At high roughness, the generated surface features are unique to the FPWJ process.

Figure 4 shows cross sections of pure aluminum CS coatings interface for all prepared surfaces. The deposited coatings were 1.4 ± 0.2 mm thick, measured from the highest profile peak of each analyzed substrate surface. The resulting high coating density is attributed to extensive particle deformation. Coatings average porosity was evaluated at $0.3 \pm 0.2\%$.

Figure 5(a) presents a high magnification cross section of the coating sprayed on the FPWJ-5 substrate. The pure aluminum coating has been etched to reveal particle-to-particle boundaries and resulting particle stacking process otherwise not visible. Etching reveals highly deformed particles with irregular and disorganized piling process. Splats with varying level of flatness ratio are seen. High plastic flow enabled particles to adjust during their deformation according to the substrate surface topography, consequently filling all crevices at the substrate surface. Figure 5(b) shows a fully dense coating deposited within an intricate channel with thin passages created at the substrate surface by the FPWJ process. This demonstrates that despite the high substrate roughness and presence of complex gaps, the pure aluminum particles deform sufficiently to fill all features regardless of their complexity. Evidence of material continuation between adjacent particles and substrate, indicative of metallurgical bonding, was impossible to discern from cross-sectional optical analysis.

Figure 5(a) also shows the presence of substrate deformation upon particle impacts through hooks collapse. Highlighted are two cases of hook deformation, which are distinguished by the severity of the distinct collapse. The folding process illustrated by 'Case 1' is a full collapse of the original hook down to the substrate surface. This type of substrate deformation does not increase the coating mechanical adhesion since the contact surface between the coating and substrate is reduced. Instead, the area below the hook becomes a void. 'Case 2' illustrating a partial hook collapse is expected to accentuate the adhesion due to

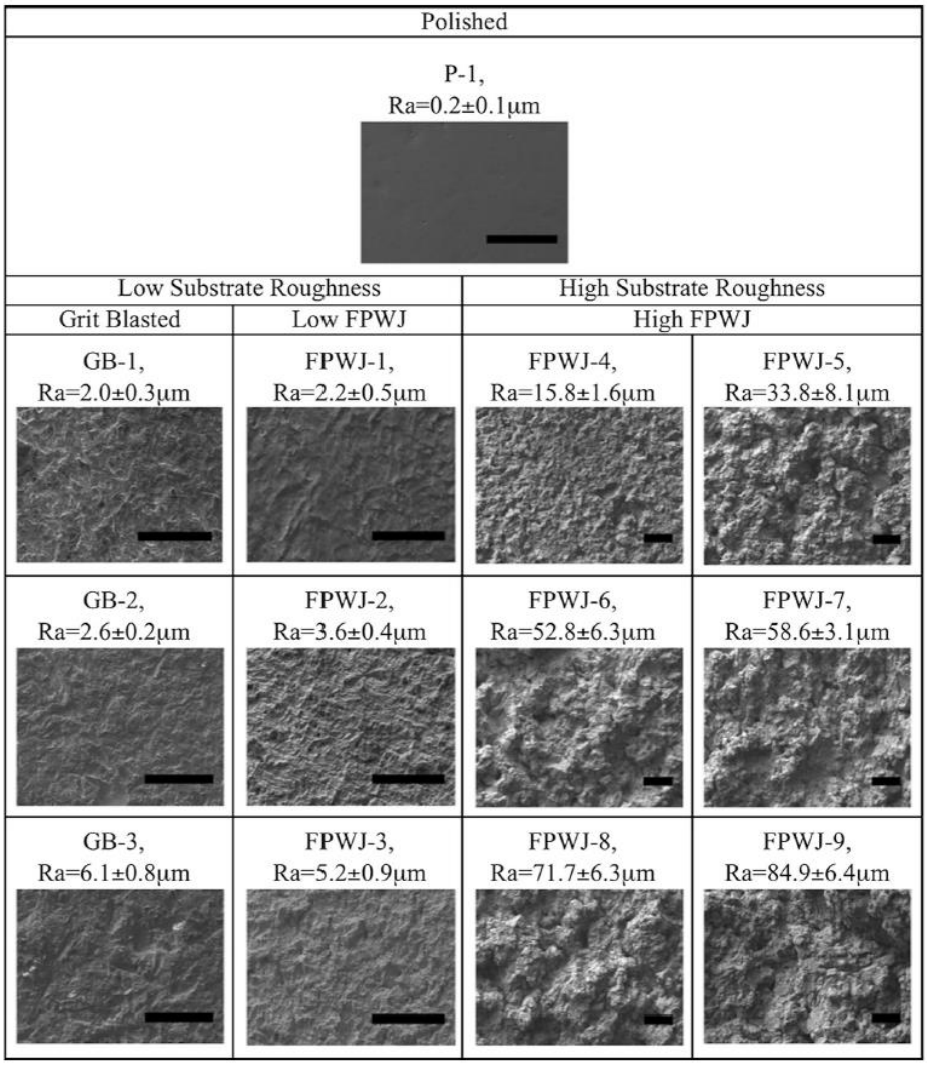

Fig. 3 SEM images of substrates top surface topography and resulting roughness (Scale = 200 μm)

the additional mechanical anchoring it provides to the underlying coating.

Adhesion Strength Tests and Fracture Surface Analysis

Adhesion Strength Tests

Results of the adhesion strength tests as a function of surface preparation method/substrate roughness are shown in Fig. 6. The coatings sprayed on polished substrates failed at 31.0 ± 5.7 MPa. The coating bond strength was reduced to 6.9 ± 2.0 and 8.6 ± 3.8 MPa for the FPWJ substrate with a roughness of 2.2 ± 0.5 μm and the grit-blasted surface of 2.1 ± 0.3 μm roughness, respectively. According to these results, for the same substrate arithmetic roughness, both the FPWJ and grit-blasted surfaces have similar adhesion strengths. Moreover, from the cross sections shown in Fig. 4, both surfaces have very similar profiles, which reveal that the adhesion level is directly related to the substrate surface topography irrespective of the surface treatment used. Similarly, for FPWJ samples of

J Therm Spray Tech (2017) 26:1461–1483

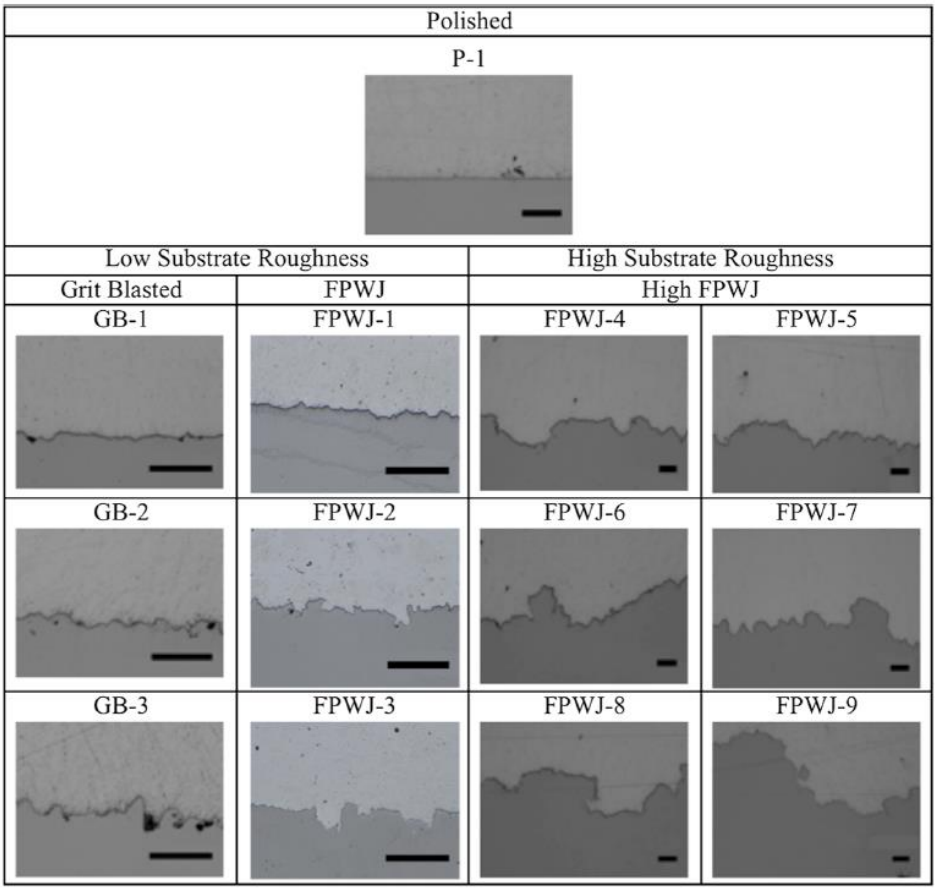

Fig. 4 Optical microscope cross-sectional images of the deposition interface for all produced surfaces (Scale = 100 μm)

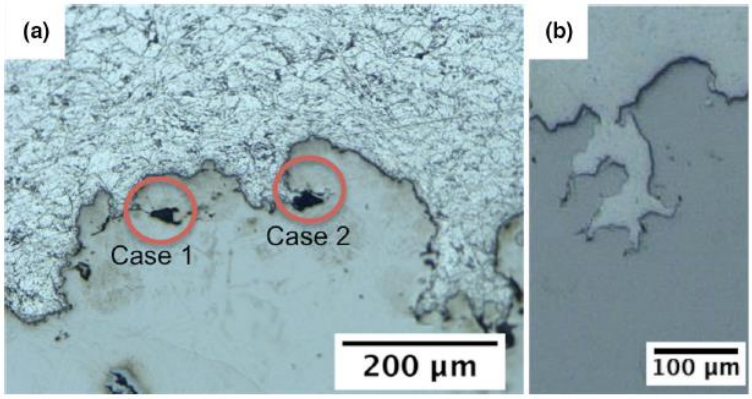

Fig. 5 (a) Etched coating illustrating particle deformation and stacking process. Substrate collapses (Case 1 and Case 2) are circled. (b) Optical image of a FPWJ channel filled by the sprayed particles illustrating particles high plastic flow

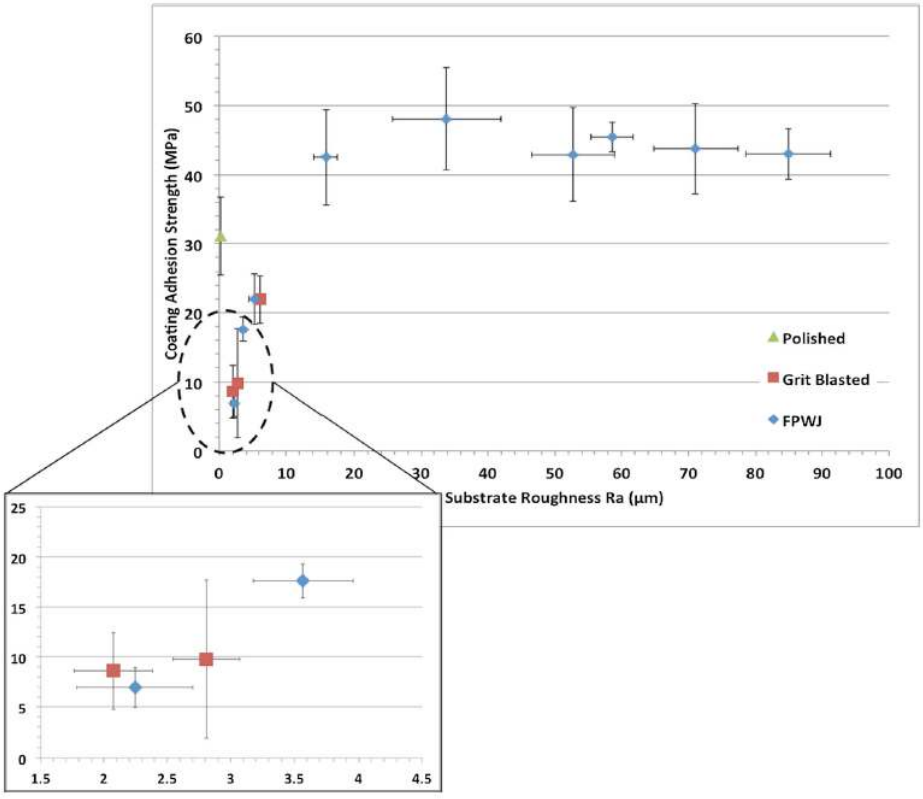

Fig. 6 Pure aluminum cold spray coatings adhesion strength (ASTM-C633) on various 300M steel substrate surface roughnesses

5.2 ± 0.8 μm roughness and grit-blasted surfaces of 6.2 ± 1.3 μm Ra, the resulting adhesions are almost identical with values of 22.0 ± 3.7 and 22.0 ± 3.4 MPa for FPWJ and grit-blasted surfaces, respectively.

For grit-blasted and FPWJ treated substrates surfaces with roughness less than 20 μm, the coating adhesion strength increases in a linear trend unrelatedly to the preparation method used. For larger surface roughness values, the highest coating adhesion strength of 48.0 ± 7.3 MPa is reached for FPWJ-5 samples. Subsequent increases in substrate surface roughness lead to a small but consistent decrease in adhesion strength. Values close to 42.5 ± 6.9 MPa are obtained for samples with substrate surface roughness larger than 33.8 ± 8.1 μm.

Fracture Surface

Coating and substrate surfaces have been examined after the adhesion strength tests. For each substrate preparation method, the particle and substrate deformation, the adhesion mechanism and the influence of surface roughness on coating adhesion strength are analyzed.

Polished Surface Figure 7(a) shows both the substrate and coating surfaces after the adhesion tests of polished substrates. As can be observed, the 300M steel substrate does not experience any major plastic deformation since the mirror-finish polish is retained after particle impact, coating deposition and once delamination occurred from the adhesion strength test. Figure 7(b) shows the delaminated coating surface that was in contact with the substrate surface. From the flatness of particles at zones of contact with the substrate, it is shown that the aluminum particles experience large plastic deformations during the high velocity impact process. The ductile behavior of the aluminum powder and lack of plastic flow of the steel substrate are attributed to the strength and hardness of each material. Given that the aluminum material is initially significantly softer than the steel substrates, the plastic deformation will predominantly be located at the particle.

J Therm Spray Tech (2017) 26:1461–1483 1471

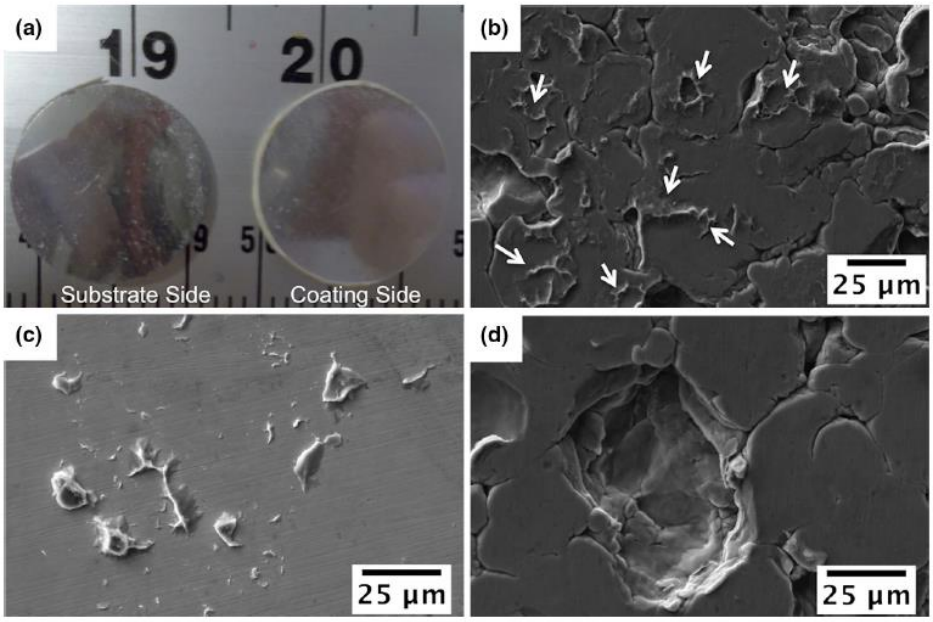

Fig. 7 General features of coatings deposited onto polished substrate surfaces. (a) Substrate and coating surfaces after the adhesion test showing flat mirror surface finishes, (b) coating surface side SEM image after adhesion test with cup-and-cone like features locations shown by arrows, (c) substrate surface side showing remains of aluminum particles and (d) single particle dislodged from the coating after adhesion test showing particle/particle bonding being inferior to the particle/substrate bonding

The apparent absence of substrate surface modification/cratering suggests that mechanical interlocking does not contribute to the coating/substrate adhesion strength. Figure 7(c) shows retained aluminum material on the substrate surface after adhesion testing, which suggests that the coating adhesion strength is obtained through partial metal bonding at the particle/substrate interface. The remaining aluminum material is in the form of small fragments or well-adhered full size particles as depicted in Fig. 7(d). In general, the failure at the coating/substrate interface was of adhesive nature with limited regions fracturing in a cohesive like manner, which indicates presence of local poor particle-to-particle connectivity. Figure 7(d) shows a single particle being entirely dislodged from the coating after the adhesion test, suggesting occurrence of low particle/particle bonding but high particle/substrate metallurgical bonding.

Figure 7(b) also highlights zones of protruding material and disjointed areas at the coating interface. The extruded material is attributed to particle deformation occurring during the adhesion test, which exhibits ductile behavior in a discontinuous fashion across the particle contact surface. The presence of localized and distributed cup-and-cone like fracture features also support the presence of metallurgically bonded zones. The previous results, which suggested the absence of mechanical interlocking between the coating and substrate, support the current observation and together they allow to hypothesize that the sole bonding mechanism on polished substrates is of metallurgical nature. Limited cup-and-cone like deformation at the particles surface suggests that the number of particles reaching the necessary pressure, temperature and/or energy for proper local oxide layer removal and creation of intimate contact is limited.

Grit-Blasted Surfaces Substrate fracture surfaces of grit-blasted samples are shown in Fig. 8. The topography and grit/aluminum particle embedment are shown separately through SE and BSD images. For all substrate surface roughnesses, the amount of attached aluminum particles is very low and quite similar. However, the size of the remaining particles increases with increasing substrate roughness due to the ability of larger hooks to trap larger particles. For all cases, coatings have failed in adhesion at the substrate/coating interface. From the surface topography presented in Fig. 3 and the fracture surface images, one can conclude that the substrate undergoes minimal deformation during the deposition process. The general texture appears to be the same as before deposition, and the morphology is still characterized by grit like shaped dents

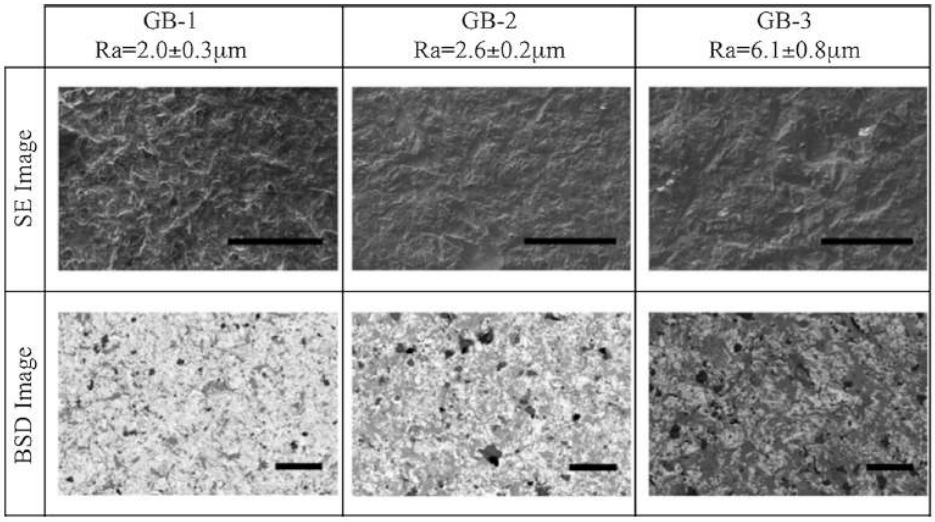

Fig. 8 Grit-blasted substrate sample surface topography and grit embedment after the adhesion tests. The steel substrate, ferrosilicate grit and aluminum particles appear in white, gray and black colors in the BSD contrast, respectively (Scale = 200 μm)

increasing in size with the surface roughness. The amount of embedded ferrosilicate grit at the substrate surface increases with increasing surface roughness. The percentage of surface grit contamination is evaluated at 4.5 ± 1.9, 34.9 ± 0.9 and 47.7 ± 5.7% for surfaces having an average roughness of 2.0 ± 0.31, 2.6 ± 0.17 and 6.1 ± 0.77 μm, respectively. Despite having similar surface roughnesses, the GB-2 set has more embedded grit than the GB-1 samples. This dissimilarity is caused mainly by the difference in coverage overlap during the surface preparation step. The GB-2 sample surfaces have been treated for longer periods of time, which has led to the same maximal reachable roughness but also to an increased grit contamination. The ferrosilicate contamination on the surface is in the form of thin grit residues and of infiltrated large fractured grit. The absence of cup-and-cone like features on the fracture surfaces, shown in Fig. 9(a), signifies poor ductility and consequently absence of metallurgical bonding at the particle/substrate interface. In contrast to the polished samples, these observations strongly suggest that for low Ra grit-blasted surfaces, the primary coating adhesion mechanism is mechanical rather than metallurgical. As previously established for the case of polished samples, reaching approximate adhesion strength of 30 MPa only requires a low amount of metallurgically bonded zones. With adhesion strength much lower than that value, it is anticipated that the grit-blasted specimens have no metallurgically bonded area. The grit presence on the aluminum coating surface side of the adhesion test sample has also been analyzed, but the detected amount was too low to be accounted for.

It is worth noticing that despite the great differences in grit embedment percentage between GB-1 and GB-2 samples, the coatings adhesion strength are practically identical. These results lead to believe that grit coverage level does not affect the coating adhesion strength. This supports the previous statement that for grit-blasted samples the adhesion is obtained through mechanical anchoring mainly. In a mechanically anchored coating, embedded grit and substrate surface have no topographical difference during coating deposition. Figure 9(b) shows possible presence of mechanical links between aluminum particles and embedded grit, which demonstrates the non-detrimental effect of grit. The rough nature of the ferrosilicate grit surface can also provide anchoring to the coating if the core of the grit is well embedded inside the substrate surface.

FPWJ Surfaces The coating and substrate fracture surfaces of the FPWJ-2 and FPWJ-5 samples, which have an adhesion of 17.6 ± 1.7 and 48.1 ± 7.3 MPa, respectively, are shown in Fig. 10. Only these samples are shown as they describe the general substrate and coating fracture surfaces observed for low to high substrate roughnesses. It is apparent from Fig. 10(a) and (c) that the substrate surface undergoes minimal deformation based on the similarities with the initial FPWJ surface topography. According to Fig. 10(b) and (d), the coating fracture surface follows an

J Therm Spray Tech (2017) 26:1461–1483 1473

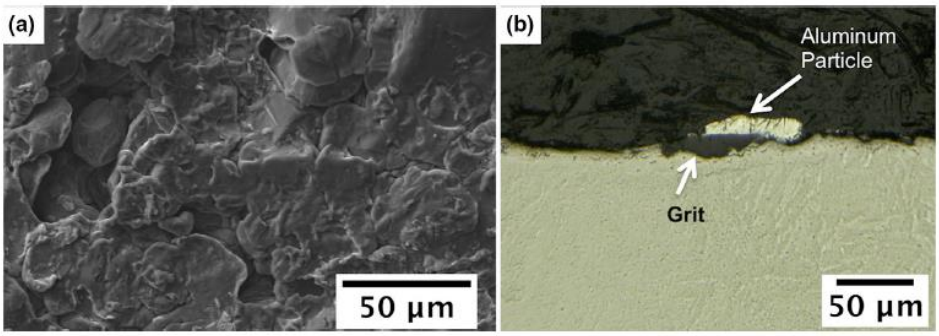

Fig. 9 Coating/substrate interface after adhesion test. (a) SEM image showing the absence of cup and cone features on the coating surface of grit-blasted substrates and (b) anchored aluminum particle above the surface of an embedded grit

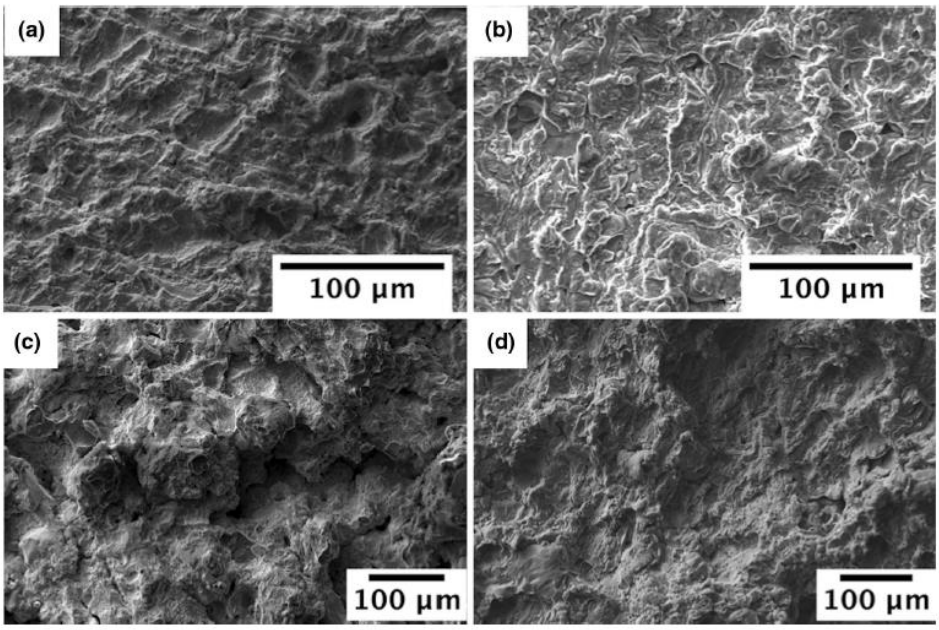

Fig. 10 SEM images after adhesion test of (a) substrate and (b) coating of FPWJ-2 sample and of (c) substrate and (d) coating of FPWJ-5 sample

intergranular path with no apparent particle ductile deformation. The lack of coating deformation during the adhesion tests suggests that the failure occurs when the substrate hooks align with the pull direction releasing the coating from the substrate grips. Thus, the delamination process is controlled by the geometry and strength of the substrate hooks, which explains the increase in adhesion with surface roughness increase. It is noteworthy to mention that all coatings have failed in adhesion at the interface.

The amount of attached aluminum on the substrate side after failure is hard to properly quantify due to the intricacy of the FPWJ surfaces. However, it is noticeable that the particle deformation process is highly influenced by the substrate roughness. As seen in Fig. 10(b) and (d), the aluminum coatings have a surface topography similar to the substrate. Particles during deposition follow closely the substrate profile, giving rise to very dense coatings, such that the resulting plastic flow is influenced by the substrate surface features size rather than general roughness alone.

It is also observed that the FPWJ-3 and GB-3 samples (with similar Ra) failed in adhesion at the same stress level. This supports the previous statement given for grit-blasted samples that as opposed to what has been hypothesized by others (Ref 11, 30, 34, 41, 58) the grit contamination at that roughness level does not affect the coating adhesion. The explanation of such assertion being once more the lack of metallurgical bonding at the coating/substrate interface.

Diffusion Tests

In order to elucidate further and support the hypothesis stated previously on the nature of the bonds at the interface of the different surface roughness samples, coatings have been produced and annealed for different treatment times to capture the intermetallic growth process. A mirror-finish roughness of 0.2 ± 0.2 µm was obtained with polishing, roughnesses of 2.6 ± 0.4 and 5.0 ± 0.9 µm were produced using grit blasting and a roughness of 43.9 ± 8.2 µm was reached using FPWJ. Figure 11 shows cross sections of polished, grit-blasted and FPWJ interfaces after the various heat treatments.

After 10 min, it was impossible to detect Fe-Al intermetallics at the substrate/coating interface of any sample based on SEM observations. In the case of samples heat-treated for 35 min, an intermetallic compound layer is observed at the substrate/coating interface of all treated specimens. Through EDS analysis, it was confirmed that the created intermetallics have high aluminum content with a resulting single $FeAl_3$ composition. The preferential growth direction of the intermetallic arises from the diffusion coefficient of iron in aluminum being larger than the coefficient of aluminum in iron (Ref 59). It is observed that the polished sample has the largest continuous and crack-free intermetallic interface coverage. In that sample, the $FeAl_3$ thickness is constant throughout and reaches and average value of 5.5 µm. The intermetallic layer shows some interruptions along its length, but at a lower level than for other interfaces. Lower degrees of intermetallic layers on roughened surfaces support the previous conclusion that the coating adhesion is mainly of mechanical nature for grit-blasted and FPWJ-treated surfaces. Figure 12 shows images of the interface at high magnification, revealing the intermetallic structures. It also displays the diffusion path, the intermetallic thickness, shape and continuity.

The intermetallic present on the substrates prepared with grit blasting and FWPJ is a few microns thick but its coverage is intermittent and thus limited to specific regions only. Moreover, the $FeAl_3$ exhibits an irregular shape that reflects the substrate surface profile. Similar results were obtained for the 1 h annealing treatment. The intermetallic layer geometry and composition has not changed between the three sets of tests. Its average thickness has increased to 7.5 µm for the polished interface. The thickness for the other substrate surface roughnesses is still very inconsistent and dependent on substrate topography. The significantly greater coverage of intermetallic layers on the polished samples can be interpreted as an indication of a higher metal-to-metal contact area in the as-sprayed condition (Ref 38). Larger diffusion scales are also associated with zones metallurgically bonded during the CS deposition. This suggests that during the impact process, the surface oxide removal, creation of clean surfaces and zones of high pressure and temperature are more prone to happen when particles are deposited onto polished surfaces. The discontinuity of the intermetallic formation on all substrate surfaces could be caused by the inhomogeneous nature of the native oxide layer disruption. Despite being broken during the impact, the oxide scale might not be properly removed from the substrate surface due to either being trapped by the impact of an incoming particle or from being caught between the substrate roughness boundaries (Ref 60, 61). Therefore, the diffusion during heat treatment of iron in aluminum occurs only at regions of pure metal-to-metal contact, where the particles have sufficiently deformed to induce proper oxide scale removal and suitable high localized pressure and temperature to form strong atomic links. Moreover, the grit-blasted substrate surface with an Ra of 2.6 ± 0.4 µm has more intermetallics at the interface than the grit-blasted sample with a roughness of 5.0 ± 0.9 µm. The grit contamination and larger presence of peaks, valleys and angular surfaces could explain such differences. Similarly, the intermetallic formation on the FPWJ surface is limited to specific regions only.

Finite Element Analysis

As direct and detailed visualization of particle impact is currently limited due to the low process time scales and to further support the proposed shift in adhesion mechanisms (from metallurgical to mechanical) from the results obtained, FEA was performed.

Particle Impact Simulation

The presence of a high equivalent plastic strain (PEEQ) at the particle impact surface is indicative of an adequate oxide layer removal process and a proper bonding (Ref 14, 18, 62, 63). An elevated PEEQ is also associated with a high rise in local temperature at the contact zone (Ref 13, 64-66). The friction and plastic work experienced by the particle is largely transformed to heat, which induces material softening and consequently large localized deformations. Local melting has also been shown to benefit the creation of metallurgical bonding (Ref 13, 16, 23, 67).

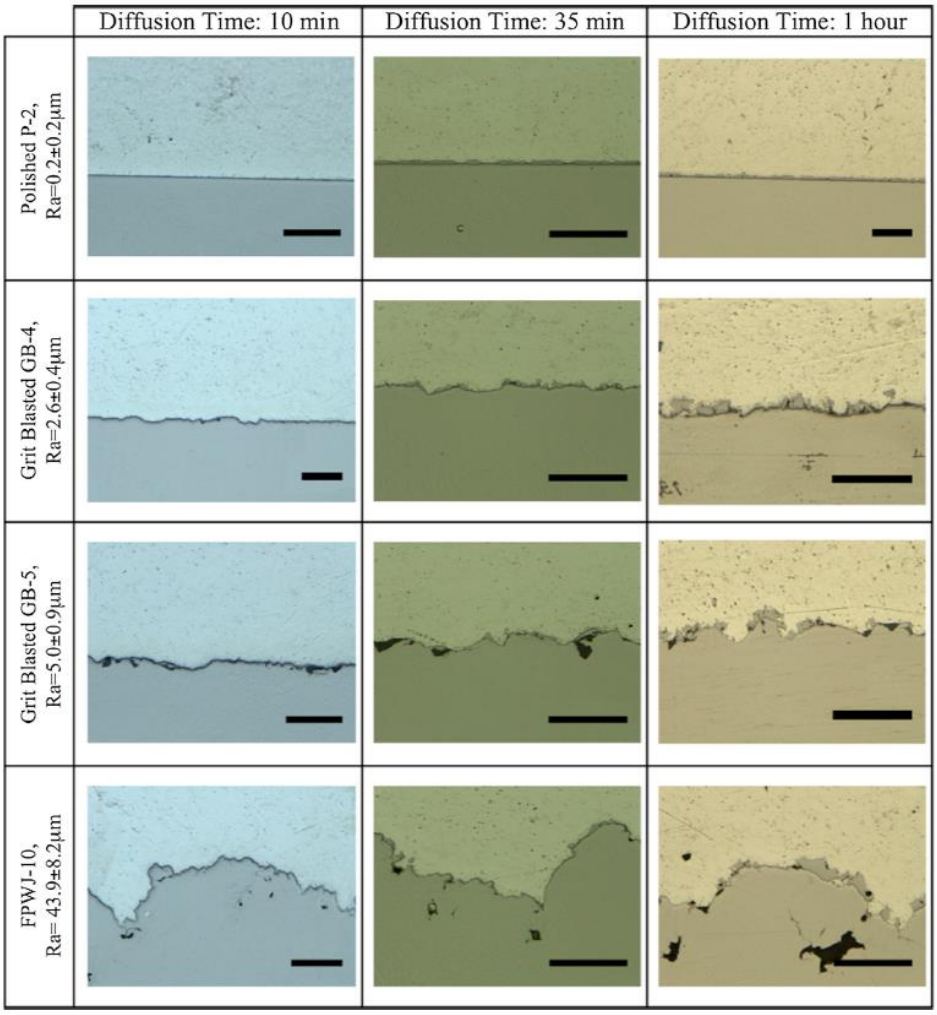

Fig. 11 Local evidence of intermetallic growth for different diffusion times on various substrate surfaces. Intermetallic layer is seen at the interface for heat treatments of 35 min and 1 h (Scale = 100 μm)

Moreover, a high pressure applied at the zone of impact under the dynamic loading enhances particle/substrate contact and promotes the formation of metallurgical bonds (Ref 12, 14, 68).

In this study, the influence of substrate surface topology/roughness on the particle deformation process during impact is analyzed. Figure 13 illustrates a surface cross-sectional portion of GB-1 sample considered for the numerical investigation. The particle impact is modeled to occur onto four different regions of the surface, shown in red in Fig. 13. To simplify the analysis, the particle geometry has been set as spherical such that only the influence of surface roughness on the particle deformation is considered. The resulting temperature, PEEQ, pressure and velocity gradient values at the particle zone of contact with the substrate have been obtained from the simulations and correlated with the particle ability to create metallurgical bonds.

Figure 14 shows simulations results at the time step for which maximal temperature is reached at the particle for all four cases. A large rise in temperature is observed at the elements in contact with the substrate surface, as a result of large deformation. With the exception of the impact with a valley, the region with largest temperature is found at the

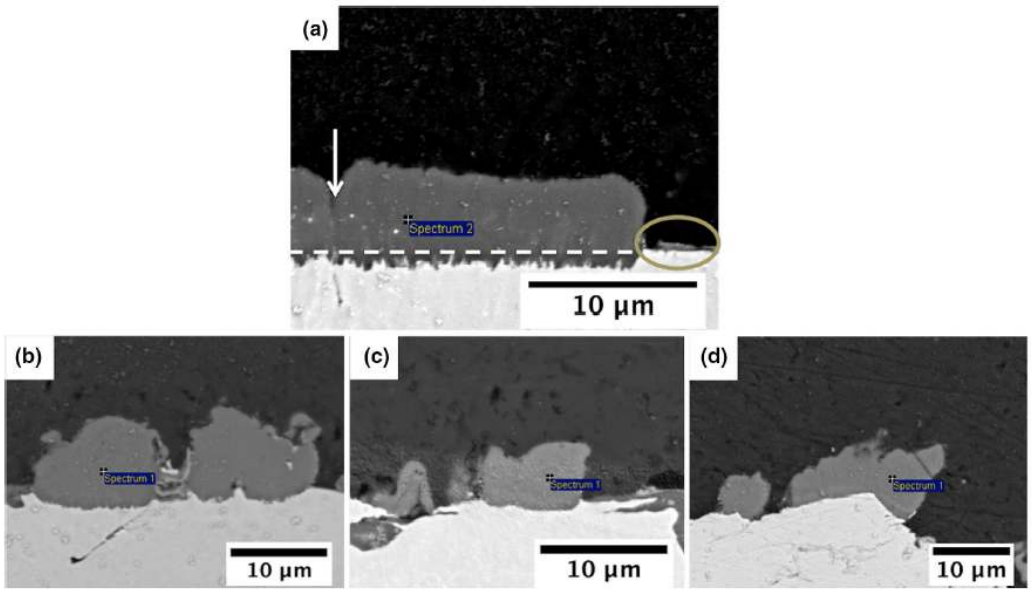

Fig. 12 SEM images of the $FeAl_3$ intermetallic layer growing in the aluminum coatings after 35 min of heat treatment on (a) P-2 surface showing its discontinuity, thickness above substrate and growth direction, (b) GB-4, (c) GB-5 and (d) FPWJ-10

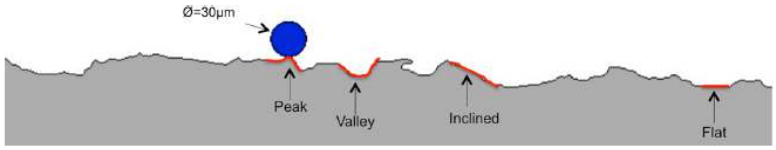

Fig. 13 Illustration of the particle impact process on different sections of a grit-blasted substrate surface

periphery of the initial contact zone, which corresponds to the region of highest localized material flow (Ref 13, 65, 69). Particles impacting a substrate valley, with two major contact zones, reach the lowest maximum temperature throughout their deformation process. Impacts for which the particle deformation is occurring in multiple non-parallel planes undergo limited localized plastic flow and heat generation, which explains the lower temperature reached at impacts with peak and valley surfaces. Thus, high particle temperature is reached during the impact with a flat and inclined surface due to peripheral flow localization. Based on these simulation results, the highest temperature is reached when the particle impacts a flat substrate with temperature at the particle periphery reaching 884 K, while it reaches a similar temperature for the impact on inclined surface (876 K). The strain rate encountered at the particle surface during the impact with a flat surface, at the time step shown, is of the order of $10^9\ s^{-1}$, while it is one order of magnitude lower for the impact on all other surface types.

The maximum PEEQ achieved on the aluminum particle surface are 4.5, 3.7, 5.4 and 2.2 for impact simulated on flat, inclined, peak and valley surfaces respectively, as shown in Fig. 15. The PEEQ at the substrate surface reaches low values close to 1.0 during the complete particle impact process. The difference in PEEQ values is directly related to the dissimilarity in strength and hardness between the particle and substrate material. The lack of substrate surface deformation correlates well with the SEM images previously shown of poorly deformed substrate mirror-finish surface. Large effective plastic strains at the particle surface are associated with improved breakage of native oxides, which is an essential process to form intimate contact between the two surfaces. The particle impact with a peak experiences the highest equivalent plastic strain, whereas the impact on a flat surface is second highest. Despite experiencing larger PEEQ values at their peaks, rough substrate profiles can possibly inhibit the removal of the disrupted oxide layer from the surface by trapping the oxide residues between the surface

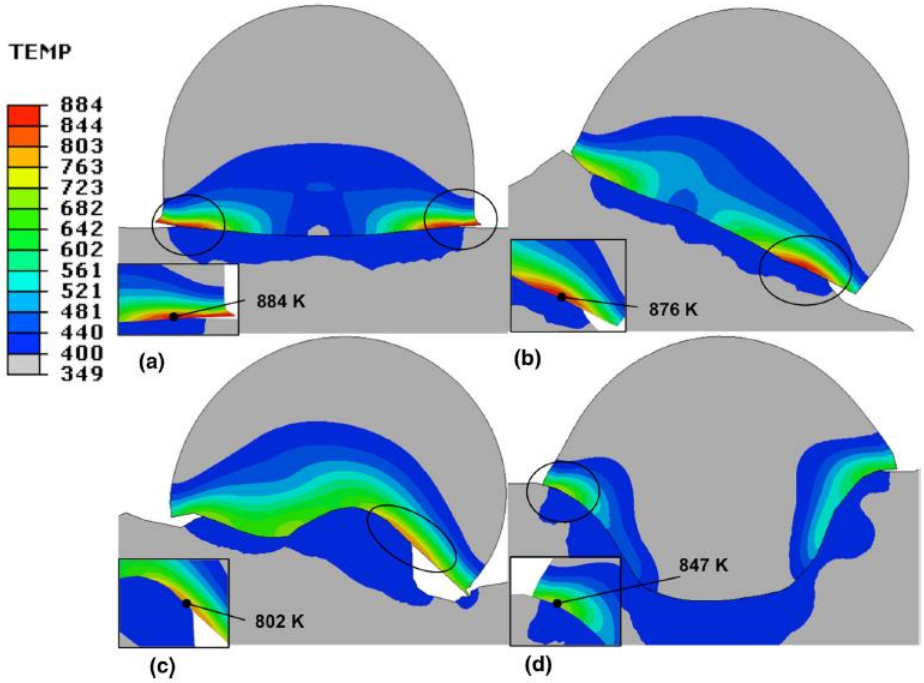

Fig. 14 Simulated surface temperature (K) results for impacts on (a) flat, (b) inclined, (c) peak and (d) valley profiles. Circled areas show the zones with the highest temperature. Inserts emphasize the circled zones providing a clearer image of the temperature gradient

undulations (Ref 61). This is easily observed on the peak and valley surfaces for which the possible oxide removal path is closed by either the particle or substrate roughness. Improper cleaning of the surfaces will obstruct intimate metal-to-metal contact, which will deprive the coating from bonding metallurgically to the substrate surface.

Figure 16 shows the contact pressure range encountered at the contact surface during impacts. The values vary from 920 MPa to 1.62 GPa, 477 to 818 MPa, 143 to 859 MPa and 155 to 620 MPa for impacts on flat, inclined, peak and valley surfaces, respectively. The contact pressure values reached at zone of highest temperature are 1.34 GPa, 681 MPa, 859 MPa and 620 MPa for impacts on flat, inclined, peak and valley surfaces, respectively. The larger the value of contact pressure, the lower the distance between the particle and substrate surfaces and in turn the more enhanced is the molecular interaction (Ref 70). In cold welding applications, pressures in the same order of magnitude are required at ambient temperature (Ref 70) for a wide range of non-ferrous material. Based on these results, the impact with the flat substrate surface shows to be the most favorable process for metallurgical bonding.

The last analyzed impact property is the velocity vector direction, shown in Fig. 17. For the specific case of the particle impacting on a flat substrate, the momentum is directed toward the substrate surface and the material at the periphery flows parallel to the surface. For both the impact on a surface peak and on an inclined surface, the particle is experiencing a rotational momentum (Ref 71-73) that generates movement away from the contact zone. The resulting inertia force tends to separate the particle from the substrate surface, which obstructs the formation of metallurgical bonds. Thus, the velocity vector mapping suggests that the presence of metallurgical bond on low roughness substrates is also limited due to the angular momentum that particles experience during impact, which prevents them to properly bond. Furthermore, the torque that the particles experience when impacting onto a non-flat surface is expected to be accentuated for irregular shaped particles. For non-spherical particles, the mass distribution with respect to the point of impact influences the material flow during its plastic deformation, which should give rise to an additional angular momentum than the one depicted in Fig. 17 and as a result extend the obstruction to create metallurgical bonds.

Impact simulation results reveal that the particle in contact with a flat substrate reaches the highest temperature and contact pressure. The PEEQ experienced at the particle

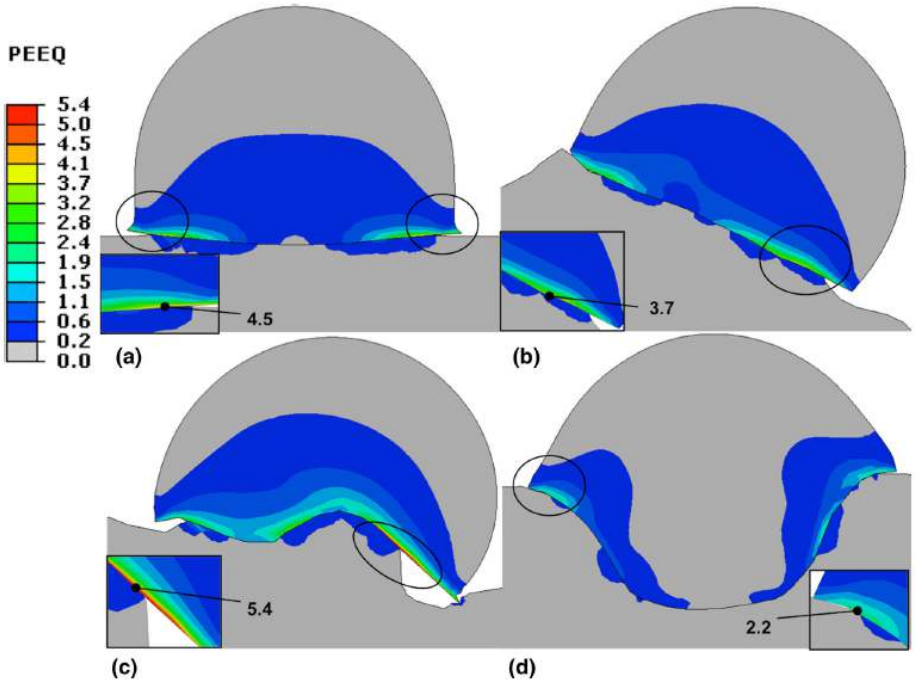

Fig. 15 Simulated surface PEEQ results for impacts on (a) flat, (b) inclined, (c) peak and (d) valley profiles. Inserts emphasize the PEEQ value at zones of highest temperature

surface is the second highest value from all tested impacts. The particle resulting momentum on such substrate surface also indicates limited rotational movement that would tend to separate the particle from the substrate surface. Moreover, Fig. 18 reveals the presence of shear localization (abrupt stress decrease with temperature increase) in elements found at the particle periphery during the impact with a flat substrate. Initially, the stress increases due to hardening effects from high strain and strain rates but is found to decrease when softening effects start dominating. Given the high material flow experienced at the shear instability location, the removal of oxides from material jetting is expected to also be enhanced and consequently the metal-to-metal contact improved. Altogether, results agree on the superiority of the impact on flat surfaces to create metallurgical bonds.

Finite Element Analysis of Coating Adhesion Strength

The following sets of analysis provide results of simulated pure aluminum coating adhesion strength for all produced FPWJ surfaces. The cross sections of all coated FPWJ substrate surfaces generated in this study have been transferred to Abaqus and adhesion tests following the ASTM-C633 standard were simulated (Ref 46). The obtained adhesion strengths correspond to the purely mechanical adhesion contribution as the modeling process method eliminates any involvement of metallurgical bonds.

Figure 19 shows the obtained simulated aluminum coating adhesion strengths for all FPWJ-treated surfaces along with their corresponding experimental values. It is clear from the results that the simulated adhesion values correspond closely to those obtained experimentally. These results suggest that coating adhesion to substrate surfaces treated by FPWJ (and potentially grit blasting by extension) is likely due to mechanical anchoring. This could be the main reason explaining the major drop in adhesion on low roughness surfaces frequently reported in CS for soft particles on hard materials (Ref 11, 30, 41). In purely mechanical adhesion, the geometry, size and quantity of hooks and anchoring sites found at the substrate surface is the major factor affecting the final adhesion strength. This reinforces the previous findings that the presence of embedded grit under traditionally grit-blasted surfaces has little impact on the final adhesion. For grit-blasted surfaces, the mechanical interlocking sites are only located at the sharp edges created from the grit plowing into the substrate

J Therm Spray Tech (2017) 26:1461–1483

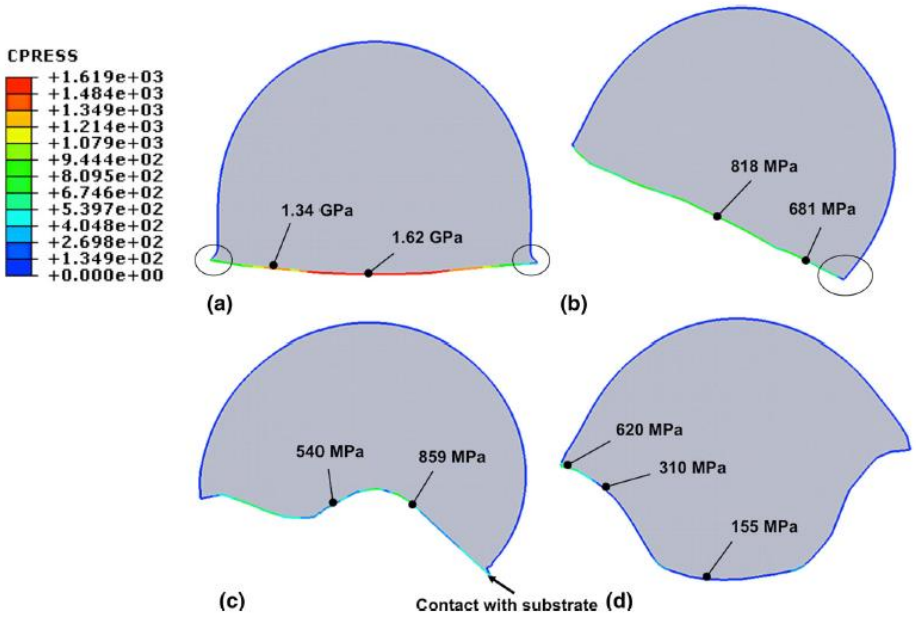

Fig. 16 Simulated surface CPRESS (MPa) results at particle interface for impacts on (a) flat, (b) inclined, (c) peak and (d) valley profiles. CPRESS values at zone of highest temperature and zones of interest are presented. Regions not in contact with the substrate are circled. CPRESS values at those regions are explained by partial mesh contact

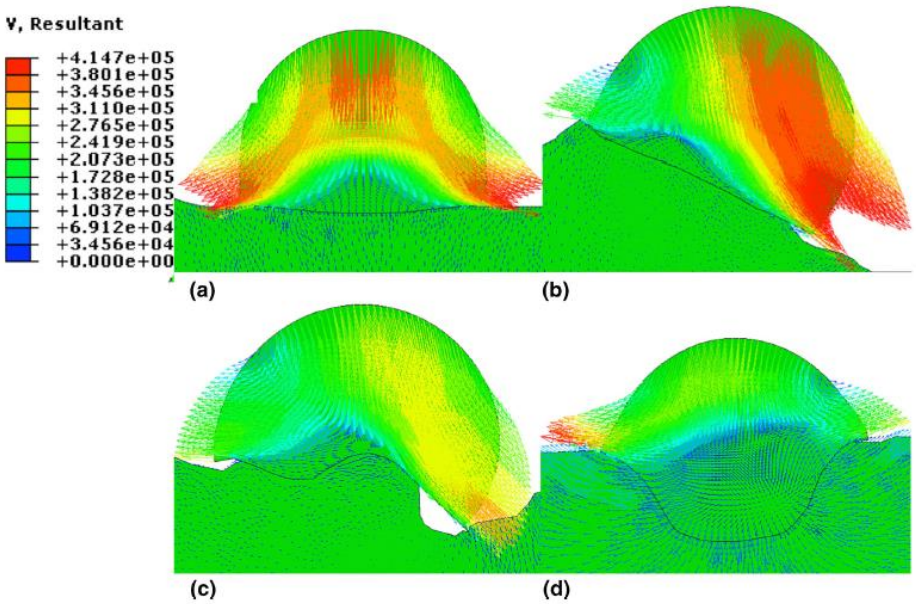

Fig. 17 Simulated surface velocity (mm/s) for impacts on (a) flat, (b) inclined, (c) peak and (d) valley profiles

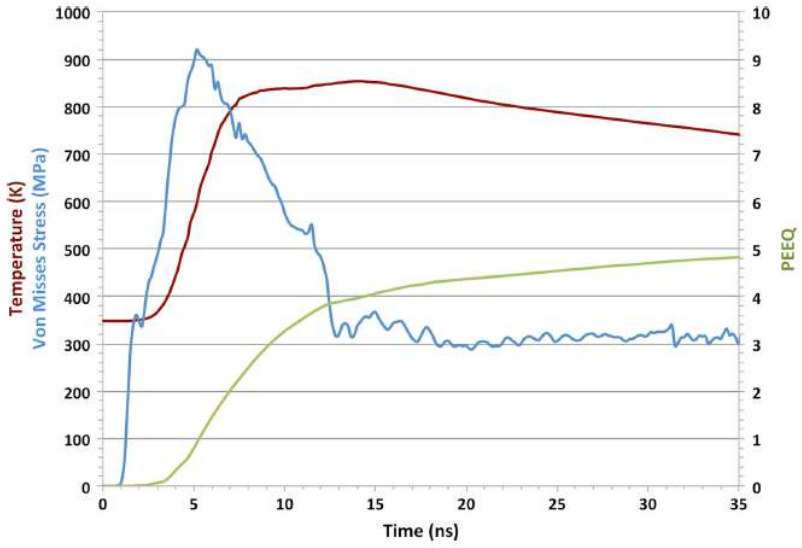

Fig. 18 Temporal evolution of temperature (K), equivalent plastic strain and Von Mises equivalent stress (MPa) during impact with a flat substrate

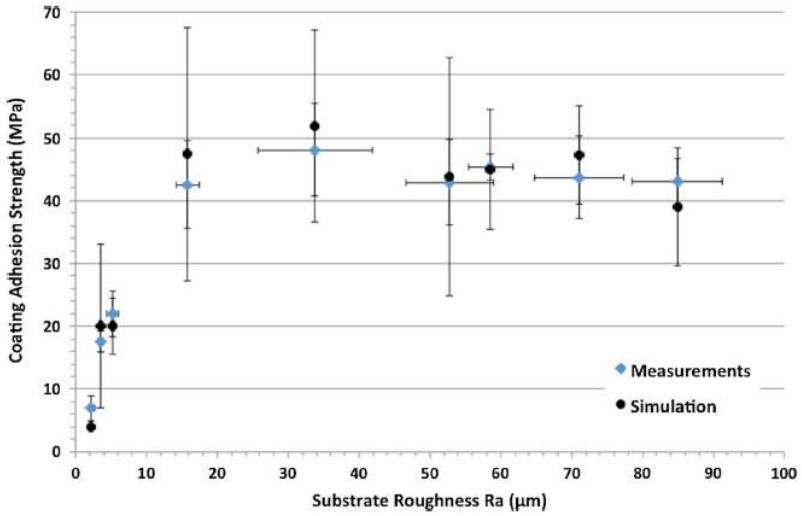

Fig. 19 Pure aluminum coating simulated adhesion strength compared to experimental results

surface, which gives rise to low adhesion. Hooks resulting from grit impact are fairly shallow and poorly defined, which consequently limits the occurrence of suitable anchoring between particles and the substrate surface. As stated previously, well embedded grit can also provide grip to the coating but the strength is limited by the size of the grit protruding above the substrate surface and strength of the embedding process. Similar explanations can be given for the low roughness FPWJ samples, where only a limited amount of crevices, serving as coating interlocking sites, are present. Larger surface roughnesses, irrespective of the surface preparation method used, produce higher adhesion strength due to the increased size and quantity of hooks.

However, the current experimental and simulated results confirm that there seems to be a limitation to the contribution of the mechanical anchoring effect on the coating adhesion. The maximum reachable adhesion strength for the current materials and spray parameters corresponds to approximately 50 MPa. The reduction of surface anchoring regions on the high roughness substrates is an evident

explanation for such limitation. Large arithmetic surface average roughness (Ra) can be measured while still having a limited number of hooks along their profile.

Conclusions

The effect of surface roughness and surface preparation method on the adhesive strength of cold-sprayed pure aluminum coatings on 300M steel substrates was studied experimentally and through finite element analysis. The bond strength and adhesion mechanism at the substrate/coating interface was correlated with the substrate surface roughness and preparation treatment. Metallurgical bond was shown to be the only mechanism responsible for coating adhesion when deposited onto a polished surface with fracture surface analysis revealing the absence of substrate deformation and also a limited number of metallurgically bonded sites. Results have also shown that depositing coatings on surfaces with roughness less than 10 μm lead to reduced adhesion strength compared to polished surfaces, irrespective of the method used (grit blasted or FPWJ) to prepare the surface prior to the deposition. Varying the grit embedment percentage on grit-blasted surfaces has also proven the inconsequential effect of superficial grit presence on the coating adhesion strength.

A finite element analysis of the particle impact and deformation process on various substrate surface profiles has demonstrated that the particle temperature, PEEQ, contact pressure and momentum limit the conditions favorable to the creation of metallurgical bonds to flat surfaces. It has also been shown that the regions of highest PEEQ reached for particles impacting onto flat substrate surfaces are limited and located near the particle periphery, which correlates well with the low percentage of bonded particles found at the fractured surfaces of adhesion test samples.

Finite element analysis was also used to predict the coating adhesion strength. The modeling results agreed with the experimental findings and thus demonstrated that only mechanical anchoring is responsible for the coating adhesion for all surfaces treated with FPWJ prior to the particle deposition process.

The findings showed in this study not only explain the causes of the drop in cold spray coating adhesion strength for low substrate roughnesses compared to polished surfaces but also prove the irrelevance of grit embedment when mechanical anchoring is the only bonding mechanism responsible for adhesion.

Acknowledgments The authors wish to thank Carpenter Technology (Canada) Ltd. for providing the necessary substrate material used in this study.

References

1. M. Faccoli, G. Cornacchia, D. Maestrini, G.P. Marconi, and R. Roberti, Cold Spray Repair of Martensitic Stainless Steel Components, *J. Therm. Spray Technol.*, 2014, **23**(8), p 1270-1280
2. V. Champagne and D. Helfritch, Critical Assessment 11: Structural Repairs by Cold Spray, *Mater. Sci. Technol.*, 2015, **31**(6), p 627-634
3. V.K. Champagne, The Repair of Magnesium Rotorcraft Components by Cold Spray, *J. Fail. Anal. Prev.*, 2008, **8**(2), p 164-175
4. F. Raletz, M. Vardelle, and G. Ezo'o, Critical Particle Velocity Under Cold Spray Conditions, *Surf. Coat. Technol.*, 2006, **201**(5), p 1942-1947
5. C.-J. Li, W.-Y. Li, and H. Liao, Examination of the Critical Velocity for Deposition of Particles in Cold Spraying, *J. Therm. Spray Technol.*, 2006, **15**(2), p 212-222
6. D.L. Gilmore, R.C. Dykhuizen, R.A. Neiser, M.F. Smith, and T.J. Roemer, Particle Velocity and Deposition Efficiency in the Cold Spray Process, *J. Therm. Spray Technol.*, 1999, **8**(4), p 576-582
7. W.-Y. Li, C. Zhang, C.-J. Li, and H. Liao, Modeling Aspects of High Velocity Impact of Particles in Cold Spraying by Explicit Finite Element Analysis, *J. Therm. Spray Technol.*, 2009, **18**(5-6), p 921
8. T. Schmidt et al., From Particle Acceleration to Impact and Bonding in Cold Spraying, *J. Therm. Spray Technol.*, 2009, **18**(5-6), p 794
9. S. Rahmati and A. Ghaei, The Use of Particle/Substrate Material Models in Simulation of Cold-Gas Dynamic-Spray Process, *J. Therm. Spray Technol.*, 2013, **23**(3), p 530-540
10. D. Zhang, P.H. Shipway, and D.G. McCartney, Cold Gas Dynamic Spraying of Aluminum: The Role of Substrate Characteristics in Deposit Formation, *J. Therm. Spray Technol.*, 2004, **14**(1), p 109-116
11. T. Hussain, D.G. McCartney, P.H. Shipway, and D. Zhang, Bonding Mechanisms in Cold Spraying: The Contributions of Metallurgical and Mechanical Components, *J. Therm. Spray Technol.*, 2009, **18**(3), p 364-379
12. M. Grujicic, C.L. Zhao, W.S. DeRosset, and D. Helfritch, Adiabatic Shear Instability Based Mechanism for Particles/Substrate Bonding in the Cold-Gas Dynamic-Spray Process, *Mater. Des.*, 2004, **25**(8), p 681-688
13. P.C. King, G. Bae, S.H. Zahiri, M. Jahedi, and C. Lee, An Experimental and Finite Element Study of Cold Spray Copper Impact Onto Two Aluminum Substrates, *J. Therm. Spray Technol.*, 2009, **19**(3), p 620-634
14. Y. Cormier, P. Dupuis, B. Jodoin, and A. Ghaei, Finite Element Analysis and Failure Mode Characterization of Pyramidal Fin Arrays Produced by Masked Cold Gas Dynamic Spray, *J. Therm. Spray Technol.*, 2015, **24**(8), p 1549-1565
15. W.-Y. Li, H. Liao, C.-J. Li, H.-S. Bang, and C. Coddet, Numerical Simulation of Deformation Behavior of Al Particles Impacting on Al Substrate and Effect of Surface Oxide Films on Interfacial Bonding in Cold Spraying, *Appl. Surf. Sci.*, 2007, **253**(11), p 5084-5091
16. W.-Y. Li, C.-J. Li, and G.-J. Yang, Effect of Impact-Induced Melting on Interface Microstructure and Bonding of Cold-Sprayed Zinc Coating, *Appl. Surf. Sci.*, 2010, **257**(5), p 1516-1523
17. G. Bae, Y. Xiong, S. Kumar, K. Kang, and C. Lee, General Aspects of Interface Bonding in Kinetic Sprayed Coatings, *Acta Mater.*, 2008, **56**(17), p 4858-4868
18. M. Grujicic, J.R. Saylor, D.E. Beasley, W.S. DeRosset, and D. Helfritch, Computational Analysis of the Interfacial Bonding Between Feed-Powder Particles and the Substrate in the Cold-

Gas Dynamic-Spray Process, *Appl. Surf. Sci.*, 2003, **219**(3-4), p 211-227
19. R.C. Dykhuizen, M.F. Smith, D.L. Gilmore, R.A. Neiser, X. Jiang, and S. Sampath, Impact of High Velocity Cold Spray Particles, *J. Therm. Spray Technol.*, 1999, **8**(4), p 559-564
20. X.-J. Ning, J.-H. Jang, H.-J. Kim, C.-J. Li, and C. Lee, Cold Spraying of Al-Sn Binary Alloy: Coating Characteristics and Particle Bonding Features, *Surf. Coat. Technol.*, 2008, **202**(9), p 1681-1687
21. C.-J. Li, W.-Y. Li, and Y.-Y. Wang, Formation of Metastable Phases in Cold-Sprayed Soft Metallic Deposit, *Surf. Coat. Technol.*, 2005, **198**(1-3), p 469-473
22. J. Wu, H. Fang, H. Kim, and C. Lee, High Speed Impact Behaviors of Al Alloy Particle Onto Mild Steel Substrate During Kinetic Deposition, *Mater. Sci. Eng., A*, 2006, **416**(1-2), p 114-119
23. W.-Y. Li, C. Zhang, X. Guo, C.-J. Li, H. Liao, and C. Coddet, Study on Impact Fusion at Particle Interfaces and Its Effect on Coating Microstructure in Cold Spraying, *Appl. Surf. Sci.*, 2007, **254**(2), p 517-526
24. S. Barradas et al., Laser Shock Flier Impact Simulation of Particle-Substrate Interactions in Cold Spray, *J. Therm. Spray Technol.*, 2007, **16**(4), p 548-556
25. D. Goldbaum et al., The Effect of Deposition Conditions on Adhesion Strength of Ti and Ti_6Al_4V Cold Spray Splats, *J. Therm. Spray Technol.*, 2012, **21**(2), p 288-303
26. G. Bae et al., Bonding Features and Associated Mechanisms in Kinetic Sprayed Titanium Coatings, *Acta Mater.*, 2009, **57**(19), p 5654-5666
27. K. Kim, M. Watanabe, and S. Kuroda, Jetting-Out Phenomenon Associated with Bonding of Warm-Sprayed Titanium Particles Onto Steel Substrate, *J. Therm. Spray Technol.*, 2009, **18**(4), p 490
28. W.-Y. Li et al., Significant Influences of Metal Reactivity and Oxide Films at Particle Surfaces on Coating Microstructure in Cold Spraying, *Appl. Surf. Sci.*, 2007, **253**(7), p 3557-3562
29. S. Barradas et al., Application of Laser Shock Adhesion Testing to the Study of the Interlamellar Strength and Coating-Substrate Adhesion in Cold-Sprayed Copper Coating of Aluminum, *Surf. Coat. Technol.*, 2005, **197**(1), p 18-27
30. T. Marrocco, D.G. McCartney, P.H. Shipway, and A.J. Sturgeon, Production of Titanium Deposits by Cold-Gas Dynamic Spray: Numerical Modeling and Experimental Characterization, *J. Therm. Spray Technol.*, 2006, **15**(2), p 263-272
31. R. Ghelichi, S. Bagherifard, M. Guagliano, and M. Verani, Numerical Simulation of Cold Spray Coating, *Surf. Coat. Technol.*, 2011, **205**, p 5294-5301
32. R. Ghelichi, S. Bagherifard, D. MacDonald, I. Fernandez-Pariente, B. Jodoin, and M. Guagliano, Experimental and Numerical Study of Residual Stress Evolution in Cold Spray Coating, *Appl. Surf. Sci.*, 2014, **288**, p 26-33
33. K. Yokoyama, M. Watanabe, S. Kuroda, Y. Gotoh, T. Schmidt, and F. Gärtner, Simulation of Solid Particle Impact Behavior for Spray Processes, *Mater. Trans.*, 2006, **47**(7), p 1697-1702
34. M.M. Sharma, T.J. Eden, and B.T. Golesich, Effect of Surface Preparation on the Microstructure, Adhesion, and Tensile Properties of Cold-Sprayed Aluminum Coatings on AA2024 Substrates, *J. Therm. Spray Technol.*, 2014, **24**(3), p 410-422
35. S. Kumar, G. Bae, and C. Lee, Influence of Substrate Roughness on Bonding Mechanism in Cold Spray, *Surf. Coat. Technol.*, 2016, **304**, p 592-605
36. P. Richer, B. Jodoin, and L. Ajdelsztajn, Substrate Roughness and Thickness Effects on Cold Spray Nanocrystalline A-Mg Coatings, *J. Therm. Spray Technol.*, 2006, **15**(2), p 246-254
37. S. Kumar, G. Bae, and C. Lee, Deposition Characteristics of Copper Particles on Roughened Substrates Through Kinetic Spraying, *Appl. Surf. Sci.*, 2009, **255**(6), p 3472-3479
38. T.S. Price, P.H. Shipway, D.G. McCartney, E. Calla, and D. Zhang, A Method for Characterizing the Degree of Inter-Particle Bond Formation in Cold Sprayed Coatings, *J. Therm. Spray Technol.*, 2007, **16**(4), p 566-570
39. M.M. Vijay, A.H. Tieu, W. Yan, and B.R. Daniels, Method and Apparatus for Prepping Surfaces with a High-Frequency Forced Pulsed Waterjet, US8550873 B2, 08 Oct 2013
40. M.M. Vijay, Apparatus and Method for Prepping a Surface Using a Coating Particle Entrained in a Pulsed Waterjet or Airjet, US8389066 B2, 05-Mar-2013
41. T. Samson, D. MacDonald, R. Fernández, and B. Jodoin, Effect of Pulsed Waterjet Surface Preparation on the Adhesion Strength of Cold Gas Dynamic Sprayed Aluminum Coatings, *J. Therm. Spray Technol.*, 2015, **24**(6), p 984-993
42. M. Fukumoto et al., Effect of Substrate Temperature on Deposition Behavior of Copper Particles on Substrate Surfaces in the Cold Spray Process, *J. Therm. Spray Technol.*, 2007, **16**(5), p 643-650
43. S. Rech, A. Trentin, S. Vezzu, J.-G. Legoux, E. Irissou, and M. Guagliano, Influence of Pre-Heated Al 6061 Substrate Temperature on the Residual Stresses of Multipass Al Coatings Deposited by Cold Spray, *J. Therm. Spray Technol.*, 2011, **20**(1-2), p 243-251
44. S. Yin, Y. Sun, X. Wang, Z. Guo, and H. Liao, Effect of Spray Angle on Temperature Distribution Within the Metallic Substrate in Cold Spraying, *J. Therm. Spray Technol.*, 2013, **22**(6), p 983-991
45. M.P. Dewar, A.G. McDonald, and A.P. Gerlich, Interfacial Heating During Low-Pressure Cold-Gas Dynamic Spraying of Aluminum Coatings, *J. Mater. Sci.*, 2011, **47**(1), p 184-198
46. ASTM C633-13, *Standard Test Method for Adhesion or Cohesion Strength of Thermal Spray Coatings*, ASTM International, West Conshohocken, PA, 2017
47. T.H. Van Steenkiste, J.R. Smith, and R.E. Teets, Aluminum Coatings Via Kinetic Spray with Relatively Large Powder Particles, *Surf. Coat. Technol.*, 2002, **154**(2-3), p 237-252
48. C. Borchers, F. Gärtner, T. Stoltenhoff, and H. Kreye, Microstructural Bonding Features of Cold Sprayed Face Centered Cubic Metals, *J. Appl. Phys.*, 2004, **96**(8), p 4288-4292
49. T. Stoltenhoff, C. Borchers, F. Gärtner, and H. Kreye, Microstructures and Key Properties of Cold-Sprayed and Thermally Sprayed Copper Coatings, *Surf. Coat. Technol.*, 2006, **200**(16-17), p 4947-4960
50. W.-Y. Li, H. Liao, C.-J. Li, G. Li, C. Coddet, and X. Wang, On High Velocity Impact of Micro-Sized Metallic Particles in Cold Spraying, *Appl. Surf. Sci.*, 2006, **253**(5), p 2852-2862
51. ASM and A. S. for Metals, *ASM Handbook: Volume 18: Friction, Lubrication, and Wear Technology*, 10th ed., ASM International, Materials Park, OH, 1992
52. T. Schmidt, F. Gaertner, and H. Kreye, New Developments in Cold Spray Based on Higher Gas and Particle Temperatures, *J. Therm. Spray Technol.*, 2006, **15**(4), p 488-494
53. É.I.J.G. Legoux, Effect of Substrate Temperature on the Formation Mechanism of Cold-Sprayed Aluminum, Zinc and Tin Coatings, *J. Therm. Spray Technol.*, 2007, **16**(5), p 619-626
54. A. Nastic, *Repair of Aluminum Alloy Aerospace Components and Cold Gas Dynamic Spray Flow Distribution Study*, Université d'Ottawa/University of Ottawa, Thesis, 2015
55. B. Banerjee, An Evaluation of Plastic Flow Stress Models for the Simulation of High-Temperature and High-Strain-Rate Deformation of Metals, *Acta Mater.*, 2010, **58**(20), p 6810-6827

56. D.L. Preston, D.L. Tonks, and D.C. Wallace, Model of Plastic Deformation for Extreme Loading Conditions, *J. Appl. Phys.*, 2003, **93**(1), p 211-220
57. R. Fernández, D. MacDonald, A. Nastić, B. Jodoin, A. Tieu, and M. Vijay, Enhancement and Prediction of Adhesion Strength of Copper Cold Spray Coatings on Steel Substrates for Nuclear Fuel Repository, *J. Therm. Spray Technol.*, 2016, **25**(8), p 1577-1587
58. J. Wu, J. Yang, H. Fang, S. Yoon, and C. Lee, The Bond Strength of A-Si Coating on Mild Steel by Kinetic Spraying Deposition, *Appl. Surf. Sci.*, 2006, **252**(22), p 7809-7814
59. X. Wang, J.V. Wood, Y. Sui, and H. Lu, Formation of Intermetallic Compound in Iron-Aluminum Alloys, *J. Shanghai Univ. Engl. Ed.*, 1998, **2**(4), p 305-310
60. S. Yin, X. Wang, W. Li, H. Liao, and H. Jie, Deformation Behavior of the Oxide Film on the Surface of Cold Sprayed Powder Particle, *Appl. Surf. Sci.*, 2012, **259**, p 294-300
61. Y. Xie, S. Yin, C. Chen, M.-P. Planche, H. Liao, and R. Lupoi, New Insights Into the Coating/Substrate Interfacial Bonding Mechanism in Cold Spray, *Scr. Mater.*, 2016, **125**, p 1-4
62. X.K. Suo, M. Yu, W.Y. Li, M.P. Planche, and H.L. Liao, Effect of Substrate Preheating on Bonding Strength of Cold-Sprayed Mg Coatings, *J. Therm. Spray Technol.*, 2012, **21**(5), p 1091-1098
63. K. Kim, W. Li, and X. Guo, Detection of Oxygen at the Interface and Its Effect on Strain, Stress, and Temperature at the Interface Between Cold Sprayed Aluminum and Steel Substrate, *Appl. Surf. Sci.*, 2015, **357**(B), p 1720-1726
64. W.Y. Li, M. Yu, F.F. Wang, S. Yin, and H.L. Liao, A Generalized Critical Velocity Window Based on Material Property for Cold Spraying by Eulerian Method, *J. Therm. Spray Technol.*, 2014, **23**(3), p 557-566
65. H. Assadi, F. Gärtner, T. Stoltenhoff, and H. Kreye, Bonding Mechanism in Cold Gas Spraying, *Acta Mater.*, 2003, **51**(15), p 4379-4394
66. F. Meng, H. Aydin, S. Yue, and J. Song, The Effects of Contact Conditions on the Onset of Shear Instability in Cold-Spray, *J. Therm. Spray Technol.*, 2015, **24**(4), p 711-719
67. S. Guetta et al., Influence of Particle Velocity on Adhesion of Cold-Sprayed Splats, *J. Therm. Spray Technol.*, 2009, **18**(3), p 331-342
68. T. Schmidt, F. Gartner, H. Assadi, and H. Kreye, Development of a Generalized Parameter for Cold Spray Deposition, *Acta Mater.*, 2006, **54**, p 729-742
69. P.C. King, C. Busch, T. Kittel-Sherri, M. Jahedi, and S. Gulizia, Interface Melding in Cold Spray Titanium Particle Impact, *Surf. Coat. Technol.*, 2014, **239**, p 191-199
70. A.D. Kuritsyna, Relation Between Hardness and Resistance to Cold Welding [Antifriction Property] of Metals and Alloys, *Met. Sci. Heat Treat. Met.*, 1959, **1**(8), p 29-32
71. S. Yin, P. He, H. Liao, and X. Wang, Deposition Features of Ti Coating Using Irregular Powders in Cold Spray, *J. Therm. Spray Technol.*, 2014, **23**(6), p 984-990
72. W.-Y. Li, S. Yin, and X.-F. Wang, Numerical Investigations of the Effect of Oblique Impact on Particle Deformation in Cold Spraying by the SPH Method, *Appl. Surf. Sci.*, 2010, **256**(12), p 3725-3734
73. G. Li, X. Wang, and W. Li, Effect of Different Incidence Angles on Bonding Performance in Cold Spraying, *Trans. Nonferrous Met. Soc. China*, 2007, **17**(1), p 116-121
74. F.P. Incropera and D.P. De Witt, *Fundamentals of Heat and Mass Transfer*, 2nd ed., John Wiley & Sons, Inc., Hoboken, NJ, 1985
75. D. Steinberg, *Equation of State and Strength Properties of Selected Materials*, Lawrence Livermore National Laboratory, Livermore, CA, 1996
76. M.C. Price, A.T. Kearsley, and M.J. Burchell, Validation of the Preston–Tonks–Wallace Strength Model at Strain Rates Approaching ~1011 s-1 for Al-1100, Tantalum and Copper Using Hypervelocity Impact Crater Morphologies, *Int. J. Impact Eng*, 2013, **52**, p 1-10
77. G.R. Johnson and W.H. Cook, A Constitutive Model and Data for Metals Subjected to Large Strains, High Strain Rates and High Temperatures, *Proc. 7th Int. Symp. Ballist.*, 1983, p 541-547
78. M. Fugate et al., Hierarchical Bayesian Analysis and the Preston–Tonks–Wallace Model, Los Alamos Technical Report, LA-UR-05-3935, 2005

5.2 RESEARCH PROJECT 2

The focus of the following paper, entitled "Evaluation of heat transfer transport coefficient for cold spray through computational fluid dynamics and particle in-flight temperature measurement using a high-speed IR camera", was to obtain particle in-flight temperature measurements and subsequently evaluate heat transfer coefficients and equations used in CGDS process computational fluid dynamics models. The importance of including the effect of particle relative Mach number and Reynolds number in the empirical Nusselt correlation has been emphasised. This peer-reviewed article addresses the objectives presented and detailed in section 3.2.

Andre McDonald
President, TSS
9639 Kinsman Road, Materials Park, Ohio, 44073-0002 USA
440.338.5417 | Fax: 440.338.6614
john.cerne@asminternational.org
www.asminternational.org

April 18, 2019

Dear Ms. Nastic and Dr. Jodoin:

On behalf of the Journal of Thermal Spray Technology Editorial Committee Chair Dr. Robert Vaßen, JTST Editor Dr. Armelle Vardelle, and Chair of the JTST Best Paper Award Selection Committee Dr. Jiri Matejicek, it is my pleasure and privilege to extend sincere congratulations to your group for the selection of your paper "Evaluation of Heat Transfer Transport Coefficient for Cold Spray Through Computational Fluid Dynamics and Particle In-Flight Temperature Measurement Using a High-Speed IR Camera" as the JTST Volume 27 Best Paper Award Winner.

Your paper was selected by a panel of 36 international thermal spray scientists, who commented that your paper is a "Very detailed, mathematically rigorous description of the formation of microstructure in cold sprayed coatings. Perfect combination of non-trivial experiment with rigorous modeling. One of the best papers I ever saw in JTST." Another judge commented that your paper is "A very thorough theoretical analysis, combined with development of a new particle temperature measurement technique, to provide a rigorous grounding of heat transfer phenomena in the cold spray process. This work provides new insights and better fidelity for process modeling and will enable improved predictive capability for understanding and developing new processes and materials."

By winning this award, your team has demonstrated a high level of scientific and engineering achievement. Your wonderful accomplishment will be formally acknowledged during ITSC in Yokohama, Japan, next month. Congratulations on contributing to JTST at the highest possible level! We look forward to receiving more of your high quality contributions to JTST in the future.

Best regards,

Mary Anne Fleming
Senior Content Developer
Journals, Magazines, News, and APD Publications
ASM International

Thermal Spray Society
ASM INTERNATIONAL

2018 results/Jury additional comments

1st place – best paper:

Evaluation of Heat Transfer Transport Coefficient for Cold Spray Through Computational Fluid Dynamics and Particle In-Flight Temperature Measurement Using a High-Speed IR Camera

By: A. Nastic, B. Jodoin

Monitoring the particle history in cold spray technique is a key to predict the microstructure. Authors have done a great job to describe a methodology for particle diagnostic. This is a good particle diagnostic work combining the experimental and computational approach. Results are discussed in depth with a thorough scientific discussion.

Particle velocity is the key factor to determine the quality of coatings. This paper focus on the experimental measurement of in-flight particle temperature using a high-speed, high-definition infrared imaging technique. It is to initiate efforts to improve the understanding of particle heating process in CS by focusing on the experimental measurement of particle temperature.

The paper presents first reliable measurements of particle temperatures in Cold Spray, which is a considerable achievement in itself. Furthermore, the accompanying simulation not only give great insight into this rapidly evolving technology but also will encourage more realistic modelling of CS process in the near future.

Very detailed mathematically rigorous description of the formation of microstructure in cold sprayed coatings. Perfect combination of non-trivial experiment with rigorous modeling. One of the best papers I ever saw in JTST.

The authors used the latest measuring equipment and a profound simulation to shed some light into the particle temperature problematic in CS. They put a lot of efforts into selecting the most accurate material values and were well aware of the limitations of each method. They selected the experimental conditions accordingly, to get the largest possible overlap between theory and practical experiment.

This paper presents an excellent and comprehensive study of cold spray process. The work is both computational as well as experimental. The final correlation proposed for the Nusselt number will be useful for researchers in this field.

This paper represents an excellent effort of high scientific merit, at a very challenging yet interesting technical problem.

A very thorough theoretical analysis, combined with development of a new particle temperature measurement technique, to provide a rigorous grounding of heat transfer phenomena in the cold spray process. This work provides new insights and better fidelity for process modeling and will enable improved predictive capability for understanding and developing new processes and materials.

The work involves experiments and analysis as well as methods for improving the quality of cold-sprayed materials, e.g. intermetallic bonding. Since cold-spray is being explored for spraying of functional materials with tailored thermophysical properties, such studies can help overcome many of the key challenges encountered during cold-spraying.

J Therm Spray Tech (2019) 28:1103–1104
https://doi.org/10.1007/s11666-019-00892-y

Journal of Thermal Spray Technology Volume 27 Best Paper Awards

The *Journal of Thermal Spray Technology* (JTST) is pleased to announce the winners of the JTST Volume 27 Best Paper Awards, as chosen by an international committee of expert judges. The awards were presented to the winning authors at the International Thermal Spray Conference and Exposition 2019, in Yokohama, Japan.

The Editorial Committee of the journal believes it is important to evaluate the quality of engineering and scientific contributions published in JTST and to provide recognition of excellent work and its publication. Each paper is reviewed and evaluated on its merits for scientific and engineering content, originality, and presentation style. The following papers are recognized as outstanding and the authors received awards of recognition for their excellent publications.

Aleksandra Nastic

Bertrand Jodoin

The *Journal of Thermal Spray Technology* Volume 27 Best Paper Award

"Evaluation of Heat Transfer Transport Coefficient for Cold Spray Through Computational Fluid Dynamics and Particle In-Flight Temperature Measurement Using a High-Speed IR Camera" by Ms. Aleksandra Nastic and Dr. Bertrand Jodoin, Cold Spray Research Laboratory, University of Ottawa.

The *Journal of Thermal Spray Technology* Volume 27 Best Paper Honorable Mention

"Novel Method of Aluminum to Copper Bonding by Cold Spray" by Mr. Si-Lin Fu, Dr. Cheng-Xin Li, Mr. Ying-Kang Wei, Dr. Xiao-Tao Luo, Prof. Guan-Jun Yang, and Prof. Chang-Jiu Li, School of Materials Science and Engineering, Xi'an Jiaotong University; and Prof. Jing-Long Li, School of Materials Science and Engineering, Northwestern Polytechnical University.

The international committee of judges, led by Dr. Jiri Matejicek, chair of the *Journal of Thermal Spray Technology* Best Paper Subcommittee, is as follows: Andrew Siao Ang, Emine Bakan, Kirsten Bobzin, Jose Colmenares-Angulo, Frank Gaertner, Ashish Ganvir, Sarka Houdkova, Tanvir Hussain, Anup Keshri, Ondrej Kovarik, Anand Kulkarni, Chengxin Li, Jie Li, Rogerio Lima, Javad Mostaghimi, Radek Musalek, Kazuhiro Ogawa, KeeHyun Park, Shiladitya Paul, Pavel Rohan, James Ruud, Richard Schmid, Ramachandran Chidambaram Seshadri, Igor Sevostianov, Atin Sharma, Kentaro Shinoda, Karel Slamecka, Pawel Sokolowski, Mahder Tewolde, Richard Trache, Anirudha Vaidya, Alfredo Valarezo, Federico Venturi, Petri Vuoristo, Guan-Jun Yang, and Lei Zuo.

J Therm Spray Tech (2018) 27:1491–1517
https://doi.org/10.1007/s11666-018-0787-y

PEER REVIEWED

Evaluation of Heat Transfer Transport Coefficient for Cold Spray Through Computational Fluid Dynamics and Particle In-Flight Temperature Measurement Using a High-Speed IR Camera

A. Nastic[1] · B. Jodoin[1]

Submitted: 20 August 2018 / in revised form: 16 October 2018 / Published online: 12 November 2018

Abstract This work aims at obtaining experimental particle temperature readings during the cold spray (CS) process using a high-speed, high-definition infrared (IR) camera for multiple gas stagnation parameters to infer the suitability and accuracy of Nusselt number and drag coefficient correlations widely used in CS modeling. Measured particle temperatures are compared with values obtained through numerical modeling. Measured particle velocity using recorded data from the IR camera, based on particle streak and particle tracking velocimetry methods, is compared to values obtained from simulations. Additionally, particle velocities acquired using a Cold Spray Meter are also considered. Results demonstrate that only one of all common Nusselt correlations typically used in CS modeling results in accurate particle temperature predictions. Furthermore, the study shows that the drag coefficient correlation must incorporate the particle Mach number in order to provide acceptable particle velocity predictions.

Keywords cold spray · heat transfer transport coefficient · IR camera · particle temperature

List of symbols

Particle/gas interactions

a_1, a_2, a_3	Drag coefficient constants (–)
A_p	Particle cross-sectional area (m^2)
A_{sp}	Particle surface area (m^2)
C_1, C_2	Sutherland constants $\left(kg/ms\,K^{1/2}\right)$, (K)
c	Gas local speed of sound (m/s)
C_D	Drag coefficient (–)
$C_{p(g,f)}$	Gas specific heat at constant pressure evaluated at film temperature (kJ/kg K)
$C_{p,g}$	Gas specific heat at constant pressure (kJ/kg K)
$C_{p,w}$	Gas specific heat at constant pressure evaluated at particle surface temperature (kJ/kg K)
C_p	Particle specific heat at constant pressure (kJ/kg K)
C_v	Particle specific heat at constant volume (kJ/kg K)
d_p	Particle diameter (m)
F_b	Body force (N)
$f_{correction}$	Nusselt number correction factor (–)
$\bar{h}$	Average convective heat transfer coefficient ($W/m^2\,K$)
k_B	Boltzmann's constant (J/K)
$k_{g,f}$	Gas thermal conductivity evaluated at film temperature (W/m K)
K_n	Knudson number (–)
k_r	Gas thermal conductivity evaluated at recovery temperature (W/m K)
m_p	Particle mass (kg)
M_p	Particle Mach number (–)
$\overline{Nu}$	Nusselt number (–)
R_g	Gas constant (J/kg K)
Re_∞	Gas free stream Reynolds number (–)
Re_p	Particle Reynolds number (–)
S_M	Additional momentum source term (kg/m s)
S_T	Additional energy source term (J)
T_f	Film temperature (K)
T_g	Gas temperature (K)

✉ A. Nastic
[redacted]

[1] Cold Spray Research Laboratory, University of Ottawa, Ottawa, ON, Canada

T_p	Particle temperature (K)
T_r	Recovery temperature (K)
V_g	Gas velocity (m/s)
V_p	Particle velocity (m/s)
μ_g	Gas dynamic viscosity (Pa s)
$\mu_{g,f}$	Gas dynamic viscosity evaluated at film temperature (Pa s)
μ_w	Dynamic viscosity evaluated at particle surface temperature (Pa s)
ρ_g	Gas density (kg/m^3)
$\rho_{g,f}$	Gas density evaluated at film temperature (kg/m^3)
ρ_w	Gas density evaluated at particle surface temperature (kg/m^3)
Bi	Biot number (–)
d	Gas molecule diameter (m)
$\mathcal{M}$	Gas molecular weight (kg/mol)
$\mathcal{N}$	Number of gas molecules per mole constant (1/mol)
Pr	Prandtl number (–)
r	Recovery factor (–)
γ	Ratio of specific heats (–)

Radiation principles

C_3,C_4	First and second radiation constants (W m^2), (m K)
E_a	Emitted infrared energy by the atmosphere (W/m^2)
E_g^B	Radiation emitted from a blackbody at the surrounding temperature (W/m^2)
E_{mean}	Mean radiance emitted (W/m^2)
E_p^B	Radiation emitted by a blackbody at the particle temperature (W/m^2)
E_p	Emitted infrared radiation by the particle (W/m^2)
E_r	Emission of the surroundings reflected by the particle (W/m^2)
E_{ref}^B	Blackbody emitted energy at the atmospheric temperature (W/m^2)
$E_{\lambda b}$	Blackbody spectral emissive power (W/m^2)
$E_{\lambda p}$	Spectral electromagnetic radiation emitted by the particle (W/m^2)
W_{tot}	Total infrared radiation captured by the IR camera (W/m^2)
α_g	Surrounding gas transmittance (–)
ε_p	Particle emissivity (–)
$\varepsilon_{\lambda,T}$	Hemispherical spectral emissivity (–)
λ_1,λ_2	Specified wavelengths (μm)
$\tilde{\lambda}$	Intermediate wavelength (μm)
B,F, R	Plank's law parameters (–)
P	Gas static pressure (Pa)
T	Temperature (K)
t	Time (s)

Introduction

Cold spray (CS) uses a converging/diverging nozzle to accelerate a gas (usually nitrogen, helium or air) to the supersonic regime (Ref 1). Metallic particles are injected in the flow and propelled to velocities ranging between 300 and 1200 m/s (Ref 2, 3). During their flight inside the nozzle, the particles also exchange energy with the propellant gas, resulting in particles having temperatures below their melting point throughout their flight (Ref 4, 5). Upon impact with the substrate, up to 90% of the in-flight particle's kinetic energy is converted into heat (Ref 6-8), while the remaining is converted into viscoelastic deformation and elastic energy. Substrate temperature and properties such as hardness and roughness can easily be measured/monitored, allowing for a direct observation/correlation of their influence on the deposition process. Accuracy of models simulating the heat transfer between substrate and gas flow has been validated by many using experimental data, which have led to understanding the contribution of substrate preheating on coating deposition processes (Ref 9-11). However, measuring the particle thermal state during its flight and upon impact proves to be technically challenging. Over the years, models have been developed and used to predict the gas flow and particles properties during the CS process (Ref 12-17). These models' accuracy is highly dependent on the assumptions made, which can lead to erroneous conclusions (Ref 18). As an example, the isentropic solution of the gas exit velocity at low stagnation pressure significantly deviates from results obtained through full Navier–Stokes viscous flow solutions as the losses through shocks and viscous effects are not included in the analysis as well as the effect of nozzle geometry (Ref 13, 18). While being a convenient tool for rough estimates, it is too simplistic to accurately describe and predict flow and consequently particle characteristics upon impact (Ref 19). Alkhimov et al. (Ref 20) presented a model which includes the presence of the bow shock at the substrate and the effects of nozzle boundary layer, showing the importance of considering both phenomena to forecast the particle properties at impact. Similarly, Kosarev et al. (Ref 21) developed an analytical model based on empirical equations to describe the gas flow using two-dimensional relations and including the outside supersonic jet flow structure, bow shock and heat transfer processes with the substrate. Despite providing a more realistic estimate of particle flow, both models use complex formulations, which makes them less versatile and reduces their practicality (Ref 18).

Consequently, to optimize accuracy of results, computational fluid dynamics (CFD) has become a widely used

approach to simulate the CS process. Results obtained through CFD such as gas flow pattern and particle velocity have shown good agreement with experimental data (Ref 22-25). Shock-wave structure visualization using Schlieren imaging (Ref 22) and particle velocity measurement using laser light sheet (Ref 24) and laser two-focus velocimetry (Ref 23) have been used to validate CFD results for flow structure and particle velocity.

However, a difficulty arises when trying to measure and model the in-flight particle temperature, required to fully describe the particle behavior. In the CS process, the particle temperature has only been reported on the foundation of theoretical analysis and CFD modeling, without any validation with experimental data. Lack of particle temperature measurement results from technological limitations due to the particle relatively low temperature and high velocity. In thermal spray processes, two-color optical pyrometry for in-flight particle temperature measurement has been used based on the Planck's law of thermal radiation (Ref 26-30). The high thermal emission radiated by the particles heated to or near their melting point allows for suitable detection (Ref 31, 32). Recently, a one-color camera approach has also been developed to provide the radiation spectral analysis of in-flight particles with visual information of both the temperature and velocity distribution of particles within their trajectory in the thermal plasma spray plume (Ref 31). Spectroscopic techniques have also been used to identify and filter the thermal emission of particles in a plasma plume by collecting spectral signature signals of the plume alone (Ref 33). However, classical pyrometric particle temperature measurement can only provide information on particle temperature with reasonable precision above 1200 °C, which is by far superior to the CS stagnation parameters (Ref 34).

The lack of experimental data to support the CFD modeling of particle temperature challenges the reliability and accuracy of the heat transfer analysis and correlations currently used to describe the particle-gas interactions in CS processes. Nusselt number correlations frequently used in CS modeling lack validation for this specific flow configuration. Current calculations are made based on various theoretical assumptions from larger scale applications under different flow regimes. Multiple correlations to express the Nusselt number have been used in other fields to include the effect of either a large Reynolds number (Ref 35), high Mach number (Ref 36) or the boundary layer surrounding the particle periphery (Ref 37). To date, comparisons between existing Nusselt number correlations for CS processes have not been made due to the absence of experimental data required for proper validation.

The main goal of the current work is to initiate efforts to improve the understanding of particle heating process in CS by focusing on the experimental measurement of particle temperature using a high-speed, high-definition infrared imaging technique. In-flight particle temperature measurements in the CS process have never been reported previously. Hence, assessment of such data, even in a limited set such as the one provided by this early initiative, will provide the ability to evaluate the accuracy of the currently used heat transfer correlations subsequently allowing a better understanding of the interactions between particle and gas flow in the CS process in general. To achieve this goal, an infrared camera operating in the mid-wave infrared (MWIR) spectral range (3-5 μm) is used to capture in-flight titanium particle temperature at the exit of a CS nozzle. The recorded data are also used to evaluate the in-flight particle velocity. Those measurements are used to assess the accuracy and precision of the Nusselt and drag correlations typically used in CS CFD studies.

Background

The particles motion and heat transfer processes are influenced by the flow-field characteristics, the particle drag, energy transfer coefficients and the particle properties. In analyzing micron-sized particles traveling conditions in supersonic CS flows, the inertial, rarefaction and compressibility effects must be considered.

Particle Motion

Particle acceleration is obtained by integrating the force balance equation acting on the particle;

$$m_p \frac{dV_p}{dt} = \frac{1}{2} C_D \rho_g A_p \left(V_g - V_p\right)^2 + F_b \quad \text{(Eq 1)}$$

where m_p, V_p, C_D, ρ_g, V_g, A_p and F_b are the particle mass, particle velocity, particle drag coefficient, gas density, gas velocity, particle cross-sectional area and body force, respectively. The body force can include gravity force (Ref 38), thermophoretic force (Ref 39), lift force (Ref 40), electrostatic force (Ref 38) and adverse pressure gradient from the shock wave (Ref 25).

The dependence of the drag resulting from pressure and viscous stresses applied at the particle surface on the magnitude of the particle relative velocity is expressed through the particle Reynolds number (Re_p);

$$Re_p = \frac{\rho_{g,f} |V_g - V_p| d_p}{\mu_{g,f}} = \frac{\text{Inertial forces}}{\text{Viscous forces}} \quad \text{(Eq 2)}$$

where μ_g is the gas dynamic viscosity and d_p is the particle diameter. The subscript f refers to the properties evaluated at the film temperature given by;

$$T_f = \frac{T_p + T_g}{2} \quad \text{(Eq 3)}$$

where T_p and T_g are the particle and gas temperatures, respectively.

Figure 1 shows the effect of increased inertial forces, i.e., increased Reynolds number, on the flow characteristics and the resulting drag coefficient, C_D.

A symmetrical fully attached flow structure is encountered at low Re_p and C_D reaches values up to 200. The laminar symmetrical flow starts to separate from the particle surface as inertial forces increase. Vortices are subsequently generated, which create a lower pressure at the rearward particle zone. Further increase in Re_p leads to vortex shedding. Reynolds number from 1000 to a critical value of 3×10^5 introduces a turbulent wake zone with a laminar separation, which brings the C_D to a constant value of 0.4. Further increase in Re_p leads to a turbulent separation and the wake zone initiation location is moved rearward resulting in a decreased pressure and consequently a lower drag coefficient. This analysis is, however, limited to low-speed incompressible flows. A large number of studies in CS have used a $C_D = f(Re_p)$ to predict particle velocities (Ref 41-44). Others have, however, incorporated the influence of Mach number and compressibility effects (Ref 16, 45-47).

In particle laden flows, the presence of shock patterns near the particle surface resulting from compressibility effects can drastically affect the particle motion (Ref 48). In the current CS study, as particles are injected in the supersonic flow region, compressible effects are expected. The non-dimensional parameter controlling the compressibility factor is the particle Mach number, M_p, defined as;

$$M_p = \frac{|V_g - V_p|}{c} = \frac{|\Delta V|}{\sqrt{\gamma R_g T_g}} \quad \text{(Eq 4)}$$

where c is the gas local speed of sound, γ is the ratio of specific heats, $\gamma \equiv {C_p}/{C_v}$, R_g is the gas constant, and T_g is the local gas temperature. For $M_p \ll 1$, the flow is considered incompressible, while for Mach number above 0.6 significant effect of compressibility is expected (Ref 49). Figure 2 shows the variation of CD with M_p for low and high Re_p.

For low Re_p, the drag coefficient uniformly decreases as a rarefied flow prevails (Fig. 2, line a). The occurrence of rarefaction is related to the Knudsen number, K_n, defined as;

$$K_n = \sqrt{\frac{\pi\gamma}{2}}\left(\frac{M_p}{Re_p}\right) = \frac{\lambda}{d_p} \quad \text{(Eq 5)}$$

where λ represents the mean free path of molecules. For continuum, conventional no-slip boundary condition is found for $K_n \leq 0.01$. In a non-continuum flow, partial-slip condition occurs and leads to three flow regime conditions: slip flow ($0.01 \leq K_n \leq 0.1$), transition flow ($0.1 \leq K_n \leq 10$) and free-molecular flow ($K_n \geq 10$) (Ref 50). Studies have shown that gas–particle interaction in rocket nozzles encounter all described flow regimes (Ref 36, 51, 52). As a result, all flow regimes are expected to occur in similar processes such as in the CS amid the use of a wide particle size range.

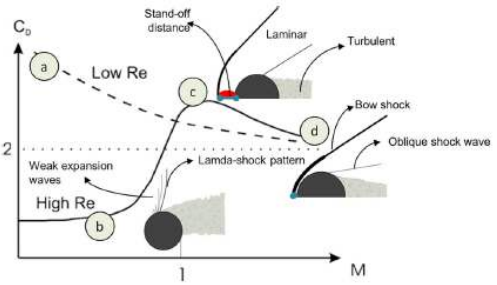

Fig. 2 Drag coefficient dependence on relative Mach number for low and high Re_p ($Re_p > 1.0 \times 10^4$). Insets illustrate the pressure flow structure around the particle for different M_p at high Re_p. The red zone shows the subsonic region created by the bow shock. The standoff distance between the shock and particle surface is also illustrated

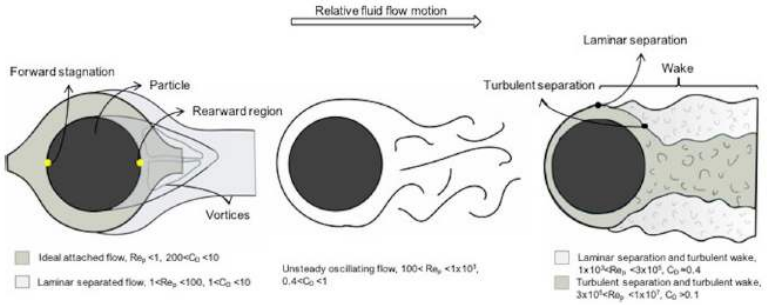

Fig. 1 Illustration of flow characteristics around a spherical particle for increasing Re_p using stream structures. The variation of C_D is also provided. The fluid flows from left to right

As depicted in Fig. 2, at increasing M_p (near 1) and high Re_p, shock-wave structures appear. Weak expansion waves form at the particle surface followed by a lambda shock pattern, while the flow becomes locally supersonic. As a result of boundary layer/shock interactions, flow separation occurs earlier than for incompressible flows and the drag coefficient starts to increase (Fig. 2, point b). When a supersonic M_p is reached, a bow shock forms in front of the particle and the flow separation moves rearward: the drag coefficient increases and reaches a maximum value (Fig. 2, point c). Further increase in M_p brings the bow shock closer to the particle surface, and the following expansion wave further delays the flow separation process. Once the flow reaches the supersonic regime, it stabilizes as the previous general flow instabilities and shock initiations are reduced. Consequently, the drag coefficient decreases and eventually reaches a constant value of 2, unaffected by Re_p for $M_p > 1.5$ (Fig. 2, point d).

Multiple studies have been conducted to ensure that the drag coefficient gives proper representation of the flow field surrounding a particle (Ref 36, 52-56). As such, considerable collection of drag coefficient correlations is available in the literature. However, only a few rely on experimental data and are in a suitable form for computer programming/calculations. In the current study, the Henderson law is used to express the drag in the subsonic, transonic and supersonic relative flow as compressibility effects are of crucial importance in CS (Ref 18, 25, 53, 57, 58). It includes the continuum, slip, transition and molecular flow for M_p numbers up to 6 and for Re_p up to the laminar-turbulent transition. The effect of a temperature gradient on drag is also evaluated (Ref 53). Thermophoretic forces have been shown to arise at the particle surface from the temperature gradient in the continuous surrounding fluid and consequently the kinetic energy gradient from the surrounding molecules. Molecules found at the hot side of the gas are characterized by a higher collision rate than the ones located on the cold side, which results in a net force driving particles from hot to cold temperatures (Ref 50, 59). The Henderson drag coefficient is given as follows;

For $M_p \leq 1.0$, C_{D1};

$$C_{D1} = 24\left(Re_p + S\left(4.33 + \left(\frac{3.65 - 1.53\frac{T_p}{T_g}}{1 + 0.353\frac{T_p}{T_g}}\right) \times \exp\left(-0.247\frac{Re_p}{S}\right)\right)\right)^{-1} + \exp\left(-\frac{0.5M_p}{Re_p^{1/2}}\right)\left(\frac{4.5 + 0.38\left(0.03Re_p + 0.48Re_p^{1/2}\right)}{1 + 0.03Re_p + 0.48Re_p^{1/2}} + 0.1M_p^2 + 0.2M_p^8\right) + 0.6S\left(1 - \exp\left(-\frac{M_p}{Re_p}\right)\right) \quad \text{(Eq 6)}$$

For $1.0 < M_p < 1.75$, C_{D2};

$$C_{D2} = C_{D1}(1.0, Re_p) + \frac{4}{3}(M_\infty - 1)\left(C_{D3}(1.75, Re_\infty) - C_{D1}(1.0, Re_p)\right) \quad \text{(Eq 7)}$$

For $M_p \geq 1.75$, C_{D3};

$$C_{D3} = 0.9 + \frac{0.34}{M_\infty^2} + 1.86\left(\frac{M_\infty}{Re_\infty}\right)^{1/2} \times \left(2 + \frac{2}{S_\infty^2} + \frac{1.058}{S_\infty}\left(\frac{T_p}{T_g}\right)^{1/2} - \frac{1}{S_\infty^4}\right) \times \left(1 + 1.86\left(\frac{M_\infty}{Re_\infty}\right)^{1/2}\right)^{-1} \quad \text{(Eq 8)}$$

where M_∞ = 1.75, $C_{D1}(1.0, Re_p)$ and $C_{D2}(1.75, Re_\infty)$ represent the drag coefficient calculated using Eq 6 and 8, respectively, T_p is the temperature of the particle assumed isothermal, T_g is the temperature of the gas in the free stream, and S is the molecular speed ratio given by;

$$S = M_p\sqrt{\gamma/2} \quad \text{(Eq 9)}$$

In the current work, two other drag coefficients have been used and compared to results obtained from the Henderson correlation. Both of these drag coefficient correlations are used in CS applications to simulate particle velocity (Ref 40, 41, 44, 60, 61). The simplest form of drag coefficient expressed for spheres is defined by Schiller and Naumann (Ref 41) and given by;

$$C_D = \begin{cases} 0.44 & Re_p > 1000 \\ \frac{24}{Re_p}\left(1 + 0.15Re_p^{0.687}\right) & Re_p \leq 1000 \end{cases} \quad \text{(Eq 10)}$$

This relation accounts for any deviation from Stokes law at medium and high Reynolds numbers but disregards the effect of particle relative M_p.

The third evaluated drag model is the relation provided by Morsi and Alexander (Ref 40), which accounts for a particle Mach number greater than 0.4, given by;

$$C_D = a_1 + \frac{a_2}{Re_p} + \frac{a_3}{Re_p^2} \quad \text{(Eq 11)}$$

where the constants, given in Appendix A, apply for smooth spherical particles over a wide range of Re_p number.

Particle Heat Transfer

In transient particle heating encountered in the CS process, the Biot number (the ratio of external convective to internal conductance resistance to heat transfer) is calculated for spherical objects by (Ref 62);

$$Bi = \bar{h}\left(d_p/6\right)/k_p \quad \text{(Eq 12)}$$

where $\bar{h}$ and k_p are the average convective heat transfer coefficient and the thermal conductivity of the particle material, respectively. For Biot number values falling below 0.1, the temperature within the particle can be assumed uniform and the lumped capacitance method (LCM) can be used for the heat transfer analysis, as it has been done in some CS analyses (Ref 5, 57, 63-65). In the current work, the particle diameter is 150 µm and the particle (made of pure titanium) thermal conductivity only varies between 17 and 19.3 W/mK for temperatures between 27 and 727 °C (Ref 66). The approximate calculated average convective heat transfer coefficient using the Nusselt number correlations presented and described further in this section is in the order of 36×10^3 W/m^{2}K. This leads to a Biot number smaller than 0.1. As such, the LCM is considered valid and the energy balance from the first law of thermodynamics yields;

$$m_p C_p \frac{dT_E}{dt} = A_{sp}\bar{h}\left(T_r - T_p\right) \quad \text{(Eq 13)}$$

where m_p, C_p, A_{sp} and T_r are the particle mass, particle specific heat, particle surface area and the recovery temperature, respectively. The recovery temperature represents the gas temperature in the boundary layer surrounding the particle, which can be much higher than the free stream gas temperature due to the viscous heat dissipation effects when compressibility is not negligible (Ref 18, 57). The recovery temperature, T_r, is function of the particle Mach number and is expressed as follows;

$$T_r = T_g\left(1 + r\frac{\gamma - 1}{2}M_p^2\right) \quad \text{(Eq 14)}$$

where r is the recovery coefficient, close to 1 for gases (Ref 18). In the current study, as a laminar flow occurs at the particle front due to a Re_p close to 2000, the recovery factor is found to be expressed as (Ref 67, 68);

$$r = \sqrt{Pr} = \sqrt{\left(\frac{\mu_{g,f} C_{p(g,f)}}{k_{g,f}}\right)} \quad \text{(Eq 15)}$$

The difficulty in predicting the particle temperature in the CS process resides in the uncertainty of evaluating the convection coefficient of the high-speed flow surrounding the particle. Commonly, $\bar{h}$ has been calculated using the non-dimensional Nusselt number ($\overline{Nu}$), which represents the non-dimensional temperature gradient at the surface and is expressed as;

$$\overline{Nu} = \frac{\bar{h}d_p}{k_r} \quad \text{(Eq 16)}$$

The gas thermal conductivity, k_r, is evaluated at the recovery temperature. The gas thermal conductivity is assumed to be only function of temperature and is given as follows (Ref 62);

$$k = \frac{9\gamma - 5}{4}\frac{C_v}{\pi d^2}\sqrt{\frac{\mathcal{M}k_B T_r}{\mathcal{N}\pi}} \quad \text{(Eq 17)}$$

where $\mathcal{N} = 6.022 \times 10^{23}$ molecules/mole is the Avogadro's number, k_B is the Boltzmann's constant, $k_B = 1.381 \times 10^{-23}$ J/K, d is the gas molecule diameter, and $\mathcal{M}$ is the molecular weight.

For forced flow over spherical particles, the Ranz and Marshall correlation (Ref 69) is expressed as:

$$\overline{Nu} = 2 + 0.6Re_p^{0.5}Pr^{0.33} \quad \text{(Eq 18)}$$

where Pr is the Prandtl number and is defined as the ratio of momentum diffusivity over thermal diffusivity. This correlation has been extensively used in the CS field (Ref 18, 41, 60, 70-73). However, it is very general in nature as it only expresses the effect of flow transition and separation encountered in incompressible flows (Ref 62). For a more accurate representation of particle heating experienced during CS, parameters such as the high particle Reynolds number (Ref 35), the boundary layer at the particle surface (Ref 37) and the high Mach number (Ref 36) must be considered in the calculation of the Nusselt number. Compressibility and rarefaction effects at the particle surface affect the flow boundary layer and consequently the heating processes (Ref 74). A few studies of particle traveling in the hot gas flow have used a correction factor along with Eq 18 to account for gas temperature variations in the boundary layer and the non-continuum effect. The correction factor is expressed as follows (Ref 37, 75-77);

$$f_{correction} = \left(\frac{C_{p,g}}{C_{p,w}}\right)^{0.38} \cdot \left(\frac{\rho_g \mu_g}{\rho_w \mu_w}\right)^{0.6} \quad \text{(Eq 19)}$$

where C_p is the specific heat at constant pressure and the subscripts g and w refer to the gas and particle surface, respectively. The specific heat variation with temperature relation is taken as (Ref 78);

$$\overline{C_p} = 39.060 - 512.79\theta^{-1.5} + 1072.7\theta^{-2} - 820.40\theta^{-3} \quad \text{(Eq 20)}$$

where θ = T(K)/100. The change in dynamic viscosity with temperature is expressed using the Sutherland two constant coefficients law given by;

$$\mu = \frac{C_1 T_f^{3/2}}{T_f + C_2} \quad \text{(Eq 21)}$$

where C_1 and C_2 are 1.663×10^{-5}kg/m s $K^{1/2}$ and 273.11 K, respectively. The density in the boundary layer corresponds to the gas density evaluated at the film temperature.

Other studies on CS particle temperature have included the Mach number effect on heat transfer. Multiple modified versions of the Nusselt expression given by Eq 18 exist, which introduce the effect of compressibility, such as;

$$\overline{Nu} = 2 + 0.44 Re_p^{0.5} Pr^{0.33} \exp(0.1 + 0.872 M_p) \quad \text{(Eq 22)}$$

valid only for $M_p > 0.24$ and when the gas temperature is larger than T_p (Ref 5). Another more general correlation that has been used in the CS field is expressed as (Ref 36, 57);

$$\overline{Nu} = \frac{2 + 0.459 Re_p^{0.55} Pr^{0.33}}{1 + \dfrac{3.42 M_p \left(2 + 0.459 Re_p^{0.55} Pr^{0.33}\right)}{Re_p Pr}} \quad \text{for} \quad M_p > 1$$

$$\overline{Nu} = 2 + 0.459 Re_p^{0.55} Pr^{0.33} \quad \text{for} \quad 0 \le M_p \le 1 \quad \text{(Eq 23)}$$

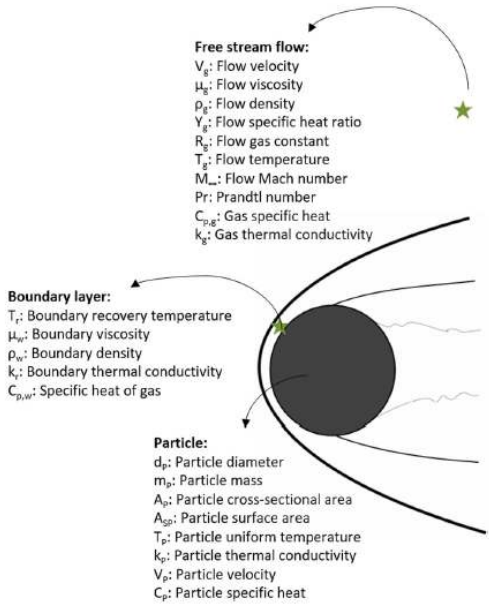

Fig. 3 Illustration of particle and surrounding flow characteristics used to solve the particle heat transfer and motion analysis

where the gas thermal conductivity in the Prandtl number, k_g, is evaluated at the recovery temperature. These account for inertial and rarefaction effects by including both the continuum and transition region Nusselt number expressions.

Figure 3 summarizes the characteristics of the far-field flow, boundary layer and particle in reference to the presented equations. While multiple Nusselt number correlations have been used in CS for particle heat transfer description, lack of a more general correlation to account for all flow phenomena concurrently occurring at the particle surface is still missing. Moreover, as opposed to the case of the drag coefficient, it is yet to be determined if the accuracy of any of the available correlations is acceptable. The procedure described hereafter aims at evaluating these correlations using experimental validation for the CS process.

Experimental Setup

Powder Material

The feedstock powder used in the current study was a commercially pure gas atomized titanium powder with a 45 to 150 µm size (CP Ti Grade 1, Crucible Research, PA, USA). As the original powder exhibits a wide particle size range, the powder has been sieved to collect only particles in the range of 125 to 150 µm. Figure 4 shows the scanning electron microscope (SEM) images of the resulting sieved powder feedstock material, which displays a diameter size of 150 ± 22µm in average with small satellites attached at the particle surface. Due to the manufacturing process, the powder exhibits a spherical shape.

The selected particle diameter in this study has been chosen primarily to facilitate individual particle tracking during temperature readings. It is expected that larger particles with higher mass will travel at lower velocities in the flow (Ref 73) allowing ease of detection by the camera sensor. Studies have evaluated that the particle diameter has an effect on particle temperature and velocity, which consequently affects the coating quality (Ref 19, 79, 80). However, as the current study is not pursuing optimal coating deposition efficiencies or coating characteristics, decrease in particle velocity is of no concern but is rather sought. Additionally, despite having larger particle diameter than the typically sprayed powder size in CS applications ($\sim$ 1 to 100µm (Ref 57, 79-81)), the flow physics and analysis procedure remain the same as the one presented in "Background" section as the particle diameter influence on the particle/gas interaction is scaled through the non-dimensional factors such as M_p, Re_p and K_n.

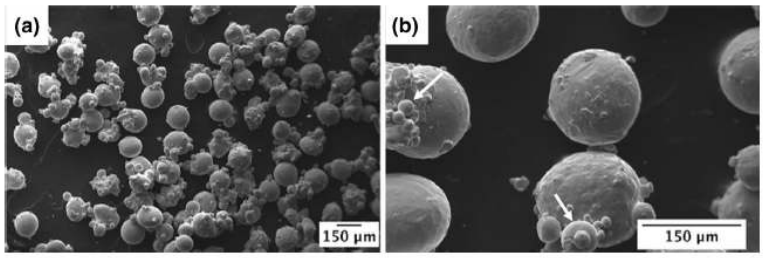

Fig. 4 (a) Sieved spherical titanium powder with final uniform diameter of 150 µm and (b) arrows pointing to satellites

Table 1 Cold spray parameters

Parameters	Test 1	Test 2	Test 3
Gas temperature, °C	200	400	500
Gas pressure, MPa	0.69	0.69	0.69

Cold Spray Details

The cold spraying process was performed with the commercially available EP Series SST Cold Spray System (Centerline (Windsor) Ltd., Windsor, Ontario, Canada). The system runs using a 15-kW heater that can provide a maximum temperature of 650 °C and a maximum operating pressure of 3.45 MPa. A de Laval steel nozzle with a throat diameter of 2 mm and a divergent section length and exit diameter of 120 mm and 6.6 mm, respectively, was used for the current work. The sieved feedstock powder was fed using a commercially available AT-1200HP powder feeder (Thermach Inc., Appleton, WI, USA). The powder feed rate used was limited between 5 g/min to 8 g/min, to reduce the interaction between particles in the flow and facilitate individual particle tracking. All tests were performed without the presence of a substrate. Table 1 presents the stagnation pressures and temperatures for which the particles in-flight temperatures were measured. Nitrogen has been used as the propellant gas for all tests.

To ensure proper particle detection and temperature visualization during the single frame exposure time duration, the particle velocity was reduced to an appropriate level while maintaining high gas temperature to maximize particle heating. To reduce gas exit speed and consequently decrease particle velocity while maintaining a high stagnation temperature and supersonic conditions in part of the nozzle flow, the stagnation pressure was lowered down to 0.69 MPa. As a result, nozzle internal shockwaves are expected to occur, allowing the Mach number and gas velocity to decrease and the temperature to increase prior to the exit (Ref 13). This ensures that the testing conditions encompass as many flow regimes as possible to evaluate the correlations performance throughout these regimes. Stagnation temperature was varied, as shown in Table 1, to obtain particle temperature difference with inlet operating gas temperature. As stated previously, these CS parameters are expected to generate low titanium coating quality as they are far from being optimal for coating production (Ref 4). However, the current study focuses on understanding heat transfer fundamentals at the particle level and obtaining particle temperature readings for model validation, which requires the chosen low spray parameters. Increasing the spray parameters to optimal values would not alter the heat transfer and momentum processes; therefore, the approach of the current study remains valid to the general CS deposition window.

Infrared Camera Setup

In order to measure the in-flight particle temperature as it travels in the flow outside the nozzle, a FAST M2 k high-speed camera has been used (FAST M2 k, Telops, QC, CA). The camera is equipped with an indium antimonide (InSb) MW detector and a narrowband cooled filter. A real-time temperature calibration (RTTC) technique is used as a calibration method. The approach is based on the detected characteristic fluxes (DL/µs units) instead of the in-band radiance or observation of the variation in digital levels and blackbody comparisons used in common calibration techniques (Ref 82). The main advantage of the current calibration method is that it allows taking the integration time implicitly into account, which reduces the quantity of calibration data needed to be stored and acquired. Indeed, with traditional calibration methods, the radiometric characterization is applied using high-accuracy blackbodies over a range of temperature of interest and for all required exposure times, while in the current case, the fluxes represent the sensitivity of the camera readings with respect to the used exposure time. When applying this calibration method, the counts are first converted mathematically into fluxes, which consists of subtracting any count offsets related to circuitry readout present even at zero scene radiance and dividing by the exposure time. The RTTC method can also be applied to nonlinearly increasing detector-counts with integration time by proper modeling

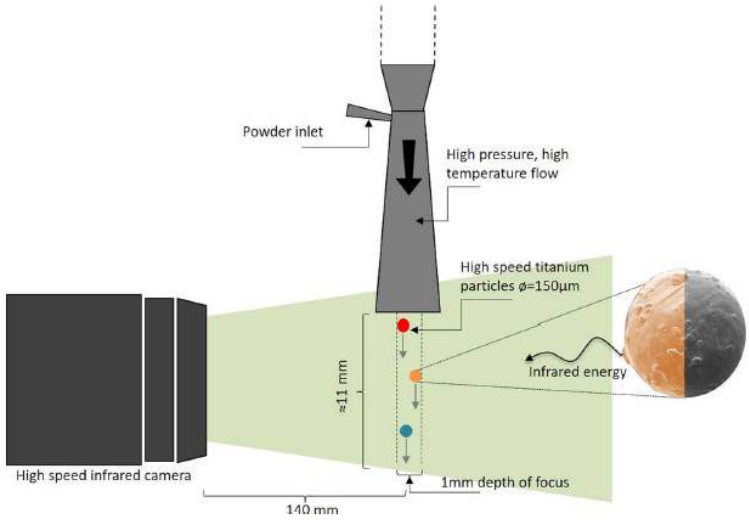

Fig. 5 Cold spray of titanium particles and infrared imaging processes setup for particle surface temperature readings. The camera is positioned to frame both the nozzle exit area and in-flight particles

and parameterization. After the conversion to fluxes, all pixels are made equivalent by applying a pixel-wise offset and gain coefficients, which creates a single flux versus temperature relationship to be used for all pixels and all integration times. Hence, this calibration technique is also capable of adjusting to dynamically modified exposure times. The equations used to describe the instrument response, the radiometric gain and offset coefficients and the residual error can be found in the literature (Ref 82). Moreover, details on the steps required to implement the described calibration method are also provided in the study conducted by Tremblay et al. (Ref 82) and as such details are omitted here for conciseness.

The experimental setup and details are illustrated in Fig. 5. The camera has a 5 µs exposure time, which relates to the integration period used to capture a single frame of data. Its resolution was set to 320 × 16 window with pixel size of 55.6 µm, which are non-optimal but still appropriate to capture and observe the microscale particles in-flight characteristics used in the current study. An acquisition rate of 24,000 frames per second was used to obtain sequences of the spray, which allowed capturing the thermal signature of fast moving particles. The working distance between the far end lens and the gas flow target, set at the center of the flow, was fixed to 140 mm to ensure proper analysis optical window size and resolution. The depth of field at the studied position was of 1 mm. The measurements obtained provide information about the particle mean surface temperature. The particle temperature in the gas flow was measured from the nozzle exit up to a standoff distance of approximately 11 mm. A statistical distribution of temperature with respect to traveling distance was thus obtained. The IR camera provides a precision of ± 1 °C on temperature readings, which has been validated using a blackbody with a corresponding known emissivity of 0.99.

Individual particle in-flight velocity was also measured in the same range of distance from the nozzle exit. The velocity was obtained by means of two separate methods using the recorded IR camera imaging sequences. The first approach consisted of dividing the corresponding particle streak length by the exposure time as similarly accomplished in particle streak velocimetry (PSV) (Ref 83). The streak length is created by the frame superimposition on the image processor caused by particle movement within a single frame of time equal to the exposure time. In the current study, due to the limited powder feed rate, accurate streak lengths were obtained as particle streak overlapping was avoided. The second approach uses the particle position in sequential frames and the time between the corresponding frames to identify the resulting velocities, as analogously performed in particle tracking velocimetry (PTV) (Ref 83). Proper identification and tracking of the same particle need to be ensured between sequential frames in order to obtain the correct characteristic velocity. In the current study, only particles traveling straight within the flow were analyzed as their trajectory could easily be tracked, seen and predicted between frames.

Principles of Temperature Measurements

The radiation energy depends on the analyzed signal wavelength and the object temperature. The

electromagnetic radiation emitted by the particle, $E_{\lambda p}$, at a specific wavelength λ and temperature T, can be expressed using Planck's law;

$$E_{\lambda p}(\lambda, T) = \varepsilon_{\lambda,T} \frac{C_3}{\lambda^5 \left(e^{\frac{C_4}{\lambda T}} - 1\right)} \quad \text{(Eq 24)}$$

where C_3 and C_4 are the first and second radiation constants, respectively, given by;

$$C_3 = 2\pi hc^2 = 3.741771 \times 10^{-16}\ \mathrm{Wm}^2$$
$$C_4 = \frac{hc}{k_B} = 1.438775 \times 10^{-2}\ \mathrm{mK} \quad \text{(Eq 25)}$$

where c is the velocity of light, h is Planck's constant, T is the particle temperature and k_B is the Boltzmann constant. The term $\varepsilon_{\lambda,T}$ is the hemispherical spectral emissivity defined as;

$$\varepsilon_{\lambda,T} = \frac{E_{\lambda p}(\lambda, T)}{E_{\lambda b}(\lambda, T)} \quad \text{(Eq 26)}$$

where $E_{\lambda b}(\lambda, T)$ is the spectral emissive power of a blackbody at the evaluated wavelength and temperature. Moreover, since the used IR camera operates in a specific wavelength range of $\lambda_1 = 3$ and $\lambda_2 = 5\,\mu$m, the mean radiance emitted by the particles between the given wavelength band is;

$$E_{\mathrm{mean}} = \frac{1}{\lambda_2 - \lambda_1} \int_{\lambda_1}^{\lambda_2} E_{\lambda p}(\lambda, T) d\lambda \quad \text{(Eq 27)}$$

Subsequently, as the radiance is continuous with wavelength and according to the intermediate theorem (Ref 84), the emitted energy can be expressed as;

$$E_{\mathrm{mean}} = E_{\tilde{\lambda}} = \varepsilon_{\tilde{\lambda},T} \frac{C_1}{\tilde{\lambda}^5 \left(e^{\frac{C_2}{\tilde{\lambda} T}} - 1\right)} \quad \text{(Eq 28)}$$

where $\tilde{\lambda}$ is between 3 and 5 μm.

The total infrared radiation, W_{tot}, captured by the IR camera comes from multiple sources, which include the emitted and reflected energy by in-flight particles as follows;

$$W_{\mathrm{tot}} = E_p + E_r + E_a \quad \text{(Eq 29)}$$

where E_P is the emitted infrared radiation by the particle, E_r is the emission of the surroundings that is reflected by the particle, and E_a is the emitted infrared energy by the atmosphere. The detected energy is integrated over Δt and at the wavelength band, $\tilde{\lambda}$, typical of the used sensor. In the MWIR spectral region, the atmospheric transmittance is of approximately 90% (Ref 85), which indicates a low absorptivity of incident radiation by the air particles. The diatomic nitrogen molecules are also transparent to the radiation (Ref 86). As a result, a higher radiation emission is seen by the camera sensor from the analyzed object. Hence, the emission from the supersonic nitrogen flow at the nozzle exit, in which the particles are submerged, is also assumed to be transparent as the absorption is almost null at the CS working temperatures (Ref 87). Moreover, Eq 29 can be rewritten as;

$$W_{\mathrm{tot}} = \varepsilon_p \alpha_g E_p^B + (1 - \varepsilon_p) \alpha_g E_{\mathrm{ref}}^B + (1 - \alpha_g) E_g^B \quad \text{(Eq 30)}$$

where α_g is the surrounding gas transmittance, ε_p is the particle emissivity, E_p^B is the radiation emitted by a blackbody at the particle temperature, T_p, E_{ref}^B is the blackbody emitted energy at the atmospheric temperature, and E_g^B corresponds to the radiation emitted from a blackbody at the surrounding temperature, T_g. These terms are also shown in Fig. 6 for the setup of the current study. For sake of clarity and simplicity, Eq 30 is presented such that it disregards the dependence from T and $\tilde{\lambda}$, although these have been taken into account. In addition, if the particles are treated as opaque gray bodies, their reflectivity is given by $\rho_p = (1 - \varepsilon_p)$. In summary, in Eq 30, the term $\varepsilon_p \alpha_g E_p^B$ expresses the emission from the particle captured by the IR camera detector, $(1 - \varepsilon_p) \alpha_g E_{\mathrm{ref}}^B$ is the reflected emission by the particle surface from sources surrounding the particle for $(1 - \varepsilon_p)$ being the particle surface reflectivity, and finally $(1 - \alpha_g) E_g^B$ represents the emission from the atmosphere with $(1 - \alpha_g)$ representing the atmospheric emissivity. As noted earlier, since the atmospheric transmittance, α_g, is approximately 90%, the E_g^B has very little influence on the particle temperature measurement and as a result the entire atmospheric emission has been disregarded in the analysis. Consequently, combining Eq 28 and 30, a semi-empirical Planck's law adaptation with parameters R, B and F can be found to express the detected signal by the IR camera as follows (Ref 84, 88, 89);

$$W_{\mathrm{tot}} = \varepsilon_{\tilde{\lambda}, T_p} \frac{R}{\exp\left(\frac{B}{T_p}\right) - F} + \left(1 - \varepsilon_{\tilde{\lambda}, T_p}\right) \frac{R}{\exp\left(\frac{B}{T_{\mathrm{ref}}}\right) - F} \quad \text{(Eq 31)}$$

where R is function of the integration time and wavelength band, B is function of wavelength only and F is positive with a value close to 1.

Experimental Limitations

Based on the previous discussion on experimental setup and principles of particle temperature measurements, there are several fundamental limitations to successful particle temperature readings using the current high-speed IR camera. If the same optical window size and resolution are kept, a minimum powder size of 150 μm in diameter must

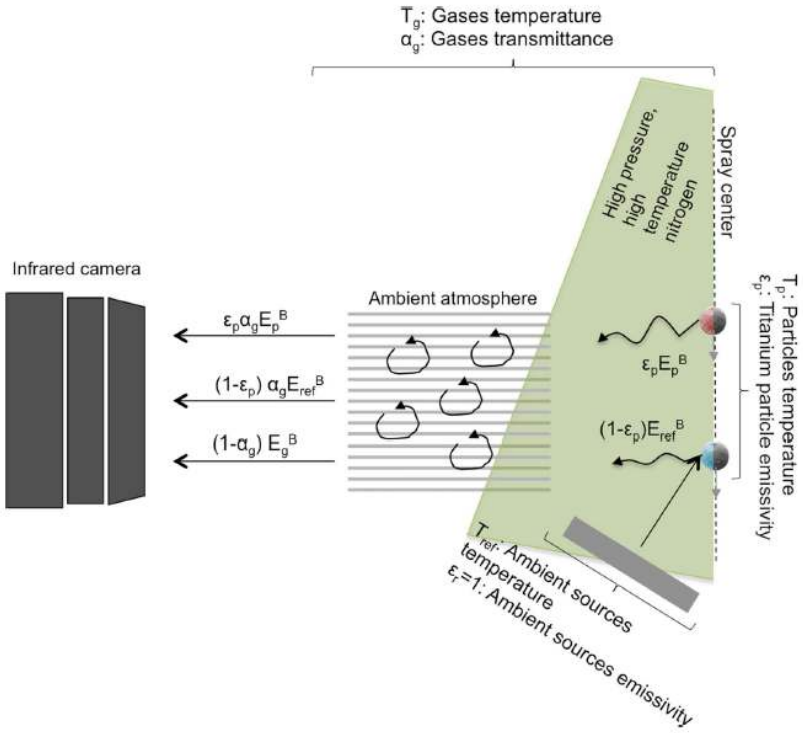

Fig. 6 Radiation received by the IR camera

be used to generate 3 pixels per particle and thus obtain a suitable surface temperature average. The current achievable acquisition rate limits a 150-µm particle velocity to about 225 m/s to ensure proper particle visualization between two consecutive frames. This maximal velocity value also includes the streak lengths that would be obtained during a 5 µs exposure time. Consequently, the CS parameters need to be adjusted to ensure such particle exit maximal velocity. Additionally, this analysis is easiest for spherical particles; however, if irregular particles are to be used, the irregularities must be larger than a pixel size to be visible. In terms of particle material, the limitations are mostly based on material/surface emissivity that must allow detection by the thermal camera sensor in the 3 to 5 µm wavelength range.

Particle Emissivity

The emissivity of pure titanium powder analyzed in the current study has been set to the absorptance, A, measured by Tolochko et al. for the same powder material and size (Ref 90-92). If it is assumed that all surrounding sources enclosing the analyzed particles are at the same temperature, T_{ref}, then based on Kirchhoff's law, the emissivity and absorptivity of the particles are equal in magnitude at any given temperature and wavelength (Ref 62). The absorptance is defined as the ratio of absorbed to incident radiation. Hence, Tolochko et al. have measured the absorptance of pure titanium powder to be 0.77 at a wavelength of 1.06 µm and decreases to 0.59 at a wavelength of 10.6 µm. A reasonable number of studies have measured the spectral emissivity of pure titanium material and oxidized titanium (Ref 93-98). All measured values of spectral emissivity show a slow decrease with increasing wavelength, in accordance with Tolochko et al. work, and a gradual increase with rising temperature, which is generally the rule by which metal emissivity abides (Ref 62, 99). As a linear trend is generally observed for pure titanium emissivity with wavelength up to 10.6 µm, an emissivity of 0.71 is calculated appropriate for the current study given the analyzed MWIR range and based on emissivity boundary values evaluated by Tolochko et al. (Ref 93, 98). In spite of the importance of powder emissivity value, the temperature measurement uncertainty due to powder emissivity value is decreased when the analyzed emitted radiation is reduced to shorter wavelengths (Ref 100). Consequently, any small deviation of emissivity from the chosen value in the current study is expected to result in minimal measured temperature variation.

Cold Spray Meter Setup

The in-flight particle velocity at a standoff distance of 5 mm from the nozzle exit, without the presence of a substrate, has also been measured using a Cold Spray Meter (CSM) eVolution (Tecnar Automation Ltd., St-Bruno, Canada). This technique is widely accepted and used for the measurement of particle velocity of various types and sizes (Ref 3, 25). A continuous laser with an 810 nm wavelength illuminates the particles during their flight. A dual-slit photomask captures the diffracted light from each individual particle as they pass in front the sensor. The signature intensity of diffracted light from each particle is first amplified and filtered before being sent to an internal interpreting system. Subsequently, the velocity of particles is calculated internally by using the traveling distance and time interval between the two mask slits. The device is designed to output particle velocities ranging between 10 to 1200 m/s for particle diameters in the range of 5 to 300 µm. This measuring process has been operated for spray parameters used in Test 1 and Test 3 as they represent the lowest and highest spray parameters, respectively, as shown in Table 1. Consequently, obtained velocity results have been compared to those calculated using the infrared imaging techniques to verify the correctness of particle identification in the latter process and its accuracy. Moreover, the comparison is used to provide possible additional means of measuring particle velocity in CS processes.

CFD Details

Computational Domain

The commercially available Computational Fluid Dynamic (CFD) package ANSYS Fluent 18 software was used to model the gas and particle flow inside and outside the nozzle. A two-dimensional, axisymmetric model was used due to the symmetrical characteristic of the flow, and particles were injected at the symmetry line. Figure 7 shows the full assembly, which includes the nozzle with a throat diameter of 2 mm, an exit diameter of 6.6 mm and a conically diverging length of 120 mm. The boundary conditions used in the current study are summarized in Table 2.

Domain Meshing

The computational domain of the 2D axisymmetric nozzle shown in Fig. 7 has been meshed using ANSYS WB Meshing Tool. The domain has been discretized into separate grids, and edge sizing was used to simplify the control of the meshing process. A structured quadrilateral non-uniform mesh was used, as shown in Fig. 8, as it provides a larger convergence capability. A biased 1.2 growth rate was used on vertical edges to provide higher precision and resolution near the walls.

The selected grid meshing consists of 486,275 elements with mesh quality of minimal orthogonal quality equal to 0.7 and maximum aspect ratio of 30. The grid density allows good accuracy in regions of complex flow phenomenon. The solution is iterated until convergence is reached by demonstrating first a decrease in residuals by at least three orders of magnitude and then by ensuring that the net mass and energy imbalances are below 0.01%.

Governing Equations

Gas Flow

The Navier–Stokes equations for compressible flows have been used to solve the gas stream motion. Mass, momentum and energy conservation have been used as governing equations as follows;

$$\frac{\partial \rho}{\partial t} + \frac{\partial}{\partial x_i}(\rho u_j) = 0 \qquad \text{(Eq 32)}$$

$$\frac{\partial}{\partial t}(\rho u_i) + \frac{\partial}{\partial x_j}(\rho u_i u_j) = \frac{\partial}{\partial x_j}\left[-P\delta_{ij} + \mu\left(\frac{\partial u_i}{\partial x_j} + \frac{\partial u_j}{\partial x_i}\right)\right] + S_M \qquad \text{(Eq 33)}$$

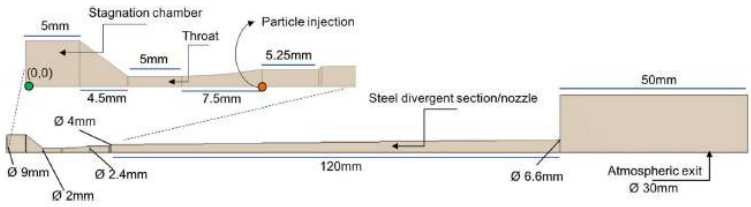

Fig. 7 Computational domain dimensions. The stagnation chamber, converging section and throat are magnified for clarity. Particle downstream injection location on the x-axis is provided in orange, and upstream injection is shown at a (0,0) position in green (Color figure online)

Table 2 Boundary conditions

Location	P	v	T
Nozzle inlet	Specified stagnation	$\frac{\partial v}{\partial n}=0$	Specified stagnation
Surrounding atmosphere	Ambient condition	$\frac{\partial v}{\partial n}=0$	$\frac{\partial T}{\partial n}=0$
Nozzle walls	$\frac{\partial P}{\partial n}=0$	0	$\frac{\partial T}{\partial n}=0$
Symmetrical axis	$\frac{\partial P}{\partial r}=0$	$\frac{\partial v}{\partial r}=0$	$\frac{\partial T}{\partial r}=0$

Fig. 8 Domain meshing details

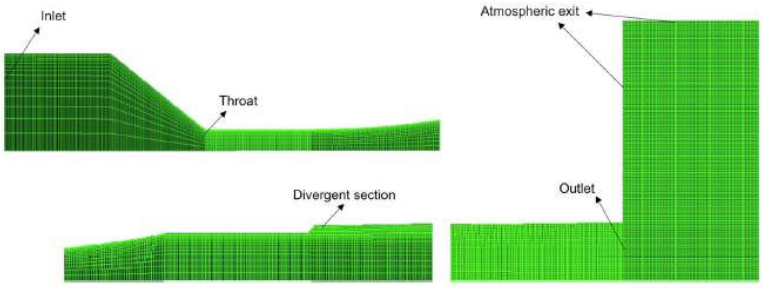

$$\frac{\partial}{\partial t}\left(\rho C_{\mathrm{p}} T\right)+\frac{\partial}{\partial x_j}\left(\rho u_j C_{\mathrm{p}} T\right)=\frac{\partial}{\partial x_j}\left(\lambda \frac{\partial T}{\partial x_j}\right)+S_{\mathrm{T}} \qquad \text{(Eq 34)}$$

where, t, P, Cp, u_i, μ, S_{M} and S_{T} are the time, gas static pressure, specific heat at constant pressure, gas velocity components, dynamic viscosity, additional source terms in momentum and energy equation, respectively. The additional terms (S_{M} and S_{T}) have been neglected since low powder feed rates have been used. These terms are disregarded for high Stokes number, St, and low momentum interaction parameter Π_{mom} (Ref 39). In the current study, given the low particle flow rate, in which the injected particles represent only a minor volume fraction within the nitrogen medium, it is reasonable to assume lack of particle–particle interaction. Hence, the particle phase has been simulated through a Lagrangian process as an inert point in space. Similarly, the gas phase momentum is not affected by the presence of particles due to the very small particle loading encountered in the current study and commonly in general CS applications. A pressure-based solver with a Green-Gauss node-based gradient method has been used to simulate the nitrogen flow. In addition, a second-order accuracy spatial discretization was used to model the pressure while a QUICK scheme has been set to solve the density and momentum equations.

Gas Properties Hypotheses

To account for compressibility effects, the ideal gas law is used. The compressibility factor of nitrogen for pressures and temperatures up to 10 MPa and 627 °C, respectively, exhibit only a deviation of less than 4%, which supports the use of the ideal gas assumption (Ref 78). A two-coefficient temperature-dependent Sutherland law is used to account for viscosity variation with temperature, which has been demonstrated to be important in high-speed compressible flows (Ref 46, 63).

Turbulence Model

Due to the high velocity of the supersonic flow, inertia forces are expected to dominate the viscous dissipation effects, which would lead to a high resulting Reynolds number. As a consequence, the flow was assumed to be turbulent. Most turbulence models used to simulate the gas flow in the CS process are based on the closure of the Reynolds Averaged Navier–Stokes (RANS) equations. Models such as the standard k-ε (Ref 24, 57), the RNG k-ε (Ref 13, 45, 58), the realizable k-ε (Ref 25), the RSM, the SST k (Ref 22), the Spalart–Allmaras (Ref 14), the compressibility modified k-ε (Ref 44), the thermally modified k-ε (Ref 41, 101) and the multi-phase modified k-ε (Ref 102) have been used in the simulation of the CS process. In the current study, the RNG k-ε model has been chosen, as it has proven to significantly improve accuracy and precision in calculating the flow structure (Ref 18).

Discrete Phase Coupling

The titanium particle phase was injected in the nozzle domain near the throat section, as illustrated in Fig. 7, parallel to the CS flow stream. The forces and heat transfer

Table 3 Simulated phases properties

Property	Nitrogen flow	Titanium particle (∅ = 150 μm)	Copper particle (∅ = 15 μm)
CS parameters	N/A	0.69 MPa, 200 °C/400 °C/500 °C	3.45 MPa, 650 °C
Injection location	N/A	Downstream	Downstream and upstream
Density, kg/m^3	Ideal gas	4850	8978
Specific heat capacity, J/kg K	1040.67	544.25	381
Thermal conductivity, W/mK	0.0242	18	387.6
Viscosity, kg/ms	Sutherland law	N/A	N/A
Initial velocity, m/s	0.1	0	0
Initial temperature, °C	25	25	25

from the continuum applied to the particle surface were calculated using Newton's balance equation and the lumped capacitance method as described in "Background" section. The drag coefficients expressed using Eq 10 and 11 have been selected within the Fluent software interface. However, the drag equation described using Eq 6 to 9 has been separately programmed using C language through Visual Studio, subsequently compiled in Fluent solver and attached as a user-defined function. Similarly, the entire heat transfer analysis, described by Eq 12 up to Eq 23, has been written in C programming language and dynamically loaded as a build in user-defined function. Table 3 presents the material properties used to simulate the experimentally conducted downstream injection spray of the titanium particles. A one-way coupled Lagrangian approach was chosen to solve the particle-related equations based on the local gas properties.

In addition to the titanium particle downstream injection model, two additional simulations have been performed. Both have been conducted using regular spray parameters consisting of high inlet stagnation pressure and temperature of 3.45 MPa and 650 °C as well as common powder particle size and material used in the CS community to obtain proper particle deposition. The injection of a single 15 μm copper particle was first made downstream, at the location illustrated in Fig. 7, and the second simulation was conducted for upstream injection at the domain inlet. The copper particle material and size have been selected as they are most widely used in the CS field. The material properties for all simulations as well as details of spray parameters and powder injection location are given in Table 3. The copper particle velocity has been simulated using all three presented drag coefficients using Eq 6 to 9, Eq 10 and 11. Similarly, to obtain in-flight particle resulting temperature, all four Nusselt expressions have been tested (Eq 18, 19, 22 and 23).

The main purpose of the high spray parameters simulations is to evaluate the temperature error caused if less accurate correlations are used for a high deposition CS parameter process. Although the correct and most accurate correlations have already been found with the conducted tests using large titanium particles, the significance of the error encountered during high deposition spray parameters is of upmost relevance for a wide range of applications and thus its evaluation is crucial.

Results and Discussion

CFD General Flow

Figure 9 shows the gas temperature and velocity contours in the converging/diverging nozzle and nozzle exit vicinity section for stagnation temperature conditions presented in Table 1. When the inlet stagnation temperature is 200 °C, the maximal gas temperature and velocity reached within the diverging nozzle section correspond to 187 °C and 827 m/s, respectively. The lowest temperature of − 129 °C is reached 0.0285 m after the throat in the supersonic region at a flow Mach number of 3.33. For the case of an inlet stagnation temperature of 400 °C, the maximal temperature and velocity of the gas in the diverging section are 377 °C and 985 m/s, respectively. At 0.0285 m, the temperature reaches only − 66 °C at a region with a Mach number of 3.37. Similarly, for the case of a 500 °C inlet temperature, the gas reaches 477 °C and 1060 m/s in the diverging section of the nozzle. The lowest temperature after the throat reaches − 35 °C at a flow Mach number of 3.36.

The model also predicts the occurrence of a shock train initiated approximately 70.75 mm from the powder inlet location. Once the flow is at M = 2.5, the acceleration process is suddenly interrupted. As the pressure ratio is much lower than the pressure ratio for which the nozzle is designed, a shock wave is induced (with reflections also being generated) to reach and recover the ambient pressure at the nozzle exit. This occurrence is the main advantage of utilizing low inlet stagnation pressure as it forces particles

J Therm Spray Tech (2018) 27:1491–1517 1505

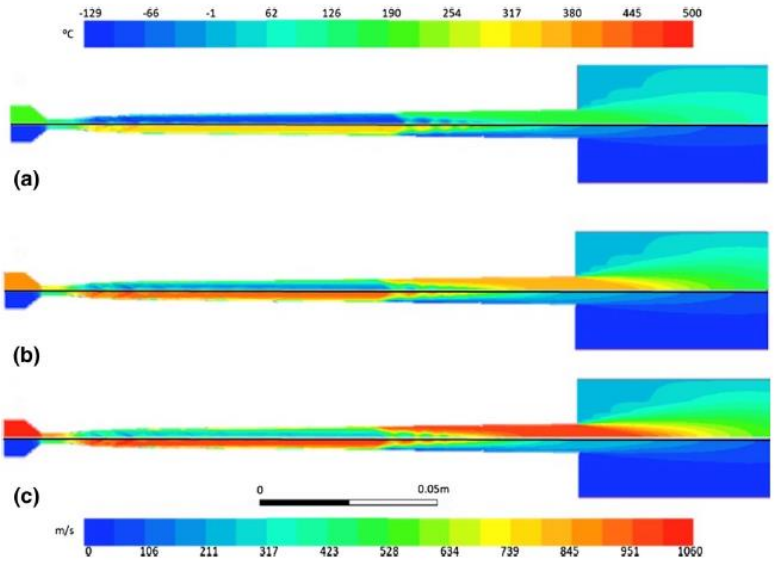

Fig. 9 2D axisymmetric model of nitrogen flow velocity (bottom) and temperature (top) contours in the diverging/converging section and atmospheric outlet for an inlet pressure of 0.69 MPa and gas stagnation temperature of (a) 200 °C, (b) 400 °C and (c) 500 °C

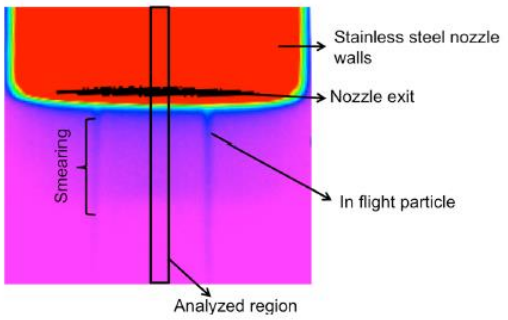

Fig. 10 Large IR camera view of the entire nozzle and in-flight particles exiting during spray showing the testing setup. For particle velocity and temperature measurements, the IR camera has been set to only view and analyze the region delineated by the rectangle

to heat up and slow down prior to the exit, which is crucial for the current study to cover all complex flow regimes encountered in CS.

Particle Velocity

Experimental Measurements

Figure 10 gives details of the analyzed region for particle temperature and velocity measurements. The shown zone has been taken with an exposure time of 50 µs, in which two particles are seen to exit the nozzle. The IR camera view for subsequent particle characteristics measurements (temperature and velocity) is delineated by the rectangular shape. As mentioned previously, during particle velocity and temperature readings, a section of the nozzle and the exit particle laden flow are both seen by the IR sensor.

The individual particle velocity measurement procedure using the particle visualization across two subsequent frames in the analyzed region, at different stagnation temperatures, is shown in Figure 11. The analyzed region is 17.74 mm by 0.83 mm, which includes 6.62 mm of nozzle length and 11.12 mm of nitrogen particle laden flow length outside the nozzle, as depicted also in Figure 10. Particle shape and position are easily discernable and position readings have been made either at the particle rear end or front surface. The time interval between two successive frames corresponds to 41.5 µs.

Results indicate particle velocity of 175 ± 28, 179 ± 17 and 194 ± 16 m/s for gas stagnation temperatures of 200, 400 and 500 °C, respectively. As seen, the measurements have been taken for particles without or slight trajectory deviations in the flow, which renders the particle velocity readings between subsequent frames possible and accurate. Moreover, the obtained images confirm low particle feeding rate required to have low particle loading effect on the gas flow. A low particle density in the flow along with short duration time between two images is needed for this method to accurately provide

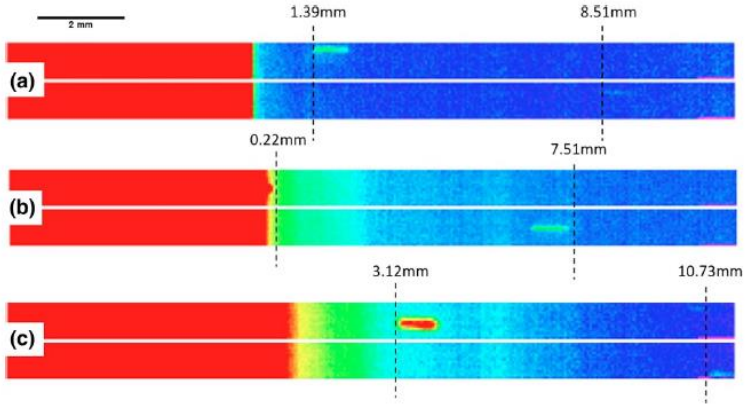

Fig. 11 Particle velocity measurement using the PTV procedure between two consecutive frames for stagnation gas temperature of (a) 200 °C, (b) 400 °C and (c) 500 °C. Results indicate a velocity of (a) 172 m/s, (b) 176 m/s and (c) 184 m/s for the illustrated particles. A scale is provided at the top left corner

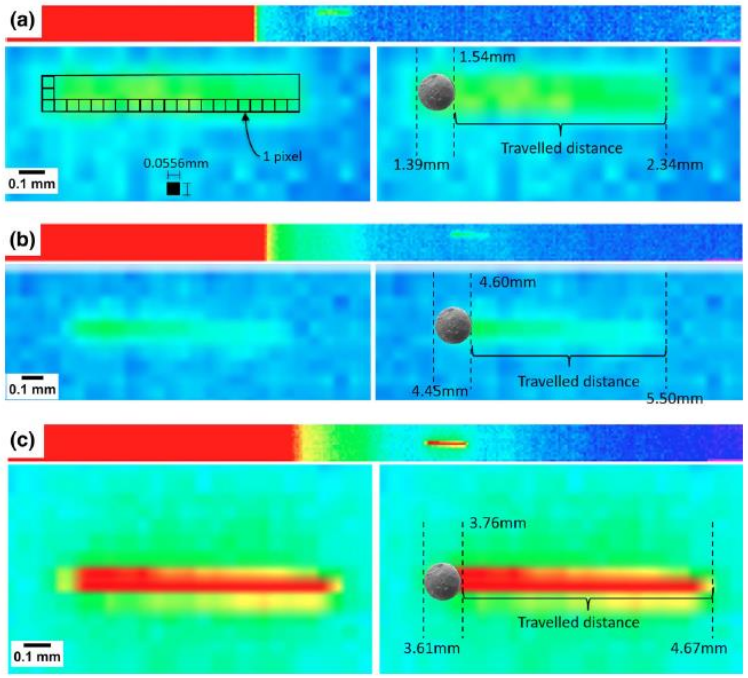

Fig. 12 Particle velocity measurement using the PSV procedure obtained under a 5 µs exposure time for stagnation gas temperature of (a) 200 °C, (b) 400 °C and (c) 500 °C. Results indicate a velocity of (a) 160 m/s, (b) 180 m/s and (c) 182 m/s for the illustrated particles. A particle diameter of 150 µm was assumed. The pixel size and resulting error that can occur in measurement due to the pixel resolution is also illustrated in (a)

velocity measurements. Results show that the large titanium particles reach higher kinetic energy at higher stagnation temperatures, which is in accordance with gas dynamic principles.

Figure 12 shows the results of particle velocity measurement through streak analysis. In contrast to the PTV method, the PSV is capable of providing velocity data as a function of distance from nozzle exit as the streak length is measured locally. Results indicate a velocity of 153 ± 27, 169 ± 26 and 183 ± 47 m/s for gas stagnation temperatures of 200, 400 and 500 °C, respectively. Additionally, measurements show that the velocity within a distance of approximately 11 mm from the nozzle exit is kept constant across the spray plume for all three tested stagnation

temperatures. A particle diameter of 150 μm was used for the calculations, which can lead to minor deviations in PSV measurements as the actual diameter might slightly differ from the average. Moreover, increased particle blurriness based on the particle pixel definition can also lead to small errors.

The particle velocities measured through the CSM, the PTV and PSV method using the IR camera, from the nozzle exit up to 11 mm downstream, are compared in Fig. 13 for the cases of stagnation temperatures of 200 and 500 °C. The results are represented using a box and whisker plot. A large range in velocities is observed for results obtained using the CSM, which is mainly associated with the broadness of the analyzed region. Slower particles found at the flow boundaries and smaller faster particles located in the center of the stream are both detected by the CSM while they are outside of the IR scope and its associated depth of focus. Although results obtained using the CSM show a large scatter, the median correlated with the average size particle velocities is compared with the PTV and PSV methods for future correlations with CFD results. At a gas stagnation of 200 °C, the particle average velocity is measured to be 183 ± 32, 164 ± 24 and 153 ± 27 m/s when measured using the CSM, IR PTV and IR PSV methods, respectively. At 500 °C, the average reaches 195 ± 54, 177 ± 17 and 169 ± 31 m/s under the analysis using the CSM, IR PTV and IR PSV, respectively.

Particle speeds obtained through the PSV method at both stagnation temperatures show the largest decline in median values when compared to the velocities obtained using the CSM and PTV technique. An approximate difference of 36 and 23 m/s occurs between the average for particles traveling in a gas of 200 and 500 °C stagnation temperatures, respectively. All three techniques include an uncertainty related to the measurement process principle they use. Both the CSM and PTV methods rely on the measurement of particle distance traveled within the flow under a specific time. Consequently, both methods include, although being very small, intrinsic errors associated with particle path deviation. The CSM includes a pattern recognition analysis that allows only particles that deviate from their traveling path by an angle less than 10° to be properly detected, which provides increased particle velocity measurement accuracy. Similarly, due to the visual aspect of the PTV velocity evaluation process, particle with perceivable angular position can be eliminated from the analysis. In addition, the PTV process includes some uncertainty arising from the difficulty of assuring that the same particle is being tracked between subsequent measuring steps, which could also be an existing problematic for the CSM. For the PSV process, as stated previously, errors associated with any deviation from the used average particle diameter size leads to measurement inaccuracies. As reported in Fig. 12, a single square pixel has a size of 0.0556 mm, which would lead to a particle diameter precision of ± 27.5 μm. Additionally, the velocity precision obtained through the PSV method is also highly dependent on the IR camera pixel resolution, as illustrated in Fig. 12, which would result in a velocity precision of ± 5.5 m/s.

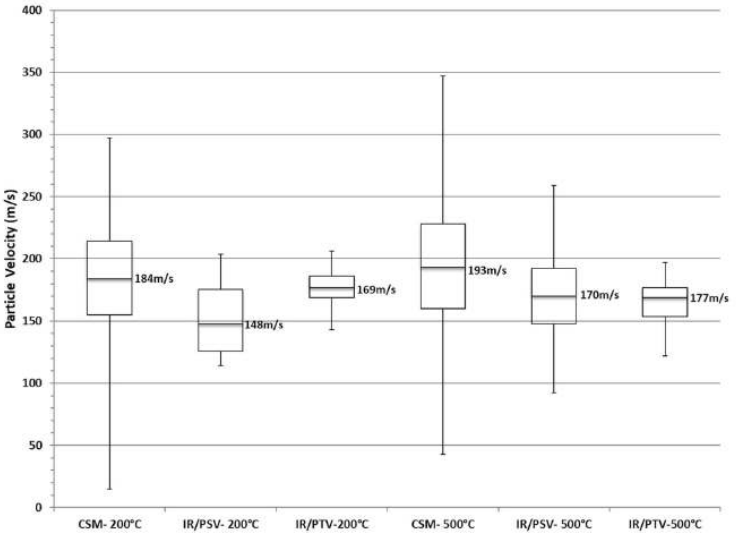

Fig. 13 Comparison between particle velocity measurements obtained using the IR camera and the CSM at stagnation temperatures of 200 and 500 °C. Median values for all three tests are provided directly on the graph

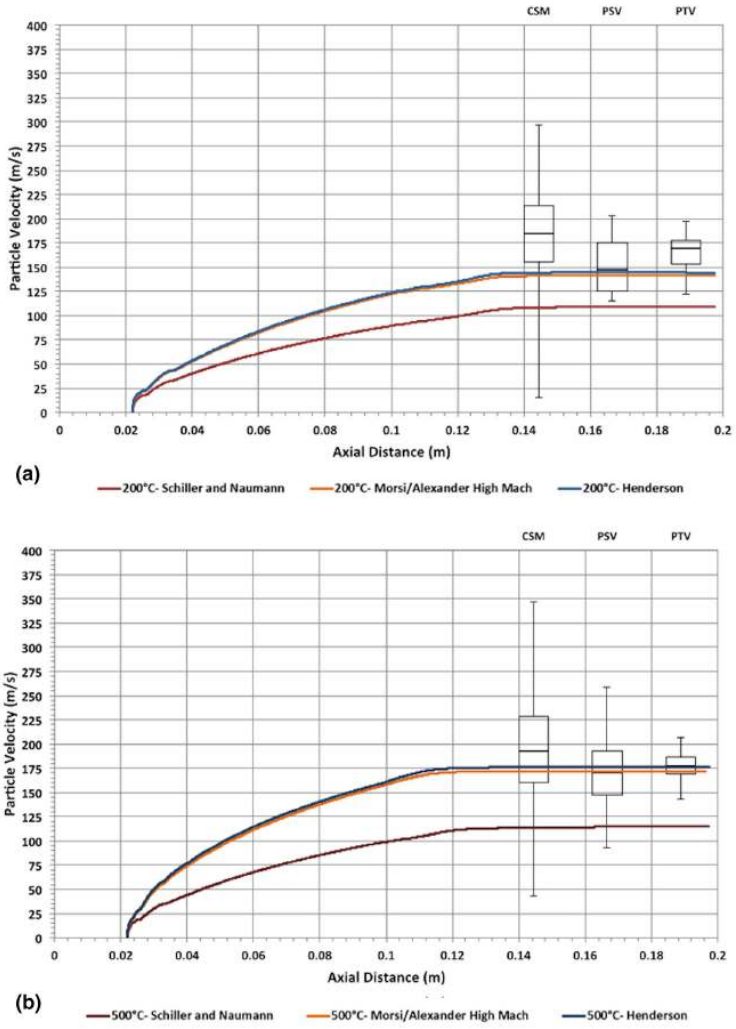

Fig. 14 Drag coefficient equation confirmation by comparison with particle experimental velocity measurements

Numerical Results

The momentum transfer from the CS nitrogen flow to the titanium particles is dependent on the drag coefficient, as described previously. Figure 14 gives the simulated particle velocity from the injection point up to the end of the numerical domain boundary at 0.20 m for three different drag coefficients at stagnation temperatures of 200 and 500 °C. Experimental results obtained using all three particle velocity measurement procedures have been used to validate the drag coefficient relation for the current flow simulation and consequently the CFD model description. The drag described by Schiller and Naumann (Eq 10), which is already implemented in the Fluent interface, leads to the lowest particle velocity. The model is derived from experimental data and provides means of calculating particle velocity for Re_p number ranging between 10^{-3} and 10^4. However, it lacks to include the influence of the particle M_p and as a consequence the velocities obtained are 107 and 115 m/s for tests conducted using a stagnation

J Therm Spray Tech (2018) 27:1491–1517 1509

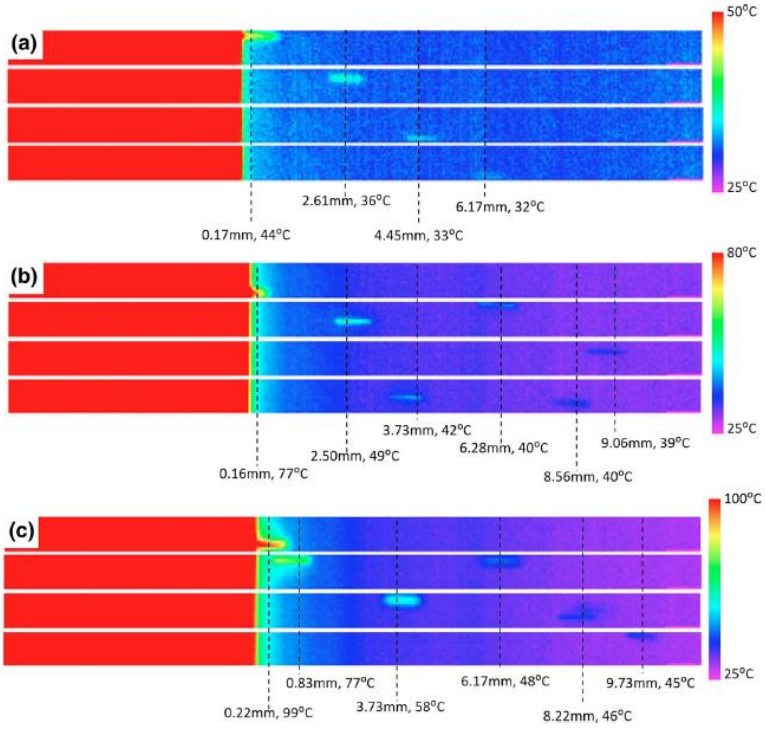

Fig. 15 Particle temperature measurement after the nozzle exit during CS at a stagnation temperature of (a) 200 °C, (b) 400 °C and (c) 500 °C. Individual particle location and temperature within the gas flow at the nozzle exit are provided

temperature of 200 and 500 °C, respectively. The second tested C_D correlation is also included in Fluent and is based on the correlation given by Morsi and Alexander that integrates a correction factor to account for a M_p greater than 0.4 (Eq 11). The obtained velocities are much higher than the ones resulting from the Schiller and Naumann and as a result are much closer to the experimental values. For gas stagnation of 200 and 500 °C, the simulated resulting velocities are 141 and 173 m/s, respectively. The last correlation given by Henderson, which is presented in detail in "Particle Motion" section, has been implemented separately through a user-defined function (UDF). Values attained are similar to results obtained with the drag coefficient correlation developed by Morsi and Alexander. Simulated particle velocity values reach 145 and 176 m/s for inlet gas temperature of 200 and 500 °C, respectively. Both correlations that include the influence of the relative Mach number provide an acceptable particle speed value when compared to experimental results. Consequently, the necessity to use a C_D coupled with the M_p values is of upmost importance. Additionally, based on results presented in Fig. 14, the PSV method seems to provide the most accurate and precise particle velocity reading. The large data deviation in the CSM particle velocity results lowers its precision and consequently prohibits any direct comparison to be made with the CFD calculated values since a velocity value for a single particle diameter is sought in the current study.

Furthermore, the particle velocity stays constant throughout its travel in the CS plume although the gas reaches speed values below particle velocity. The higher mass and consequently larger inertia of the titanium particles used in the current study hinder rapid particle deceleration although the gas velocity reaches values as low as 75 m/s for both tested gas stagnation temperatures at a position of 0.18 m.

Particle Temperature

Experimental Measurements Analysis and Effect of Nozzle Reflected Temperature

During particle temperature measurements, few particles have been simultaneously observed in a single frame due to the low selected feeding rate, as shown in Fig. 15. For all cases, the highest recorded particle temperature is measured

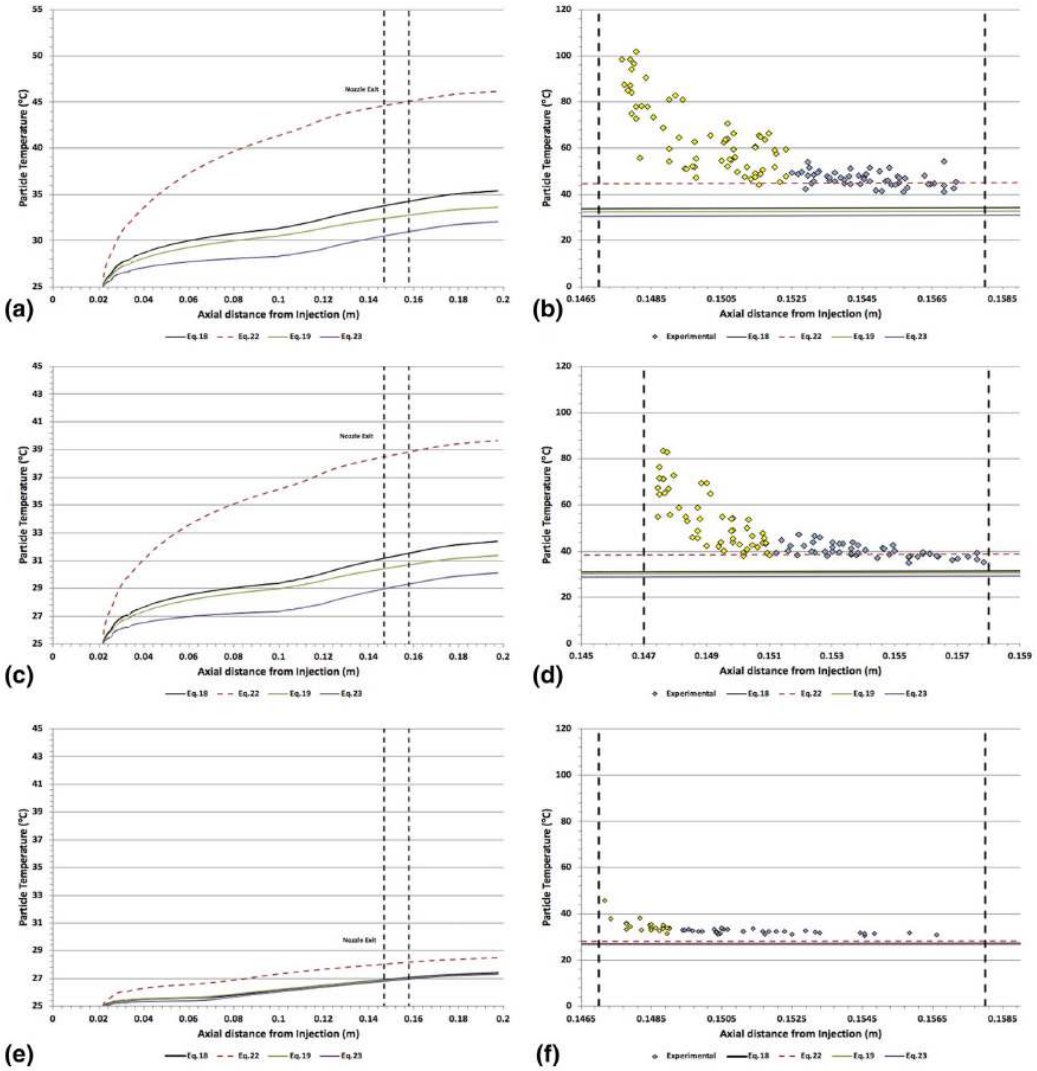

Fig. 16 For gas stagnation temperatures of 500 °C (a, b), 400 °C (c, d) and 200 °C (e, f), the particle simulated and measured temperatures after the nozzle exit are provided. Dotted lines indicate the region analyzed using the IR camera. Plots on the left (a, c, and e) show the general trend of simulated particle temperature after injection calculated using all four Nusselt equations. Plots on the right (b, d and f) provide a comparison between simulated and measured particle temperature in the zone analyzed by the IR camera (within the dotted region). The excluded measurements affected by the nozzle reflected temperature are highlighted in yellow (Color figure online)

near the nozzle exit with approximate values of 44, 77 and 99 °C for gas stagnation temperatures of 200, 400 and 500 °C, respectively. These temperatures are decreasing until reaching a constant value in the observation zone after a distance that is function of the stagnation temperature, as shown in Fig. 15. These constant temperature values reach 32, 39 and 45 °C at a gas stagnation temperature of 200, 400 and 500 °C, respectively. The measured decreasing particle temperature trend is physically impossible as the simulated gas temperature remains at a constant and higher temperature than the particle surface throughout the experimentally visible section, as shown in Fig. 9.

To explain the decreasing particle temperature process from the exit to the near nozzle exit region of the zone

observed using the IR camera, the concept of reflected temperature is used. The notion of reflected temperature is based on the effect of steel nozzle wall temperature onto the particle reflected energy. The closer the particle is to the exit, the higher is the effect of reflection from the nozzle. However, due to the CS process nature, i.e., high-speed and high-temperature exit gas flow and particle surface size, the measurement of reflected temperature from the nozzle onto the particle surface is particularly difficult to measure. Hence, in the current study, this measurement has been omitted and particle temperature readings obtained far from the nozzle exit have been taken as representative and accurate of the particle current temperature. In accordance with Eq 31, particles found near the nozzle exit experience a high T_{ref} value, which increases the signal detected by the IR camera from the in-flight particles. As stated, since the reflected temperature value is hard to measure, the true particle temperature, T_p, is consequently hard to evaluate. However, it is expected that particles found far enough from the nozzle exit experience a room temperature T_{ref}, making it possible to obtain a reading of particle temperature, T_p, value with higher precision. As a result, temperatures measured for particles found far from the nozzle exit are considered to be representative of the true particle temperature.

Verification of Nusselt Number

Figure 16 provides a summary of the obtained simulated particle temperature using all four tested Nusselt correlations in comparison with measured temperatures obtained in the zone observed using the IR camera. The particle in-flight temperature within the nozzle as well as through the exit ambient region is provided for the simulated cases. For all cases, the particle temperature continuously increases following the curves depicted in Fig. 16. Additionally, for all cases and outside the nozzle reflection affected zone, as depicted in Fig. 16(b), (d) and (f), the simulated temperature is constant (increase of 0.1%) throughout the entire section analyzed experimentally using the IR camera. Figure 16(a) shows the predicted particle temperature from their injection location to the end of the computation domain for a gas stagnation temperature of 500 °C. The Nusselt correlation given by Eq 18, and used by many in the CS field, predicts a temperature of 34 °C in the region analyzed by the IR camera, while this value reaches 33 and 31 °C using Eq 19 and 23, respectively. Moreover, the Nusselt correlation described by Eq 22 gives a higher predicted temperature of 45 °C. This predicted value falls quite precisely onto the experimentally obtained results, as shown in Fig. 16(b).

Similarly, for the spray conducted at a stagnation temperature of 400 °C, the predicted particle temperature

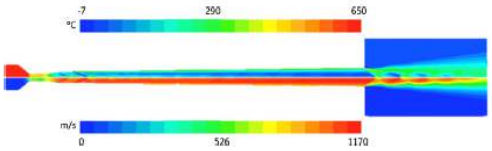

Fig. 17 High stagnation parameter spray (3.45 MPa, 650 °C) resulting flow temperature (top) and velocity (bottom) inside and outside the nozzle

increases throughout their flight within and outside the nozzle, to reach values of 31, 31 °C and 29 °C using Eq 18, 19 and 23, respectively in the experimentally observed zone. Once again, the temperature corresponding more closely to the measured value is obtained using Eq 22 with a resulting value of 39 °C. Analogously, the spray produced at an inlet stagnation temperature of 200 °C results in predicted temperatures at the analyzed zone of 27 °C with the use of Eq 18, 19 and 23. The temperature obtained using Eq 22, which has been demonstrated to be reasonably in agreement with measured temperature values for sprays conducted at higher stagnation values, results in a particle predicted temperature of 28 °C. Consequently, a difference of 4 °C is observed between predicted and measured particle values for this case. This difference can be attributed to temperature evaluation difficulties caused by the small temperature difference between background and particles. As depicted in Fig. 15(a), particles are barely seen after a distance of 6.17 mm from the nozzle outlet when using the shown scale.

Additionally, from Fig. 16(a), (c) and (e), it is seen that a similar increasing particle temperature trend is observed for all tested gas stagnation temperatures. As the particle is injected, its temperature increases sharply as it comes in contact with a low-speed high-temperature flow after the nozzle throat. During its flight in the progressively accelerating flow, the particle temperature increases rate gradually declines.

The effect of emissivity on measured temperature and the influence of particle diameter size on the simulated particle temperature have been evaluated. The emissivity has been varied from $\varepsilon = 0.40$ to $\varepsilon = 0.85$ for measured values, and the particle temperature for titanium powder with a diameter of 125 μm has been simulated for all cases using the generated model. The chosen diameter represents the smallest titanium particle obtained after the sieving process. The simulated particle temperature has indicated an increase in surface temperature with a decrease in particle diameter. Similarly, decreasing the emissivity has increased the particle observed temperature. In general, results have shown that both parameters induce differences of less than 3% with current values and as such lead to the same conclusion that the Nusselt correlation expressed by

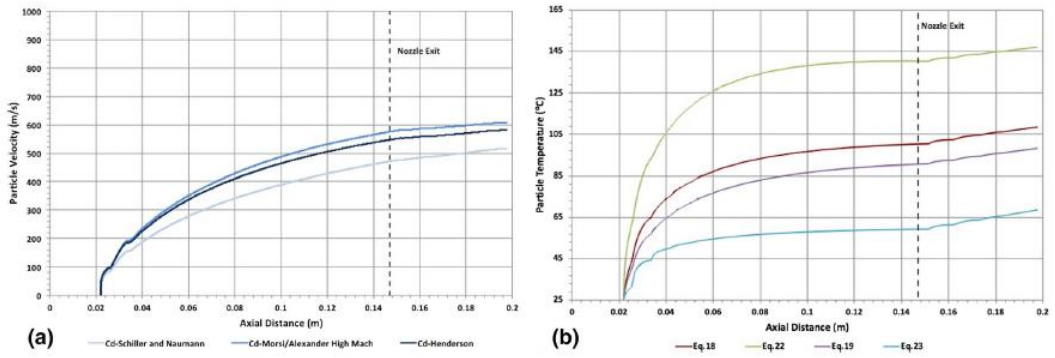

Fig. 18 Copper particle with 15 µm diameter (a) velocity and (b) temperature after being injected in a downstream fashion. Velocity results using various drag coefficient correlations are given. Particle temperature obtained using different Nusselt expressions is also provided. For temperature calculations, the particle velocity was predicted using the Henderson drag correlation

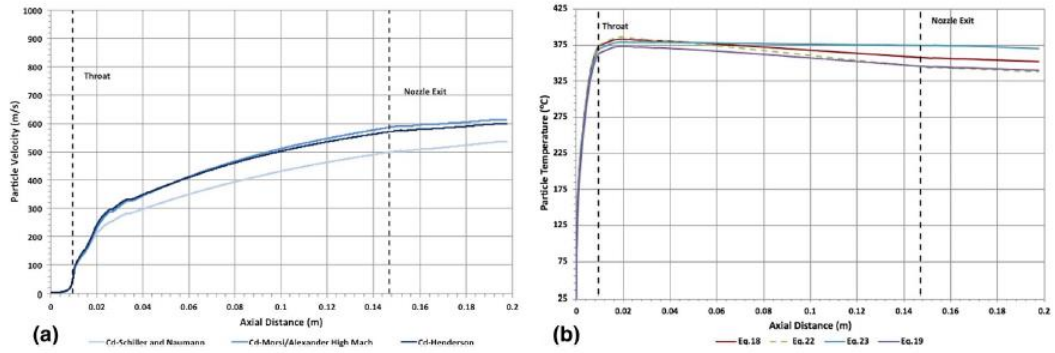

Fig. 19 Copper particle with 15 µm diameter (a) velocity and (b) temperature after being injected in an upstream fashion. Results using different drag coefficient and Nusselt correlations are given. Particle temperature has been obtained using the velocity predicted by the Henderson drag correlation

Eq 22 provides the most accurate numerical particle temperature estimate. In addition, these results also support that any inaccuracy in the emissivity value ($\varepsilon = 0.71$) leads to minor changes in resulting particle temperatures and the influence is inconsequential on the drawn conclusions.

High Pressure and Temperature Flow

Figure 17 shows the resulting gas temperature and velocity within the nozzle and at the free jet location for a gas stagnation pressure and temperature of 3.45 MPa and 650 °C, respectively. As mentioned previously, these parameters have been selected to give insight into the influence of particle/flow correlations for high deposition efficiency CS processes. A maximal gas velocity and temperature of 1093 m/s and 61 °C, respectively, are reached at the nozzle exit. As expected, due to the nozzle geometry, an internal shock is still present after the nozzle throat. At the exit, the flow is over-expanded as a pressure of approximately 50 kPa is reached prior to the exit in the atmospheric region. Spherical copper particle with a diameter of 15 µm has been injected in the flow in an upstream and downstream position of the nozzle throat. The following sections present the results for downstream and upstream powder injections.

Downstream Particle Injection Figure 18(a) shows the copper particle velocity after injection in the high-speed flow using different drag coefficient correlations. An exit velocity of 471, 546 and 574 m/s is obtained using the Schiller and Naumann (Eq 10), Henderson (Eq 6 to 9) and Morsi and Alexander (Eq 11) correlations, respectively.

Similarly to previous low stagnation pressure simulations, the obtained particle velocities calculated using all three correlations give different results whether or not the particle Mach number is considered.

Figure 18(b) provides the particle temperature predicted by all four tested Nusselt number correlations using the particle velocity calculated through Henderson drag law. An exit particle temperature with values of 59, 91, 100 and 140 °C is predicted by correlations expressed using Eq 23, 19, 18 and 22, respectively. A difference of 81 °C (20%) is obtained between the lowest and highest, confirmed formerly to be the most accurate, predicted copper particle temperatures at the nozzle exit. All four Nusselt correlations predict a steeper increase in particle temperature after their exit from the nozzle due to the presence of the external shock waves. Particle heating is promoted in a gas flow of highly varying properties such as through shock waves.

Upstream Particle Injection Figure 19(a) gives the copper particle velocity when injected upstream on the nozzle axis in the converging section, as shown in Fig. 7. The particle slowly accelerates to low speeds in the converging section prior to the nozzle throat. Once propelled in the diverging high-speed nozzle section, the velocity of the particle increases to reach exit speeds of 494, 570 and 585 m/s using the drag coefficient given by Schiller and Naumann (Eq 10), Henderson (Eq 6 to 9) and Morsi and Alexander (Eq 11), respectively. Correlations given by Henderson as well as Morsi and Alexander provide reasonably the same particle velocity values within the nozzle up to 0.08 m. However, slight divergence in particle velocity using the two M_p dependent drag coefficient correlations is observed after 0.08 m. Results from the Henderson correlation have been taken as representative of the true particle velocity.

Figure 19(b) shows the copper particle temperature variation within the nozzle and at the exit. The particle temperature sharply increases in the hot converging inlet nozzle region to values close to 382 °C for all tested Nusselt expressions as one would expect since this region does not exhibit large compressibility effect as it is mostly low subsonic flow regime. Once in the diverging section, the particle temperature decreases to 346 °C at the nozzle exit when using both Eq 19 and 22. This value, however, reaches 356 °C and 374 °C when using the Nusselt correlation expressed by Eq 18 and 23, respectively. As seen in Fig. 19(b), the correlation expressed by Eq 19 provides the same accuracy as Eq 22, which has been asserted most accurate from previous results. The gas flow temperature and Mach number at the exit reach values of approximately 61 °C and 3, respectively. Although the gas reaches low temperatures as it expands in the diverging section, the particle high velocity allows only an approximate 50 °C of temperature drop to occur, as shown in Fig. 19(b).

Conclusions

Newly available infrared camera with high spatial resolution along with fast readout speed has allowed obtaining the first particle temperature measurement in the CS field. However, the IR camera used is limited to a wavelength range of 3 to 5 μm. This is not ideal for low temperature readings, as the radiation at low temperatures is easier to detect at longer wavelengths. Additionally, although the exposure time of the used IR camera is considered very small, lower exposure times would lead to clearer and higher detection rates. This also limits the velocity at which particles can travel, in order to be properly detected by the camera without any large streak, to a few hundred m/s and limits the number of particles detected per optical window. Although the resolution is high, small particles of 30 μm, more generally used in the CS field, would not be perceivable with the current IR camera as the resolution consists of pixels with 55 μm size.

Nevertheless, measurements of CS particle temperature have been successfully achieved for 150 μm titanium particles injected downstream in the cold spray gas flow. Results of particle temperature at the nozzle exit vicinity for various gas inlet temperatures were obtained and compared to measured particle temperatures. Evaluation of Nusselt number correlations for heat transfer analysis provided that the following equation is most accurate in predicting the particle temperature;

$$\overline{Nu} = 2 + 0.44 Re_p^{0.5} Pr^{0.33} \exp\left(0.1 + 0.872 M_p\right)$$

Using other correlations can lead to considerable particle temperature differences. These differences can lead to incorrect particle to substrate impact behavior during impact modeling, which has been significantly used in the CS community to provide insight to the impact phenomenon and material deformation processes. Hence, the current study has provided insight with regard to the most appropriate Nusselt correlation to use when modeling CS particles.

In addition, the IR camera has also been utilized as an additional tool for particle in-flight velocity measurement. As the testing process provides visual data of particles during their flight at the exit of the nozzle and up to a standoff distance of approximately 11 mm, particle tracking velocimetry and particle streak velocimetry methods have been used to obtain readings of velocity. Results have been compared to values measured using the commercial Cold Spray Meter equipment. All three measuring techniques validate the accuracy of the Henderson drag law correlation in predicting particle velocity. The particle

streak velocimetry has shown that in addition to providing local particle size and location, it can be utilized to measure individual particle velocity at specific location within the flow. The PSV method has shown to provide the most accurate particle velocity range compared to the CSM and particle tracking velocimetry based on numerically calculated velocity values for 150 μm diameter particles.

With continuously developing technology, the current work provides foundation to future studies that could potentially be made using more advanced IR camera to provide particle temperature readings for any particle diameter traveling at any velocity commonly found in the CS process.

Acknowledgments The authors wish to thank Vincent Farley and Karl-Alexandre Jahjah from Telops Inc. for providing the necessary equipment for temperature measurement used in the current study and for their input into the data analysis process.

Appendix A

The drag coefficients from Eq 11 for various Re_p numbers are given as follows;

$$C_D = \frac{24.0}{Re_p} \quad \text{for} \quad 0 < Re_p < 0.1,$$

$$C_D = 3.69 + \frac{22.73}{Re_p} + \frac{0.0903}{Re_p^2} \quad \text{for} \quad 0.1 < Re_p < 1$$

$$C_D = 1.222 + \frac{29.1667}{Re_p} - \frac{3.8889}{Re_p^2} \quad \text{for} \quad 1 < Re_p < 10,$$

$$C_D = 0.6167 + \frac{46.50}{Re_p} - \frac{116.67}{Re_p^2} \quad \text{for} \quad 10 < Re_p < 100$$

$$C_D = 0.3644 + \frac{98.33}{Re_p} - \frac{2778}{Re_p^2} \quad \text{for} \quad 100 < Re_p < 1000$$

$$C_D = 0.357 + \frac{148.62}{Re_p} - \frac{47500}{Re_p^2} \quad \text{for} \quad 1000 < Re_p < 5000$$

$$C_D = 0.46 - \frac{490.546}{Re_p} - \frac{57.87 \times 10^4}{Re_p^2} \quad \text{for} \quad 5000 < Re_p < 10000$$

$$C_D = 0.5191 - \frac{1662.5}{Re_p} - \frac{5.4167 \times 10^6}{Re_p^2} \quad \text{for} \quad Re_p \geq 10{,}000$$

References

1. B. Jodoin, Cold Spray Nozzle Mach Number Limitation, *J. Therm. Spray Technol.*, 2002, **11**(4), p 496-507
2. W.-Y. Li, C. Zhang, C.-J. Li, and H. Liao, Modeling Aspects of High Velocity Impact of Particles in Cold Spraying by Explicit Finite Element Analysis, *J. Therm. Spray Technol.*, 2009, **18**(5-6), p 921-933
3. T. Schmidt, H. Assadi, F. Gartner, H. Richter, T. Stoltenhoff, H. Kreye, and T. Klassen, From Particle Acceleration to Impact and Bonding in Cold Spraying, *J. Therm. Spray Technol.*, 2009, **18**(5-6), p 794-808
4. A.E. Segall, A.N. Papyrin, J.C. Conway, and D. Shapiro, A Cold-Gas Spray Coating Process for Enhancing Titanium, *JOM J. Miner. Met. Mater. Soc.*, 1998, **50**, p 52-54
5. T. Stoltenhoff, H. Kreye, and H.J. Richter, An Analysis of the Cold Spray Process and Its Coatings, *J. Therm. Spray Technol.*, 2002, **11**(4), p 542-550
6. R. Kapoor and S. Nemat-Nasser, Determination of Temperature Rise during High Strain Rate Deformation, *Mech. Mater.*, 1998, **27**(1), p 1-12
7. J. Manson, A. Rosakis, and G. Ravichandran, On the Strain and Strain Rate Dependence of the Fraction of Plastic Work Converted to Heat: An Experimental Study Using High Speed Infrared Detectors and the Kolsky Bar, *Mech. Mater.*, 1994, **17**(2-3), p 135-145
8. T. Børvik, O.S. Hopperstad, T. Berstad, and M. Langseth, Perforation of 12 Mm Thick Steel Plates by 20 Mm Diameter Projectiles with Flat, Hemispherical and Conical Noses: Part II: Numerical Simulations, *Int. J. Impact Eng.*, 2002, **27**(1), p 37-64
9. S. Yin, X. Wang, W. Li, and X. Guo, Examination on Substrate Preheating Process in Cold Gas Dynamic Spraying, *J. Therm. Spray Technol.*, 2011, **20**(4), p 852-859
10. A.G. McDonald, A.N. Ryabinin, E. Irissou, and J.-G. Legoux, Gas-Substrate Heat Exchange During Cold-Gas Dynamic Spraying, *J. Therm. Spray Technol.*, 2013, **22**(2-3), p 391-397
11. J.G. Legoux, E. Irissou, and C. Moreau, Effect of Substrate Temperature on the Formation Mechanism of Cold-Sprayed Aluminum, Zinc and Tin Coatings, *J. Therm. Spray Technol.*, 2007, **16**(5-6), p 619-626
12. W.-Y. Li, H. Liao, G. Douchy, and C. Coddet, Optimal Design of a Cold Spray Nozzle by Numerical Analysis of Particle Velocity and Experimental Validation with 316L Stainless Steel Powder, *Mater. Des.*, 2007, **28**(7), p 2129-2137
13. M.-W. Lee, J.-J. Park, D.-Y. Kim, S.S. Yoon, H.-Y. Kim, S.C. James, S. Chandra, and T. Coyle, Numerical Studies on the Effects of Stagnation Pressure and Temperature on Supersonic Flow Characteristics in Cold Spray Applications, *J. Therm. Spray Technol.*, 2011, **20**(5), p 1085-1097
14. A. Sova, A. Okunkova, S. Grigoriev, and I. Smurov, Velocity of the Particles Accelerated by a Cold Spray Micronozzle: Experimental Measurements and Numerical Simulation, *J. Therm. Spray Technol.*, 2012, **22**(1), p 2013-2075
15. R. Ghelichi, S. Bagherifard, M. Guagliano, and M. Verani, Numerical Simulation of Cold Spray Coating, *Surf. Coat. Technol.*, 2011, **205**, p 5294-5301
16. M. Karimi, A. Fartaj, G. Rankin, D. Vanderzwet, W. Birtch, and J. Villafuerte, Numerical Simulation of the Cold Gas Dynamic Spray Process, *J. Therm. Spray Technol.*, 2006, **15**(4), p 518-523

17. W.-Y. Li, H. Liao, H.-T. Wang, C.-J. Li, G. Zhang, and C. Coddet, Optimal Design of a Convergent-Barrel Cold Spray Nozzle by Numerical Method, *Appl. Surf. Sci.*, 2006, **253**(2), p 708-713
18. S. Yin, M. Meyer, W. Li, H. Liao, and R. Lupoi, Gas Flow, Particle Acceleration, and Heat Transfer in Cold Spray: A Review, *J. Therm. Spray Technol.*, 2016, **25**(5), p 874-896
19. H. Assadi, T. Schmidt, H. Richter, J.-O. Kliemann, K. Binder, F. Gärtner, T. Klassen, and H. Kreye, On Parameter Selection in Cold Spraying, *J. Therm. Spray Technol.*, 2011, **20**(6), p 1161-1176
20. A.P. Alkhimov, V.F. Kosarev, and S.V. Klinkov, The Features of Cold Spray Nozzle Design, *J. Therm. Spray Technol.*, 2001, **10**(2), p 375-381
21. V.F. Kosarev, S.V. Klinkov, A.P. Alkhimov, and A.N. Papyrin, On Some Aspects of Gas Dynamics of the Cold Spray Process, *J. Therm. Spray Technol.*, 2003, **12**(2), p 265-281
22. B. Samareh, O. Stier, V. Lüthen, and A. Dolatabadi, Assessment of CFD Modeling via Flow Visualization in Cold Spray Process, *J. Therm. Spray Technol.*, 2009, **18**(5-6), p 934-943
23. D.L. Gilmore, R.C. Dykhuizen, R.A. Neiser, M.F. Smith, and T.J. Roemer, Particle Velocity and Deposition Efficiency in the Cold Spray Process, *J. Therm. Spray Technol.*, 1999, **8**(4), p 576-582
24. B. Jodoin, F. Raletz, and M. Vardelle, Cold Spray Modeling and Validation Using an Optical Diagnostic Method, *Surf. Coat. Technol.*, 2006, **200**(14-15), p 4424-4432
25. V.K. Champagne, D.J. Helfritch, S.P.G. Dinavahi, and P.F. Leyman, Theoretical and Experimental Particle Velocity in Cold Spray, *J. Therm. Spray Technol.*, 2011, **20**(3), p 425-431
26. S.P. Mates, D. Basak, F.S. Biancaniello, S.D. Ridder, and J. Geist, Calibration of a Two-Color Imaging Pyrometer and Its Use for Particle Measurements in Controlled Air Plasma Spray Experiments, *J. Therm. Spray Technol.*, 2002, **11**(2), p 195-205
27. G. Mauer, R. Vaßen, and D. Stöver, Plasma and Particle Temperature Measurements in Thermal Spray: Approaches and Applications, *J. Therm. Spray Technol.*, 2011, **20**(3), p 391-406
28. B. Aziz, P. Gougeon, and C. Moreau, Temperature Measurement Challenges and Limitations for In-Flight Particles in Suspension Plasma Spraying, *J. Therm. Spray Technol.*, 2017, **26**(4), p 695-707
29. J. Vattulainen, E. Hämäläinen, R. Hernberg, P. Vuoristo, and T. Mäntylä, Novel Method for In-Flight Particle Temperature and Velocity Measurements in Plasma Spraying Using a Single CCD Camera, *J. Therm. Spray Technol.*, 2001, **10**(1), p 94-104
30. T.C. Hanson, C.M. Hackett, and G.S. Settles, Independent Control of HVOF Particle Velocity and Temperature, *J. Therm. Spray Technol.*, 2002, **11**(1), p 75-85
31. B.H. Wang, B.Q. Li, H. Yang, and Y. Bai, Radiation Spectral Analysis and Particle Temperature/Velocity Measurement in Plasma Spray with One-Color Camera, *J. Therm. Spray Technol.*, 2017, **26**(7), p 1632-1640
32. J. Mishin, M. Vardelle, J. Lesinski, and P. Fauchais, Two-Colour Pyrometer for the Statistical Measurement of the Surface Temperature of Particles under Thermal Plasma Conditions, *J. Phys. E*, 1987, **20**(6), p 620-625
33. K. Hollis and R. Neiser, Particle Temperature and Flux Measurement Utilizing a Nonthermal Signal Correction Process, *J. Therm. Spray Technol.*, 1998, **7**(3), p 392-402
34. P. Fauchais and M. Vardelle, Sensors in Spray Processes, *J. Therm. Spray Technol.*, 2010, **19**(4), p 668-694
35. G.A. Hughmark, Mass and Heat Transfer from Rigid Sphere, *AlChE J.*, 1967, **13**(6), p 1219-1221
36. D.J. Carlson and R.F. Hoglund, Particle Drag and Heat Transfer in Rocket Nozzles, *AIAA J.*, 1964, **2**(11), p 1980-1984
37. Y.P. Wan, V. Prasad, G.-X. Wang, S. Sampath, and J.R. Fincke, Model and Powder Particle Heating, Melting, Resolidification, and Evaporation in Plasma Spraying Processes, *J. Heat Transf.*, 1999, **121**(3), p 691-699
38. T.-C. Jen, L. Pan, L. Li, Q. Chen, and W. Cui, The Acceleration of Charged Nano-Particles in Gas Stream of Supersonic de-Laval-Type Nozzle Coupled with Static Electric Field. *Appl. Therm. Eng.*, 2006, **26**(5-6), 613-621
39. H. Tabbara, S. Gu, D.G. McCartney, T.S. Price, and P.H. Shipway, Study on Process Optimization of Cold Gas Spraying, *J. Therm. Spray Technol.*, 2011, **20**(3), p 608-620
40. T. Jen, L. Li, W. Cui, Q. Chen, and X. Zhang, Numerical Investigations on Cold Gas Dynamic Spray Process with Nano- and Microsize Particles, *Int. J. Heat Mass Transf.*, 2005, **48**(21-22), p 4384-4396
41. M. Faizan-Ur-Rab, S.H. Zahiri, S.H. Masood, T.D. Phan, M. Jahedi, and R. Nagarajah, Application of a Holistic 3D Model to Estimate State of Cold Spray Titanium Particles, *Mater. Des.*, 2016, **89**, p 1227-1241
42. G. Huang, D. Gu, X. Li, L. Xing, and H. Wang, Numerical Simulation on Syphonage Effect of Laval Nozzle for Low Pressure Cold Spray System, *J. Mater. Process. Technol.*, 2014, **214**(11), p 2497-2504
43. X.K. Suo, T.K. Liu, W.Y. Li, Q.L. Suo, M.P. Planche, and H.L. Liao, Numerical Study on the Effect of Nozzle Dimension on Particle Distribution in Cold Spraying, *Surf. Coat. Technol.*, 2013, **220**, p 107-111
44. D.-M. Chun, J.-O. Choi, C.S. Lee, and S.-H. Ahn, Effect of Stand-off Distance for Cold Gas Spraying of Fine Ceramic Particles (5 μm) under Low Vacuum and Room Temperature Using Nano-Particle Deposition System (NPDS), *Surf. Coat. Technol.*, 2012, **206**, p 2125-2132
45. S. Yin, M. Zhang, Z. Guo, H. Liao, and X. Wang, Numerical Investigations on the Effect of Total Pressure and Nozzle Divergent Length on the Flow Character and Particle Impact Velocity in Cold Spraying, *Surf. Coat. Technol.*, 2013, **232**, p 290-297
46. J. Pattison, S. Celotto, A. Khan, and W. O'Neill, Standoff Distance and Bow Shock Phenomena in the Cold Spray Process, *Surf. Coat. Technol.*, 2008, **202**(8), p 1443-1454
47. X. Suo, S. Yin, M.-P. Planche, T. Liu, and H. Liao, Strong Effect of Carrier Gas Species on Particle Velocity During Cold Spray Processes, *Surf. Coat. Technol.*, 2014, **268**, p 1-4
48. C.T. Crowe, J.D. Schwarzkopf, M. Sommerfeld, and Y. Tsuji, *Multiphase Flows with Droplets and Particles*, CRC Press, Boca Raton, 2011
49. M.A. Saad, *Compressible Fluid Flow*, Prentice-Hall, Englewood Cliffs, NJ, 1985
50. E. Loth, Compressibility and Rarefaction Effects on Drag of a Spherical Particle, *AIAA J.*, 2008, **46**, p 2219-2228
51. I.-S. Chang, One- and Two-Phase Nozzle Flows, *AIAA J.*, 1980, **18**(12), p 1455-1461
52. C.T. Crowe, Drag Coefficient of Particles in a Rocket Nozzle, *AIAA J.*, 1967, **5**(5), p 1021-1022
53. C.B. Henderson, Drag Coefficients of Spheres in Continuum and Rarefied Flows, *AIAA J.*, 1976, **14**(6), p 707-708
54. J. Aroesty, Sphere Drag in a Low-Density Supersonic Flow, in *Rarefied Gas Dynamics, Volume 2, Proceedings of the Third International Symposium*, (NY), Academic Press, pp. 261-277 (1963)
55. A.B. Bailey and J. Hiatt, Sphere Drag Coefficients for a Broad Range of Mach and Reynolds Numbers, *AIAA J.*, 1972, **10**(11), p 1436-1440
56. G. Mishin and G. Mishin, "Experimental Investigation of the Flight of a Sphere in Weakly Ionized Air," in *15th Applied*

Aerodynamics Conference, (Atlanta, GA), American Institute of Aeronautics and Astronautics, pp. 1997-2298 (1997)
57. T. Han, Z. Zhao, B.A. Gillispie, and J.R. Smith, Effects of Spray Conditions on Coating Formation by the Kinetic Spray Process, *J. Therm. Spray Technol.*, 2005, **14**(3), p 373-383
58. S.V. Klinkov, V.F. Kosarev, A.A. Sova, and I. Smurov, Calculation of Particle Parameters for Cold Spraying of Metal-Ceramic Mixtures, *J. Therm. Spray Technol.*, 2009, **18**(5-6), p 944-956
59. L. Talbot, R.K. Cheng, R.W. Schefer, and D.R. Willis, Thermophoresis of Particles in a Heated Boundary Layer, *J. Fluid Mech.*, 1980, **101**(4), p 737-758
60. X.-J. Ning, Q.-S. Wang, Z. Ma, and H.-J. Kim, Numerical Study of In-Flight Particle Parameters in Low-Pressure Cold Spray Process, *J. Therm. Spray Technol.*, 2010, **19**(6), p 1211-1217
61. S.A. Abdulaziz and A.B. Gregory, Characterization of the Interacting Gas-Particle Dynamic System in Cold Spray Nozzles in Dimensional and Non-Dimensional Form, *Powder Technol.*, 2018, **338**, p 1-47
62. T.L. Bergman, F.P. Incropera, D.P. DeWitt, and A.S. Lavine, *Fundamentals of Heat and Mass Transfer*, Wiley, Hoboken, NJ, 2011
63. A. Sova, M. Doubenskaia, S. Grigoriev, A. Okunkova, and I. Smurov, Parameters of the Gas-Powder Supersonic Jet in Cold Spraying Using a Mask, *J. Therm. Spray Technol.*, 2013, **22**(4), p 551-556
64. M.P. Dewar, A.G. McDonald, and A.P. Gerlich, Interfacial Heating during Low-Pressure Cold-Gas Dynamic Spraying of Aluminum Coatings, *J. Mater. Sci.*, 2012, **47**(1), p 184-198
65. H. Katanoda, Numerical Simulation of Temperature Uniformity within Solid Particles in Cold Spray, *J. Solid Mech. Mater. Eng.*, 2008, **2**, p 58-69
66. B.I. Ermolaev, Thermal Conductivity and Electrical Conductivity of Materials Based on Titanium and Its Alloys at Temperatures from 20-80 to 1000°K, *Met. Sci. Heat Treat.*, 1974, **16**, p 1049-1051
67. I.E. Beckwith and J.J. Gallagher, Heat Transfer and Recovery Temperature on a Sphere with Laminar, Transitional and Turbulent Boundary Layers at Mach Numbers of 2.00 and 4.15. Washington, (1957)
68. S. Forrest, Survey of Literature on Convective Heat Transfer Coefficients and Recovery Factors for High Atmosphere Thermometry, Utah, USA (1973)
69. W.E. Ranz and W.R. Marshall Jr., Evaporation from Drops Part I, *Chem. Eng. Prog.*, 1952, **48**, p 141-146
70. V. Champagne, D. Helfritch, P. Leyman, R. Lempicki, and S. Grendahl, The Effects of Gas and Metal Characteristics on Sprayed Metal Coatings, *Model. Simul. Mater. Sci. Eng.*, 2005, **13**(7), p 1119
71. D. Helfritch and V. Champagne Jr., A Model Study of Powder Particle Size Effects in Cold Spray Deposition, in *Proceedings of the Army Science Conference (26th)*, (Orlando), p 6 (2008)
72. M. Faizan-Ur-Rab, S.H. Zahiri, P.C. King, C. Busch, S.H. Masood, M. Jahedi, R. Nagarajah, and S. Gulizia, Utilization of Titanium Particle Impact Location to Validate a 3D Multicomponent Model for Cold Spray Additive Manufacturing, *J. Therm. Spray Technol.*, 2017, **26**(8), p 1874-1887
73. W.-Y. Li and C.-J. Li, Optimal Design of a Novel Cold Spray Gun Nozzle at a Limited Space, *J. Therm. Spray Technol.*, 2005, **14**(3), p 391-396
74. E.E.S. Michaelides, *Heat and Mass Transfer in Particulate Suspensions*, Springer, Fort Worth, 2013
75. H. Katanoda, M. Fukuhara, and N. Iino, Numerical Study of Combination Parameters for Particle Impact Velocity and Temperature in Cold Spray, *J. Therm. Spray Technol.*, 2007, **16**(5-6), p 627-633
76. A. Aissa, M. Abdelouahab, A. Noureddine, M. El Ganaoui, and B. Pateyron, Ranz and Marshall Correlations Limits on Heat Flow Between a Sphere and Its Surrounding Gas at High Temperature, *Therm. Sci.*, 2015, **19**(5), p 1521-1528
77. F. Ben Ettouil, B. Pateyron, H. Ageorges, M. El Ganaoui, P. Fauchais, and O. Mazhorova, Fast Modeling of Phase Changes in a Particle Injected Within a d.c Plasma Jet, *J. Therm. Spray Technol.*, 2007, **16**(5-6), p 744-750
78. C. Borgnakke and R.E. Sonntag, *Fundamentals of Thermodynamics*, 9th ed., Wiley Global Education, Michigan, 2016
79. T.H.V. Steenkiste, J.R. Smith, and R.E. Teets, Aluminum Coatings via Kinetic Spray with Relatively Large Powder Particles, *Surf. Coat. Technol.*, 2002, **154**(2-3), p 237-252
80. E.H. Kwon, S.H. Cho, J.W. Han, C.H. Lee, and H.J. Kim, Particle Behavior in Supersonic Flow During the Cold Spray Process, *Met. Mater. Int.*, 2005, **11**(5), p 377-381
81. R.C. Dykhuizen and M.F. Smith, Gas Dynamic Principles of Cold Spray, *J. Therm. Spray Technol.*, 1998, **7**(2), p 205-212
82. P. Tremblay, L. Belhumeur, M. Chamberland, A. Villemaire, P. Dubois, F. Marcotte, C. Belzile, V. Farley, and P. Lagueux, Pixel-Wise Real-Time Advanced Calibration Method for Thermal Infrared Cameras, in *Proceedings Volume 7662, Infrared Imaging Systems: Design, Analysis, Modeling, and Testing XXI*, ed. by G.C. Holst and K.A. Krapels, Orlando, p 766212 (2010)
83. Y. Tanida and H. Miyashiro, Flow Visualization VI, in *Proceedings of the Sixth International Symposium on Flow Visualization*, ed. by H. Tanida, Yoshimichi, Miyashiro, (Springer, Yokohama), p 904 (2013)
84. A. Ianiro and G. Cardone, Measurement of Surface Temperature and Emissivity with Stereo Dual-Wavelength IR Thermography, *J. Mod. Opt.*, 2010, **57**(18), p 1708-1715
85. R. Usamentiaga, P. Venegas, J. Guerediaga, L. Vega, J. Molleda, and F. Bulnes, Infrared Thermography for Temperature Measurement and Non-Destructive Testing, *Sensors*, 2014, **14**(7), p 12305-12348
86. M.V. Möllmann, *Infrared Thermal Imaging: Fundamentals, Research and Applications*, 2nd ed., Wiley-VCH, Weinheim, 2017
87. T.K. Bose, *"High Temperature Gas Dynamics: An Introduction for Physicists and Engineers*, 2nd ed., Springer, Kolkata, West Bengal, 2014
88. M. Ochs, T. Horbach, A. Schulz, R. Koch, and H.J. Bauer, A Novel Calibration Method for an Infrared Thermography System Applied to Heat Transfer Experiments, *Meas. Sci. Technol.*, 2009, **20**(7), p 1-9
89. G.M. Carlomagno and G. Cardone, Infrared Thermography for Convective Heat Transfer Measurements, *Exp. Fluids*, 2010, **49**(6), p 1187-1218
90. N.K. Tolochko, Y.V. Khlopkov, S.E. Mozzharov, M.B. Ignatiev, T. Laoui, and V.I. Titov, Absorptance of Powder Materials Suitable for Laser Sintering, *Rapid Prototyp. J.*, 2000, **6**(3), p 155-161
91. Y. Li and D. Gu, Thermal Behavior during Selective Laser Melting of Commercially Pure Titanium Powder: Numerical Simulation and Experimental Study, *Addit. Manuf.*, 2014, **1-4**, p 99-109
92. N.K. Tolochko, M.K. Arshinov, A.V. Gusarov, V.I. Titov, T. Laoui, and L. Froyen, Mechanisms of Selective Laser Sintering and Heat Transfer in Ti Powder, *Rapid Prototyp. J.*, 2003, **9**(5), p 314-326
93. F. Zhang, K. Yu, K. Zhang, Y. Liu, Y. Zhao, and Y. Liu, Infrared Spectral Emissivity Property of Pure Titanium in the 473-1035 K Temperature Range, *Appl. Spectrosc.*, 2016, **70**(10), p 1717-1725
94. Z.W. Wang, Y.M. Wang, Y. Liu, J.L. Xu, L.X. Guo, Y. Zhou, J.H. Ouyang, and J.M. Dai, Microstructure and Infrared

Emissivity Property of Coating Containing TiO 2 Formed on Titanium Alloy by Microarc Oxidation, *Curr. Appl. Phys.*, 2011, **11**(6), p 1405-1409
95. G. Teodorescu, P.D. Jones, R.A. Overfelt, and B. Guo, High Temperature Emissivity of High Purity Titanium and Zirconium, (Alabama) (2018)
96. E.A. Belskaya, Emissivity and Electrical Resistivity of Titanium Alloys with Aluminum and Vanadium, *High Temp.*, 2012, **50**(4), p 475-478
97. F.J. Bradshaw, The Optical Emissivity of Titanium and Zirconium, *Proc. Phys. Soc. Sect. B*, 1950, **63**(8), p 573
98. J.M. Jones, P. Mason, and A. Williams, A Compilation Of Data On The Radiant Emissivity Of Some Materials At High Temperatures. J. Energy Inst. (2018) (in press)
99. M.F. Modest, *Radiative Heat Transfer*, 3rd ed., Academic Press, Amsterdam, 2013
100. B. Lane, S. Moylan, E. Whitenton, and L. Ma, Thermographic Measurements of the Commercial Laser Powder Bed Fusion Process at NIST, *Rapid Prototyp. J.*, 2016, **22**(5), p 778-787
101. S.H. Zahiri, T.D. Phan, S.H. Masood, and M. Jahedi, Development of Holistic Three-Dimensional Models for Cold Spray Supersonic Jet, *J. Therm. Spray Technol.*, 2014, **23**(6), p 919-933
102. B. Samareh and A. Dolatabadi, Dense Particulate Flow in a Cold Gas Dynamic Spray System, *J. Fluids Eng.*, 2008, **130**(8), p 1-11

5.3 RESEARCH PROJECT 3

This paper investigates the effect of particle inherent size-dependent temperature on the particle deposition behavior, deposition efficiency and coating adhesion strength. Three size sets of pure aluminum powder have been deposited on polished and grit-blasted steel substrate surfaces. The experimental results are used to design a CFD model capable of providing the complete particle impact characteristics (position within the CS flow, size, temperature and velocity) of aluminum powder material. This paper addresses the objectives set in the study presented in section 3.3. Results show the importance of particle impingement process on the adhesion strength of the first deposited layer. Additionally, a rise in particle impact temperature has been shown to increase the deposition efficiency, and lead to a decrease in adhesion with particle size increase.

Surface & Coatings Technology 406 (2021) 126735

Contents lists available at ScienceDirect

Surface & Coatings Technology

journal homepage: www.elsevier.com/locate/surfcoat

Particle temperature effect in cold spray: A study of soft particle deposition on hard substrate

A. Nastic [a,*], B. Jodoin [a], D. Poirier [b], J.-G. Legoux [b]

[a] University of Ottawa Cold Spray Laboratory, Ottawa, ON, Canada
[b] National Research Council of Canada, Boucherville, QC, Canada

ARTICLE INFO

Keywords:
Particle temperature influence
Upstream/downstream injection
Numerical critical velocity
Coating adhesion
Pseudo-plasticity
In-situ peening

ABSTRACT

In cold spray, the interactions between feedstock particles and propellant gas control deposition outcome. The particle impact temperature, along with impact velocity, governs the deposition due to its effect on the impact deformation processes. As bonding mechanisms rely primarily on the particle/substrate plastic flow upon impact, particle impact temperature holds a predominant role in process optimization.

The current work studies the effect of pure aluminum particle impact temperature on deposition phenomena when propelled onto a hard steel substrate. Particle impact temperature was varied while achieving the same particle impact velocity, using low and high-pressure cold spray systems. Three different particle diameters are studied, with varying resulting inherent impact temperatures, to provide size dependent insight on deposition/adhesion.

Experimental results demonstrate that at low particle impact temperature, i.e. 50 °C, coating adhesion is controlled by in-situ peening. Adhesion shifts to particle in-flight characteristics dependent bonding, i.e. $\eta = V/V_c$, as particle temperature increases. At low particle impact temperatures, the coating bond strength increases with increasing in-situ impingement intensity and frequency, i.e. decreasing deposition efficiency with increasing particle size. At higher particle impact temperatures, in-situ peening rate decreases and the adhesion strength increases with decreasing particle size. In addition to affecting the impact process (DE, V_c and adhesion), the particle impact temperature also influences the coating mechanical properties through the creation of temperature-dependent crack propagation mechanisms, i.e. deflection, bridging and acceleration, and of particle-particle structural arrangement related to deformation processes, i.e. fish scale effect and pseudo-plasticity behavior.

1. Introduction

The cold gas dynamic spray (CGDS) process, or simply cold spray (CS), is used for the deposition of various materials and has become a promising method in multiple material processing fields, including additive manufacturing [1–3]. CGDS is based on the energy exchange between a gas flow and injected powder material. The gas stream (nitrogen, helium or air) is directed through a converging/diverging nozzle to reach the supersonic regime. Particles are injected into the nozzle and propelled to high velocities reaching values between 300 m/s and 1200 m/s [4,5]. Upon impact with a target surface (substrate), up to 90% of the particle kinetic energy is converted into heat, while the remaining energy is used for viscoelastic and elastic deformations of particle and substrate. The successful adhesion of the impacting material depends on various phenomena that initiate due to the high strain rate plastic deformation occurring at the impact boundaries [5–8]. Reported strain and strain rates at the particle/substrate interface reach values of 10 and 10^9 s^{-1}, respectively [9], which are far beyond values commonly encountered in classical powder manufacturing methods [10,11]. These extreme material deformation phenomena lead to surface oxide layer breakup, localized melting, amorphization, diffusion, shear instability and hydrodynamic plasticity [8,12,13], which have all been associated to bonding processes.

Aside from the particle material properties, the CGDS impact dynamics rely on in-flight particle/gas momentum and energy exchange processes. The process gas stagnation pressure and temperature govern the flow dynamics and thus particle in-flight characteristics [14–16]. The particle/gas mixture undergoes large changes in many properties inside and outside the nozzle. Furthermore, the occurrence of oblique

* Corresponding author.
E-mail address: [redacted] (A. Nastic).

https://doi.org/10.1016/j.surfcoat.2020.126735
Received 23 September 2020; Received in revised form 14 November 2020; Accepted 5 December 2020
Available online 10 December 2020

List of symbols

P	flow pressure (N/m^2)
V	flow velocity (m/s)
T	flow temperature (K)
u_i	gas velocity component in i-direction (i = 1, 2, 3) (m/s)
ρ	density (kg/m^3)
C_D	drag coefficient (–)
t	time (s)
k	turbulent kinetic energy (m^2/s^2)
ϵ	turbulent dissipation rate (m^2/s^3)
μ	viscosity (kg/m s)
α_ϵ	inverse effective Prandtl number for turbulent dissipation rate (–)
Pr_t	turbulent Prandtl number (–)
S_M	particle phase influence on gas momentum (kg/m^2 s^2)
Y_M	contribution of the fluctuating dilatation in compressible turbulence to dissipation rate (kg/m s^3)
G_k	generation of turbulence kinetic energy due to mean velocity gradient (kg/m s^3)
G_b	generation of turbulence kinetic energy due to buoyancy (kg/m s^3)
$C_{1,\ 2,\ 3\epsilon}$	RNG k-ϵ turbulent model constants (–)
h_{tot}	total system enthalpy (kg m^2/s^2)
n	normal direction coordinate (–)
k_1	particle-size-dependent fitting parameter (–)
x_i	Cartesian coordinate in the i-direction (i = 1, 2, 3) (m)
n_s	spread factor (–)
Re_p	particle Reynolds number (–)
L_p	average distance between particles (m)
L	characteristic length (m)
Z	mass ratio, powder/gas (–)
d	particle diameter (m)
$Volume$	volume flow rate (m^3/s)
$\dot{m}$	mass flow rate (kg/s)
$\dot{\rho}$	density flow rate (kg/m^3 s)
F_b	body force (kg m/s^2)
A	cross-sectional area (m^2)
D	level of particle interactions (–)
Π_{mom}	momentum coupling (kg m^2/s^2)
λ	thermal conductivity (kg m/s^3 K)
α_k	inverse effective Prandtl number for turbulent kinetic energy (–)
τ	stress tensor in viscous dissipation term (kg/m s^2)
S_k, S_ϵ	user-defined source terms (kg/m s^3)
C_v	specific heat at constant volume (m^2/s^2 K)
β, η_0	RNG constants (–)
S	modulus of the mean rate-of-strain tensor (1/s)
σ	particle m material tensile strength (N/m^2)
Y_d	cumulative percentage (%)
$\overline{Nu}$	average Nusselt number (–)
M_p	particle Mach number (–)

Abbreviations

BSD	backscattered detector
CFD	computational fluid dynamics
CGDS	cold gas dynamic spray
CS	cold spray
CSM	cold spray meter
DE	deposition efficiency
DRW	discrete random walk
FEM	finite element model
HPCS	high pressure cold spray
HPIT	high particle impact temperature
LPCS	low pressure cold spray
LPIT	low particle impact temperature
PBI	polybenzimidazole
RANS	Reynolds Averaged Navier-Stokes
RNG	re-normalized group
SEM	scanning electron microscopy
V_c	critical velocity
R_a	arithmetic surface roughness

Subscripts

eff	effective
g	gas
i	ith coordinate variable (=1, 2, 3 vector component)
j	Einstein summation of j = 1, 2, 3
m	melting
p	particle
t	turbulent

shocks and Mach disks, inducing abrupt discontinuity and instantaneous variation in gas flow characteristics can significantly affect the particle thermal history prior to impact [17,18]. A few studies have captured the gas stream phenomenological characteristics using Schlieren photography [19,20]. Computational fluid dynamics (CFD) models have also been used to study the driving gas behavior with the objective of assessing the particle impact velocity and temperature. These CFD efforts have generated physically realistic flow simulations [17,18,21,22]. CGDS particle velocities have been measured through laser-light sheet, laser two focus velocimetry and high speed cameras [23–31]. These experimental observations have been used to develop proper momentum transfer models, contributing to adequate prediction of the particle impact velocity influence on deformation and deposition [32–36]. However, the low particle temperatures in the CGDS process coupled with high particle velocities prohibit the use of classical optical pyrometry, which makes any CGDS particle temperature measurement a technical challenge. In a recent study, CGDS particle in-flight temperature measurements have been successfully reported [14], allowing the evaluation and development of a proper particle transient heat transfer model. Many have reported various benefits of increasing particle impact temperature on deposition and adhesion, which have been related to improved particle deformation promoting the creation of zones suitable for bonding [37–39]. To support this assertion, use of external powder preheating systems has shown to increase DE and adhesion in low-pressure CS systems using downstream injection [39–42]. Analogously, in high-pressure CS systems, in which the powder injection is made axially in the converging section, reported DE's reach up to 95% (Cu on Al) [33,43] as heat transfer processes are promoted in the stagnant pre-chamber high temperature gas.

Therefore, the primary objective of the current work is to investigate the effect of particle impact temperature and size on deposition for soft particle/hard substrate material combination. The influence of particle impact temperature on deposition characteristics (deposition efficiency and critical velocity), adhesion and coating properties (apparent ductility) are studied. Low and high-pressure cold spray systems (LPCS and HPCS) have been utilized to generate deposits with similar particle impact velocities but different particle impact temperatures. Since particle impact temperature measurement is impossible at the chosen working parameters, validated CFD model correlations are applied to obtain particle impact temperature values [14]. Particle velocities are measured and used to additionally validate the developed CFD model's accuracy. The particle injection location and particle trajectory are used

to explain the statistical particle in-flight characteristics. The experiments are conducted for three distinct particle size ranges to provide a size-dependent analysis.

2. Experimental procedures

2.1. Feedstock powder

Spherical commercially pure aluminum feedstock powder has been used (Equispheres, ON, CA) in the generated deposits. Three distinct sets of powders with different size diameter distributions have been selected to study the effect of particle size on impact temperature and its influence on coating deposition and bonding developments. Fig. 1a presents the particle size distribution for all three powder sets. The powder sets are referred to as set 1, set 2 and set 3 and present an average powder size of 40 μm, 58 μm and 68 μm respectively. As shown in Fig. 1b, c and d, using electron microscopy (SEM, Zeiss, EVO-MA10, UK) images under the detection of backscattered electron detector (BSD), all three powder sets exhibit a spherical shape with negligible presence of satellites.

2.2. Substrate material

A common low carbon steel material, SAE1018 (25.4 mm diameter and 40 mm height) with measured hardness of 90.5 ± 0.3HRB has been used as substrate, which ensures a proper study of soft material impact on hard target surface. Surface preparation and coating depositions were performed on the flat ends of the cylindrical samples. Two surface preparation methods have been utilized. A mirror finish surface has been obtained by gradual grinding and polishing steps up to a final process using 3 μm abrasive suspensions. A grit blasting method using a 20mesh (850 μm) ferrosilicate abrasive was also utilized as a second surface preparation method to roughen the substrate surface. Prior to the deposition process, all substrates have been cleaned and degreased using ethanol. During coating deposition, all substrates have been thermally insulated from the surroundings to avoid uncontrolled substrate temperature variations. A portable profilometer (PHASE II SRG-4000A, NJ, USA) equipped with a diamond stylus has been used to obtain the arithmetic surface roughness, R_a, of polished substrates. A digital optical microscope (VHX-2000 Keyence Corporation, Osaka, Japan) has been utilized, on the other hand, to obtain profile depths of grit blasted samples, which have been subsequently imported in Matlab for the calculation of surface R_a [44].

2.3. Cold spray depositions

Commercially available CS systems (SST-EP, CenterLine Limited, Windsor, ON, CA and Oerlikon Metco KINETICS 4000, Schwytz, CH) have been utilized to deposit the aluminum powders. In the SST-EP system, the powder is injected radially in the diverging nozzle section. A PBI nozzle has been used for all deposition made with the LPCS [45]. Due to the significant particle trajectory deviation shown to occur after particle nozzle wall deterioration from impact wear [45], a new unworn PBI nozzle has been utilized for all deposits. The powder injection in the HPCS system is located in the center of the converging nozzle section, parallel to the nozzle axis. A SiC nozzle has been used in the KINETIKS 4000 system. The nozzles geometries and dimensions are presented in detail in Section 3.1. Table 1 presents the spray parameters used when operating each system, which ensured comparable particle impact velocities while providing different particle impact temperatures.

Powder feeding rate was kept similar for all sprays (≈20 g/min). Deposition efficiency (DE) has been measured using the specimen weight gain with respect to the total powder weight propelled at the

Table 1
CGDS process deposition parameters and features.

	SST-EP		KINETICS 4000
Powder injection location	Downstream	Downstream	Upstream
Nozzle material	Polymer	Polymer	SiC
Stagnation temperature	500 °C	500 °C	500 °C
Stagnation pressure	3.4 MPa	3.4 MPa	3.4 MPa
Traverse velocity	10 mm/s	150 mm/s	150 mm/s
Number of passes	1	15	2–5
Stand-off distance (SOD)	15 mm	15 mm	15 mm
Step size	1 mm/pass	1 mm/pass	1 mm/pass

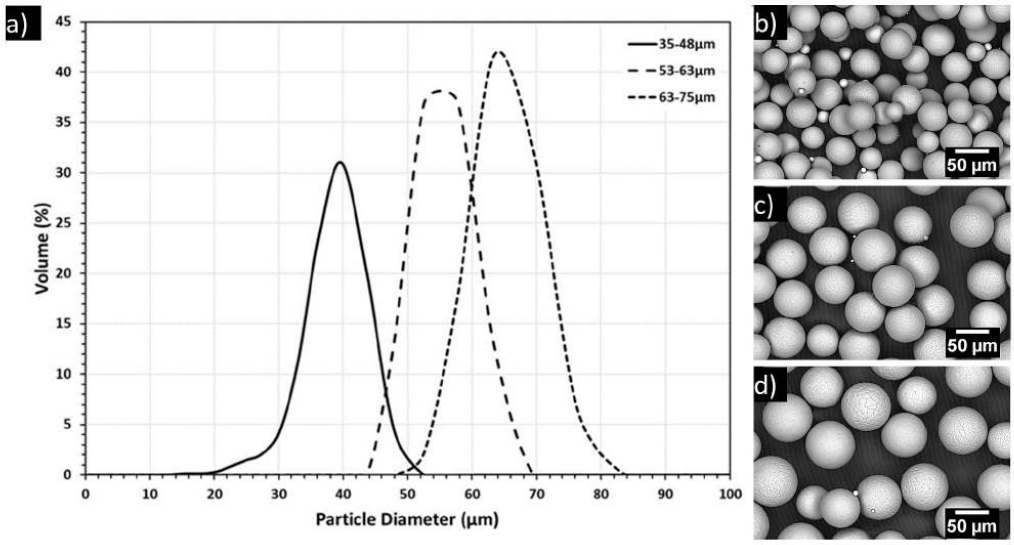

Fig. 1. a) Feedstock powder size distribution. The geometry and size of all three powder sets are depicted in b) set 1, c) set 2 and d) set 3 using backscattered scanning electron microscope (BSD-SEM) images.

substrate surface. As presented in Table 1, the LPCS deposits have been made using two gun traverse velocities, i.e. 10 mm/s and 150 mm/s, while only 150 mm/s was utilized for HPCS deposits due to the robot minimum speed limit. For the LPCS, spot sprays, i.e. powder deposition at a single gun position, have also been carried out to characterize the particle spatial position upon deposition. Obtained coating microstructural analysis has been performed through digital optical microscopy and scanning electron microscopy using secondary (SE) and back-scattered detectors.

2.4. Particle velocity measurement

The in-flight particle velocity was measured at a distance of 15 mm from the nozzle exit using a Cold Spray Meter (CSM) eVolution (Tecnar Automation Ltd., St-Bruno, Canada). The CSM is equipped with a continuous 810 nm wavelength laser that illuminates particles as they cross a dual-slit photomask. The diffracted light is subsequently captured and collected data filtered by an internal interpreting system. The velocity is calculated using the traveling distance and time interval that the detected particle takes to cross two mask slits. For statistical purposes, a minimum of 1000 individual particle velocities have been measured for each conducted tests. The velocity readings have been made at the center of the nozzle for all cases.

2.5. Adhesion tests

Coating adhesion strength values have been obtained and evaluated following the ASTM-C633 standard [46]. A thermally curing elastomeric adhesive, FM-1000 (Cytec Engineering Materials, MD, USA) has been used to glue the cylindrical coated substrates to counter uncoated steel cylindrical specimens. Prior to testing, all coatings have been machined to a 550 μm thickness. Once cured and cooled to room temperature, the assembly has been pulled using a universal tensile testing machine (Instron Series 4482, MA, US) at a rate of 0.017 mm/s and failed coating fracture surfaces have been subsequently analyzed. Three to five coatings have been tested per spray set.

2.6. Bend-to-break tests

Bend-to-break tests have been performed, following a procedure similar to the ASTM D4145-10 standard [47], using coatings deposited on grit blasted surfaces. After machining the coatings down to 550 μm thickness, natural interfacial delamination occurring during high speed saw cutting processes allowed proper coating removal from the steel substrate. The machined surface was placed under tension while the other side (initially bonded to the roughened substrate surface) was put under compression to avoid pre-mature crack propagation and arbitrary surface roughness dependant results.

3. Computational fluid dynamics

3.1. Geometry and operating conditions

The commercially available Computational Fluid Dynamics (CFD) ANSYS Fluent 19 software was used to model the carrier and driving gas flows and particulate phase for both spray systems. The three-dimensional meshing systems, comprised of approximately 2 million cells, are shown in Fig. 2. The meshing process was generated through ANSYS WB Meshing Tool by discretizing the computational domain into separate grids and using edge sizing with a biased growth rate to increase resolution near the nozzle walls. A grid dependency study was performed to determine the appropriate grid size ensuring grid independency. The substrate surface, modeled as an adiabatic wall, was placed at the end of the atmospheric environment at the corresponding 15 mm stand-off distance. The surrounding environment was set at a radius of 80 mm to avoid disturbance on the flow field. The solutions were considered converged when the residuals were decreased by at least three orders of magnitude. In addition, the mass imbalance was also verified (~$8e^{-8}$ kg/s) at convergence.

Pressure-based boundary conditions were applied at the main gas

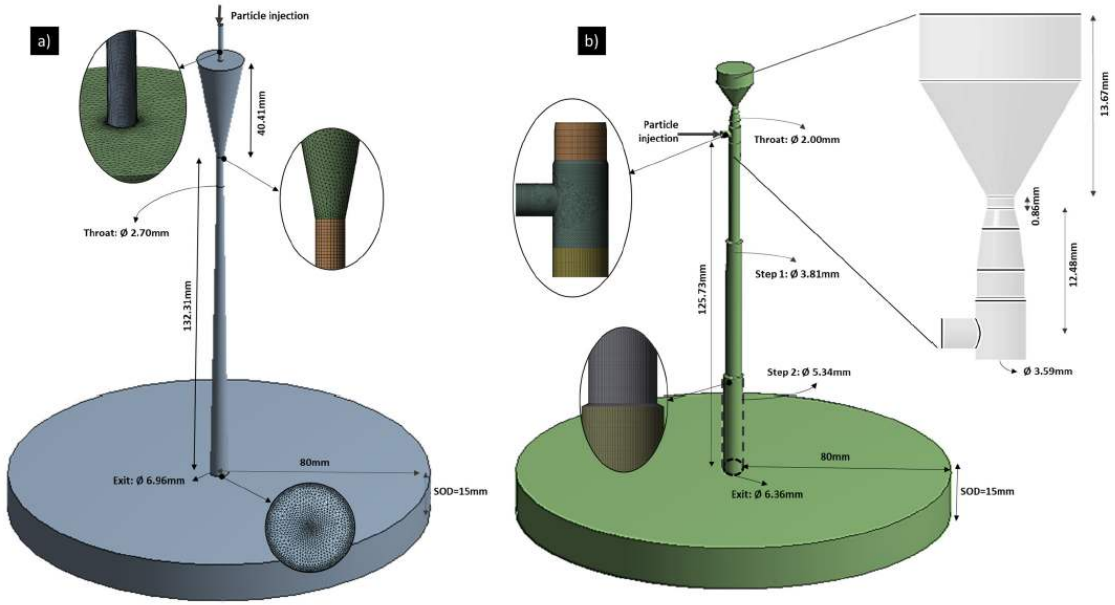

Fig. 2. Three-dimensional computational domain dimensions and meshing details for both CGDS systems. a) Upstream powder injection (HPCS system) and b) downstream powder injection (LPCS system).

inlet and outlet of each nozzle and the flow was treated as a compressible flow. Mass flow rate boundary conditions, based on used experimental set-up, were set to 0.00033 kg/s and 0.0036 kg/s for the powder feeding line nitrogen flow in the LPCS and HPCS cases respectively. A no-slip condition was enforced on all nozzle walls. The various boundary conditions are summarized in Table 2.

3.2. Gas flow model

The Reynolds Averaged Navier-Stokes (RANS) equations along with the re-normalized group (RNG k-ϵ) turbulence model were utilized to model the gas flow structure inside and outside the converging/diverging nozzle. The RANS-based model accounts for the effect of turbulence while greatly reducing the required computational resources. A total of six governing equations have thus been utilized: conservation of mass and energy, momentum balance (in three dimensions) and turbulent kinetic energy. The continuity equation is written as follow;

$$\frac{\partial \rho}{\partial t}+\frac{\partial}{\partial x_i}(\rho u_i)=0, \tag{1}$$

where ρ is the gas flow density, t is the time, u_i is the flow velocity in the i direction and x_i is a coordinate variable in space. The momentum balance is provided by;

$$\frac{\partial}{\partial t}(\rho u_i)+\frac{\partial}{\partial x_j}(\rho u_i u_j)=\frac{\partial}{\partial x_j}\left[-P+\mu_{eff}\left(\frac{\partial u_i}{\partial x_j}+\frac{\partial u_j}{\partial x_i}\right)\right]+S_M, \tag{2}$$

where P is the pressure, which includes an additional term due to the turbulent normal stress, S_M represents the mass added to the gas phase from the dispersed particulate phase or the momentum change it generates to the gas phase in each coordinate system and μ_{eff} accounts for turbulent viscosity as follow;

$$\mu_t=\rho C_\mu \frac{k^2}{\epsilon}, \tag{3}$$

where $C_\mu = 0.0845$ [48]. The k and ϵ terms are obtained using the following respective differential transport equations;

$$\frac{\partial}{\partial t}(\rho k)+\frac{\partial}{\partial x_i}(\rho k u_i)=\frac{\partial}{\partial x_j}\left[\mu_{eff}\alpha_k\left(\frac{\partial k}{\partial x_j}\right)\right]+G_k+G_b-Y_M+S_k-\rho\epsilon, \tag{4}$$

and

$$\frac{\partial}{\partial t}(\rho \epsilon)+\frac{\partial}{\partial x_i}(\rho \epsilon u_i)=\frac{\partial}{\partial x_j}\left[\mu_{eff}\alpha_\epsilon\left(\frac{\partial \epsilon}{\partial x_j}\right)\right]+C_{1\epsilon}\frac{\epsilon}{k}(G_k+C_{3\epsilon}G_b)-C_{2\epsilon}\rho\frac{\epsilon^2}{k}+S_\epsilon-R_\epsilon, \tag{5}$$

where $C_{1\epsilon}$, $C_{2\epsilon}$ and $C_{3\epsilon}$ are turbulent constants depending on the application and simulation conditions [49]. The α_ϵ and α_k quantities are the inverse effective Prandtl numbers for k and ϵ terms, respectively. G_k and G_b represent the generation of turbulent kinetic energy due to the mean velocity gradients and due to the buoyancy, respectively, while the S_k and S_ϵ are user-defined source terms. The RNG additional term, R_ϵ, in the dissipation rate equation is given by;

$$R_\epsilon=\frac{C_\mu \rho \eta^3(1-\eta/\eta_0)}{1+\beta\eta^3}\frac{\epsilon^2}{k}, \tag{6}$$

where $\eta \equiv Sk/\epsilon$ and in which S refers to the modulus of the mean rate-of-strain tensor, $\eta_0 = 4.33$ and $\beta = 0.012$ [48].

The model total energy or total enthalpy (h_{tot}) modified for the Reynolds average energy equation is given by;

$$\frac{\partial}{\partial t}(\rho h_{tot})-\frac{\partial P}{\partial t}+\frac{\partial}{\partial x_j}(\rho u_j h_{tot})=\frac{\partial}{\partial x_j}\left(\lambda\frac{\partial T}{\partial x_j}+\frac{\mu_t}{Pr_t}\frac{\partial h}{\partial x_j}\right)+\frac{\partial}{\partial x_j}\left[u_i(\tau_{ij}-\rho\overline{u_i u_j})\right]+S_T, \tag{7}$$

where Pr_t is the turbulent Prandtl number, S_T is the source term expressing the heat transfer between the flow and particles, τ is the stress tensor and λ is the thermal conductivity. The total enthalpy refers to the total energy of the system including viscous work, such that;

$$h_{tot}=C_v T+\frac{1}{2}(u_i u_i)+k. \tag{8}$$

The additional terms, i.e. S_M and S_T, provided in Eqs. (2) and (7) respectively, have been neglected due to the high Stokes number, St, and low momentum coupling interactions parameter, Π_{mom} obtained in the current study. The momentum coupling expressed in the following equation, is used to assess the impact of the aluminum particle phase on the nitrogen gas flow;

$$\Pi_{mom}=\frac{Z}{\frac{\rho_p d^2 V}{18\mu_g L}+1}, \tag{9}$$

where the subscript p and g refer to the particle and gas phase respectively, d is the particle diameter, L is the characteristic length, i.e. diameter of the nozzle at a specific location, and Z is the mass ratio of powder to gas. The momentum coupling parameter has been calculated and is less than 5% in all cases, such that the gas phase momentum variation due to the presence of particles has not been included [50]. In addition, many have used the volumetric, $\dot{Volume}$, particle to gas flow ratio to evaluate the significance of the particle phase influence on the gas flow [41,51,52];

$$\frac{\dot{Volume}_p}{\dot{Volume}_g}=\frac{\dot{m}_p}{\dot{m}_g}\frac{\dot{\rho}_g}{\dot{\rho}_p}, \tag{10}$$

where $\dot{m}$ and $\dot{\rho}$ are the mass and density flow rate, respectively. Provided that $\rho_g \ll \rho_p$ holds and that the powder feed rate used in the current study is 20 g/min, a ratio less than 1% is obtained indicating negligible effects. Particle-particle interactions can also influence the behavior of the particulate flow. The particle level of interactions can be described using the mean distance between particles, L_p, to the average particle diameter, $d_{average}$;

$$D=\frac{L_p}{d_{average}}. \tag{11}$$

Since values over ten have been obtained in the current study, the particles are considered isolated and the particle to particle interactions have been neglected [52]. Based on the above discussion details and analysis, a one-way coupled Lagrangian particle tracking method has been assessed as appropriate [50,51,53,54]. A density-based solver with a Green-Gauss node-based gradient method was utilized to model the nitrogen gas stream features. The ideal gas law has been used to account for the compressibility effects and a two-coefficient temperature-dependant Sutherland law is used to express viscosity variations with temperature [14]. Table 3 provides a summary of the gas and particle characteristics utilized in the current computational work.

Table 2
Numerical model boundary conditions.

Location	P	V	T
Nozzle inlet	Specified stagnation	$\frac{\partial V}{\partial n}=0$	Specified stagnation
Powder inlet	N/A (mas flow rate specified)	$\frac{\partial V}{\partial n}=0$	Room temperature
Surrounding atmosphere	Ambient condition	$\frac{\partial V}{\partial n}=0$	$\frac{\partial T}{\partial n}=0$
Substrate/nozzle walls	$\frac{\partial P}{\partial n}=0$	0	$\frac{\partial T}{\partial n}=0$

Table 3
Simulated phase properties included in the computational work.

	Nitrogen gas	Aluminum particles
Diameter	N/A	Set measured distribution
Stagnation parameters	500 °C, 3.45 MPa	N/A
Density	Ideal gas	2710 kg/m^3
Specific heat capacity	1040.67 J/kg K	910 J/kg K
Thermal conductivity	0.0242 W/m K	210 W/m K
Viscosity	Sutherland law	N/A
Initial velocity at carrier gas injection (LPCS, HPCS)*	(30 m/s, 33 m/s)	(30 m/s, 33 m/s)
Initial temperature at carrier gas injection (LPCS, HPCS)	(25 °C, 25 °C)	(25 °C, 25 °C)

* The particulate phase reaches the carrier gas flow velocity upon its injection into the driving gas flow.

3.3. Discrete phase/particle

3.3.1. Momentum and heat transfer

The particle phase was modeled as an inert point in space using a Lagrangian method. The velocity and trajectory of the discrete phase, i.e. the aluminum particles, in the two-phase model was computed using a drag force balance, i.e. Newton's balance equation.

$$m_p\frac{dV_p}{dt}=\frac{1}{2}C_D\rho A_p\left(V-V_p\right)^2+F_b \tag{12}$$

where m_p, C_D, A_p and F_b are the particle mass, particle drag coefficient, particle cross-sectional area and additional body forces. The particle possible deceleration due to the adverse pressure gradient generated at the substrate surface bow shock is also taken into account and included in the F_b term. The body force per unit mass is given as;

$$F_b=\left(\frac{\rho}{\rho_p}\right)V_p\cdot\nabla V \tag{13}$$

No other additional body forces have been added to the equation as the common gravity, lift, thermophoretic and electrostatic forces provide little influence on the particle momentum in the CGDS process.

The Henderson drag correlations, for C_D term definition, have been used to describe the particle momentum [55]. According to previous studies, the Henderson correlation, which covers a wide range of particle Mach and Reynolds numbers and describes flow motion from incompressible to free molecular regimes, has shown accurate results based on experimental particle–laden flow measurements [14,15,56–60]. The transient particle heat transfer processes are calculated assuming a lumped capacitance method and the energy balance equation from the first law of thermodynamics is used [14,23,61]. Details describing the terms involved in the analysis can be found in a previous study [14]. The following Nusselt, $\overline{Nu}$, correlation has been utilized to define the average convective heat transfer coefficient;

$$\overline{Nu}=2+0.44{Re_p}^{0.5}Pr^{0.33}exp\left(0.1+0.872M_p\right), \tag{14}$$

which is valid for particle Mach numbers above 0.24. In all other cases the common Ranz-Marshall model is utilized [62]. The correlation described in Eq. (14) has been shown to provide accurate particle temperature readings based on recent CGDS experimental work [14].

3.3.2. Stochastic trajectory

Since the flow is turbulent, a stochastic tracking approach, referred to as the discrete random walk (DRW) model, is applied to simulate the particle turbulent dispersion ensuring representative particle trajectories. Numerous studies conducted in the CGDS field have shown that the DRW does provide an accurate particle dispersion [41,51,54,63]. DRW computes the trajectory of each particle based on the statistical sum of the mean and turbulent velocity component of the gas. In addition to the statistical velocity measurement, an integral time scale is utilized, which accounts for the rate of turbulent kinetic energy dissipation. This time scale is linked to the characteristic lifetime of an eddy. It is assumed that a particle is in contact with the turbulent eddy for whichever time is shorter between the eddy lifetime and eddy crossing time. Sufficiently large numbers of DRW runs have been used to ensure that trajectories include the statistical effect of turbulent dispersion.

3.3.3. Numerical size distribution

To model the particle size distribution for each powder set, the Rosin-Rammler distribution function has been utilized to generate proper particle size bins in ANSYS Fluent using;

$$Y_d=e^{-\left(d/\overline{d}\right)^{n_s}}, \tag{15}$$

where Y_d represents the cumulative percent retained at size d and $\overline{d}$ and n_s are fitting parameters, referred to as the average diameter and spread factor. The obtained spread factor is 4.07, 13.87 and 14.33 for set 1, set 2 and set 3 respectively. Following the injection of accurate particle diameter bins, a function generating a random selection of particles in each bin size has been included to obtain the actual measured distribution.

3.3.4. Particle/nozzle wall interactions

In the HPCS, the powder injection line is estimated to be perfectly aligned with the nozzle axis. As the feeder tube size is the same as the nozzle throat, the particle radial acceleration and movement is limited and particle-nozzle interactions are expected to be low [52]. The particle collisions are estimated to be perfectly elastic and as the particle-nozzle impact collisions are anticipated to be limited such estimation would have little effect on results if inaccurate. For the LPCS, however, significant particle/wall interactions are expected to occur due to the radial injection process. Experimental evaluation of the coefficient of restitution for impacts between metal particles and PBI material are not found in the literature. Wu et al. have investigated the rebound behavior of spheres traveling at 5 m/s during elastic-plastic oblique impacts using FEM [64]. Although the velocity is far below the particle velocities reached in the CGDS process, particles are expected to travel with much higher axial velocity than radial velocity due to the strong axial gas flow momentum. Based on their study, the tangential and normal coefficient of restitution are both chosen to be 0.8 in the current simulation work [52,64].

4. CFD results

The current section covers the CFD results used to assess the particle in-flight temperature, which cannot be measured [14]. The heat transfer analysis and correlations used have been validated elsewhere [14]. In addition, the accuracy and validity of the models for the current study have been evaluated using particle velocity measurements and single spot deposit. The CFD results are also used to visualize the flow structure and particle trajectory.

4.1. Gas flow properties

Fig. 3 shows the gas velocity contour maps of both spray systems up to the substrate surface. The gas velocity along the HPCS nozzle varies gradually and reaches about 1000 m/s at the nozzle exit, with a thin boundary layer all along the nozzle length. Cross-sectional inserts reveal that the carrier gas affects the driving gas, producing a slower core at the nozzle center, although mixing seems to minimize the effects towards the nozzle exit. In comparison, the gas velocity reaches high values much earlier in the LPCS system, with similar exit velocity. The expansion of the gas at each sharp step of the LPCS nozzle generates the formation of an expansion wave/oblique shock wave system, creating an

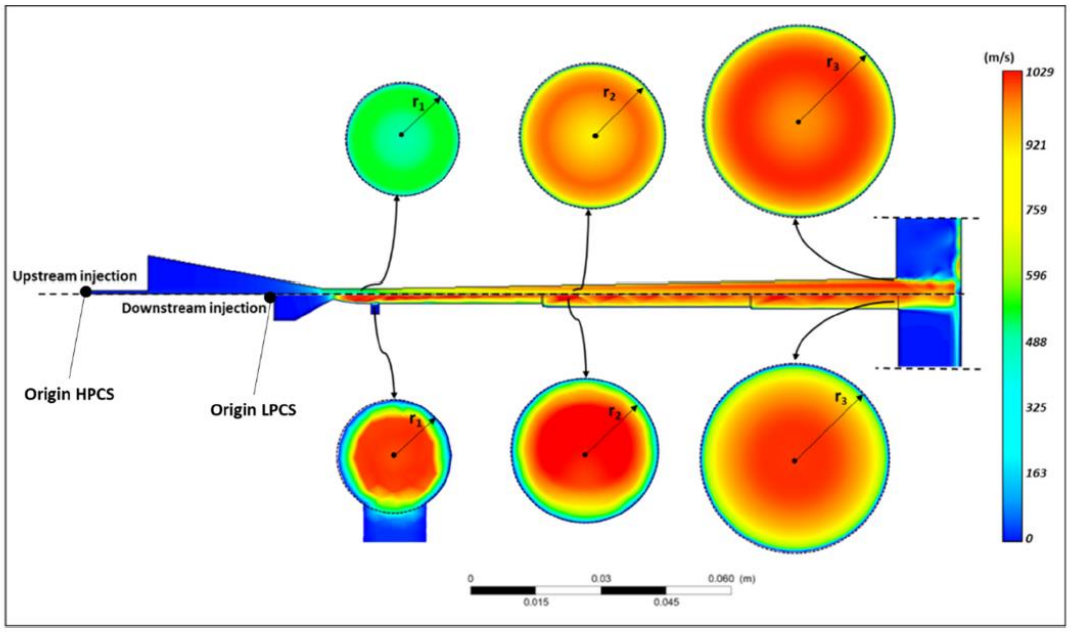

Fig. 3. 2D axial cross-sectional view of the gas flow velocity contour across the nozzle and exit region in the HPCS (top) and LPCS (bottom) systems. The gas velocity across the nozzle diameter at three selected regions (r_1, r_2 and r_3) is shown in provided inserts.

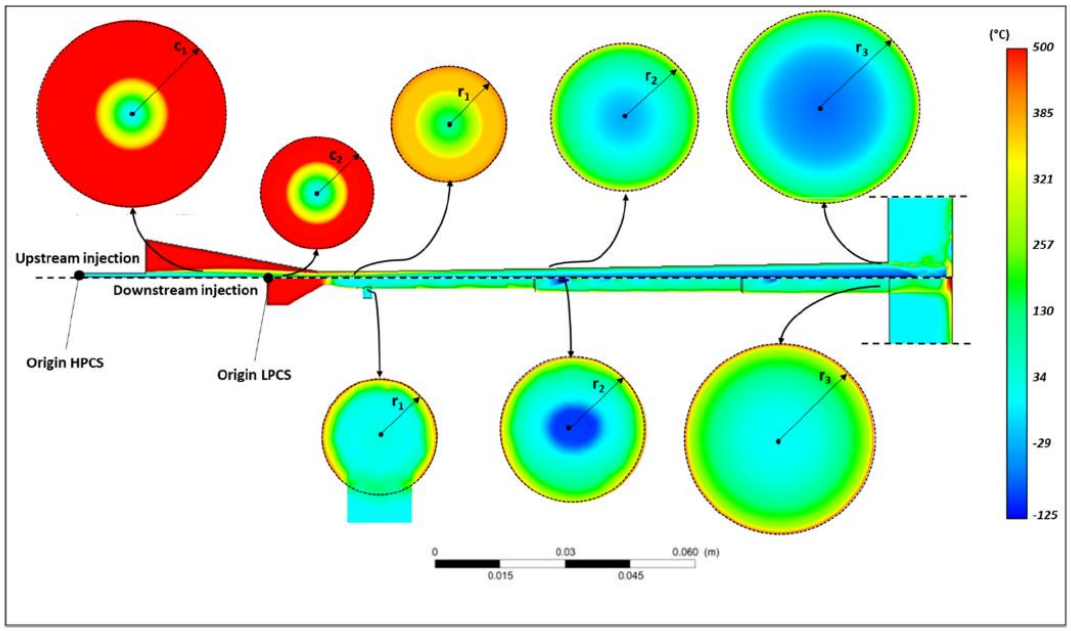

Fig. 4. 2D axial cross-sectional view of the nitrogen flow temperature contour across the nozzle and atmospheric regions in high (top) and low (bottom) pressure CS systems are provided. In the HPCS, the gas temperature in the converging section is illustrated using two cross-sectional inserts (c_1 and c_2). The gas temperature across the nozzle diameter at three regions in the diverging section (r_1, r_2 and r_3) is shown using provided inserts for both systems.

oscillatory pattern in the gas flow that maintains/replenishes a high gas velocity outside the boundary layer zone. These structures stabilize after multiple reflections due to viscous effects, homogenizing the flow profile. Furthermore, the radial carrier gas injection also affects the driving gas properties. This main flow disturbance remains following the wall boundary layer, such that the high shock trail flow appears as a dissymmetrical phenomenon. The carrier gas effect is damped after the first nozzle step.

The gas static temperature contour maps are shown in Fig. 4. In the HPCS nozzle, the gas temperature decreases gradually to reach around −75 °C in the core, at the nozzle exit, as thermal energy is converted into kinetic energy. The cold carrier gas is clearly visible in r_1 and r_2 regions, which generates a colder central flow surrounded by the high temperature main flow. This cold core also limits the stagnation temperature in the converging section, i.e. regions c_1 and c_2. In the LPCS nozzle, the oscillatory shock wave system generates local zones of very low temperature in the diverging nozzle section (−125 °C in r_2). The gas core exits at around 50 °C, due to the low nozzle expansion ratio and with an almost uniform thermal energy distribution.

Fig. 5 shows the gas temperature and velocity maps near the substrate surface for both CS systems. A normal bow shock occurs as a result of the flow adjustment to the downstream stagnation perturbation (substrate). An outward radial deflection of the primary flow follows. While this flow is attached for the LPCS configuration, it is a recirculating flow in the HPCS system, as shown in Fig. 5b. This difference has been associated to the dissimilar Reynolds number (*Re*) that each flow reach in both systems, i.e. increasing *Re* have been linked to the generation of downstream wall-jet recirculation[65]. The flow mechanisms controlling the wall jet features are mainly the jet-edge expansion and its reflexion from the sonic line and wall-jet boundaries [66]. One can observe that while the LPCS jet reaches a stagnation temperature of 500 °C in the zone under the normal shock, the HPCS jet reaches a temperature of 327 °C only. It is expected that these temperatures could have an effect on the substrate temperature during spraying [65,67].

4.2. Effect of particle injection and size on in-flight characteristics

Examination of LPCS particle streak lines (only one streak line is shown as an example) reveals that all powder sets come into contact with the nozzle wall in zone 2, prior to the first nozzle step. This location corresponds to the zone shown to experience important nozzle erosion [45], confirming the accuracy of the computed particle path lines. The powder rebound path is dependent on particle size with larger particles being able to recoil further towards the nozzle center and cross the shock wave trail on their path from the wall to the center due to their higher inertia. This is reflected through the particle distribution in the velocity/temperature maps presented in Fig. 6. In addition, smaller particles are seen to accelerate and decelerate faster in the stream center and shear layer respectively. Hence, set 1 particles reach velocities up to 680 m/s at the nozzle exit while powder set 3 reaches 620 m/s. Analogously, smaller particles heat transfer rate is larger than that of larger particles due to their larger specific surface. Although the particle temperature is seen to slightly increase in the high temperature shear layer at the nozzle wall, with a larger increase for smaller particles, their limited time in the wall boundary combined with fast velocities and trajectory in the cold central supersonic gas stream only permits slight increase in temperature. At the nozzle exit, particles from set 1, set 2 and set 3 reach temperatures up to 72 °C, 58 °C and 41 °C respectively.

Fig. 7 shows the particle characteristics and overall spread in the HPCS. The high symmetry footprint of particle dispersion is attributed to the injection alignment with the nozzle axis. From zone 1 to zone 2, the particle stream widens due to the presence of turbulence and low gas velocity in the gas mixing area. Smaller particle having less inertia contribute mostly to the radial dispersion. However, from zone 2 to zone 4, the presence of the narrow throat and higher gas central velocity confines the majority of particles in the nozzle center. At the nozzle exit stream center, particle set 1 reaches velocities up to 690 m/s while set 3 particles are accelerated up to 625 m/s. Smaller particles are heated to a higher temperature as their spread towards the nozzle wall is more pronounced in the converging gas mixing area in zone 2. Analogously, colder particles at the exit of the nozzle originate from a mixture of cold particles coming from the cold un-mixed converging-throat center and from radially dispersed particles traveling in the cold slow diverging flow. As a result, set 1, 2 and 3 feedstock powder particles reach a wide spread of in-flight temperatures with values reaching 327 °C, 227 °C and 202 °C respectively, at the nozzle exit.

In addition, for the three powder size sets and for both utilized CGDS systems, it was found that the bow shock and the 15 mm particle flow distance from the nozzle exit do not drastically affect the particle in-flight characteristics.

5. Experimental results

5.1. Particle in-flight velocity

In order to validate the model predictions and ensure particle temperatures can be inferred adequately from the model, particle velocity measurements were conducted at the center of the gas stream, and at distance of 15 mm from the nozzle exit, using feedstock powder set 2. The measurements provided average particle velocities of 668 m/s and 660 m/s for the HPCS and LPCS systems respectively. In addition, the numerical average particle velocities obtained at the same location generated average velocities of 620 m/s and 600 m/s for the HPCS and LPCS system respectively. This agreement between experimental and numerical results provides some reliability of the simulations and its additional use in finding particle in-flight characteristics. Consequently, as both systems provided similar particle impact velocities, it is assumed that all results can be properly compared for each powder set between the two CS systems.

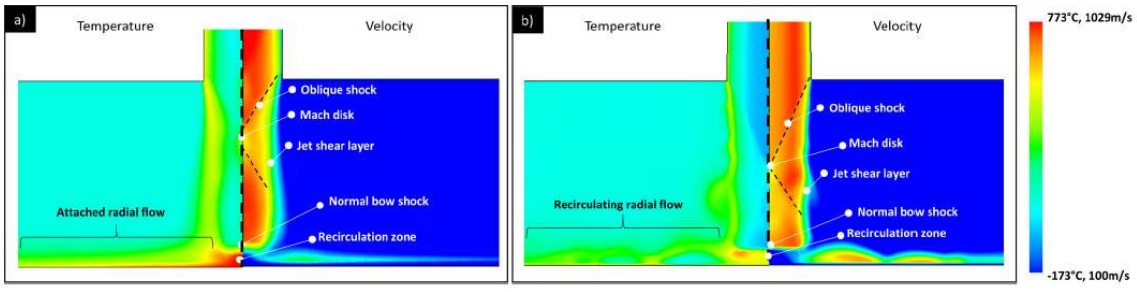

Fig. 5. Flow temperature and velocity at the substrate vicinity showing the radial gas flow regimes obtained in the a) LPCS and b) HPCS systems.

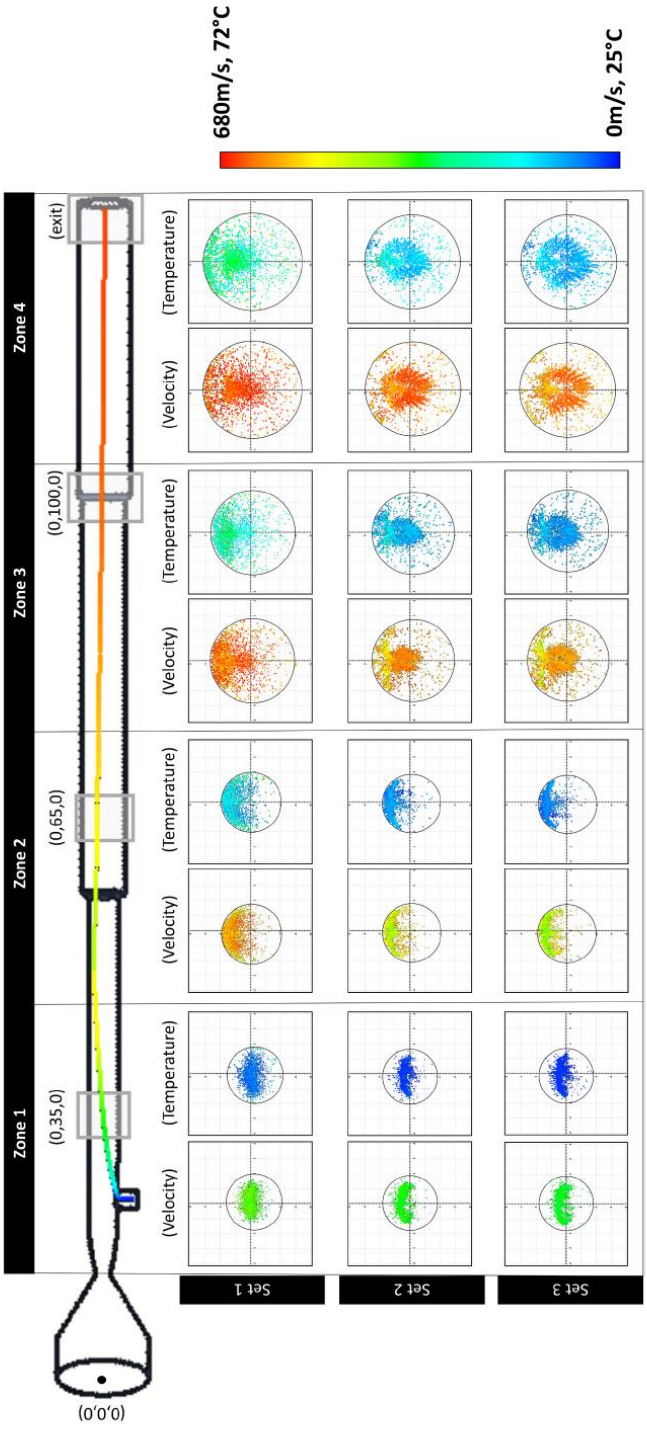

Fig. 6. LPCS particle velocity and temperature from near powder injection location to nozzle exit. Particle radial distribution and spatial temperature and velocity at different locations are provided, i.e. 35 mm (zone 1), 65 mm (zone 2), 115 mm (zone 3) and 147 mm (zone 4) with respect to the set origin (0,0) position. A single in-flight velocity streak line of a 40 μm particle is depicted to demonstrate the effect of nozzle impact on the particle overall momentum.

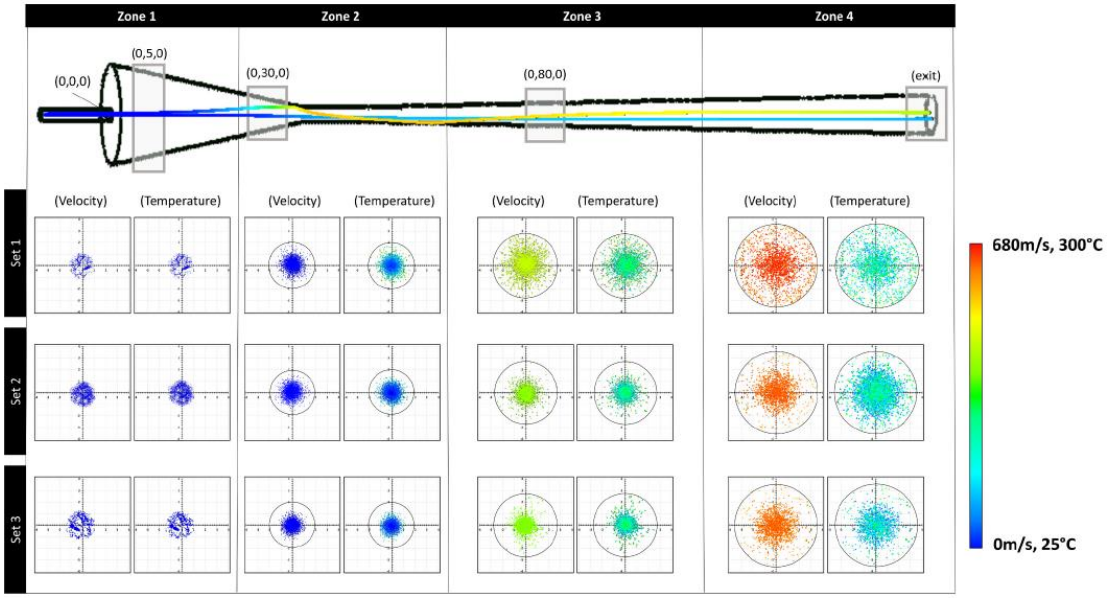

Fig. 7. HPCS particle velocity and temperature from powder injection to nozzle exit. Particle radial distribution and spatial temperature/velocity at different locations are provided, i.e. 5 mm (zone 1), 30 mm (zone 2), 80 mm (zone 3) and 172.5 mm (zone 4) with respect to the set origin (0,0) location. Two particle streak lines, i.e. central cold and hot scatter, of a 40 μm particle are depicted to show the influence of particle spreading in the sonic zone on the in-flight particle exit temperature.

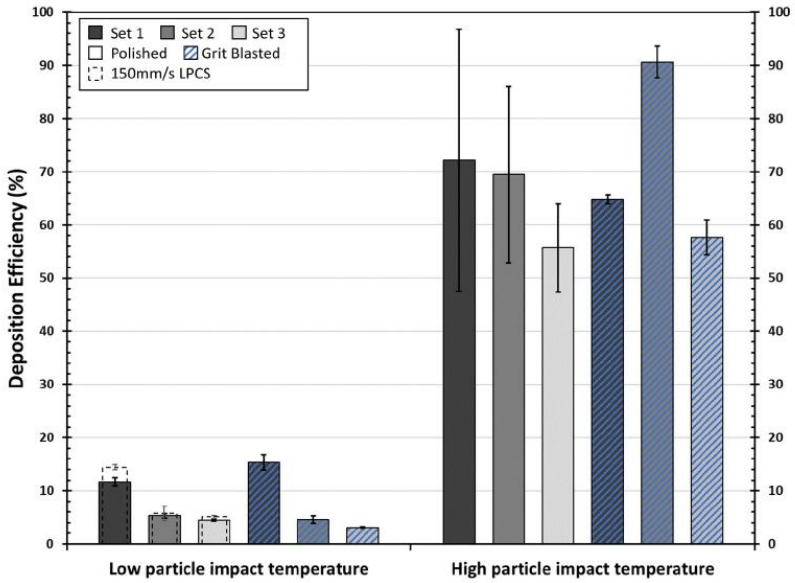

Fig. 8. Coating DE for various particle size range (sets) and substrate surface roughness deposited using both LPIT and HPIT depositions. Data shown as solid fill represents deposits made on polished surfaces while patterns filled data correspond to coatings generated on grit blasted substrates. Superimposed dashed columns in the LPIT represent the DE for coatings sprayed at a gun traverse speed of 150 mm/s on polished surfaces.

5.2. Deposition efficiency

Fig. 8 shows the DE of all deposited aluminum coatings in the current study. For coatings produced with low particle impact temperature (LPIT) using the LPCS system, the DE is low and the particle size noticeably affects it. The feedstock powder set 1 is almost double the DE values obtained for powder set 2 and set 3, i.e. 13% vs ~5%. Fig. 8 also shows that the CS gun traverse speed has minor influence on the measured DE. A significant improvement in DE is recorded when particle impact temperature is increased with average DEs of 81%, 76% and 57% for powder sets 1, 2 and 3 respectively, which shows a decrease with particle size increase. Finally, the substrate surface roughness with a measured R_a of 6.3 ± 1.8 μm and 0.3 ± 0.1 μm after grit blasting and polishing respectively, expected to affect primarily the deposition of the first layer of particles [68,69], does not influence the overall measured DE in all sprays. The sudden drop in DE of the high particle impact temperature (HPIT), generated using the HPCS system, feedstock set 1 onto the grit blasted sample is believed to be caused due to inconsistent powder feeding resulting from local clogging/deposition inside the nozzle.

Fig. 9 shows the top surface of the produced coatings using both LPIT and HPIT depositions illustrating the effect of different impact dynamics occurring due to particle size and particle impact temperature. LPIT deposits exhibit much smoother coating surfaces as the particles are more deformed, and this effect is enhanced with increasing particle size. The coating top surface features for LPIT depositions generated under both traverse speeds are the same such that only one is shown for conciseness. The top surface of HPIT coatings shows minimal particle deformation upon impact, as seen in Fig. 9b, d and f, as the particle original spherical shape is easily detectable.

5.3. Coating adhesion strength

Fig. 10 shows the coatings adhesion/cohesion strength for all sprayed cases. The substrate surface roughness generated using a grit blasting process induces a low adhesion strength irrespectively of particle impact temperature and size. The average adhesion strength on grit blasted surfaces for both low and high particle impact temperatures is 10.9 ± 4.5 MPa. Similar adhesion strength values have been observed in a previous work with irregularly shaped pure aluminum powder

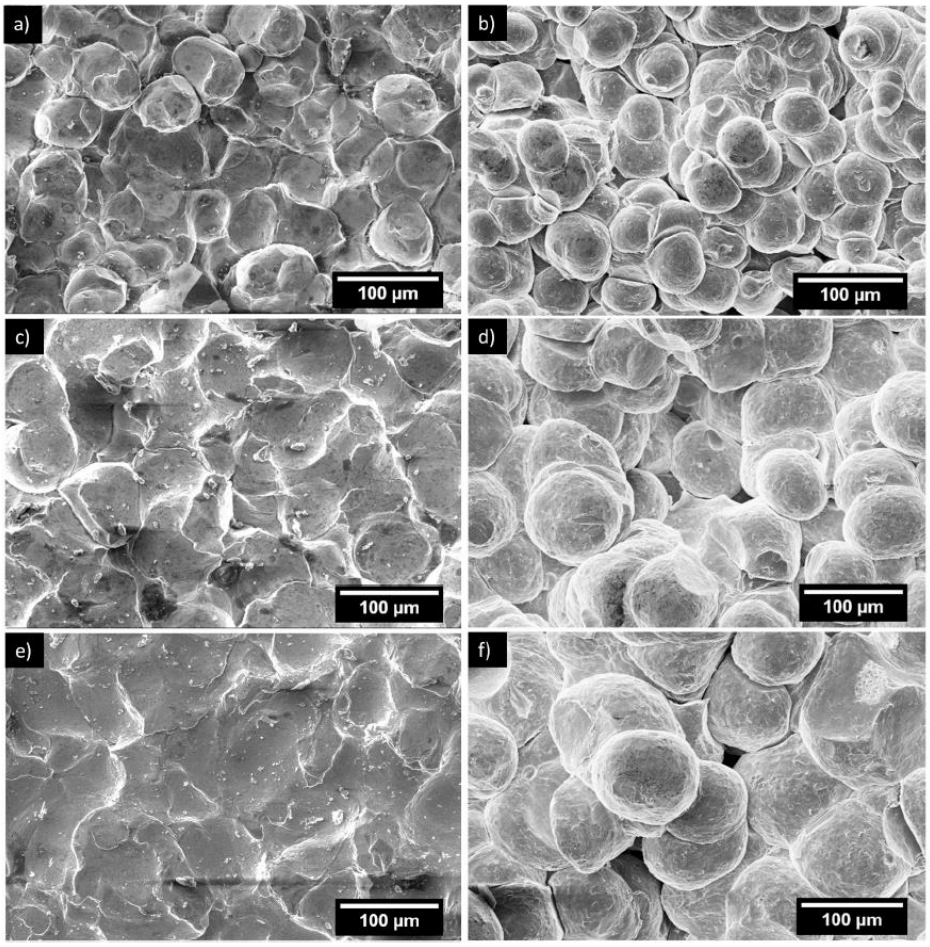

Fig. 9. Coating top surface topography after spray illustrating the contrast in impingement phenomena when utilizing low (left) and high (right) particle in-flight temperatures for powder (a–b) set 1, (c–d) set 2 and (e–f) set 3.

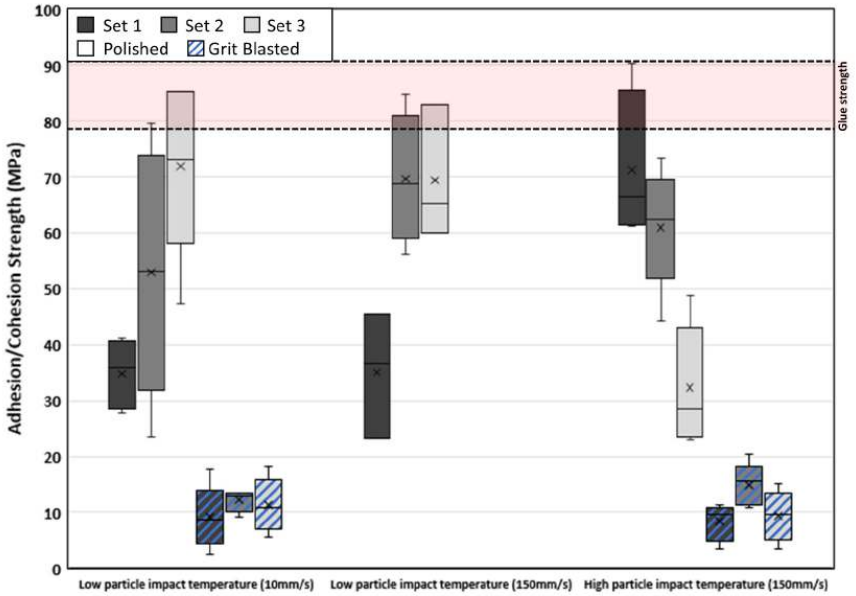

Fig. 10. Coating adhesion/cohesion strength based on particle size (sets 1–3) and substrate roughness for sprays generated using low and high particle impact temperatures. The box shows the position of the 25th percentile, median and 75th percentile. Whisker lines illustrate the data variability outside the upper and lower quartiles while the 'x' marker displays the mean data value. The minimum and maximum values exclude outliers.

material [5].

An increase in coating adhesion strength is observed with the increase of particle diameter for LPIT deposits. The average value increases from 34.8 MPa to 71.7 MPa for set 1 to set 3 powder size sets. The CS nozzle traverse speed for LPIT sprays shows minor influence on the general bond strength trend across all three sets of deposited powders. A decrease in adhesion/cohesion strength is observed with particle size increase for the case of HPIT sprays, from 71.2 MPa to 32.3 MPa for set 3 and set 1 respectively. This trend is the opposite of the one observed for LPIT.

Fracture surface topologies of the pull test sets have also been obtained for deposits made on polished surfaces, as shown in Fig. 11, to characterize the phenomena responsible for coating failure. Imaging of grit blasted surfaces fracture surface topologies was omitted due to the coating consistent low adhesion stress failure. The fracture topology imaging describes the fracture zones by providing the failure location inside the layered pull test set, i.e. glue, coating (cohesion) and/or substrate/coating (adhesion).

Complete coating separation at the interface is detected for all sets sprayed using LPIT at a traverse speed of 10 mm/s, as shown in Fig. 11a–c. The coatings, irrespective of particle size and unrelatedly to the recorded bond strength, fail in complete adhesion. As shown in Fig. 11a–c, the substrates surfaces after adhesion tests retained their mirror finish polish i.e. observable through the reflective surface feature, indicating that the recorded adhesion failures primarily involve metallic bonding and lack mechanical anchoring. Coatings sprayed at LPIT and at a traverse speed of 150 mm/s display a similar complete coating separation from the substrate surface, with limited residual aluminum particles, for powder set 1. However, local adhesion fracture is observed for powder set 2–3, as seen in Fig. 11e–f.

Finally, localized irregular adhesion fracture is seen for coatings deposited with HPIT, as depicted in Fig. 11g and h. Powder set 3, however, characterized with the lowest bond strength, failed in a mixed adhesion/cohesion process. This rupture nature is observed on the entire substrate surface, which excludes distinctive localized fracture developments.

5.4. Bend-to-break tests and fractography

As shown in Fig. 12a, coatings generated using LPIT sustain large deformations prior to crack initiation and eventual full propagation, suggesting high apparent ductility. Prior to failure, tested coatings had to be bent multiple times to initiate fracture. HPIT coatings, on the other hand, broke abruptly, as shown in Fig. 12b–c, with limited crack deflection and at restricted curvature.

The resulting fracture surfaces from the bend-to-break tests are shown in Fig. 13. The LPIT coating fracture surfaces show presence of very irregular and jagged features, representative of highly impinged particle network, enhanced particle to particle contact, fish scale particle-particle architectural arrangement and some level of intra-particle fracture. For the HPIT samples, the fracture surfaces exhibit a prevailing inter-particle crack propagation route, leading to a smooth path characteristic of the highly noticeable spherical particle geometry.

6. Analysis and discussion

The current section provides a detailed analysis of the numerical and experimental results to associate generated coating properties and characteristics to particle impact temperature and size. A deeper look into the numerical work offers a statistical view of particle impact characteristics, dependent on flow trajectory and size, necessary for successful deposition and improved adhesion.

6.1. Deposition efficiency and critical velocity (V_C)

The influence of particle impact temperature and size as well as substrate state on DE and V_C are presented in the current sub-section.

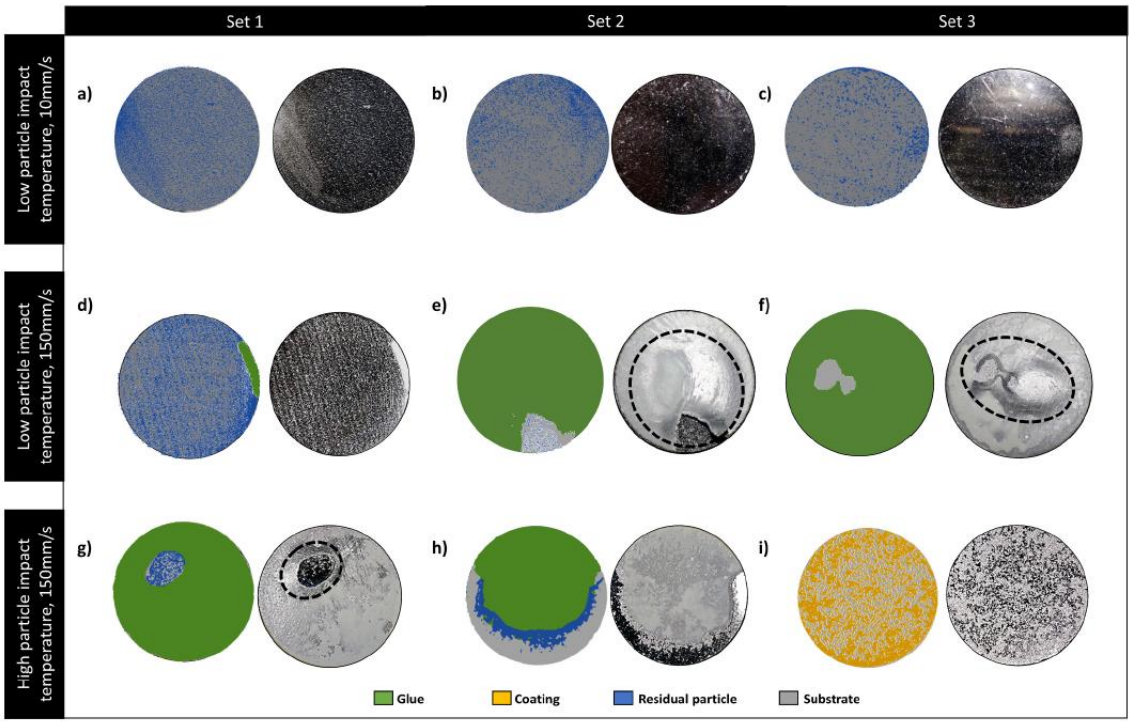

Fig. 11. Representative failure features after pull test of the substrate side only. For each case, the right image shows the actual state of the coated substrate surface after pull test while the left provides distinction between different zones on the same substrate side using a color code, which is defined in the legend. The resulting strength at failure for each shown case (and corresponding particle size set) is a) 40 MPa (set 1), b) 68 MPa (set 2) and c) 74 MPa (set 3), d) 45 MPa (set 1), e) 67 MPa (set 2) and f) 72 MPa (set 3), g) 70 MPa (set 1), h) 65 MPa (set 2), i) 49 MPa (set 3). Dotted lines delineate zones of protruding coating. (For interpretation of the references to color in this figure legend, the reader is referred to the web version of this article.)

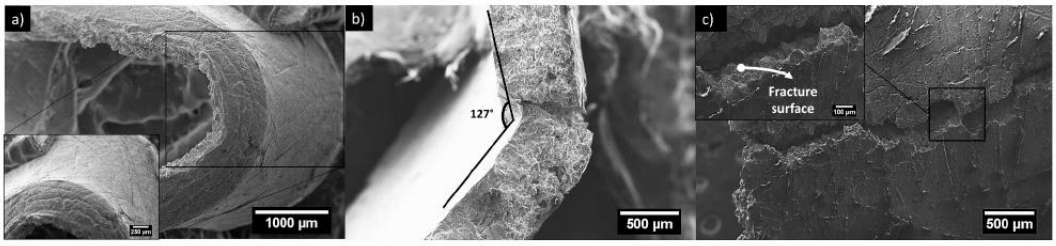

Fig. 12. SE SEM images of coatings during the bend-to-break process using feedstock powder set 2 with a) LPIT deposits showing no sign of cracking during the first phase of the bend-to-break test and b–c) HPIT deposits. A fracture surface from the HPIT coating is highlighted in image c).

6.1.1. Particle temperature influence

It is seen from Figs. 6 and 7 that the spray parameters and nozzle configurations used allowed reaching LPITs (around 50 °C) and HPITs (above 200 °C) for similar particle impact velocity, for each feedstock powder set. This increase in particle temperature facilitates dislocation motion such as climbing and cross-slip, enabling dislocation-based material softening, enhancing particle deformation, increasing local heating, with potentially larger interfacial regions reaching $0.5T_{melting}$ due to the conversion of kinetic energy into heat during the impact process and improving oxide layer fracture and removal processes [36,37,70]. Altogether, these effects increase fresh metal surface contact available for bonding and decrease V_C [37,39], which results in the increase of DE for high particle impact temperature cases, seen in Fig. 8, for the three feedstock sets compared to the cases of LPIT.

Detailed analysis of the data from Figs. 6 and 7 allows generating a statistical particle velocity distribution for each tested case, shown in Fig. 14. To capture the actual powder size distribution, particles have been selected randomly from each size range following the measured number distribution percentage. A total of 10,000 particles have, thus, been used for each analyzed powder set.

The results show similar overall particle velocity distribution trends and average particle velocity between both particle impact temperatures for all three sets of powders. The V_C values for each case have been obtained from Fig. 14 data by grouping fastest particles together until

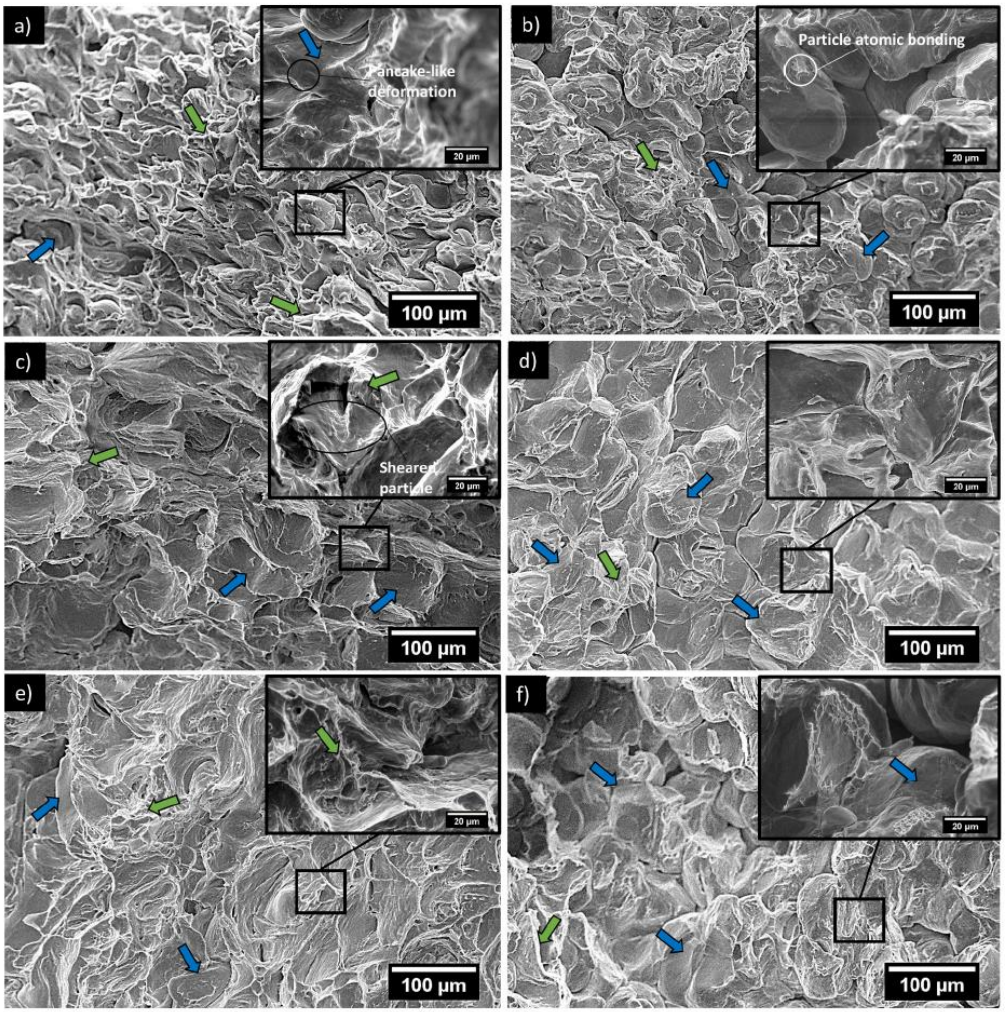

Fig. 13. Fracture surfaces from the bend-to-break tests for coatings generated with low (left) and high (right) particle impact temperatures. Shown coatings correspond to (a–b) set 1, (c–d) set 2 and (e–f) set 3. Blue arrows point to zones of inter-particle separation and green arrow indicate presence of intra-particle failure. (For interpretation of the references to color in this figure legend, the reader is referred to the web version of this article.)

their amount percentage over the overall particle population matched the measured DE [36]. The slowest particle velocity in these grouped particle population was chosen as the corresponding V_C of the studied powder set. Fig. 14 highlights, i.e. in black and green, all particles traveling faster than the critical velocity evaluated for each case, while Table 4 summarizes the obtained V_C values. The increase of particle impact temperature results in a decrease of V_C for each powder set, as suggested by theoretical models that predict a decrease in V_C as particle impact temperature increases [71].

6.1.2. Particle size effect

The particle native oxide layer thickness and oxide content can influence V_C and thus DE. The thicker the oxide layer, the more kinetic energy is required to break and remove this shell, reducing the energy available for particle and substrate plastic deformations that lead to bonding. Particle oxygen content was detected through inert gas fusion method for the current particle sets. Assuming that the oxygen content is solely associated to the surface oxide, it was found that this layer decreased from 15.4 ± 3.3 nm for powder set 1 to 10.2 ± 2.8 nm for particle set 3 [72], which can also be used to partially explain the V_C observed reduction with particle size. If the oxygen content originates from oxygen inclusions present at grain boundaries, it is expected that the oxide-dispersion strengthening process during deformation will be of less consequence for larger particle size due to the lower oxide concentration in larger particle volumes, leading again to a lower V_C as particle size increases. This size dependent influence on V_C is more easily demonstrated for LPIT as the impact temperature remains low and almost constant for all three particle sets, thus only the diameter is changed. It is observed that particle V_C decreases with increasing particle size.

Fig. 8 shows that the measured DE of all coatings decreases with particle size. As particle size increases, Fig. 14 shows that the velocity distribution shifts towards slower speeds, following approximately the relation $V_p \propto d^{-1/2}$ given between particle velocity vs particle diameter

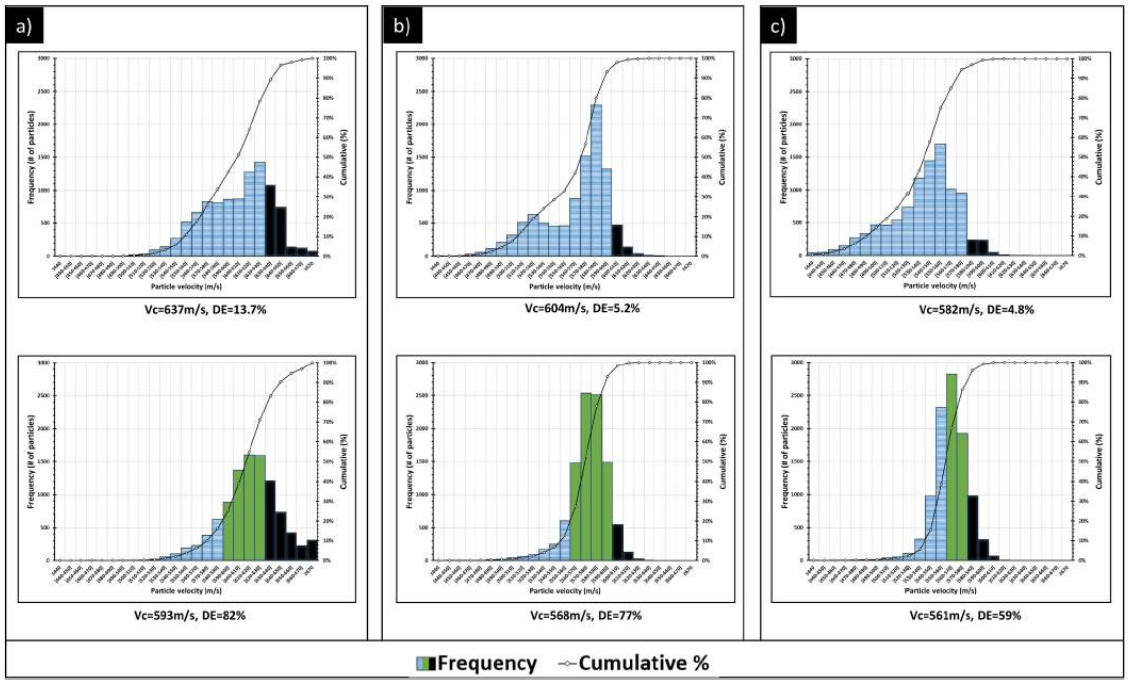

Fig. 14. Model results of particle velocity distribution and cumulative sum at the nozzle exit for 10,000 representative particles from a) set 1, b) set 2 and c) set 3. Top and bottom row refer to deposits generated with LPIT, through the LPCS system, and HPIT, through the HPCS, respectively. In black: particles traveling above the LPIT V_C. In green: particles traveling at HPIT V_C. In blue: particles traveling below their respective V_C. V_C are evaluated based on experimental DE measurements. Corresponding numerical V_C and DEs are indicated for each powder set. (For interpretation of the references to color in this figure legend, the reader is referred to the web version of this article.)

Table 4
V_C for all three powder sets and both low and high particle impact temperature.

Powder size	Set 1 ($\phi_{average}$ = 40 μm)	Set 2 ($\phi_{average}$ = 53 μm)	Set 3 ($\phi_{average}$ = 63 μm)
LPIT V_C	637 m/s	604 m/s	582 m/s
HPIT V_C	593 m/s	568 m/s	561 m/s

[72]. This results in lower DE despite the reduction of V_C associated with larger particle size as the particle impact velocity decreases more rapidly than its V_C.

6.1.3. Substrate surface state influence

6.1.3.1. Roughness. The substrate surface roughness, which mostly affects the first layer of deposited material, shows no influence/trend on measured DE, as presented in Fig. 8. If any, the effects, which would take place only at the interface between the first particle layer and substrate, are being suppressed by the overall averaging process involved in DE measurement. Analogously, the V_C determined from Fig. 14 is almost inclusively the V_C amongst the CS aluminum particle layers, which also disregards the influence of substrate surface properties. However, due to the harder nature of the steel substrate in comparison to the CS aluminum, the V_C values of the first impinging particles are expected to be lower than the reported numerical values in the current study [71,73].

6.1.3.2. Temperature. The substrate temperature in the current study has been indirectly varied by adjusting the gun traverse speed in the LPCS system to induce varying gas/substrate impact interaction times. Based on obtained results shown in Fig. 8, the substrate temperature shows no significant influence on measured DE. This can be associated to the DE measurement averaging process and/or limited instant local surface temperature rise the change in gun traverse speed generates and/or restricted heat transfer processes it produces across the interface. As the most probable and substantial cause is related to the DE measurement process, actual local temperature effects can be present. If any, the effects of temperature rise, through gun traverse speed modifications, on V_C are twofold. A temperature rise can enhance substrate deformation during impact, which can promote proper substrate oxide fracture and removal resulting in a decrease of V_C. In addition, the increase in temperature and extended jet time from decreased gun traverse speed can also improve surface cleaning processes i.e. organic debris, permitting proper fresh-metal contact for eventual bonding. On the other hand, substrate surface temperature rise can likewise increase V_C from possible substrate oxide scale growth during the cooling process within the atmospheric environment occurring once the hot supersonic nitrogen stream leaves the substrate surface. As the growth of an oxide scale has a direct measurable impact on adhesion, this possible influence of temperature will be verified and discussed in the next section.

6.2. Adhesion strength

While the DE and V_C can simply be defined based on a binary "successful vs unsuccessful" deposition criteria, the coating properties such as adhesion strength account for the variety of particle impact characteristics. This is particularly the case for the HPIT cases in which a large population of particles with different impact characteristics achieves

successful deposition while only a limited collection does deposit in the case of LPIT as revealed by the lower DE. This breadth of particle impact characteristics is expected to affect the coating overall structure and adhesion.

The particle impact characteristics variance is presented in Fig. 15, which illustrates the particle population at the nozzle exit reaching speeds above V_C, from the particle streak results presented in Section 4.2. One can observe that the particles spread for the LPIT case corresponds well with the experimental single spot sprays (nozzle not moving) included in Fig. 15a and c for set 1 and set 3 respectively. This dispersion confirms the departure of particle distribution from stream symmetry and attests skewed particle size dependent trajectory. In the HPIT cases, the particle spread includes a clear high particle concentration at the nozzle center and a gradual decrease in particle stream density following a Gaussian-like distribution, as most commonly observed in CS depositions [74]. In addition to all particles reaching warmer temperatures than in LPIT cases, a large temperature distribution is also detected for all three sets.

6.2.1. Particle temperature effect

For a set particle diameter, V_C can vary significantly as the impact particle temperature can fluctuate from one particle to another based on their in-flight history. To relate particle impact characteristics to the inherent individual particle V_C, the following expression is used for material impacting on the same material [75];

$$V_c = k_1 \sqrt{c_p\left(T_m - T_p\right) + 16\,\frac{\sigma}{\rho_p}\left(\frac{T_m - T_p}{T_m - 293}\right)} \tag{16}$$

where T_m is the particle melting temperature, T_p is the particle impact temperature, σ is the tensile strength of the particle material at 293 K, k_1 is a particle size-dependent fitting parameter and c_p is the specific heat of the particle material. To find the size-dependent dimensionless fitting parameter, k_1, the LPIT characteristics have been utilized as their temperature has been found to be very similar for all particle size range. The T_p term has been taken as the average particle exit temperature and V_C as the numerically calculated V_C of each powder set. The resulting particle size dependent fitting parameters are 0.56, 0.59 and 0.62 for powder sets 1, 2 and 3 respectively, which fits within the range anticipated during the development of Eq. (14) [75].

Using these values of k_1, the dimensionless parameter $\eta = V / V_C$ is used to qualitatively evaluate the extent at which each particle exceeds its inherent V_C for each deposited feedstock set and for both LPIT and HPIT cases. The results are outlined in Fig. 16 using a box and whisker plot in which the quartile calculation excludes the median and upper outliers. For particles impacting on the same material, larger η values would lead to larger adhesion/cohesion strengths [75], but this is not always the case for the adhesion of dissimilar materials [76]. In the current work, since all studied conditions generate a minor substrate deformation compared to the particle, the provided trends in Fig. 16 are considered representative. However, no quantitative significance is given to values of η as the overall influence of substrate nature on deposition is disregarded in both the current calculated V_C values and Eq. (14).

One can observe that for the same feedstock set and for both LPIT and HPIT cases, the average value of η is slightly larger for the latter case, as a result of the increased particle impact temperature. One should expect the HPIT cases to exhibit larger adhesion/cohesion strengths than their low particle temperature counterparts that were sprayed at the same impact velocity but lower η. Although only the effect on cohesion has been recorded through powder set 3 measured strength, it is expected that both powders set 1 and set 2 follow the trend despite the glue failure and consequently unknown actual adhesion strength.

However, this expected trend is not observed. This suggests that the adhesion strength might be governed by other factors than solely by those included in the η parameter. It is anticipated that the extensive in-

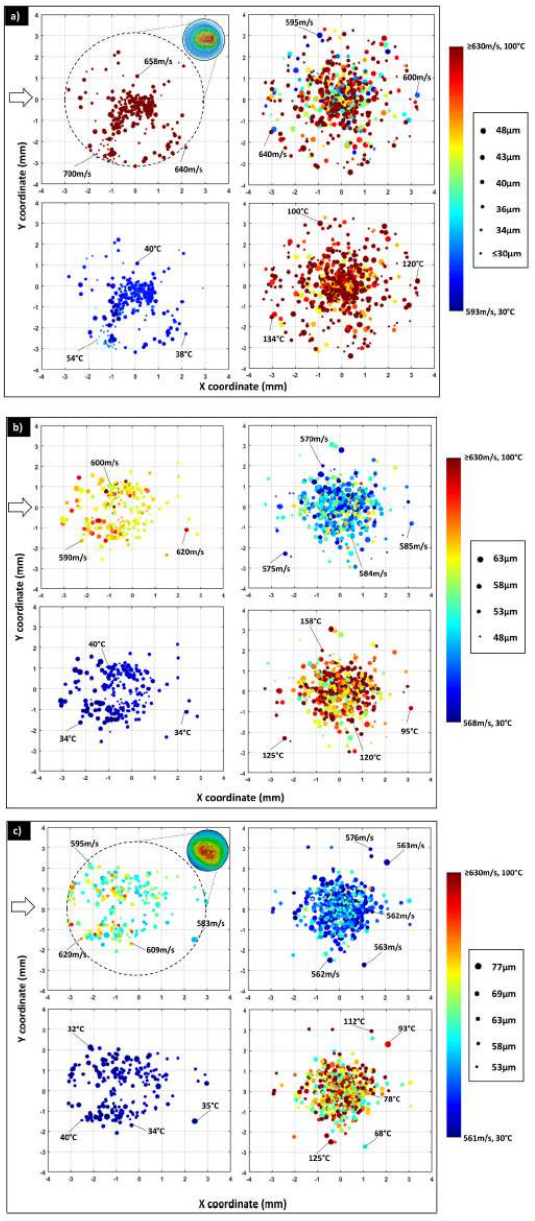

Fig. 15. Particle spread colored based on local particle velocity (top) and temperature (bottom) for the low (left) and high (right) particle impact temperature deposits, and for a) set 1, b) set 2 and c) set 3. Particle individual size, within each set, is illustrated by varying the representative dot dimensions. The powder injection in the LPCS is oriented from the negative-x axis towards the origin as demonstrated by the included arrows. Inserts of experimental LPCS spot spray deposits are incorporated to additionally demonstrate the simulation result accuracy.

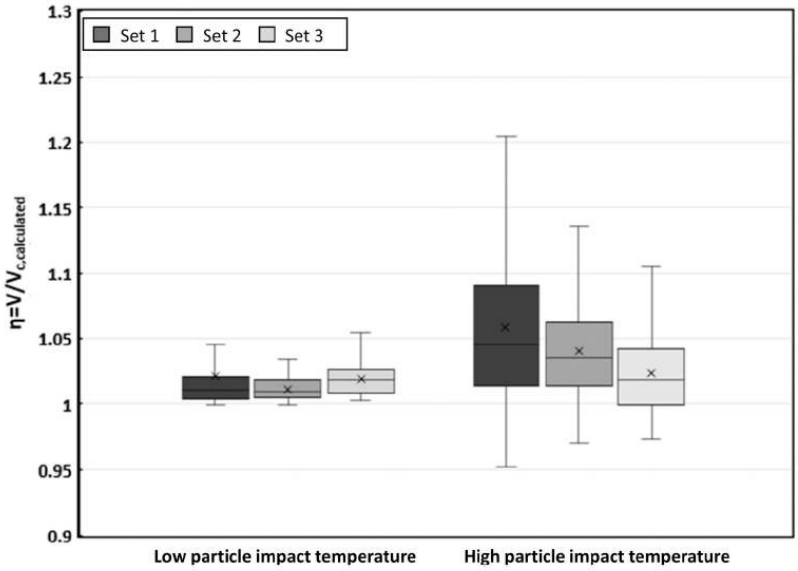

Fig. 16. Particle $\eta = V / V_C$ for all three sets of feedstock powder and for deposits generated at varying particle in-flight temperature. The minimum and maximum values exclude outliers.

situ hammering as a result of low DE for the LPIT cases must govern the adhesion/cohesion results for these three sets. Bouncing off particles provide significant in-situ hammering/shot peening to increase the deformation of deposited particles, improve the oxide film removal through shear and enhance interfacial fresh metal contact pressure of particles adhered to the substrate surface, all of which are considered factors contributing to adhesion. The results also suggest a particle impact temperature threshold under which impingement becomes the primary factor governing adhesion/cohesion strength.

6.2.2. Particle size effect

For the LPIT cases, an increase in bonding strength with an increase in particle size is observed and is associated primarily to the decrease of DE with particle size, which enhances the impingement effect as previously explained. In addition, the slower cooling rates associated with larger particles following deposition can lessen thermal stresses and shrinkage related local in-situ de-bonding processes, favoring developments and subsistence of atomic bonding [77]. For the HPIT cases, the influence of particle size on adhesion is associated to both the particle size dependent impact temperature and velocity. As observed in Fig. 15, an increase in particle size leads to an important drop in temperature and velocity distribution, which together lower the particle population capable of exceeding velocities well above their V_C, i.e. reduced η, leading to the observed reduction in adhesion with particle size. Analogously, the inter-particle cohesion strength is also expected to decrease with decreasing η values, which is shown to occur in the current study as the coating fracture mode shifts from adhesion (set 1 and set 2) to a mixture of cohesion/adhesion (set 3) with increasing size, as shown in Fig. 11g–h–i.

6.2.3. Substrate surface state influence

6.2.3.1. Roughness. The low coating adhesion strength of LPIT cases on grit blasted surfaces, as presented in Fig. 10, is associated to the substrate topography influence on particle deformation. The roughened surface restricts material flow localization, heat generation and contact pressure, which deprives the interface of processes required for the generation of strong metallic bonds [44]. In addition, rough surface profiles can trap disrupted oxide film residues serving directly as a barrier to fresh-metal contact [44]. Since the same adhesion trend is observed for the HPIT cases, it can be hypothesized that the η parameter values reached in the current study are insufficient to alter the contact processes. Provided that the adhesion values fall below 20 MPa, the coating connection onto the substrate results predominantly, if not entirely, from mechanical anchoring [44].

6.2.3.2. Temperature. In the LPIT deposits, the powder set 1 and set 2 minor adhesion decline as the traverse speed is decreased to 10 mm/s, might be associated to an oxide scale growth process rendering direct fresh metal contact difficult. As discussed in Section 6.1.3, the oxide growth can result from the substrate surface exposure to the environment after being heated by the impacting supersonic gas flow at low traverse speed. This oxide film influence is inclined to be more noticeable for smaller particle size as they travel at lower E_K alongside an initially larger native oxide film. On the other hand, since the HPIT deposits have been generated at the highest gun traverse speed, i.e. 150 mm/s, and that the observed wall jet radial flow and recirculating stagnation zone are found to be at much colder temperatures than in the LPCS system, it is evident that the substrate temperature effects, if any, are diminished. Consequently, all measured coating bonding strength outcomes reflect predominantly the exposed particle characteristics influence on adhesion, which is also in agreement with the previously proposed conclusions provided in Section 6.2.1.

6.2.4. Crack propagation mechanisms

Although LPIT deposits sprayed at 10 mm/s and 150 mm/s undergo similar in-situ peening processes and reach overall comparable bonding/failure strengths, they undergo dissimilar fracture processes, as shown in Fig. 11 in which the powder set 2–3 present a predominant glue failure when sprayed at 150 mm/s. Due to the low DE under which both coatings are deposited, general microstructural features such as pancake-like particle-particle deformation, presence of mechanical

anchoring at particle junctions and intermingled particle splat contact area are expected to exist in both deposits. Neglecting impact associated recrystallisation feature dissimilarities, the different fracture processes can be linked to the dissimilar thermal history/in-situ annealing associated with gun traverse speed and to the different number of deposit layers utilized. Lack of a complete microstructural evaluation, however, restricts the confirmation of the exact impact related phenomena that lead to the dissimilar fracture surfaces in both LPIT depositions.

For the HPIT cases, the limited in-situ peening process inherent to the high DE restricts particle deformation as observed in Fig. 9. The coating cohesion failure, recorded for powder set 3 and shown in Fig. 11i confirms the significance of particle-particle boundary characteristics, associated to the η value under which deposition occurs, and the presence of preferable low energy crack propagation paths on coating strength and effective properties. Powder set 1 and set 2 exhibit increased particle-particle cohesion strength due to their depositions under larger η parameter, resulting in a localized coating fracture rather than a cohesive failure or full adhesion separation.

6.3. Bend-to-break tests

The improved apparent ductility of the LPIT coatings, observed in Fig. 12a, can be attributed to the presence of crack blunting, crack deflection mechanisms and/or particle-particle fish scale structural effect [78] serving to distribute the deformation, mitigate stress concentration and provide pseudo-plasticity, i.e. deformation facilitated by particle boundary sliding [78,79]. These mechanisms related to the particle microstructural arrangement resulting from the high level of in-situ peening, lead to the irregular fracture surface depicted in Fig. 13.

For the HPIT coatings, despite the larger η values compared to the LPIT deposits, the reduced apparent ductility and brittle fracture occurring during the bend-to-break tests, as shown in Fig. 12b–c, are attributed to increased cohesion bonding that limits the fish scale effect. Recognizing that a crack path propagates along the easiest low-energy route, existing porosity and microcracks may all lead to premature fracture of the tested samples. The fracture surface of a fast growing and propagating crack, in a particle network, theoretically shows limited material deformation and fragmentation, original particle surface features and overall low coating bending ability, which is observed in the fracture surfaces of Fig. 13.

7. Conclusions

The current work studied the influence of pure aluminum particle impact temperature, i.e. colder vs warmer particles, for a given particle size, on steel substrate cold spray deposition and coating properties, using both experimental and modeling results. The following conclusions are drawn:

For sprays characterized by colder particle impact temperature

1. The DE is low (below 10%) for all particle size ranges, as most particles do not experience sufficient deformation upon impact with the substrate to achieve bonding. The DE decreases with increasing particle size as the reduction of their impact velocity is not compensated by the decrease of their critical velocity.
2. The coating adhesion strength increases drastically with particle size, under constant η depositions, as a result of the severe in-situ hammering processes induced by decreasing DE with particle size.
3. The in-situ shot-peening also leads to the formation of important fish scale effect, which provides the coating with pseudoplasticity and apparent ductility.

For sprays characterized by warmer particle impact temperature

1. The DE is large (above 60%) due to sufficient particle deformation upon impact with the substrate, promoted by the warmer particle impact temperature. The DE decreases with particle size as their decrease in impact velocity is not counterbalanced by their decline in critical velocity.
2. The coating adhesion/cohesion strength decreases with particle size and is governed by the non-dimensional parameter η. Despite their intrinsically increasing V_C, smaller particles reach much higher impact temperatures, which sufficiently decreases their V_C, and much higher impact velocity due to their lower mass. With increasing particle size and constant gas stagnation parameters, larger particles are inherently heated to lower temperatures, which are sufficient to increase DE from room temperature impact deposition but observed to be consequently detrimental for cohesion processes.
3. Higher particle cohesion related to high η values limit fish-scale like effects during deformation. However, the high level of defects (porosity, unbonded areas) lead to brittle-like fracture characterized by a straight crack trajectory.

Declaration of competing interest

The authors declare that they have no known competing financial interests or personal relationships that could have appeared to influence the work reported in this paper.

Acknowledgements

This project was funded by the Government of Canada. The authors would like to acknowledge the work of the technical officer's team in Boucherville: K. Bricault, F. Belval, P. Dionne and C. Hoang.

References

[1] N. Sanpo, M.L. Tan, P. Cheang, K.A. Khor, Antibacterial property of cold-sprayed HA-ag/PEEK coating, J. Therm. Spray Technol. 18 (2009) 10–15, https://doi.org/10.1007/s11666-008-9283-0.
[2] H. Che, X. Chu, P. Vo, S. Yue, Cold spray of mixed metal powders on carbon fibre reinforced polymers, Surf. Coatings Technol. 329 (2017) 232–243, https://doi.org/10.1016/j.surfcoat.2017.09.052.
[3] M. Yamada, H. Isago, H. Nakano, M. Fukumoto, Cold spraying of TiO2 photocatalyst coating with nitrogen process gas, J. Therm. Spray Technol. 19 (2010) 1218–1223, https://doi.org/10.1007/s11666-010-9520-1.
[4] H. Katanoda, M. Fukuhara, N. Iino, Numerical study of combination parameters for particle impact velocity and temperature in cold spray, J. Therm. Spray Technol. 16 (2007) 627–633, https://doi.org/10.1007/s11666-007-9087-7.
[5] A. Nastic, M Vijay, A Tieu, S Rahmati, B Jodoin, Experimental and numerical study of the influence of substrate surface preparation on adhesion mechanisms of aluminum cold spray coatings on 300M steel substrates, J. Therm. Spray Technol. 26. doi:https://doi.org/10.1007/s11666-017-0602-1 (n.d.).
[6] Y. Cormier, P. Dupuis, B. Jodoin, A. Ghaei, Finite element analysis and failure mode characterization of pyramidal fin arrays produced by masked cold gas dynamic spray, J. Therm. Spray Technol. 24 (2015) 1549–1565, https://doi.org/10.1007/s11666-015-0317-0.
[7] S. Yin, X. Wang, W. Li, H. Liao, H. Jie, Deformation behavior of the oxide film on the surface of cold sprayed powder particle, Appl. Surf. Sci. 259 (2012) 294–300, https://doi.org/10.1016/J.APSUSC.2012.07.036.
[8] M. Hassani-Gangaraj, D. Veysset, K.A. Nelson, C.A. Schuh, Impact-bonding with aluminum, silver, and gold microparticles: toward understanding the role of native oxide layer, Appl. Surf. Sci. 476 (2019) 528–532, https://doi.org/10.1016/J.APSUSC.2019.01.111.
[9] P.C. King, S.H. Zahiri, M. Jahedi, Microstructural refinement within a cold-sprayed copper particle, Metall. Mater. Trans. A Phys. Metall. Mater. Sci 40 (2009) 2115–2123, https://doi.org/10.1007/s11661-009-9882-5.
[10] Y. Sheng, C.J. Lawrence, B.J. Briscoe, C. Thornton, Numerical studies of uniaxial powder compaction process by 3D DEM, in: Eng. Comput. (Swansea, Wales), 2004, pp. 304–317, https://doi.org/10.1108/02644400410519802.
[11] L. Tan, Y. Li, F. Liu, Y. Nie, L. Jiang, Microstructure evolutions of a powder metallurgy superalloy during high-strain-rate deformation, J. Alloys Compd. 789 (2019) 506–517, https://doi.org/10.1016/j.jallcom.2019.03.080.
[12] Y. Xiong, K. Kang, G. Bae, S. Yoon, C. Lee, Dynamic amorphization and recrystallization of metals in kinetic spray process, Appl. Phys. Lett. 92 (2008), 194101, https://doi.org/10.1063/1.2928218.
[13] W.-Y. Li, C. Zhang, X.P. Guo, G. Zhang, H.L. Liao, C. Coddet, Deposition characteristics of Al–12Si alloy coating fabricated by cold spraying with relatively large powder particles, Appl. Surf. Sci. 253 (2007) 7124–7130, https://doi.org/10.1016/J.APSUSC.2007.02.142.

[14] A. Nastic, B. Jodoin, Evaluation of heat transfer transport coefficient for cold spray through computational fluid dynamics and particle in-flight temperature measurement using a high-speed IR camera, J. Therm. Spray Technol. 27 (2018) 1491–1517, https://doi.org/10.1007/s11666-018-0787-y.

[15] X.J. Ning, Q.S. Wang, Z. Ma, H.J. Kim, Numerical study of in-flight particle parameters in low-pressure cold spray process, J. Therm. Spray Technol. 19 (2010) 1211–1217, https://doi.org/10.1007/s11666-010-9548-2.

[16] W.-Y. Li, H. Liao, H.-T. Wang, C.-J. Li, G. Zhang, C. Coddet, Optimal design of a convergent-barrel cold spray nozzle by numerical method, Appl. Surf. Sci. 253 (2006) 708–713, https://doi.org/10.1016/j.apsusc.2005.12.157.

[17] R.N. Raoelison, L.L. Koithara, S. Costil, C. Langlade, Turbulences of the supersonic gas flow during cold spraying and their negative effects: a DNS CFD analysis coupled with experimental observation and laser impulse high-speed shadowgraphs of the particles in-flight flow, Int. J. Heat Mass Transf. 147 (2020), https://doi.org/10.1016/j.ijheatmasstransfer.2019.118894.

[18] B. Samareh, O. Stier, V. Lüthen, A. Dolatabadi, Assessment of CFD modeling via flow visualization in cold spray process, J. Therm. Spray Technol. 18 (2009) 934–943, https://doi.org/10.1007/s11666-009-9363-9.

[19] J. Pattison, S. Celotto, A. Khan, W. O'Neill, Standoff distance and bow shock phenomena in the cold spray process, Surf. Coatings Technol. 202 (2008) 1443–1454, https://doi.org/10.1016/j.surfcoat.2007.06.065.

[20] V.F. Kosarev, S.V. Klinkov, A.P. Alkhimov, A.N. Papyrin, On some aspects of gas dynamics of the cold spray process, J. Therm. Spray Technol. 12 (2003) 265–281, https://doi.org/10.1361/105996303770348384.

[21] S. Yin, M. Zhang, Z. Guo, H. Liao, X. Wang, Numerical investigations on the effect of total pressure and nozzle divergent length on the flow character and particle impact velocity in cold spraying, Surf. Coatings Technol. 232 (2013) 290–297, https://doi.org/10.1016/j.surfcoat.2013.05.017.

[22] G. Huang, D. Gu, X. Li, L. Xing, H. Wang, Numerical simulation on syphonage effect of laval nozzle for low pressure cold spray system, J. Mater. Process. Technol. 214 (2014) 2497–2504, https://doi.org/10.1016/j.jmatprotec.2014.05.014.

[23] A. Bacciochini, S. Bourdon-Lafleur, C. Poupart, M. Radulescu, B. Jodoin, Ni-Al nanoscale energetic materials: phenomena involved during the manufacturing of bulk samples by cold spray, J. Therm. Spray Technol. 23 (2014) 1142–1148, https://doi.org/10.1007/s11666-014-0078-1.

[24] D. MacDonald, S. Leblanc-Robert, R. Fernández, A. Farjam, B. Jodoin, Effect of nozzle material on downstream lateral injection cold spray performance, J. Therm. Spray Technol. 25 (2016) 1149–1157, https://doi.org/10.1007/s11666-016-0426-4.

[25] H. Che, X. Chu, P. Vo, S. Yue, Metallization of various polymers by cold spray, J. Therm. Spray Technol. 27 (2018) 169–178, https://doi.org/10.1007/s11666-017-0663-1.

[26] D. MacDonald, R. Fernández, F. Delloro, B. Jodoin, Cold spraying of Armstrong process titanium powder for additive manufacturing, J. Therm. Spray Technol. 26 (2017) 598–609, https://doi.org/10.1007/s11666-016-0489-2.

[27] S. Bagherifard, I. Fernàndez Pariente, R. Ghelichi, M. Guagliano, S. Vezzù, Effect of shot peening on residual stresses and surface work-hardening in cold sprayed coatings, Key Eng. Mater. 417–418 (2009) 397–400, https://doi.org/10.4028/www.scientific.net/KEM.417-418.397.

[28] J.-O. Kliemann, H. Gutzmann, F. Gärtner, H. Hübner, C. Borchers, T. Klassen, Formation of cold-sprayed ceramic titanium dioxide layers on metal surfaces, J. Therm. Spray Technol. 20 (2011) 292–298, https://doi.org/10.1007/s11666-010-9563-3.

[29] E. Sansoucy, P. Marcoux, L. Ajdelsztajn, B. Jodoin, Properties of SiC-reinforced aluminum alloy coatings produced by the cold gas dynamic spraying process, Surf. Coatings Technol. 202 (2008) 3988–3996, https://doi.org/10.1016/J.SURFCOAT.2008.02.017.

[30] E. Sansoucy, G.E. Kim, A.L. Moran, B. Jodoin, Mechanical characteristics of Al-Co-Ce coatings produced by the cold spray process, J. Therm. Spray Technol. 16 (2007) 651–660, https://doi.org/10.1007/s11666-007-9099-3.

[31] W. Wong, A. Rezaeian, E. Irissou, J.G. Legoux, S. Yue, Cold spray characteristics of commercially pure Ti and Ti-6Al-4V, Adv. Mater. Res. 89–91 (2010) 639–644, https://doi.org/10.4028/www.scientific.net/AMR.89-91.639.

[32] V.S. Bhattiprolu, K.W. Johnson, O.C. Ozdemir, G.A. Crawford, Influence of feedstock powder and cold spray processing parameters on microstructure and mechanical properties of Ti-6Al-4V cold spray depositions, Surf. Coatings Technol. 335 (2018) 1–12, https://doi.org/10.1016/J.SURFCOAT.2017.12.014.

[33] D.L. Gilmore, R.C. Dykhuizen, R.A. Neiser, M.F. Smith, T.J. Roemer, Particle velocity and deposition efficiency in the cold spray process, J. Therm. Spray Technol. 8 (1999) 576–582, https://doi.org/10.1361/105996399770350278.

[34] T.H.V. Steenkiste, J.R. Smith, R.E. Teets, Aluminum coatings via kinetic spray with relatively large powder particles, Surf. Coatings Technol. 154 (2002) 237–252, https://doi.org/10.1016/S0257-8972(02)00018-X.

[35] F. Raletz, M. Vardelle, G. Ezo'o, Critical particle velocity under cold spray conditions, Surf. Coatings Technol. 201 (2006) 1942–1947, https://doi.org/10.1016/j.surfcoat.2006.04.061.

[36] X.-J. Ning, J.-H. Jang, H.-J. Kim, The effects of powder properties on in-flight particle velocity and deposition process during low pressure cold spray process, Appl. Surf. Sci. 253 (2007) 7449–7455, https://doi.org/10.1016/J.APSUSC.2007.03.031.

[37] S. Yin, X. Wang, X. Suo, H. Liao, Z. Guo, W. Li, C. Coddet, Deposition behavior of thermally softened copper particles in cold spraying, Acta Mater. 61 (2013) 5105–5118, https://doi.org/10.1016/j.actamat.2013.04.041.

[38] W.-Y. Li, H. Liao, G. Douchy, C. Coddet, Optimal design of a cold spray nozzle by numerical analysis of particle velocity and experimental validation with 316L stainless steel powder, Mater. Des. 28 (2007) 2129–2137, https://doi.org/10.1016/J.MATDES.2006.05.016.

[39] Y. Xie, M.P. Planche, R. Raoelison, P. Hervé, X. Suo, P. He, H. Liao, Investigation on the influence of particle preheating temperature on bonding of cold-sprayed nickel coatings, Surf. Coatings Technol. 318 (2017) 99–105, https://doi.org/10.1016/j.surfcoat.2016.09.037.

[40] C.W. Ziemian, W.J. Wright, D.E. Cipoletti, Influence of impact conditions on feedstock deposition behavior of cold-sprayed Fe-based metallic glass, J. Therm. Spray Technol. 27 (2018) 843–856, https://doi.org/10.1007/s11666-018-0720-4.

[41] A. Sova, S. Grigoriev, A. Kochetkova, I. Smurov, Influence of powder injection point position on efficiency of powder preheating in cold spray: numerical study, Surf. Coatings Technol. 242 (2014) 226–231, https://doi.org/10.1016/j.surfcoat.2013.10.078.

[42] H.J. Kim, C.H. Lee, S.Y. Hwang, Fabrication of WC-Co coatings by cold spray deposition, Surf. Coatings Technol. 191 (2005) 335–340, https://doi.org/10.1016/j.surfcoat.2004.04.058.

[43] M.R. Rokni, S.R. Nutt, C.A. Widener, V.K. Champagne, R.H. Hrabe, Review of relationship between particle deformation, coating microstructure, and properties in high-pressure cold spray, J. Therm. Spray Technol. 26 (2017) 1308–1355, https://doi.org/10.1007/s11666-017-0575-0.

[44] A. Nastic, M. Vijay, A. Tieu, S. Rahmati, B. Jodoin, Experimental and numerical study of the influence of substrate surface preparation on adhesion mechanisms of aluminum cold spray coatings on 300M steel substrates, J. Therm. Spray Technol. 26 (2017), https://doi.org/10.1007/s11666-017-0602-1.

[45] A. Nastic, Repair of Aluminum Alloy Aerospace Components and Cold Gas Dynamic Spray Flow Distribution Study, Univeristy of Ottawa, 2015. https://ruor.uottawa.ca/handle/10393/32998.

[46] A. International, Standard Test Method for Adhesion or Cohesion Strength of Thermal Spray Coatings, C633 - 13(2017), in: West Conshohocken, 2017.

[47] ASTM D4145 - 10(2018) standard test method for coating flexibility of prepainted sheet (n.d.). https://www.astm.org/Standards/D4145.htm (accessed September 2, 2020).

[48] ANSYS FLUENT 12.0 theory guide - 15.2.2 turbulent dispersion of particles (n.d.). https://www.afs.enea.it/project/neptunius/docs/fluent/html/th/node242.htm (accessed April 3, 2020).

[49] ANSYS FLUENT 12.0 theory guide - release 12.0, ANSYS-Guide. https://www.afs.enea.it/project/neptunius/docs/fluent/html/th/node59.htm, 2009. (Accessed 10 August 2020).

[50] H. Tabbara, S. Gu, D.G. McCartney, T.S. Price, P.H. Shipway, Study on process optimization of cold gas spraying, J. Therm. Spray Technol. 20 (2011) 608–620, https://doi.org/10.1007/s11666-010-9564-2.

[51] P. Liebersbach, A. Foelsche, V.K. Champagne, M. Siopis, A. Nardi, D.P. Schmidt, CFD simulations of feeder tube pressure oscillations and prediction of clogging in cold spray nozzles, J. Therm. Spray Technol. 29 (2020) 400–412, https://doi.org/10.1007/s11666-020-00992-0.

[52] O.C. Ozdemir, C.A. Widener, Influence of powder injection parameters in high-pressure cold spray, J. Therm. Spray Technol. 26 (2017) 1411–1422, https://doi.org/10.1007/s11666-017-0606-x.

[53] R. Lupoi, W. O'Neill, Powder stream characteristics in cold spray nozzles, Surf. Coatings Technol. 206 (2011) 1069–1076, https://doi.org/10.1016/j.surfcoat.2011.07.061.

[54] X. Suo, S. Yin, M.P. Planche, T. Liu, H. Liao, Strong effect of carrier gas species on particle velocity during cold spray processes, Surf. Coatings Technol. 268 (2015) 90–93, https://doi.org/10.1016/j.surfcoat.2014.04.039.

[55] C.B. Henderson, Drag coefficients of spheres in continuum and rarefied flows, AIAA J. 14 (1976) 707–708, https://doi.org/10.2514/3.61409.

[56] B. Jodoin, F. Raletz, M. Vardelle, Cold spray modeling and validation using an optical diagnostic method, Surf. Coatings Technol. 200 (2006) 4424–4432, https://doi.org/10.1016/j.surfcoat.2005.02.209.

[57] T. Han, Z. Zhao, B.A. Gillispie, J.R. Smith, Effects of spray conditions on coating formation by the kinetic spray process, J. Therm. Spray Technol. 14 (2005) 373–383, https://doi.org/10.1361/105996305X59369.

[58] V.K. Champagne, D.J. Helfritch, S.P.G. Dinavahi, P.F. Leyman, Theoretical and experimental particle velocity in cold spray, J. Therm. Spray Technol. 20 (2011) 425–431, https://doi.org/10.1007/s11666-010-9530-z.

[59] S.V. Klinkov, V.F. Kosarev, A.A. Sova, I. Smurov, Calculation of particle parameters for cold spraying of metal-ceramic mixtures, J. Therm. Spray Technol. 18 (2009) 944–956, https://doi.org/10.1007/s11666-009-9346-x.

[60] T. Saito, M. Saba, M. Sun, K. Takayama, The effect of an unsteady drag force on the structure of a non-equilibrium region behind a shock wave in a gas-particle mixture, Shock Waves 20 (2007) 255–262, https://doi.org/10.1007/s00193-007-0109-7.

[61] A.M. Birt, V.K. Champagne, R.D. Sisson, D. Apelian, Microstructural analysis of Ti–6Al–4V powder for cold gas dynamic spray applications, Adv. Powder Technol. 26 (2015) 1335–1347, https://doi.org/10.1016/J.APT.2015.07.008.

[62] T. Stoltenhoff, H. Kreye, H.J. Richter, An analysis of the cold spray process and its coatings, J. Therm. Spray Technol. 11 (2002) 542–550.

[63] X.K. Suo, T.K. Liu, W.Y. Li, Q.L. Suo, M.P. Planche, H.L. Liao, Numerical study on the effect of nozzle dimension on particle distribution in cold spraying, Surf. Coatings Technol. 220 (2013) 107–111, https://doi.org/10.1016/J.SURFCOAT.2012.09.029.

[64] C.Y. Wu, C. Thornton, L.Y. Li, Rebound behaviour of spheres during elastic-plastic oblique impacts, in: Int, World Scientific Publishing Company, J. Mod. Phys. B, 2008, pp. 1095–1102, https://doi.org/10.1142/s0217979208046372.

[65] O.C. Ozdemir, Q. Chen, S. Muftu, V.K. Champagne, Modeling the continuous heat generation in the cold spray coating process, J. Therm. Spray Technol. 28 (2019) 108–123, https://doi.org/10.1007/s11666-018-0794-z.
[66] J.C. Carling, B.L. Hunt, The near wall jet of a normally impinging, uniform, axisymmetric, supersonic jet, J. Fluid Mech. 66 (1974) 159–176, https://doi.org/10.1017/S0022112074000127.
[67] A.G. McDonald, A.N. Ryabinin, E. Irissou, J.-G. Legoux, Gas-substrate heat exchange during cold-gas dynamic spraying, J. Therm. Spray Technol. 22 (2013) 391–397, https://doi.org/10.1007/s11666-012-9828-0.
[68] R. Singh, K.H. Rauwald, E. Wessel, G. Mauer, S. Schruefer, A. Barth, S. Wilson, R. Vassen, Effects of substrate roughness and spray-angle on deposition behavior of cold-sprayed Inconel 718, Surf. Coatings Technol. 319 (2017) 249–259, https://doi.org/10.1016/j.surfcoat.2017.03.072.
[69] P. Richer, B. Jodoin, L. Ajdelsztajn, E.J. Lavernia, Substrate roughness and thickness effects on cold spray nanocrystalline Al-Mg coatings, J. Therm. Spray Technol. 15 (2006) 246–254, https://doi.org/10.1361/105996306X108174.
[70] S. Shin, S. Yoon, Y. Kim, C. Lee, Effect of particle parameters on the deposition characteristics of a hard/soft-particles composite in kinetic spraying, Surf. Coatings Technol. 201 (2006) 3457–3461, https://doi.org/10.1016/j.surfcoat.2006.07.255.
[71] H. Assadi, F. Gärtner, T. Stoltenhoff, H. Kreye, Bonding mechanism in cold gas spraying, Acta Mater. 51 (2003) 4379–4394, https://doi.org/10.1016/S1359-6454(03)00274-X.
[72] K. Spencer, M.-X. Zhang, Optimisation of stainless steel cold spray coatings using mixed particle size distributions, Surf. Coatings Technol. 205 (2011) 5135–5140, https://doi.org/10.1016/J.SURFCOAT.2011.05.020.
[73] J. Henao, A. Concustell, S. Dosta, N. Cinca, I.G. Cano, J.M. Guilemany, Influence of the substrate on the formation of metallic glass coatings by cold gas spraying, J. Therm. Spray Technol. 25 (2016) 992–1008, https://doi.org/10.1007/s11666-016-0419-3.
[74] V.N. Zaikovskii, S.V. Klinkov, V.F. Kosarev, B.M. Melamed, G.V. Trubacheev, Control of spray spot shape in cold spray technology. Part 2. Spraying process, Thermophys. Aeromechanics. 21 (2014) 223–230, https://doi.org/10.1134/S0869864314020085.
[75] H. Assadi, T. Schmidt, H. Richter, J.-O. Kliemann, K. Binder, F. Gärtner, T. Klassen, H. Kreye, On parameter selection in cold spraying, J. Therm. Spray Technol. 20 (2011) 1161–1176, https://doi.org/10.1007/s11666-011-9662-9.
[76] J.G. Legoux, E. Irissou, C. Moreau, Effect of Substrate Temperature on the Formation Mechanism of Cold-sprayed Aluminum, Zinc and Tin Coatings. doi:https://doi.org/10.1007/s11666-007-9091-y (n.d.).
[77] T. Schmidt, F. Gärtner, H. Assadi, H. Kreye, Development of a generalized parameter window for cold spray deposition, Acta Mater. 54 (2006) 729–742, https://doi.org/10.1016/J.ACTAMAT.2005.10.005.
[78] A. Browning, C. Ortiz, M.C. Boyce, Mechanics of composite elasmoid fish scale assemblies and their bioinspired analogues, J. Mech. Behav. Biomed. Mater. 19 (2013) 75–86, https://doi.org/10.1016/j.jmbbm.2012.11.003.
[79] R.G. Crookes, B. März, H. Wu, Ductile deformation in alumina ceramics under quasi-static to dynamic contact impact, Mater. Des. 187 (2020), 108360, https://doi.org/10.1016/j.matdes.2019.108360.

5.4 RESEARCH PROJECT 4

The following section presents the results obtained under the fourth research project, which has studied the influence of particle impact characteristics effect on interfacial phenomena developed upon impact. Wipe tests, i.e. well distributed single particle deposition, have been produced and the contact surface of both deposited and rebounded particles has been studied. The substrate surface impacted zone has also been analysed to further understand the phenomena occurring upon particle bonding and rebounding processes. The study first demonstrates the presence of asymmetrical deformation for all tested impact characteristics, which has been associated to particle preferential grain orientation. Secondly, pressure dependent melting features have been detected and the melt front trajectory explained through FEM. The interfacial high temperature zones characteristics have been shown to affect the substrate surface and the particle bonding. Insufficient particle temperature increase has shown to lead to both poor adhesion and cohesion processes, while peening phenomena, as described in the previous work of section 5.3, have been shown to enhance the bonding of cold particles.

Particle Impact Characteristics Influence on Cold Spray Bonding: Investigation of Interfacial Phenomena for Soft Particles on Hard Substrates

A. Nastic[a], B. Jodoin[a], J-G. Legoux[b] and D. Poirier[b]

[a] University of Ottawa Cold Spray Laboratory, Ottawa, ON Canada

[b] National Research Council of Canada, Boucherville, QC, Canada

Abstract

The influence of particle impact temperature and size on adhesion of soft particle/hard substrate material in cold spray has been scarcely studied. While the relationship between particle impact conditions and particle/substrate bonding are commonly established through FEM studies, they typically lack comparison to experimental data. In the current study, spherical aluminum particles were deposited on polished steel substrates using the cold spray process. Interfacial characterization was conducted to describe the influence of particle size and impact temperature on deposition with particular focus on the generation of metallurgical bonds for the soft/hard material combination. Characterization was performed by post-mortem observation of removed adhered particles and collected rebounded particles contact surfaces. Impacts have also been simulated to correlate experimental observations to interfacial temperature and pressure values provided by the model that are otherwise impossible to measure in-situ. The influence of pressure on melting temperature and of its temporal evolution with particle deformation on bonding are studied.

Evidence of anisotropic particle deformation associated to microstructural orientation and grain geometrical features has been observed irrespective of particle size and impact temperature and velocity. Experimental evidence shows that the particle south pole experiences restricted deformation as the original powder grain morphology was observed even after impact. Interfacial melt features have been detected for both low and high impact temperature sprays and the pressure dependent melt zone generation, propagation, stagnation and regression tracked through FEM has shown important influence on single impact adhesion processes. It was determined that the melt zone increases with the increase of particle size and impact temperature. Observed metallic bonding features and FEM indicate that increasing particle velocity, i.e. decreasing particle size, accelerates particle bonding processes to occur within tens of nanoseconds. Contact compressive pressure and interfacial expansion increases with particle increasing velocity and temperature.

Keywords: Pressure Dependent Melting, Melt Front, Metallic Bonding, Impact Temperature, Peening, Oxide Layer

1 INTRODUCTION

The cold gas dynamic spray (CGDS) process accelerates micron-size particles to high velocities (400m/s - 1000 m/s), using a supersonic gas flow. After exiting the nozzle, the high-speed particles impact a target surface generating localized material heating and cooling rates up to 10^9 K/s, strain levels above 10 and strain rates up to 10^9 s^{-1}. These impact phenomena lead to physical/chemical processes such as melting (Ref 1,2), phase transformation (Ref 3), amorphization (Ref 4), jetting (Ref 5), oxide layer fragmentation (Ref 6), twinning (Ref 7) and most importantly atomic (also often referred to as metallurgical or metallic) bonding (Ref 8).

It is widely accepted that solid-state atom-to-atom bonding requires oxide-free clean surfaces to be put in contact under high localised pressure (Ref 9,10). Finite element modeling (FEM) has been used to confirm these findings and visualize the bonding process during impact, as the process length (microns) and time (nanoseconds) scales prevent experimental measurements during CGDS (Ref 11–14). Evidence of metallic bonding at particle/substrate interfaces has been mostly based on cross-sectional interface examinations, which have shown that the metallurgically bonded zone is almost always ring-shaped, between the particle south pole and the location of jetted material (Ref 15–18).

Most studies have focused on the analysis of metallurgical bonding occurrence and features for particle/substrate of similar mechanical properties, referred to as hard/hard and soft/soft material pairs (Ref 2,6,8,17,19–22). Material combinations with comparable hardness to elastic modulus ratio inevitably include concurrent interfacial mechanical and metallurgical bonding mechanisms for which the separate effects on adhesion are hardly dissociable. However, for soft particle/hard substrate material pairs, the substrate deformation is limited, and mechanical anchoring is negligible. However, this limited substrate deformation restricts proper native oxide layer removal and fresh-metal contact impeding the creation of metallic bonds. For such material pair, studies have demonstrated that increasing substrate temperature can improve its deformation enough to enhance metallic adhesion without generating mechanical anchoring (Ref 23–25). Nevertheless, the study of substrate preheating on particle bonding is limited (Ref 26). Similarly, the influence of particle impact temperature on adhesion for soft/hard material pairs is scarce. The reported benefits of increasing particle temperature in similar material combinations, such as the rise in interfacial temperature promoting thermally softened zones, deformation, oxide fracture, atomic mixing and consequently bonding (Ref 27–30), might not be relevant to the soft/hard material pair. An increase in particle temperature would only accentuate further the particle deformation without significant change to the substrate plastic flow.

A study on particle impact temperature influence on coating adhesion strength has reported that soft aluminum deposited under cold particle impact temperatures on hard steel provided increasing strengths with increasing particle size (Ref 31). This rise in bonding has been predominantly associated to the increasing in-situ peening frequency of cold particles bouncing off instead of bonding to the substrate with increasing particle size. The in-situ peening was correlated with coating deposition efficiency, which has shown to be very low for cold impact temperatures, i.e. 5 to 13%, and declining with increasing particle size (Ref 17,31). In comparison, for particles reaching the substrate at a higher impact temperature, the coating adhesion strength has shown a rise in coating adhesion with particle decreasing size. The heated particles allowed an important increase in deposition efficiency, i.e. 50 to 90%, which has shifted the bonding mechanism to particle impact characteristics (velocity and temperature) rather than in-situ peening. While these results contribute to the understanding of soft/hard material bonding processes, the influence of particle impact temperature on interfacial features and bonding processes at the individual particle level has not been studied.

Consequently, the aim of the current study is to analyse the effect of particle impact temperature and size on impact characteristics and adhesion strength for the soft/hard material combination at the individual particle level. Spherical aluminum particles of varying size are deposited at low and high impact temperature, while maintaining a similar impact velocity, on a hard steel substrate material. The current study provides a detailed characterisation of interfacial phenomena based on particle size and impact temperature. Adhered particles are removed from the substrate, and the fracture surfaces are examined to characterize the metallurgical bonding zones size, geometry, and location. Rebounded particles are collected, and their surfaces analysed. In addition, finite element modeling (FEM) is used to correlate the experimental observations to interfacial characteristics (pressure and temperature).

2 EXPERIMENTAL PROCEDURES

2.1 Feedstock powder

The feedstock powder used is a commercially available pure aluminum powder (Equispheres, ON, CA). The powder manufacturing process produces solely spherical particles, as shown in Figure 1 (a, b and c). This eliminates/reduces the geometrical effects related to teardrop and irregular powder shapes (Ref 12,32), such as generation of particle

angular momentum, unclear initial impact contact point and untraceable original geometry. In addition, the aluminum particles have been sieved to yield three distinct powder diameter ranges, as depicted in Figure 1 (a, b and c), to allow a size dependent study. The average diameters are 40µm, 58µm and 68µm for set 1, set 2 and set 3, respectively.

Equiaxed, dendritic and columnar grains surface microstructures, shown in Figure 1 (d, e and f), are observed in all three particle size sets. These microstructural variations result from directional solidification, heterogeneous nucleation sites, particle to particle contact and cooling rate during manufacturing (Ref 33–35). The solidification rates can differ between the particle external shell and interior bulk material (Ref 34,35). In the current study, as shown in Figure 1 (g, h and i), the microstructure is uniform throughout the particle suggesting homogeneous solidification rates. The same grain types are also detected in the etched powder cross-sections.

Since loss in ductility is usually observed with the presence of oxide dispersion, leading to reduced particle deformation upon impact, an elemental analysis focusing on oxygen detection has been conducted for all powder sets. The powder oxygen concentration has been measured using an oxygen analyser (Leco ONH836, MI, USA) through the inert gas fusion (IGF) method following the ASTM E 1019-03 standard. According to the analysis, presented in Table 1, the oxygen concentration in the powder set 1 (smallest size range) is almost twice the concentration detected in set 2 and set 3. From these measurements, the surface oxide layer thickness has been approximated using the assumptions that the oxygen is confined to the particle surface and is of constant thickness (Ref 6) and the following relation;

$$\frac{V_{ox}\rho_{ox}}{V_{Al}\rho_{Al} + V_{ox}\rho_{ox}} = X_{ox\,(wt.\%)} \qquad Eq.\ 1$$

where X_{ox} is the oxygen weight percent contribution to the Al-powder from the surface oxide scale, ρ_{ox} and ρ_{Al} are the aluminum oxide and pure aluminum densities, respectively and V_{ox} and V_{Al} are the oxide shell and spherical pure aluminum volume, respectively.

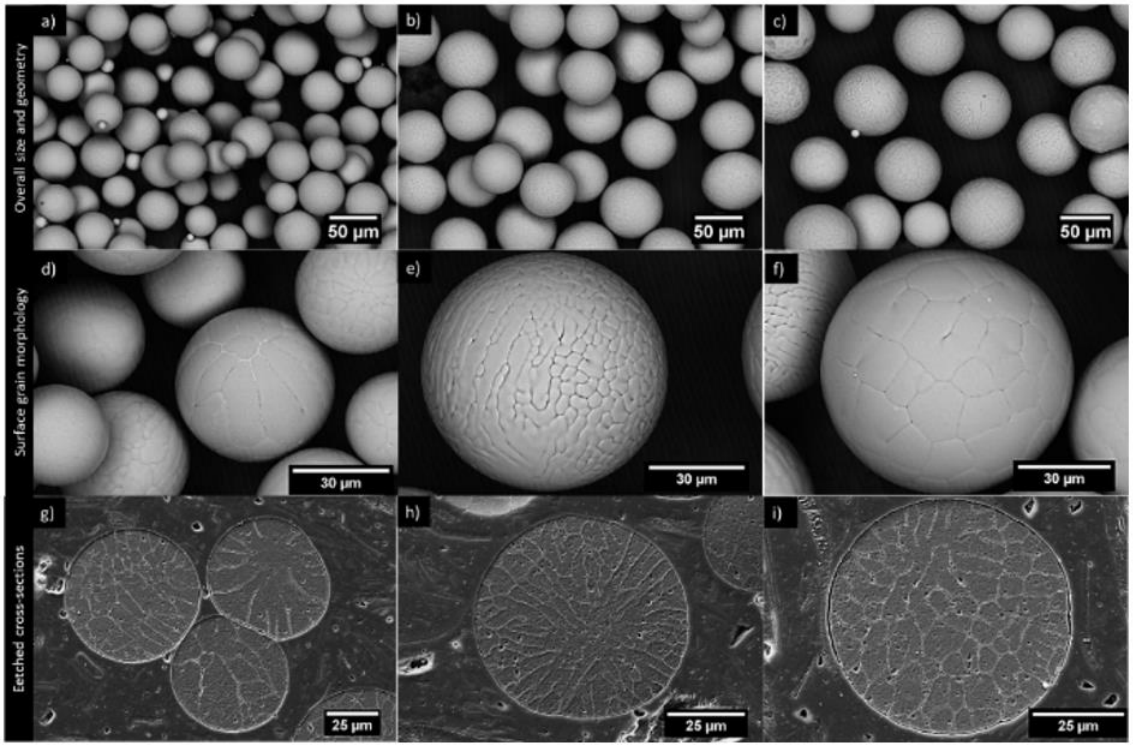

Figure 1: BSD images of powders with diameter range between a) 13-48µm with scarce powder below 13µm (set 1), b) 48-63µm (set 2) and c) 53-76 µm (set 3). d-f) Types of surface morphologies observed through BSD, i.e. equiaxed, dendritic and columnar grains, and detected in all three powder sets. BSD analysis of powder cross-sectional grain morphology after etching with Keller's solution (g-h-i).

The X_{ox} has been calculated using the measured oxygen concentration, O_c, as follow:

$$X_{ox\,(wt.\%)} = 1 - \left[\frac{M_{Al}(Al_2O_3)\cdot O_c}{M_O(Al_2O_3)} + O_c\right] \qquad Eq.\ 2$$

where $M_{Al}(Al_2O_3)$ and $M_O(Al_2O_3)$ are the molecular weight of aluminum and oxygen in alumina, respectively.

Table 1 presents the measured oxygen content (ppm) along with the corresponding calculated oxide thickness. The alumina layer thickness is 4.15nm, 3.36nm and 3.94nm for powder set 1, set 2 and set 3, respectively.

Table 1: Approximated surface oxide layer thickness (nm) calculated using measured total oxygen content through IGF method.

	38-45 µm	53-63 µm	63-75 µm
LECO (wt.%, thickness)	430ppm/4.15nm	240ppm/3.36nm	240ppm/3.94nm

The mechanical response of particles has also been evaluated using an indenter equipped with a Berkovich tip. Fifteen indents per powder sets have been analysed. The indentations have been performed at a peak load of 0.03N, a dwell time of 15s at the peak load and a loading/unloading rate of 0.017N/s. As reported in Table 2, all three sets of powder have comparable hardness. Observed deviations are expected to be caused by grain size and grain geometry variations detected in the powders, as shown previously in Figure 1, and by any epoxy damping during loading.

Table 2: Powder hardness measurement obtained using instrumented indentation.

	38-45 µm	53-63 µm	63-75 µm
Hardness	393±39MPa	368±59MPa	385±50MPa

Since the oxide thickness values obtained through IGF approach values reported for aluminum powder using transmission electron microscopy (TEM) and X-ray photoelectron spectroscopy (XPS) (Ref 36), and that the hardness results are similar, it can be concluded that the oxygen is mostly confined to the particle surface, i.e. oxide film. This is a realistic assumption since in common aluminum powder manufacturing processes, such as gas atomization, the oxygen is predominantly bound to the surface (Ref 37).

2.2 Substrate material

Low carbon steel (SAE1018) has been used as substrate. Its hardness has been measured at 90.5± 0.3HRB. Substrate samples have been cut into cylinders (25.4mm diameter and 40mm height). Cold spray deposition was made on the flat ends, which have been polished to a mirror surface finish using 3µm abrasive suspensions.

2.3 Cold spray deposition

The deposition of individual particles is made through wipe tests. In these tests, the spray jet is moved at 150mm/s, and with limited powder feed rate. Commercially available (SST-EP, CenterLine Limited, Windsor, ON, CA and Oerlikon Metco KINETIKS 4000, Schwytz, CH) CS systems have been used to achieve cold and hot particle impact temperatures for the same impact velocity. In the SST-EP system, a polymer nozzle with a 2.0 mm throat diameter, 6.4mm exit diameter and diverging length of 126mm was utilised. The powder is injected radially, after the nozzle throat. A SiC nozzle with a 2.7 mm throat diameter, 6.96 mm exit diameter and 132 mm diverging length has been used in the KINETIKS 4000 system. The powder injection is located at the center of the converging nozzle section, without a pre-chamber, and oriented parallel to the nozzle axis. Prior to the deposition process, all substrates have been cleaned and degreased in an ethanol ultrasonic bath.

The process gas stagnation parameters were set to obtain the same particle impact velocity for both systems. These velocities have been measured and reported in (Ref 31). Both systems used a gas stagnation temperature and pressure of 500°C and 3.45MPa, respectively. The standoff distance was set to 15mm. Validated CFD models have been utilized in (Ref 31) to evaluate the particle impact temperature and velocity and critical velocities, which are reported in Table 3 for both low particle impact temperature (LPIT) sprays, obtained using the SST-EP system, and high particle impact temperature (HPIT) sprays, obtained using the KINETIKS 4000 system. As shown in Table 3 the critical velocity for HPIT (V_{C_HPIT}) is much lower than the one for LPIT (V_{C_LPIT}) sprays. This decrease results from the larger particle impact temperature for HPIT depositions, which allows higher deformation and improved oxide breakage and removal (Ref 31). The impact temperature reached by particles traveling at the corresponding critical velocities is referred to as T_L and T_H for LPIT and HPIT sprays, respectively, as presented in Table 3.

Table 3: CFD results of particle in-flight velocity and temperature (average and critical) for all three sets of powder taken from (Ref 31). *The V_{C_LPIT} and V_{C_HPIT} relate to the critical velocity of LPIT and HPIT sprays, respectively. T_L and T_H refer to the LPIT and HPIT sprays particle temperature, respectively, traveling at these respective critical velocities.*

LPIT			
Particle velocity (m/s) and temperature (°C)	**40µm**	**58µm**	**68µm**
Average	651m/s,51°C	609m/s, 36°C	587m/s, 34°C
Critical (V_{C_LPIT}, T_L)	637m/s, 40°C	604m/s, 35°C	582m/s, 33°C
HPIT			
Particle velocity (m/s) and temperature (°C)	**40µm**	**58µm**	**68µm**
Average	626m/s, 123°C	586m/s, 92°C	574m/s, 85°C
Critical (V_{C_HPIT}, T_H)	593m/s, 191°C	568m/s, 123°C	561m/s, 122°C

2.4 Single particle deposition analysis

The sprayed surfaces have been analysed to characterize the interfacial phenomena generated by incoming particles. Rebounding particles have been collected during spray using a metal screen covered with double-sided carbon tape to allow the attachment of particles upon their contact with the screen, as illustrated in Figure 2a. Adhered particles have been pulled off from the substrate. As illustrated in Figure 2b, a thermally curing elastomeric adhesive, FM1000 (Cytec Engineering Materials, MD, USA), was used to attach the sprayed substrate surface to a counter sample. Upon separation of the glued samples, two surfaces are generated. The counter sample holds de-bonded particles displaying the contact interface characteristics and the substrate specimen provides information about residual bonds. Together, these surfaces provide a complete image of the achieved particle/substrate bonding. Scanning electron microscopy (SEM, Oxford Instrument, EVO-MA10, Zeiss, UK), backscattered detector (BSD) and Energy-dispersive X-ray spectroscopy (EDS) have been used to study all specimens. An optical microscope (VHX-2000 Keyence, ON, CA) has been utilized to provide both top view images and 3D particle profiles.

3 FINITE ELEMENT MODELING

3.1 Impact process

The commercially available ABAQUS/Explicit finite element analysis (FEA) software has been used to study the effect of particle impact temperature on particle/substrate impact dynamics. The impact was simulated using a Lagrangian approach with quadrilateral coupled temperature-displacement elements (CAX4RT) for the aluminum particles and steel substrate, to properly capture the effect of heating due to plastic deformation. The mesh size was set to $1/145d_p$, to ensure mesh independent results and ensure proper resolution at the contact interface elements (Ref 11,38). A fixed boundary condition was set on the substrate bottom surface. To eliminate the effect of reflective waves from substrate boundaries on the impact process and to avoid excessive computational costs, the substrate diameter and height was set to 10 times the particle diameter. The substrate was set at room temperature, 25°C, for all cases.

The contact interaction at the particle/substrate interface is modeled using the surface-to-surface kinematic constraint enforcement method, which minimizes the penetration of contacting surfaces elements and consequently increases results accuracy. The interaction properties at the contacting surfaces have been described using a tangential penalty with a coefficient of kinetic friction, μ_k, equal to 0.5 (Ref 8), a hard pressure-overclosure normal behavior and a heat generation formulation.

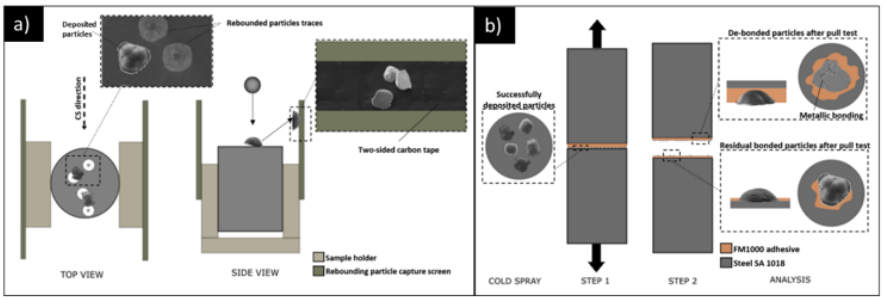

Figure 2: a) Controlled scarce particle deposition and ensuing substrate surface analysis. Collection of rebounded particles process is illustrated through the side view of the spray set-up. b) Single particle pull-test set-up providing information about the substrate and adhered particle state.

The simulation total time was set to 100ns to capture the full particle deformation and the beginning of rebound process from the substrate surface.

For a given powder size, the modeled particle impact velocity was kept constant between both HPIT and LPIT simulations to study solely the effect of impact temperature. For this purpose, a velocity of 637m/s, 604m/s and 582m/s was chosen for powder set 1, set 2 and set 3, respectively. The particle impact temperatures found at the chosen velocities in both LPIT and HPIT sprays in (Ref 31) have been set as the initial particle temperature in the simulations. Consequently, temperatures of 40°C, 35°C and 33°C in LPIT and 126°C, 93°C and 87°C in HPIT sprays for powder set 1, set 2 and set 3, respectively, have been used.

3.2 Material properties

The particle and substrate elastic response is modeled using the Mie-Grüneisen equation of state (EOS) through the linear U_s-U_p Hugoniot relation to express the hydrodynamic stress, while a linear elastic model was utilized to express the deviatoric stress (Ref 8). The plastic response of the particle has been described using the Preston-Tonks-Wallace (PTW) model developed for high strain rate applications (Ref 39). The flow stress, τ, is calculated using:

$$\hat{\tau} = \frac{\tau}{G_p(T)} = \frac{\sigma}{2G_p(T)} = 2\left[\hat{\tau}_s + \alpha \ln\left[1 - \varphi\left(-\delta - \frac{\theta\varepsilon_p}{\alpha\varphi}\right)\right]\right] \quad \text{Eq. 3}$$

where

$$\alpha = \frac{s_0 - \hat{\tau}_y}{p}, \quad \text{Eq. 4}$$

$$\delta = \frac{\hat{\tau}_s - \hat{\tau}_y}{\alpha}, \quad \text{Eq. 5}$$

and

$$\varphi = \exp(\delta) - 1. \quad \text{Eq. 6}$$

The $\hat{\tau}_s$ and $\hat{\tau}_y$ in the previous equations are the normalized work-hardening saturation stress and yields stress, respectively, θ is the strain hardening rate, ε_p is the equivalent plastic strain, s_0 is the saturation stress at 0 K, p is the strain hardening constant, σ is the Von Mises equivalent deviatoric stress and G_p is the plastic shear modulus. For simplicity, the shear modulus has been described as solely function of temperature, as previously shown to accurately describe the CGDS impacts (Ref 39);

$$G_p(T) = G_0 - \frac{D}{\exp\left(\frac{T_0}{T}\right) - 1}. \quad \text{Eq. 7}$$

In the previous equation, G_0 is the shear modulus at 0 K, D is a material constant, T_0 is a temperature material constant and T is the material temperature. The PTW model is a modified version of the Voce law such that the work hardening is described as:

$$\frac{d\hat{\tau}}{d\varepsilon} = G_p(T)\frac{\exp\left[p\frac{\hat{\tau}_s - \hat{\tau}}{s_0 - \hat{\tau}_y}\right] - 1}{\exp\left[p\frac{\hat{\tau}_s - \hat{\tau}_y}{s_0 - \hat{\tau}_y}\right] - 1}. \quad \text{Eq. 8}$$

At low strain rates, the plastic deformation process is governed by thermal activation while at high strain rates, the plastic flow is controlled by dislocation drag mechanisms. The maximum (high strain rate) and minimum (low strain rate) of the work-hardening saturation stress ($\hat{\tau}_s$) and yield stress ($\hat{\tau}_y$) are defined as:

$$\hat{\tau}_s = \max\left\{s_0 - (s_0 - s_\infty)\mathrm{erf}\left[\kappa\hat{T}\ln\left(\frac{\gamma\dot{\xi}}{\dot{\varepsilon}_p}\right)\right], s_0\left(\frac{\dot{\varepsilon}_p}{\gamma\dot{\xi}}\right)^{\beta}\right\} \quad \text{Eq. 9}$$

and

$$\hat{\tau}_y = \max\left\{y_0 - (y_0 - y_\infty)\mathrm{erf}\left[\kappa\hat{T}\ln\left(\frac{\gamma\dot{\xi}}{\dot{\varepsilon}_p}\right)\right], \min\left\{y_1\left(\frac{\dot{\varepsilon}_p}{\gamma\dot{\xi}}\right)^{y_2}, s_0\left(\frac{\dot{\varepsilon}_p}{\gamma\dot{\xi}}\right)^{\beta}\right\}\right\}, \quad \text{Eq. 10}$$

where $\hat{T} = T/T_m$, T_m is the melting temperature, s_∞ and y_∞ are the saturation and yield stress close to melting temperature, respectively, κ is the temperature dependence constant, γ is the strain rate dependence constant, $\dot{\varepsilon}_p$ is the plastic strain rate, β is the high strain rate exponent, y_0 is the yield stress at 0K, y_1 is the medium strain rate constant and y_2 is the medium strain rate exponent. The $\dot{\xi}$ term in the previous equation is defined as:

$$\dot{\xi}(\rho, T) = \frac{1}{2}\left(\frac{4\pi\rho}{3M}\right)^{1/3}\left(\frac{G_p(T)}{\rho}\right)^{1/2}, \quad \text{Eq. 11}$$

where M is the atomic mass and ρ is the density. It can be seen from inspection of Eq. 9 and Eq. 10 that the error function and the influence of T_m dominates at low strain rates. The yield strength is dominated by strain rate when the strain rate value reaches a critical constant evaluated to be between10^5s^{-1} and 10^8s^{-1} for aluminum (Ref 40). To complete the discussion on the plasticity model, the definition of the temperature change over time is also described:

$$\dot{T} = -\Gamma T\frac{\dot{v}}{v} + \frac{\sigma_{ij}\dot{\varepsilon}^p_{ij}}{\rho C_v} \quad \text{Eq. 12}$$

where Γ is the Grüneisen gamma, v is the volume, σ_{ij} is the Cauchy stress tensor, ε_{ij}^{p} is the strain tensor and C_v is the specific heat with fixed volume. The first term in Eq. 12 corresponds to the temperature rise (or drop) due to volume variations and the second term refers to the heating from plastic work. The temperature does not affect the integration of Eq. 8 as it is uncoupled with the included integration variables such as strain rate and strain. In addition, as the melting temperature is only used to normalize (scale) the temperature in the calculation of low strain rate work hardening saturation stress and yield stress, the effect of the melting temperature value is greatly diminished in high strain rate deformation such as in those experienced in CGDS impact.

The substrate plastic deformation processes have been described using the Johnson-Cook (JC) model due to the lack of material properties available for the PTW formulation. The detailed theory, deformation model description of the elastic and plastic response and the material properties of both the aluminum and steel can be found in (Ref 8).

It has been shown that the alumina native oxide layer has an amorphous or semi-crystalline structure (Ref 36). However, lack of data pertaining to the amorphous or semi-crystalline oxide layer behavior under shock loading and the vast range of reported mechanical properties (Ref 41), dependent on alumina density, prohibits an exact description of the material properties. Hence, the native layer was not modeled and experimental interfacial material features, in particular grain deformation, have been used instead to assert the oxide presence or its proper removal.

4 RESULTS AND DISCUSSION

4.1 Particle deformation

Figure 3 shows the top view surface morphology of particles after deposition onto the steel substrate. Jetting features are observed for all cases. Particle outer edge cracking is observed for all cases, as highlighted in the inserts of Figure 3**.** The jetting is more pronounced for HPIT due to the enhanced particle softening associated with the increased particle impact temperature, allowing greater material flow for the same stress field at the contact interface (Ref 42–44). The hard steel substrate undergoes no visible deformation near the particle periphery for all depositions from these top view images.

The particles deformation contours as predicted by the model are shown in Figure 4a and Figure 4b for LPIT and HPIT, respectively. Also shown, for each powder set, is a representative experimental particle outline as observed after impact on the substrate. Only a quadrant of the simulated particles is shown for each case, as the model is symmetrical, allowing better comparison with experimental results. A different color is used to distinguish each powder size set. Since constitutive phenomenological models are developed by fitting coefficients to visual inspection without any additional comparison to microstructural details such as dislocation behavior and activity (Ref 39), they inherently fail at capturing details such as the asymmetrical particle deformation observed in Figure 3, irrespective of the model dimensional space, i.e. 2D vs 3D. Nevertheless, the PTW model successfully predicts the influence of particle size and temperature on final diameter size. Figure 4c compares the measured particle average diameter after impact and the corresponding predicted deformation/diameter for both LPIT and HPIT sprays for a given particle size. For a given powder size, the particle final diameter, i.e. contact area, increases with particle impact temperature.

Additionally, the particle compression ratio (R_C), defined by

$$R_C = \frac{d_p - h_p}{d_p} \times 100\%, \qquad \textit{Eq. 13}$$

has been calculated for each set, where d_p is the original average particle diameter for each set and h_p is the height of the flattened particle in the impact direction. Due to the expected limited hard steel substrate surface deformation, the value of h_p has been estimated as the distance from the substrate to the particle top surface. The experimental and predicted R_C's values are shown in Figure 4d. For a given particle size, both results show an increase in R_C, i.e. flattening, with increasing particle impact temperature, i.e. increasing softening and plastic flow. The R_C decrease with particle size, easily observed for LPIT conditions, is solely attributed to the decrease in particle velocity rather than to the variation in particle diameter (Ref 38). Discrepancies between numerical and experimental values, presented in Figure 4c-d, stem from the lack of validated adequate PTW data for aluminum material under high strain rate deformation, as reported in the field (Ref 11,40).

As observed from Figure 3, the deposited particles shape is not spherical anymore, although particle sphericity is expected for symmetrical polycrystalline particle impacts as commonly reported to be the case in CGDS (Ref 45,46). Three specific types of particle shapes after impact have been detected. i.e. type 1: triangular, type 2: rectangular and type 3: square, and are shown in Figure 5.

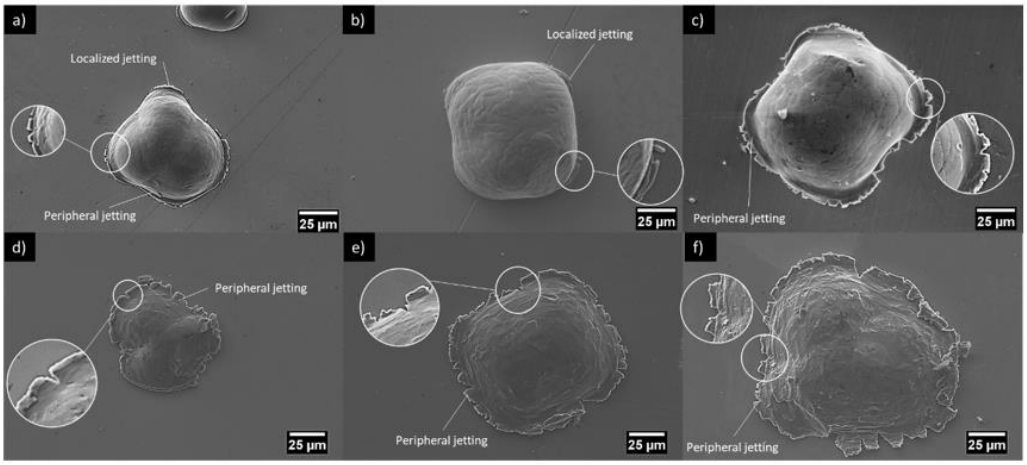

Figure 3: Single particle deposition under LPIT (a, b, c,) and HPIT (d, e, f) conditions. Localized peripheral aluminum particle material jetting is identified. Particle jetting and edge cracking are magnified. Particle size prior to impact increases from left to right, i.e. from set 1 to set 3.

Since these precise shapes have been detected for all three powder size sets, under both high and low impact temperature conditions, it is suggested that their occurrence is related to particle microstructure, i.e. crystallographic texture, rather than impact characteristics (size, temperature, and velocity). Particle microstructure influence on its final shape upon high-speed impact has been described in molecular dynamics (MD) studies. Similar powder shapes to the ones reported in the current work have been observed recently in MD impact studies for single crystal copper particles (Ref 47). The final particle shapes in the MD work have been associated to the initial particle crystal orientation with respect to the impact loading direction (Ref 47). Since the current study also deals with an FCC material, for which the slip systems are defined along {111} planes and <110> directions, the conclusions related to the particle crystal orientation influence on sliding directions, slip system activation and stacking faults formation obtained using MD are deemed relevant. The triangular particle shape, as shown in Figure 5a, has been proven to result from an initial [111] crystal orientation.

The rectangular and square shapes have been associated to single crystal particles oriented in the [110] and [100] directions, respectively. Hence, the current particle material behavior suggests presence of preferential grain orientation with narrow distribution and/or important fraction of low angle grain boundaries and/or critical grain alignment/geometry.

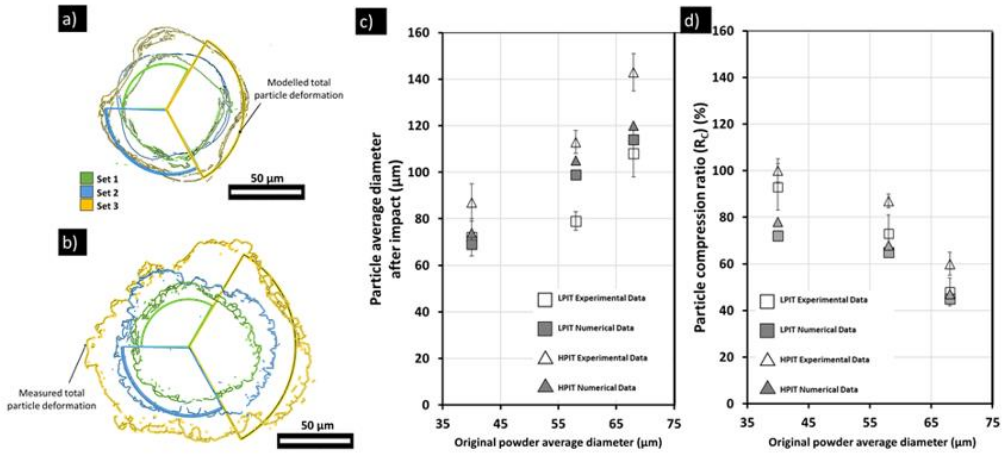

Figure 4: Predicted deformation of particles after impact for a) LPIT and b) HPIT. A single representative outline of deposited particle contours measured by microscopy is provided for each powder set along with the corresponding numerical model prediction. Experimental and numerical data of c) particle average deformed diameter and d) R_C based on particle size and impact temperature are provided.

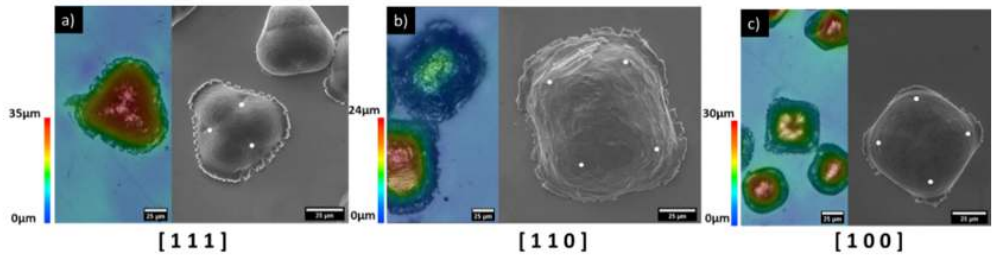

Figure 5: Deposited particles top view displaying all three detected final shapes; a) triangular, b) rectangular and c) square. Particle 3D height profile with corresponding scale along with SEM images are provided for all three shapes. The preferred grain orientation is provided for each case.

In the current study, due to the constrained substrate deformation, i.e. limited geometrical restrictions, it is believed that the particle shapes result solely from particle microstructural characteristics. This anisotropic particle behavior affects both the particle final deformation and R_C, i.e. [100] orientation allowing the greatest and [110] the lowest compression (Ref 47), which can also explain the standard deviations and divergent experimental and numerical results shown in Figure 4.

4.2 Substrate contact traces

As shown by the substrate surface images in Figure 6, circular traces are left on the steel substrate surface after the impact of unsuccessfully adhered (rebounded) particles. The circular traces have been analysed using EDS, however, the quantity of the remnant or removed material in these regions was insufficient to confirm their nature. The traces are spherical irrespective of particle size, impact characteristics and particle final shape. The LPIT traces show no remnant aluminum material while evidence of local residual aluminum is observed on all HPIT traces, as highlighted and pointed in yellow arrows in Figure 6. The remnant aluminum material is mostly detected at the trace periphery and decreases as particle size increases. Since particles within the same powder set impact the substrate at similar velocities but at different temperatures, it is suggested that the impact temperature affects the traces characteristics. Remnant material alludes to the presence of high pressure and surface expansion at the trace periphery (Ref 48). Since the compressive contact pressure, surface expansion and temperature are lowest at the particle jetting edge, the traces are considered to originate from interfacial phenomena rather than from particle total deformation.

Figure 6 also includes samples of the collected rebounded particles for each powder set (contact surface and side view). The average diameter of the collected particles, provided in Figure 6, is very close to the deposited particles diameter, shown in Figure 4, implying that their impact characteristics (velocity and temperature) are not far from critical values. Jetting-like features are observed at the rebounded particles periphery for all cases, increasing with particle temperature increase (HPIT vs LPIT), which confirms that jetting does not necessarily correlate with successful bonding (Ref 49–51). For LPIT, the collected particles present a clean interfacial surface with no signs of cup-and-cone, protruding material or any other visible features related to metallurgical bonding detectable through SEM. For HPIT, the impacted particle surface shows signs of micro-cracking, which increases as the particle size decreases. The micro-cracking can be associated to the presence of large tensile stresses related to the intensive surface expansion and/or to the presence of rapid interfacial heating and cooling processes.

The numerical model has been used to try to identify the interfacial characteristic causing the ring traces appearance on the substrate surface. Figure 7 highlights the particle contact surface area experiencing temperatures above the aluminum melting point, i.e.600°C, for LPIT powder set 3. However, as the constitutive finite element models do not account for material phase transitions, i.e. melting, results above material melting point should be analysed with proper caution. In most models involving plastic deformation, the melting temperature is assumed to be constant (Ref 39,40,53,54). However, in high strain-rate impacts involving large pressure variations, the melting temperature increases drastically with pressure. The melting curve of aluminum has shown that at 4GPa the aluminum melting temperature reaches 927°C (Ref 55). A linear trendline has been curve fitted to results of (Ref 55) to extract the relation between pressure and melting temperature up to pressures recorded in the current CGDS impact, i.e. <4GPa. Subsequently, the following ratio, φ, has been utilized to determine the particle interfacial regions that reach melting temperatures given the contact pressure they experience:

$$\varphi = T/T_{m,p},$$
$$\begin{cases} \varphi < 1, & \text{below melting} \\ \varphi = 1 & \text{at melting} \\ \varphi > 1 & \text{high temperature melting} \end{cases} \qquad \text{Eq. 14}$$

where T is the existing current element temperature and $T_{m,p}$ is the temperature required to generate melting at the exposed pressure. Figure 7 shows the effect of contact pressure on the melting temperature at the LPIT powder set 3 interface.

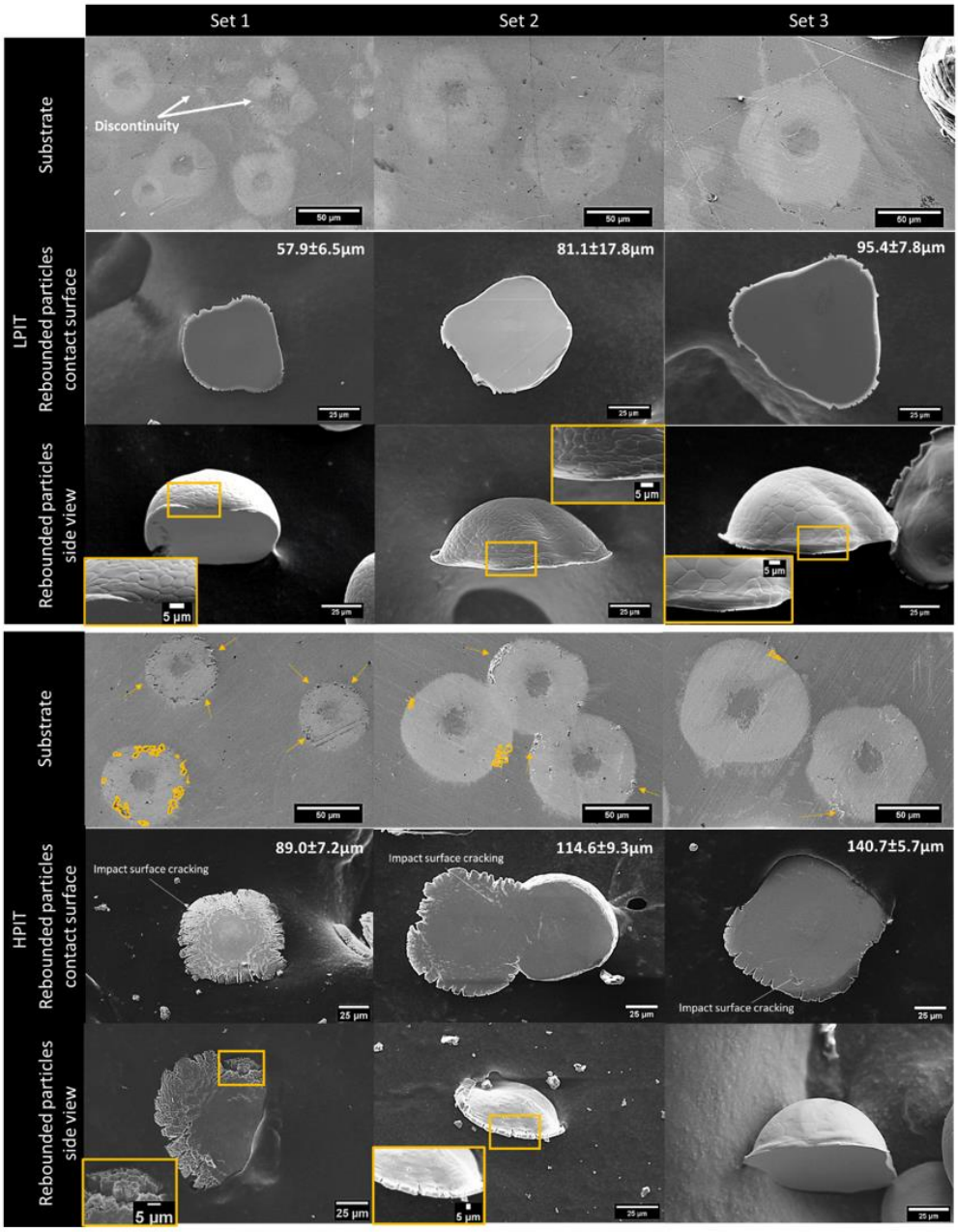

Figure 6: Traces on steel substrates left by rebounded particles for both LPIT and HPIT impacts and all three size sets. Remnant aluminum material on the steel substrate surface is highlighted in yellow. LPIT discontinuous traces are indicated by white arrows. The impacted surface and side view of collected rebounded particles for each deposition are also shown and micro-cracking processes observed for HPIT are highlighted. The average diameter of collected rebounded particles are provided.

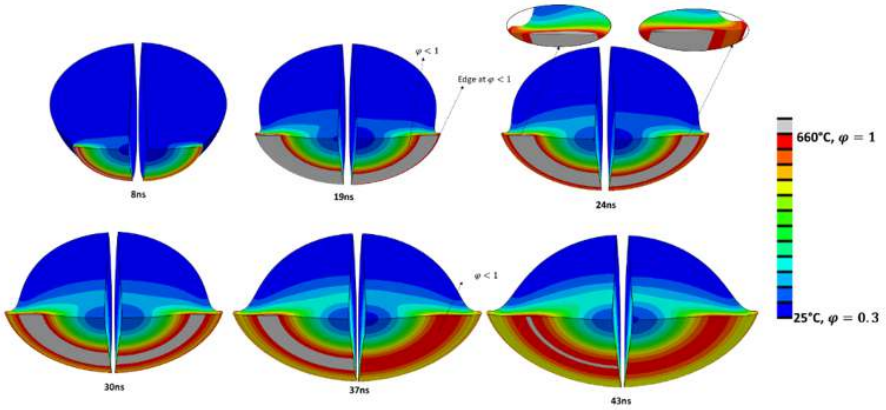

Figure 7: Numerical temporal evolution of particle temperature (left) and particle pressure-dependent melting temperature factor φ (right) are provided at the interface of LPIT powder set 3 impact. Inserts show the effect of pressure through particle thickness.

The pressure dependent melting temperature is seen to persist up to 37ns, while the pressure independent melting temperature, i.e. 600°C, holds up to 43ns. In addition to shortening the period under which melting temperatures persist, the pressure also decreases the size and thickness of particle material experiencing melting temperatures.

Figure 8a illustrates the interfacial zones found above pressure dependent melting temperature for all spray conditions. An experimental representative trace is outlined for each case. The same color code as in Figure 4 is used to discern results between powder sets. The zone with temperatures above the aluminum melting point also appears in a ring-like shape, for which the ring trace outer diameter and ring inner circle diameter are also reported in Figure 8b and Figure 8c, respectively, along with the experimental measurements. The periphery of these regions is seen to increase with particle diameter and impact temperature increase while the inner circle diameter sees only slight changes with varying particle impact characteristics, which resembles the experimental traces behavior.

The measured outer diameter increases from 48µm (set 1) to 93µm (set 3) for LPIT while these values rise from 60µm (set 1) to 100µm (set 3) for HPIT sprays. The rebounded particle diameter for each powder set and impact condition, shown in Figure 6, is also far from these ring-shape trace dimensions, which once again confirms that the traces are related to specific interfacial phenomena rather than particle deformed size. The inner circle diameters increase by less than two microns with the increase of particle temperature for a given particle size. For LPIT, an increase in the ring inner circle diameter from 15µm to 22µm is recorded with the increase of particle diameter from powder set 1 to powder set 3. These values increase from 16µm to 24µm for HPIT deposition. The same trends are observed in the numerical model, as shown in Figure 8, suggesting a link between the traces and particle high temperature zones. Deviations from experimental traces dimensions and these zones can stem, once again, from the inaccuracy of the pure aluminum properties utilized in the PTW model and its inability to predict the exact deformation and anisotropic particle behavior.

Figure 8a also shows the maximum temperature reached on the particle contact surface during its deformation. For LPIT, the maximum particle contact surface temperature decreases, from 985°C to 892°C, with decreasing particle impact velocity from 637m/s (powder set 1) to 582m/s (powder set 3). Increasing particle impact temperature, i.e. HPIT sprays, raises the temperature at the particle contact surface. An increase of 47°C and 68°C is observed for powder set 1 and powder set 3, respectively when depositing from LPIT to HPIT conditions.

4.3 Particle melting

Material features associated to melting have been detected at the particle and substrate contact surfaces, as seen in Figure 9. In the case of LPIT, small fingers radiating from the particle impact location are observed on the substrate surface, as shown in Figure 9a. The radiating fingers leave traces of contact on the substrate surface similarly to the ones detected in Figure 6, further reinforcing the association of high temperature zones with the detected traces. The BSD insert in addition to an EDS analysis of the impacted area confirm that the remnant material consists solely of aluminum. For HPIT sprays, nano-sized spheroidal particles were formed on the surface of the rebounded particles, as shown in Figure 9b. These small ejecta particles have been associated to fast solidification of liquid material (Ref 2).

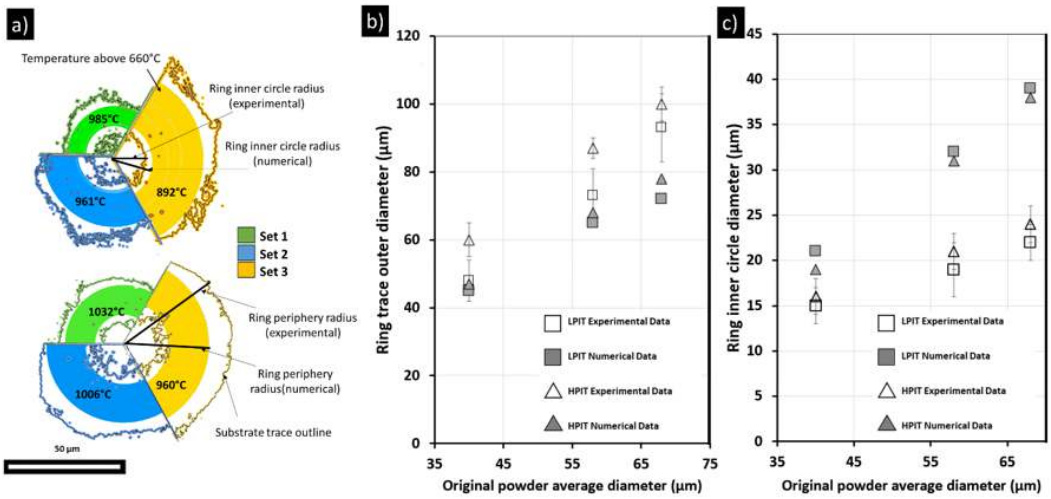

Figure 8: a) Illustrations showing a single representative trace outline along with the corresponding numerical zone experiencing melting temperatures for LPIT (top) and HPIT (bottom) impacts. b) The trace outer periphery and c) ring inner circle diameter measurements are compared with the numerical results of particle contact surface area experiencing temperatures above melting point.

Both the spheroidal particles and melt fingers validate the presence of melting temperatures, which is in good agreement with the model prediction shown in Figure 8. Melting features have been more frequently observed for HPIT than for LPIT sprays since increasing impact temperature leads to improved plastic deformation, i.e. thermal softening, and consequently to superior frictional heating and localised temperature rise. Additionally, for LPIT sprays, melting characteristics have been predominantly observed in powder set 3.

Based on the model, the material found above the aluminum melting temperature reaches a thickness of 0.45µm for LPIT powder set 1 up to 0.50µm for powder set 3. These values are larger for HPIT impacts and reach 0.60µm and 0.70µm for powder set 1 and set 3, respectively. Although the occurrence of melting, restricted to this localized thin film interfacial layer in CGDS impact, has minor influence on the overall particle deformation, melting can have an important role in the particle bonding process. Observations from Figure 9 demonstrate that the particle rebound energy is sufficient to overcome the particle adhesion. If the solidification process of the molten material is lengthier than the particle residence time on the substrate surface, the liquid melted interface hinders adhesion as it provides low mechanical particle/substrate interface strength (Ref 52).

Figure 10a shows the propagation of the interfacial zone found above melting temperatures and points to the location of potential melting. Zone 1 delineates the region that undergoes rapid cooling processes, as illustrated in Figure 10a, and the particle south pole, which not once reaches melting temperatures throughout the particle deformation process.

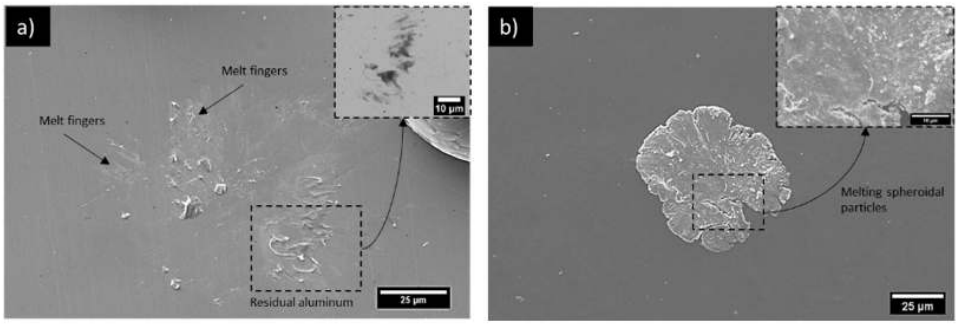

Figure 9: SEM and BSD analysis of melt related features. a) Melt fingers observed on the substrate surface after rebound of LPIT particle. b) Spheroidal particles formed on the HPIT contact surface after rebounding.

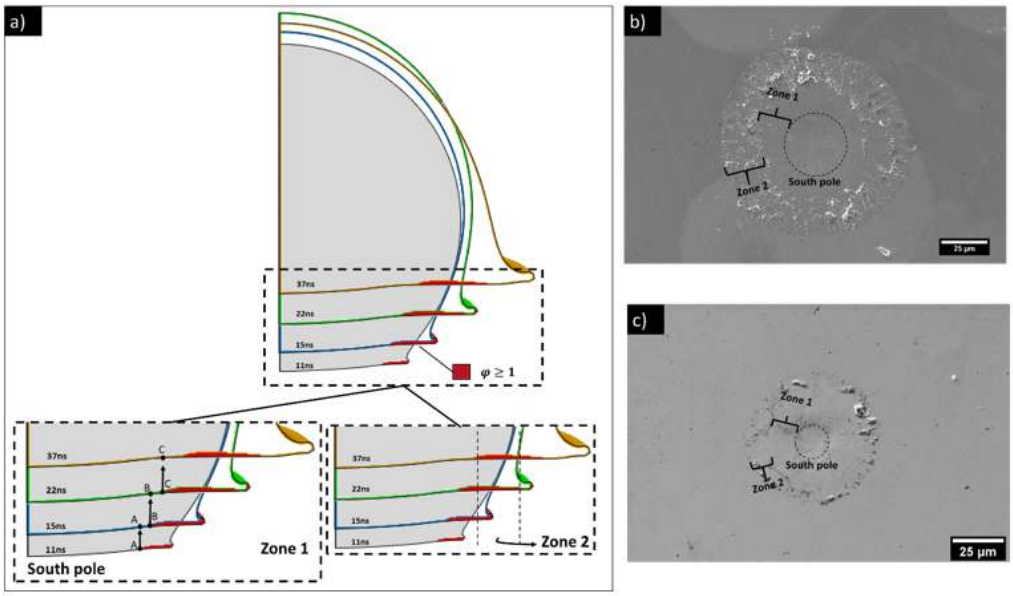

Figure 10: a) Numerical model results illustrating the propagation process of zones above melting temperature. Elements with $\varphi \geq 1$ are highlighted in red. Zone 1 is comprised of rapidly cooling elements and the south pole while Zone 2 consists of elements experiencing melting temperatures for long periods. Substrate surface after the impact and subsequent rebound of a HPIT particle from a) set 3 and b) set 1. The melt related propagation zones are delineated along with the south pole.

The strong compressive shock propagating inside the particle upon impact generates high temperatures in the particle material behind the shock front. As the shock propagates and reflects on the particle boundaries, it leads to the mentioned rapid interfacial heating and cooling processes in the first few nanoseconds of the impact, as illustrated in Figure 10a for the HPIT powder set 3. Elements referred as "A", "B" and "C" in Figure 10a are seen to cool down quickly during particle deformation.

Aside from rapidly cooled regions, an interfacial zone, referred to as Zone 2 in Figure 10a is comprised of elements which experience temperatures above melting for over tens of nanoseconds. For HPIT, this stagnant region, i.e. Zone 2, persists for 18ns and 26ns for powder set 1 and set 3, respectively, while these values reach 11ns and 18ns for LPIT conditions, thus showing an increase with both impact temperature and particle size.

Experimental observations, shown in Figure 10b and c, confirm the existence of both zones and the high temperature propagation process. Zone 1 is seen to leave no melt related features. It is within Zone 2 that a small film at the particle interface surface is believed to undergo melting, if any, as enough energy would be absorbed at the same localized region to induce melting, i.e. above the aluminum latent heat of fusion, as shown to be the case for the impacts observed in Figure 10. The outward spreading of the molten material, as observed in Figure 10b, stems from the particle simultaneous outward deformation. Experimental observation along with the numerical melt propagation validate, once more, the nature of the substrate traces.

4.4 Particle bonding

The experimental observations indicate that jetting, micro-cracking and melting features are not necessarily associated with successful bonding. The interfacial features of removed adhered particles are now analysed, and FEM contact characteristics evaluated to identify the bonding requirements under LPIT and HPIT conditions. Table 4 presents the coating adhesion for each powder set and both LPIT and HPIT conditions, as reported in (Ref 31), which will be used in the upcoming discussion on single particle bonding.

Table 4: Coating adhesion strength as reported in (Ref 31)

Coating Properties	Powder Set 1	Powder Set 2	Powder Set 3
LPIT, $\sigma_{adhesion}$, (MPa)	34.8±7.5MPa	60.0±19.4MPa	71.7±13.5MPa
HPIT, $\sigma_{adhesion.cohesion}$, (MPa)	>71.2±13.4MPa*	>61.0±10.6MPa*	32.3±10.8MPa**

* Local coating failure, refer to (Ref 31).
** Adhesion and cohesion failure

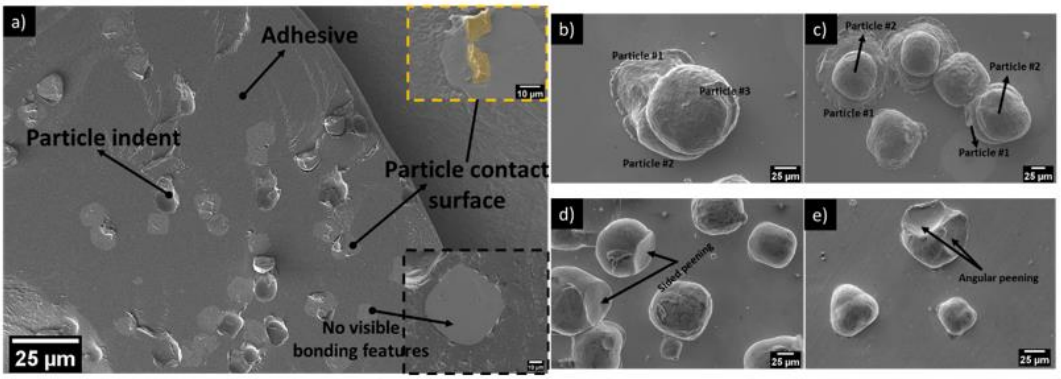

Figure 12: a) Contact surface of pulled LPIT powder set 3 particles held within the utilized adhesive. Particles with and without bonding signs are highlighted in yellow and black boxes, respectively. Deposited particles during wipe test showing presence of a) successive skewed impact, b) symmetrical consecutive impact, c) angular impact of rebounding particles and d) multiple angular impact of rebounding particles.

4.4.1 Single particle debonding

Figure 12a displays the contact surface of detached particles. A large quantity of particles, within each tested condition, did not show any signs of features related to metallic bonding, implying that the bonded regions were too small to be detected using SEM. Furthermore, some particles remained bonded to the substrate surface after pulling test, as a result of larger bond strength, i.e. leaving a particle indent in the adhesive, as shown in Figure 12a. For LPIT, the number of particles that remained adhered to the substrate surface were low irrespective of powder size, as shown in Figure 12a for powder set 3. For HPIT, the fraction of particles remaining bonded onto the substrate increased with particle size decrease, which suggests increasing bonding strength with particle decreasing size.

Pulled particles display a vast size range of metallic bonding signs within each deposited powder set and condition.

Despite deposition under wipe test conditions, sequential deposition of incoming particles on previously deposited particle and consecutive impacts followed by rebounding process have been detected in the current depositions, as shown in Figure 12b to Figure 12e, which can affect the observed bonded zones. Figure 13 shows magnified single particle contact surfaces to emphasize on the detected bonded regions. As shown, for both HPIT and LPIT sprays, regions with signs of metallic bonding are not uniformly distributed on the contact surface. This can be associated to angular impact, irregular oxide removal of non-uniform oxide thickness, distorted particle grain-dependent deformation and successive arbitrary impact (as shown in Figure 12). Although different types of bonding features have been detected within all three sets of powders, the HPIT powder set 1 shows the highest zone of metallic bonding signs on the particle contact surface, as shown in Figure 13a.

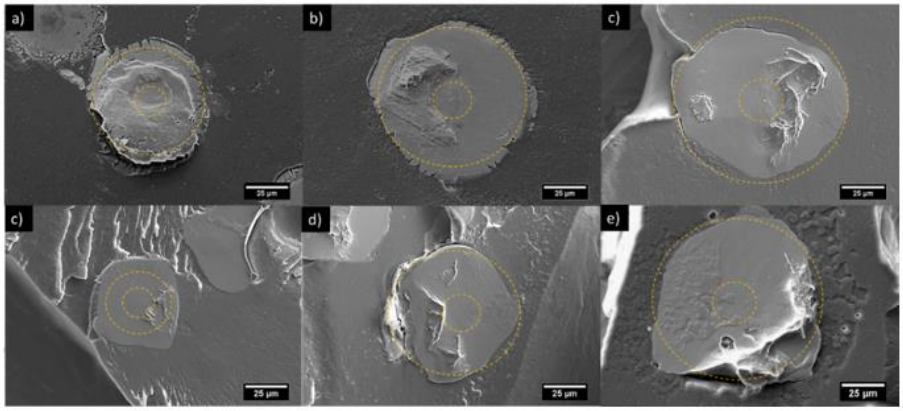

Figure 13: Particle impacted surface after removal from the substrate for all HPIT (top) and LPIT (bottom) sprays. Particles from powder set 1 (a-c), set 2 (b-d) and set 3 (c-e) are shown. The size of the measured traces on the substrate surface are delineated in yellow.

In addition to lacking visible metallic bonding features as observed in Figure 13, Figure 14 shows that the particle south pole experiences limited deformation as the original powder grain morphology is still observed even after impact for both LPIT and HPIT conditions. This confirms the lack of adequate deformation and consequently limited potential for native oxide removal at the south pole, preventing metallic bonding to occur in this region, which has only been shown through FEM in the field prior to the current observations (Ref 50,56,58,59).

4.4.2 Particle characteristics influence on bonding

Bay et al. have demonstrated that bonding between two metal surfaces cannot occur until a surface expansion ratio threshold is reached (Ref 60). A larger R_c,as reported in Figure 4, suggests improved contact surface expansion, enhanced oxide layer removal, and consequently larger bonding zones. This can explain the large adhesion strength of powder set 1 coating sprayed under HPIT conditions, as reported in Table 4. In addition, Conrad and Rice have shown that the bonding strength between two metal surfaces, deprived of native oxide layers, is function of the applied pressure, i.e. $\sigma_{adhesion} \cong \sigma_{22}$, (Ref 60). The influence of particle velocity/size and impact temperature on the evolution of interfacial σ_{22} pressure is shown in Figure 15 for three elements found at the particle contact surface of LPIT powder set 1 and set 3 and HPIT powder set 1. The first element corresponds to the location reaching first melting temperature, the second element experiences the highest temperature during deformation, and the third element is located inside Zone 2 described in Figure 10. All three elements are found in regions where bonding has been detected in the current wipe tests and within the area covered by the substrate traces. As shown in Figure 15, increasing particle impact temperature has limited influence on the interfacial σ_{22} value while the σ_{22} peek value is seen to increase with particle velocity increase, i.e. size decrease in the current study.

Figure 15 also shows that although pressure and temperature peek values are largest for HPIT powder set 1, the contact surface normal compressive stress (σ_{22}) quickly drops to values lower than those recorded in LPIT powder set 3 only after ~15ns following impact. This indicates that the strong HPIT powder set 1 metallic bonding, supported by the large metallic bonded features observed in Figure 13, high coating adhesion strength presented in Table 4 and largest quantity of unsuccessfully removed particles, must have occurred within these first 15ns. Additionally, it is within this time frame that the melt temperatures are seen to persist, as discussed in section 4.3, which emphasises on the importance of temperature in metallic bonding. The LPIT powder set 1, however, has displayed the lowest amount of metallic bonding features, as shown in Figure 13, at the contact interface. Since both HPIT and LPIT powder set 1 impacts generate similar interfacial σ_{22} values, the low coating adhesion strength reported for LPIT powder set 1 can only stem from limited surface expansion and consequently improper oxide layer extrusion within the first 15ns due to low impact temperature under which it deposits. Its bonding process is, thus, believed to occur only after the σ_{22} peek value, as shown in Figure 15.

Despite not achieving the temperature and pressure peak values of powder set 1, particles from powder set 3 hold higher contact compressive pressure, due to larger kinetic energy, and temperature after 15ns, as shown in Figure 15. The σ_{22} values after 15ns are close to 1GPa. The powder set 3 also deforms under low R_c, as reported in Figure 4d, implying that proper surface expansion might not be reached quickly following impact. An increase in compressive contact pressure and surface expansion can, however, be achieved with in-situ peening processes which have been shown to be important during LPIT coating

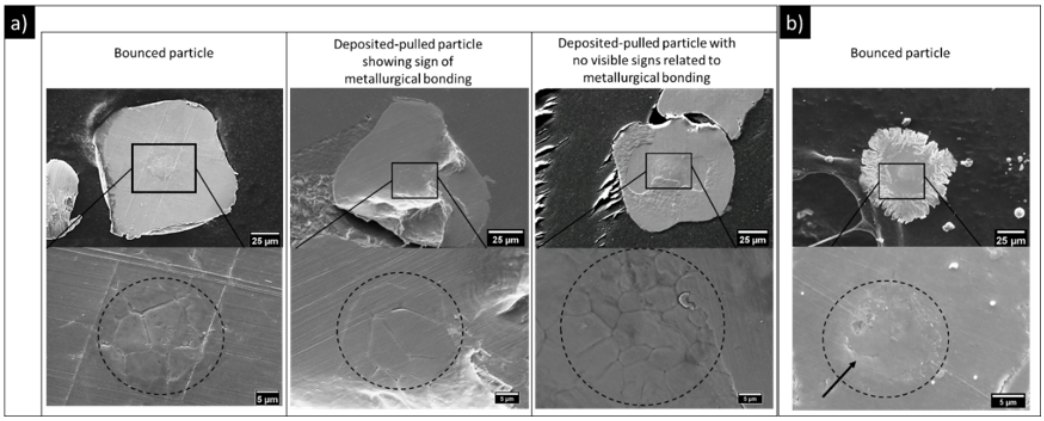

Figure 14: Experimental evidence of particle south pole limited deformation. Original powder grain morphology is detected in both a) LPIT and b) HPIT sprays.

deposition, as reported in (Ref 31). Whether the bonding and proper oxide layer removal occurs within the first 15ns or is reached after through in-situ peening processes is not possible to confirm with the current modeling work or experimental set-up. Aside from in-situ peening processes, increasing powder set 3 impact temperature (HPIT conditions) has also shown to increase its R_c, as demonstrated in Figure 4, and increase the duration of Zone 2 found above melting temperature, as discussed in section 4.3. This rise in interfacial expansion and decrease in cooling rate, however, lead to the successful deposition of particles traveling at much lower velocity, i.e. lower critical velocity (Ref 31). As particle size increases, the velocity distribution shifts drastically towards lower speeds (Ref 31), which decreases the compressive pressure at the interface and consequently lowers bond strength, as explained through Figure 15. This low bonding strength has been observed in the HPIT powder set 3 wipe tests, which have shown failure at the particle-to-particle junction, as shown in Figure 16.

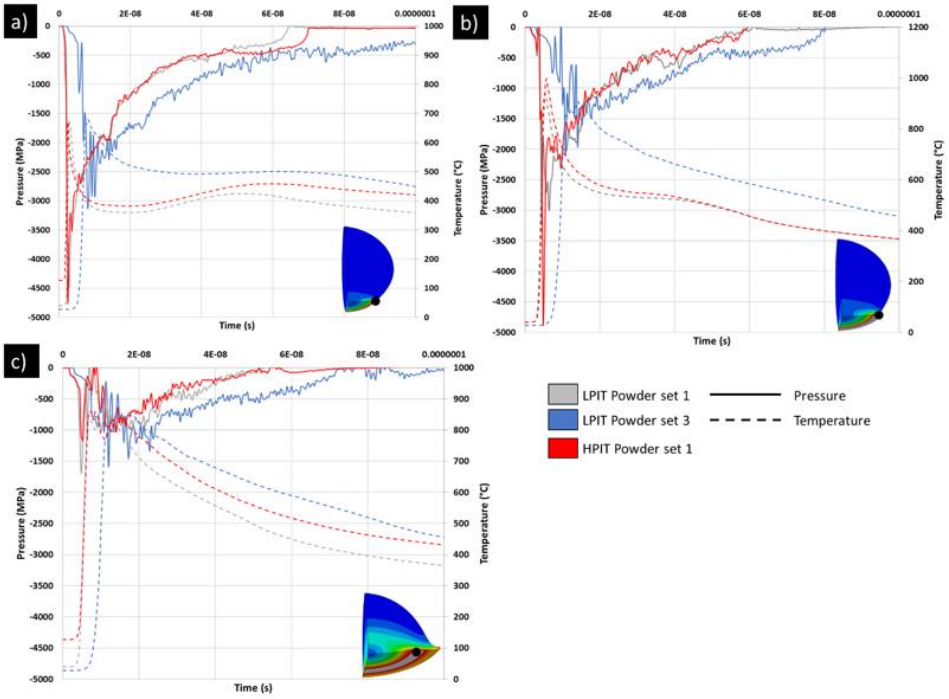

Figure 15: LPIT powder set 1 and set 3 contact pressure and temperature temporal evolution at a) the first element found above melting temperature, b) for the element found at highest temperature and c) for an element found in Zone 2. Studied elements are identified using a dot in the provided particle inserts.

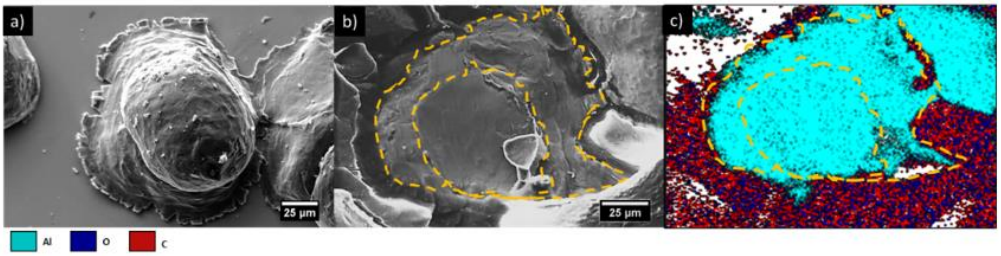

Figure 16: a) HPIT powder set 3 double impact detected in the wipe test deposition. b) Cohesion fracture after pull test showing local metallic bonding. c) EDS mapping confirming an aluminum metallic bond.

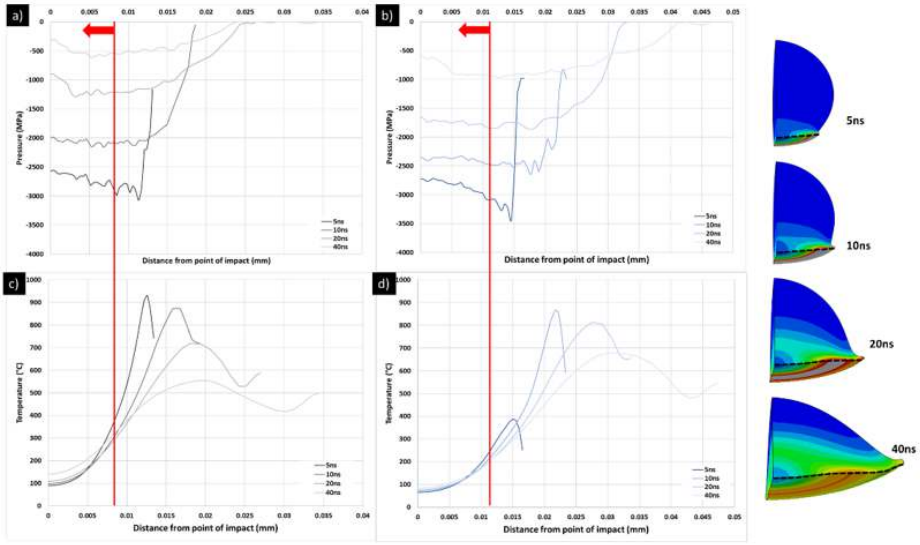

Figure 17: Particle contact surface characteristics at 5ns, 10ns, 20ns and 40ns after impact. Compression pressure for LPIT a) powder set 1 and b) powder set 3. Temperature for LPIT c) powder set 1 and d) powder set 3. The provided red line delineates the particle contact surface radius lacking metallic bonding signs based on experimental observations/measurements.

The pull test post-mortem observations of the particle-to-particle contact surface shows a clean indent with restricted asymmetrical metallic bonding. This also explains the mixed coating adhesion/cohesion failure reported in (Ref 31) and in Table 4. Particles depositing at lower velocity, due to the increase of impact temperature, thus, adhere at lower σ_{22} and consequently with lower bond strength.

The pressure and temperature along the interface at 5ns, 10ns, 20ns and 40ns for both powders set 1 and set 3 sprayed under LPIT condition is illustrated in Figure 17. The red line separates the unbonded south pole zone with the bonded ring shape regions. The highest pressure and temperature are always reached outside the south pole region and prior to the particle edge/jetting zone, as observed experimentally for both the particle/substrate and particle/particle impact.

Finally, the powder native oxide layer can also have an influence on the particle bonding process. Larger oxide thicknesses require more energy to be properly fractured and extracted from the interface, leaving less energy for deformation and consequently for bonding. In the current study, the particle surface native oxide thickness decreases from 4.15nm to 3.94nm, as presented in Table 1, from powder set 1 to powder set 3. However, a 0.21nm decrease in the passivation layer thickness might not be the sole factor affecting the particle adhesion. Studies on native oxide layer effects in the CGDS process report clear variation and influence in particle deposition for oxide thickness increase in the range of a few nanometer, which is an order of magnitude away from the thickness difference measured in the current study (Ref 36,48)

5 CONCLUSIONS

The current study investigated the interfacial phenomena occurring upon impact of adhered and rebounded soft aluminum particles on hard steel substrate material under low and high impact temperatures for three distinct powder size sets. Observed features have been associated to particle impact characteristics. The following are obtained results and drawn conclusions based on experimental and numerical data:

1. Experimental evidence of polycrystalline micro-particle grain dependent deformation, leading to distinct anisotropic deformation and final particle shape have been detected. The grain dependant deformation has been associated to preferred grain orientation with respect to the loading direction. Based on recent molecular single crystal particle impact models, the detected deformations in the current study match results obtained for grains preferentially oriented in the [111], [100] and [110] directions.
2. Original grain morphology at the particle south pole after collision and deformation processes provides experimental evidence of the low straining at the particle south pole.
3. Spherical traces left by rebounded aluminum particles on the steel substrate surface reveal zones of high interfacial particle temperatures.

4. Melted features, i.e. melt fingers and spheroidal particles, have been detected on the particle and substrate surfaces. Melting occurrence increases with impact temperature and particle size. The influence of pressure on melting temperature has shown to have major effects on the interfacial stagnant melt region duration and consequently, bonding.
5. Increasing particle impact temperature and velocity increases its compression ratio and consequently surface expansion leading to faster oxide layer removal and bonding.
6. Increasing particle size, i.e. kinetic energy, lowers the interfacial cooling rate, allows for longer high temperature zones to persist at contact and maintains suitable compressive stresses throughout deformation, which all enhance metallic bonding processes.
7. Small and fast particles have shown to adhere quickly after impact, i.e. within 15ns, due to the presence of large compressive pressures, which dissipate rapidly after impact. Increasing impact temperature ensures proper oxide removal prior to compressive pressure dissipation.

6 ACKNOWLEDGEMENTS

This project was funded by the Government of Canada. The authors would like to acknowledge the work of the technical officer's team in Boucherville: K. Bricault, F. Belval, P. Dionne and C. Hoang.

7 REFERENCES

1. P.C. King, C. Busch, T. Kittel-Sherri, M. Jahedi, and S. Gulizia, Interface Melding in Cold Spray Titanium Particle Impact, *Surf. Coatings Technol.*, Elsevier, 2014, **239**, p 191–199.
2. G. Bae, S. Kumar, S. Yoon, K. Kang, H. Na, H.J. Kim, and C. Lee, Bonding Features and Associated Mechanisms in Kinetic Sprayed Titanium Coatings, *Acta Mater.*, Pergamon, 2009, **57**(19), p 5654–5666.
3. S. Sevsek, C. Haase, W. Bleck, S. Sevsek, C. Haase, and W. Bleck, Strain-Rate-Dependent Deformation Behavior and Mechanical Properties of a Multi-Phase Medium-Manganese Steel, *Metals (Basel).*, Multidisciplinary Digital Publishing Institute, 2019, **9**(3), p 344, doi:10.3390/met9030344.
4. X.T. Luo, C.X. Li, F.L. Shang, G.J. Yang, Y.Y. Wang, and C.J. Li, "High Velocity Impact Induced Microstructure Evolution during Deposition of Cold Spray Coatings: A Review," *Surface and Coatings Technology*, Elsevier, 2014, p 11–20, doi:10.1016/j.surfcoat.2014.06.006.
5. S. Dosta, G. Bolelli, A. Candeli, L. Lusvarghi, I.G. Cano, and J.M. Guilemany, Plastic Deformation Phenomena during Cold Spray Impact of WC-Co Particles onto Metal Substrates, *Acta Mater.*, Pergamon, 2017, **124**, p 173–181, doi:10.1016/J.ACTAMAT.2016.11.010.
6. M. Hassani-Gangaraj, D. Veysset, K.A. Nelson, and C.A. Schuh, Impact-Bonding with Aluminum, Silver, and Gold Microparticles: Toward Understanding the Role of Native Oxide Layer, *Appl. Surf. Sci.*, North-Holland, 2019, **476**, p 528–532, doi:10.1016/J.APSUSC.2019.01.111.
7. D. Goldbaum, R.R. Chromik, N. Brodusch, and R. Gauvin, Microstructure and Mechanical Properties of Ti Cold-Spray Splats Determined by Electron Channeling Contrast Imaging and Nanoindentation Mapping, *Microsc. Microanal*, 2015, **21**, p 570–581, doi:10.1017/S1431927615000240.
8. A. Nastic, M. Vijay, A. Tieu, S. Rahmati, and B. Jodoin, Experimental and Numerical Study of the Influence of Substrate Surface Preparation on Adhesion Mechanisms of Aluminum Cold Spray Coatings on 300M Steel Substrates, *J. Therm. Spray Technol.*, 2017, **26**(7).
9. A.P. Semenov, The Phenomenon of Seizure and Its Investigation, *Wear*, Elsevier, 1961, **4**(1), p 1–9.
10. H.A. Mohamed and J. Washburn, Mechanism of Solid State Pressure Welding, *Weld. J.*, 1975, p vp, http://inis.iaea.org/Search/search.aspx?orig_q=RN:8330039. Accessed 21 November 2020.
11. S. Rahmati and B. Jodoin, Physically Based Finite Element Modeling Method to Predict Metallic Bonding in Cold Spray, *J. Therm. Spray Technol.*, 2020, **29**(4), p 611–629.
12. A. Nastic, • M Vijay, • A Tieu, • S Rahmati, and • B Jodoin, Experimental and Numerical Study of the Influence of Substrate Surface Preparation on Adhesion Mechanisms of Aluminum Cold Spray Coatings on 300M Steel Substrates, *J. Therm. Spray Technol.*, n.d., **26**, doi:10.1007/s11666-017-0602-1.
13. W.Y. Li, C.J. Li, and H. Liao, Significant Influence of Particle Surface Oxidation on Deposition Efficiency, Interface Microstructure and Adhesive Strength of Cold-Sprayed Copper Coatings, *Appl. Surf. Sci.*, Elsevier B.V., 2010, **256**(16), p 4953–4958.
14. S. Yoon, Y. Xiong, H. Kim, and C. Lee, Dependence of Initial Powder Temperature on Impact Behaviour of Bulk Metallic Glass in a Kinetic Spray Process, *J. Phys. D Appl. Phys*, 2009, **42**, p 5, doi:10.1088/0022-3727/42/8/082004.
15. S. Yin, X. Wang, W. Li, H. Liao, and H. Jie, Deformation Behavior of the Oxide Film on the Surface of Cold Sprayed Powder Particle, *Appl. Surf. Sci.*, North-Holland, 2012, **259**, p 294–300, doi:10.1016/J.APSUSC.2012.07.036.
16. K.H. Kim, W. Li, and X. Guo, Detection of Oxygen at the Interface and Its Effect on Strain, Stress, and Temperature at the Interface between Cold Sprayed Aluminum and Steel Substrate, *Appl. Surf. Sci.*, Elsevier B.V., 2015, **357**, p 1720–1726.
17. Y. Xie, S. Yin, C. Chen, M.P. Planche, H. Liao, and R. Lupoi, New Insights into the Coating/Substrate Interfacial Bonding Mechanism in Cold Spray, *Scr. Mater.*, Elsevier Ltd, 2016, **125**, p 1–4.
18. A. Ganesan, J. Affi, M. Yamada, and M. Fukumoto, Bonding Behavior Studies of Cold Sprayed Copper Coating on the PVC Polymer Substrate, *Surf. Coatings Technol.*, Elsevier, 2012, **207**, p 262–269, doi:10.1016/J.SURFCOAT.2012.06.086.
19. S. Yin, X. Suo, Y. Xie, W. Li, R. Lupoi, and H. Liao, Effect of Substrate Temperature on Interfacial Bonding for Cold Spray of Ni onto Cu, *J. Mater. Sci.*, Kluwer Academic Publishers, 2015, **50**(22), p 7448–7457, doi:10.1007/s10853-015-9304-6.
20. Y. Xie, C. Chen, M.-P. Planche, S. Deng, R. Huang, Z. Ren, and H. Liao, Strengthened Peening Effect on Metallurgical Bonding Formation in Cold Spray Additive Manufacturing, *J. Therm. Spray Technol.*, Springer US, 2019, **28**(4), p 769–779, doi:10.1007/s11666-019-00854-4.
21. A. Sabard and T. Hussain, Bonding Mechanisms in Cold Spray Deposition of Gas Atomised and Solution Heat-Treated Al 6061 Powder by EBSD, 2018, https://arxiv.org/abs/1811.08694. Accessed 31 January 2019.
22. G. Bae, Y. Xiong, S. Kumar, K. Kang, and C. Lee, General Aspects of Interface Bonding in Kinetic Sprayed Coatings, *Acta Mater.*, Pergamon, 2008, **56**(17), p 4858–4868.
23. R. Drehmann, T. Grund, T. Lampke, B. Wielage, C. Wüstefeld, M. Motylenko, and D. Rafaja, Essential Factors Influencing the Bonding Strength of Cold-Sprayed Aluminum Coatings on Ceramic Substrates, *J. Therm. Spray Technol.*, Springer New York LLC, 2018, **27**(3), p 446–455, doi:10.1007/s11666-018-0688-0.
24. Y. Watanabe, C. Yoshida, K. Atsumi, M. Yamada, and M. Fukumoto, Influence of Substrate Temperature on Adhesion Strength of Cold-Sprayed Coatings, n.d.
25. D.K. Christoulis, S. Guetta, E. Irissou, V. Guipont, M.H. Berger, M.

Jeandin, J.G. Legoux, C. Moreau, S. Costil, M. Boustie, Y. Ichikawa, and K. Ogawa, Cold-Spraying Coupled to Nano-Pulsed Nd-YaG Laser Surface Pre-Treatment, *J. Therm. Spray Technol.*, Springer, 2010, **19**(5), p 1062–1073.

26. R. Ortiz-Fernandez, S. Imbriglio, R. Chromik, and B. Jodoin, The Role of Substrate Preheating on the Adhesion Strength of Cold-Sprayed Soft Particles on Hard Substrates, *J. Therm. Spray Technol.*, Springer, 2021, p 1–13, doi:10.1007/s11666-020-01148-w.
27. S. Yin, X. Wang, X. Suo, H. Liao, Z. Guo, W. Li, and C. Coddet, Deposition Behavior of Thermally Softened Copper Particles in Cold Spraying, *Acta Mater.*, Elsevier Ltd, 2013, **61**(14), p 5105–5118.
28. C. Chen, X. Xie, Y. Xie, M.-P. Planche, S. Deng, G. Ji, E. Aubry, Z. Ren, and H. Liao, Cold Spraying of Thermally Softened Ni-Coated FeSiAl Composite Powder: Microstructure Characterization, Tribological Performance and Magnetic Property, *Mater. Des.*, Elsevier, 2018, **160**, p 270–283, doi:10.1016/J.MATDES.2018.09.025.
29. Y. Xie, M.P. Planche, R. Raoelison, P. Hervé, X. Suo, P. He, and H. Liao, Investigation on the Influence of Particle Preheating Temperature on Bonding of Cold-Sprayed Nickel Coatings, *Surf. Coatings Technol.*, Elsevier B.V., 2017, **318**, p 99–105.
30. A. Sova, S. Grigoriev, A. Kochetkova, and I. Smurov, Influence of Powder Injection Point Position on Efficiency of Powder Preheating in Cold Spray: Numerical Study, *Surf. Coatings Technol.*, Elsevier, 2014, **242**, p 226–231.
31. A. Nastic, B. Jodoin, D. Poirier, and J.-G. Legoux, Particle Temperature Effect in Cold Spray: A Study of Soft Particle Deposition on Hard Substrate, *Surf. Coatings Technol.*, Elsevier, 2021, **406**, p 126735, doi:10.1016/j.surfcoat.2020.126735.
32. Y. Cormier, P. Dupuis, B. Jodoin, and A. Ghaei, Finite Element Analysis and Failure Mode Characterization of Pyramidal Fin Arrays Produced by Masked Cold Gas Dynamic Spray, *J. Therm. Spray Technol.*, Springer US, 2015, **24**(8), p 1549–1565, doi:10.1007/s11666-015-0317-0.
33. H. Jones, Microstructure of Rapidly Solidified Materials, *Mater. Sci. Eng.*, Elsevier, 1984, **65**(1), p 145–156, doi:10.1016/0025-5416(84)90208-8.
34. A.M. Birt, V.K. Champagne, R.D. Sisson, and D. Apelian, Microstructural Analysis of Ti–6Al–4V Powder for Cold Gas Dynamic Spray Applications, *Adv. Powder Technol.*, Elsevier, 2015, **26**(5), p 1335–1347, doi:10.1016/J.APT.2015.07.008.
35. V.S. Bhattiprolu, K.W. Johnson, O.C. Ozdemir, and G.A. Crawford, Influence of Feedstock Powder and Cold Spray Processing Parameters on Microstructure and Mechanical Properties of Ti-6Al-4V Cold Spray Depositions, *Surf. Coatings Technol.*, Elsevier, 2018, **335**, p 1–12, doi:10.1016/J.SURFCOAT.2017.12.014.
36. J. Lienhard, C. Crook, M.Z. Azar, M. Hassani, D.R. Mumm, D. Veysset, D. Apelian, K.A. Nelson, V. Champagne, A. Nardi, C.A. Schuh, and L. Valdevit, Surface Oxide and Hydroxide Effects on Aluminum Microparticle Impact Bonding, *Acta Mater.*, Acta Materialia Inc, 2020, **197**, p 28–39.
37. H. Skoglund, M.K. Wedel, and B. Karlsson, The Role of Oxygen in Powder Processing of FeAl, *Intermetallics*, 2003, **11**(5), p 475–482.
38. W.Y. Li, H. Liao, C.J. Li, G. Li, C. Coddet, and X. Wang, On High Velocity Impact of Micro-Sized Metallic Particles in Cold Spraying, *Appl. Surf. Sci.*, Elsevier, 2006, **253**(5), p 2852–2862.
39. S. Rahmati and A. Ghaei, "The Use of Particle/Substrate Material Models in Simulation of Cold-Gas Dynamic-Spray Process," *Journal of Thermal Spray Technology*, 2014, p 530–540.
40. M.C. Price, A.T. Kearsley, and M.J. Burchell, Validation of the Preston-Tonks-Wallace Strength Model at Strain Rates Approaching ~1011 s-1 for Al-1100, Tantalum and Copper Using Hypervelocity Impact Crater Morphologies, *Int. J. Impact Eng.*, Pergamon, 2013, **52**, p 1–10.
41. J.. Barbour, J.. Knapp, D.. Follstaedt, T.. Mayer, K.. Minor, and D.. Linam, The Mechanical Properties of Alumina Films Formed by Plasma Deposition and by Ion Irradiation of Sapphire, *Nucl. Instruments Methods Phys. Res. Sect. B Beam Interact. with Mater. Atoms*, 2000, **166–167**, p 140–147, doi:10.1016/S0168-583X(99)00648-5.
42. S. Yin, X. Wang, X. Suo, H. Liao, Z. Guo, W. Li, and C. Coddet, Deposition Behavior of Thermally Softened Copper Particles in Cold Spraying, *Acta Mater.*, Elsevier Ltd, 2013, **61**(14), p 5105–5118.
43. S. Shin, S. Yoon, Y. Kim, and C. Lee, Effect of Particle Parameters on the Deposition Characteristics of a Hard/Soft-Particles Composite in Kinetic Spraying, *Surf. Coatings Technol.*, Elsevier, 2006, **201**(6), p 3457–3461.
44. C. Chen, X. Xie, Y. Xie, M.P. Planche, S. Deng, G. Ji, E. Aubry, Z. Ren, and H. Liao, Cold Spraying of Thermally Softened Ni-Coated FeSiAl Composite Powder: Microstructure Characterization, Tribological Performance and Magnetic Property, *Mater. Des.*, Elsevier Ltd, 2018, **160**, p 270–283.
45. W. Sun, A.W.Y. Tan, A. Bhowmik, I. Marinescu, X. Song, W. Zhai, F. Li, and E. Liu, Deposition Characteristics of Cold Sprayed Inconel 718 Particles on Inconel 718 Substrates with Different Surface Conditions, *Mater. Sci. Eng. A*, Elsevier Ltd, 2018, **720**, p 75–84.
46. J. Wu, H. Fang, S. Yoon, H. Kim, and C. Lee, The Rebound Phenomenon in Kinetic Spraying Deposition, *Scr. Mater.*, Elsevier Ltd, 2006, **54**(4 SPEC. ISS.), p 665–669.
47. P. Zhao, Q. Zhang, Y. Guo, H. Liu, and Z. Deng, Atomic Simulation of Crystal Orientation Effect on Coating Surface Generation Mechanisms in Cold Spray, *Comput. Mater. Sci.*, Elsevier B.V., 2020, **184**, p 109859.
48. M. Razavipour, S. Rahmati, A. Zú N ˜iga, • Denise Criado, and • Bertrand Jodoin, Bonding Mechanisms in Cold Spray: Influence of Surface Oxidation During Powder Storage, n.d., doi:10.1007/s11666-020-01123-5.
49. M. Hassani-Gangaraj, D. Veysset, V.K. Champagne, K.A. Nelson, and C.A. Schuh, Adiabatic Shear Instability Is Not Necessary for Adhesion in Cold Spray, *Scr. Mater.*, Elsevier Ltd, 2018, **158**, p 430–439.
50. H. Assadi, F. Gärtner, T. Stoltenhoff, and H. Kreye, Bonding Mechanism in Cold Gas Spraying, *Acta Mater.*, 2003, **51**(15), p 4379–4394.
51. M. Grujicic, C.. Zhao, W.. DeRosset, and D. Helfritch, Adiabatic Shear Instability Based Mechanism for Particles/Substrate Bonding in the Cold-Gas Dynamic-Spray Process, *Mater. Des.*, 2004, **25**(8), p 681–688.
52. M. Hassani, D. Veysset, and C.A. Schuh, Melting Can Hinder Impact-Induced Adhesion, *Artic. Phys. Rev. Lett.*, 2017, doi:10.1103/PhysRevLett.119.175701.
53. M.P. Dewar, A.G. McDonald, and A.P. Gerlich, Interfacial Heating during Low-Pressure Cold-Gas Dynamic Spraying of Aluminum Coatings, *J. Mater. Sci.*, Springer, 2012, **47**(1), p 184–198, doi:10.1007/s10853-011-5786-z.
54. A. Dorogoy and D. Rittel, Determination of the Johnson–Cook Material Parameters Using the SCS Specimen, *Exp. Mech.*, Springer US, 2009, **49**(6), p 881–885, doi:10.1007/s11340-008-9201-x.
55. A. Hänström and P. Lazor, High Pressure Melting and Equation of State of Aluminum, *J. Alloys Compd.*, Elsevier Sequoia SA, 2000, **305**(1–2), p 209–215.
56. K. Binder, J. Gottschalk, M. Kollenda, F. Gärtner, and T. Klassen, "Influence of Impact Angle and Gas Temperature on Mechanical Properties of Titanium Cold Spray Deposits," *Journal of Thermal Spray Technology*, Springer, 2011, p 234–242, doi:10.1007/s11666-010-9557-1.
57. Y. Ichikawa, R. Tokoro, M. Tanno, and K. Ogawa, Elucidation of Cold-Spray Deposition Mechanism by Auger Electron Spectroscopic Evaluation of Bonding Interface Oxide Film, *Acta Mater.*, Pergamon, 2019, **164**, p 39–49, doi:10.1016/J.ACTAMAT.2018.09.041.
58. X. Song, J. Everaerts, W. Zhai, H. Zheng, A.W.Y. Tan, W. Sun, F. Li, I. Marinescu, E. Liu, and A.M. Korsunsky, Residual Stresses in Single Particle Splat of Metal Cold Spray Process – Numerical Simulation and Direct Measurement, *Mater. Lett.*, Elsevier B.V., 2018, **230**, p 152–156.
59. T. Schmidt, H. Assadi, F. Gärtner, H. Richter, T. Stoltenhoff, H. Kreye, and T. Klassen, From Particle Acceleration to Impact and Bonding in Cold Spraying, *J. Therm. Spray Technol.*, Springer New York LLC, 2009, **18**(5–6), p 794–808, doi:10.1007/s11666-009-9357-7.
60. N. Bay, Mechanisms Producing Metallic Bonds in Cold Welding, *Weld. J.*, 1983, **62**(5), p 137.

CHAPTER 6

CONSLUSIONS AND FUTURE WORK

6.1 Conclusions

The general purpose of the current research work was to improve the understanding of particle impact temperature and substrate surface features on the CGDS deposition process and impact ensuing phenomena. This was achieved by conducting four clear research objectives that made use of experimental and numerical (computational fluid dynamics and finite element modeling) investigations.

The first objective concentrated on the deposition of soft particle material on hard substrate surface to ensure consistent surface roughness prior, during and after coating buildup and consequently guarantee a proper correlation of obtained results with substrate roughness. A pure aluminum powder has been sprayed on a steel surface for this purpose. The roughness has been varied from mirror finish, i.e ~R_a= 0.2±0.1µm, up to R_a= 84.9±6.4µm using polishing, grit blasting and force pulsed waterjet surface preparation techniques. A heat treatment was conducted to reveal the presence of metallurgical bonding. The generated interfacial diffusion zones, i.e. intermetallic layer, were associated with areas of fresh metal contact. Obtained results show that mechanical anchoring becomes the predominant coating adhesion process for any produced roughness, irrespective of the surface preparation method utilized, which also proves the inconsequential effect of embedded grit during grit blasting processes. In addition, the coatings achieved a maximal 50MPa adhesion strength at R_a= 50µm, which has been associated to the limited contribution of mechanical anchoring effects past this roughness. Finally, through FEM, it has been established that the particle impact with a flat surface can achieve at the interfacial contact zone a higher

temperature, contact pressure and velocity gradients favorable to the creation of metallic bonding, which explains its ability to generate metallurgical bonding, confirmed through the overwhelming observed intermetallic zones.

Following the study of the substrate state influence on deposition processes, the next research objective focused on studying the effect of particle temperature on deposition. However, since the particle temperature has never been measured in the field and the currently utilized heat transfer correlations have consequentially never been confirmed, the first step of the study focused on providing an extensive experimental investigation in goals to generate the first temperature measurement in the field. The use of large, i.e. 125µm, spherical titanium particles coupled with proper spray parameters, allowing appropriate heating, gas flow features, and particle velocity have permitted to successfully record the particle in-flight temperature using a high speed MW IR camera. The data has been analysed and a complete heat transfer and momentum analysis produced through CFD, which allowed to find the most appropriate Nusselt correlation for the description of particle flow in the CGDS field. The obtained data were established to be satisfactory and representative, and the developed set-up was evaluated to be accurate and precise. The accuracy and preciseness of the measurements have been maximized by ensuring proper camera calibration for real time temperature field variations and reliable particle velocity using particle tracking and streak velocimetry techniques from recorded IR sequences. In addition, the obtained correlations have been used to simulate the particle temperature in a high-pressure cold spray set-up equipped with a preheating converging section. The results show the importance of the current study, aside from its novelty, which demonstrates a variation of 81°C between the most common correlations utilized in the field.

The following project has investigated the deposition efficiency, adhesion strength and behavior under bend-to-break tests for coatings deposited under varying particle temperature and size. The validated particle/gas heat transfer characterization presented in the previous study has been used to define the resulting particle impact temperature after their trajectory inside both low pressure and high-pressure systems. The same material combination from the first study has been utilized, i.e. pure aluminum/steel, to provide an investigation of soft material impact on hard targeted surface, which is sparsely studied in the field. Complete three-dimensional computational fluid dynamic simulations have been included to fully characterize the particle size and injection location dependent trajectory, velocity and temperature inside the CGDS nozzles upon axial and radial injections. The obtained results first show the importance of unsuccessfully deposited particles in

the increase of coating adhesion strength for the spray at low particle impact temperatures using a low pressure CGDS system. Consequently, as the peening frequency increases, i.e. decreasing deposition efficiency, with the increase of particle size, the adhesion strength was seen to increase. However, as the particle impact temperature increased, the adhesion strength was measured to decrease with increasing particle size. The developed CFD models along with the measured deposition efficiency provided a complete characterization of successfully depositing particles in both systems, i.e. size, temperature, location, and velocity, and explain the observed coating properties.

Finally, the influence of particle size dependent impact temperature on interfacial phenomena leading to bonding has been investigated. Obtained results demonstrate the importance of incorporating the pressure in the evaluation of particle melting temperature. The melt propagation, stagnation and regressive cooling have shown to be drastically influenced by the particle size and impact velocity and temperature. The melt zone duration increases with particle increasing size and increasing temperature. Features related to melting, i.e. melt fingers, spheroidal particles and film micro-cracking, have been observed on the particle interface, which confirm melting occurrence, validate FEM modeling results and reinforce their influence in bonding processes. This study provides important experimental results and key observations, which have not been reported previously in the field. The numerical work is used to provide additional explanations to the reported observations.

6.2 Future Work

Several follow-up studies that would improve the understanding of process features affecting the bonding mechanisms in the cold gas dynamic spray field can be undertaken. In addition, although particle in-flight temperature data have been obtained for the first time in the field, which have also led to a complete heat transfer analysis and CFD numerical work, many improvements can be made to the recommended technique. Some specifics of potential future investigations are proposed in the following list.

1. To generalize the results of substrate surface roughness influence on adhesion mechanisms, different materials from the category of soft particle impact on hard substrate surface should be tested. This would provide the effect of material combination and ability of dissimilar material with different crystal structure and inherent properties to generate metallic bonding on various surface profiles.
2. Although the intermetallic-forming process under diffusion heat treatment process can be used to visualise at low magnification the presence of fresh-metal contact, a TEM analysis should be conducted to characterize locally the presence of metallic bonding.
3. The utilized mid-wave infrared camera, set-up and sequence analysis method should next be tested with higher particle in-flight temperatures. An external heating system or a high-pressure cold spray system should be used to increase particle temperature and allow improved detection. This will provide further confirmation of the results and analysis presented in the current thesis.
4. Efforts should be put into developing a long wave infrared camera, capable of providing an easier detection of in-flight particles. In addition, a set of various lenses should be tested along with a blackbody background to increase resolution, while trying to keep an appropriate depth of field, and improve contrast between particles and background, respectively.
5. Further efforts should be put in obtaining the micro-particle emissivity for different surface roughness features, oxide layer thickness, temperature and material.
6. The deposition efficiency of the first aluminum layer deposition on the used steel substate can be measured instead of the overall average to provide the exact aluminum on steel bonding characteristics. To ensure representative and valid DE measurement at such low feeding rate, visual inspection of the fraction of deposited particles over the number of

traces can be obtain over a large surface section area using stitched SEM images (or sequence of images).

7. The FEM study can additionally be supported by developing a crystal plasticity finite element model (CPFEM) to simulate the particle polycrystalline structure, in goals to understand the effect of preferred average grain orientation on overall interfacial deformation, oxide removal and adhesion. The CPFEM approach, currently inexistent in the CGDS field, would provide important microstructural texture related insights to the high speed deformation process.
8. The experimental results of interfacial phenomena observed at the contact surface of bonded and rebounded particles can be used to develop a FEM that includes metallic bonding processes. The experimental results confirming the influence of particle size and temperature on adhesion can be utilized to confirm the validity of the developed numerical metallic bonding assumptions and description.
9. A numerical model that includes material phase change, i.e. melting processes, should be developed to understand the initiation, development and propagation of melting zones and their influence on bonding.

REFERENCES

1. R.D. Guha, A.J. Sharma, P. Diwan, and P. Khanikar, Effect of Grain Orientation on High Strain-Rate Plastic Deformation, *Procedia Eng.*, Elsevier, 2017, **173**, p 1048–1055, doi:10.1016/J.PROENG.2016.12.184.
2. J.M. Park, J. Moon, J.W. Bae, M.J. Jang, J. Park, S. Lee, and H.S. Kim, Strain Rate Effects of Dynamic Compressive Deformation on Mechanical Properties and Microstructure of CoCrFeMnNi High-Entropy Alloy, *Mater. Sci. Eng. A*, Elsevier, 2018, **719**, p 155–163, doi:10.1016/J.MSEA.2018.02.031.
3. A.S. Khan, J. Liu, J.W. Yoon, and R. Nambori, Strain Rate Effect of High Purity Aluminum Single Crystals: Experiments and Simulations, *Int. J. Plast.*, Pergamon, 2015, **67**, p 39–52, doi:10.1016/J.IJPLAS.2014.10.002.
4. S. Sevsek, C. Haase, W. Bleck, S. Sevsek, C. Haase, and W. Bleck, Strain-Rate-Dependent Deformation Behavior and Mechanical Properties of a Multi-Phase Medium-Manganese Steel, *Metals (Basel).*, Multidisciplinary Digital Publishing Institute, 2019, **9**(3), p 344, doi:10.3390/met9030344.
5. A. Papyrin, V. Kosarev, K.V. Klinkov, A. Alkhimov, and V.M. Fomin, “Cold Spray Technology,” Elsevier, 2006.
6. M.M. Vijay, A.H. Tieu, W. Yan, and B.R. Daniels, “Method and Apparatus for Prepping Surfaces with a High-Frequency Forced Pulsed Waterjet,” 2013.
7. J.T. Lloyd, J.D. Clayton, R. Becker, and D.L. McDowell, Simulation of Shock Wave Propagation in Single Crystal and Polycrystalline Aluminum, *Int. J. Plast.*, Elsevier Ltd, 2014, **60**, p 118–144.
8. D.S. Cronin, K. Bui, C. Kaufmann, G. Mcintosh, T. Berstad, and D. Cronin, “Implementation and Validation of the Johnson-Holmquist Ceramic M Aterial Model in LS-Dyna,” n.d.
9. M. Ahmad, An Overview of Droplet Impact Erosion, Related Theory and Protection Measures in Steam Turbines, *Cavitation - Selected Issues*, IntechOpen, 2018, doi:10.5772/intechopen.80768.
10. D.J. Carlson and R.F. Hoglund, Particle Drag and Heat Transfer in Rocket Nozzles, *AIAA J.*, 1964, **2**(11), p 1980–1984.
11. W. Xie, A. Alizadeh-Dehkharghani, Q. Chen, V.K. Champagne, X. Wang, A.T. Nardi, S. Kooi, S. Müftü, and J.H. Lee, Dynamics and Extreme Plasticity of Metallic Microparticles

in Supersonic Collisions /639/166/988 /639/301/1023/1026 /639/301/930/12 /128 Article, *Sci. Rep.*, Nature Publishing Group, 2017, **7**(1), p 1–9, doi:10.1038/s41598-017-05104-7.

12. T. Nguyen, D.J. Luscher, and J.W. Wilkerson, A Dislocation-Based Crystal Plasticity Framework for Dynamic Ductile Failure of Single Crystals, *J. Mech. Phys. Solids*, Elsevier Ltd, 2017, **108**, p 1–29.
13. R. Chakrabarty and J. Song, A Modified Johnson-Cook Material Model with Strain Gradient Plasticity Consideration for Numerical Simulation of Cold Spray Process, *Surf. Coatings Technol.*, Elsevier B.V., 2020, **397**, p 125981.
14. M.C. Price, A.T. Kearsley, and M.J. Burchell, Validation of the Preston-Tonks-Wallace Strength Model at Strain Rates Approaching ~1011 s-1 for Al-1100, Tantalum and Copper Using Hypervelocity Impact Crater Morphologies, *Int. J. Impact Eng.*, Pergamon, 2013, **52**, p 1–10.
15. K. Ravi, T. Deplancke, K. Ogawa, J.-Y. Cavaillé, and O. Lame, Understanding Deposition Mechanism in Cold Sprayed Ultra High Molecular Weight Polyethylene Coatings on Metals by Isolated Particle Deposition Method, *Addit. Manuf.*, Elsevier, 2018, **21**, p 191–200, doi:10.1016/J.ADDMA.2018.02.022.
16. A. Joshi and S. James, Molecular Dynamics Simulation Study of Cold Spray Process, *J. Manuf. Process.*, Elsevier, 2018, **33**, p 136–143, doi:10.1016/J.JMAPRO.2018.05.005.
17. C. Chen, X. Xie, Y. Xie, M.P. Planche, S. Deng, G. Ji, E. Aubry, Z. Ren, and H. Liao, Cold Spraying of Thermally Softened Ni-Coated FeSiAl Composite Powder: Microstructure Characterization, Tribological Performance and Magnetic Property, *Mater. Des.*, Elsevier Ltd, 2018, **160**, p 270–283.
18. S. Suresh, S.-W. Lee, M. Aindow, H.D. Brody, V.K. Champagne, and A.M. Dongare, Unraveling the Mesoscale Evolution of Microstructure during Supersonic Impact of Aluminum Powder Particles, *Sci. Rep.*, Nature Publishing Group, 2018, **8**(1), p 10075, doi:10.1038/s41598-018-28437-3.
19. W. Wong, E. Irissou, A.N. Ryabinin, J.-G. Legoux, and S. Yue, Influence of Helium and Nitrogen Gases on the Properties of Cold Gas Dynamic Sprayed Pure Titanium Coatings, *J. Therm. Spray Technol.*, Springer US, 2011, **20**(1–2), p 213–226, doi:10.1007/s11666-010-9568-y.
20. T.-C. Jen, L. Li, W. Cui, Q. Chen, and X. Zhang, Numerical Investigations on Cold Gas Dynamic Spray Process with Nano-and Microsize Particles, 2005, doi:10.1016/j.ijheatmasstransfer.2005.05.008.
21. V.F. Kosarev, S. V. Klinkov, A.P. Alkhimov, and A.N. Papyrin, On Some Aspects of Gas

Dynamics of the Cold Spray Process, *J. Therm. Spray Technol.*, 2003, **12**(2), p 265–281.

22. M. Meyer and R. Lupoi, An Analysis of the Particulate Flow in Cold Spray Nozzles, *Mech. Sci*, 2015, **6**, p 127–136, doi:10.5194/ms-6-127-2015.
23. J. Perry, P. Richer, B. Jodoin, and E. Matte, Pin Fin Array Heat Sinks by Cold Spray Additive Manufacturing: Economics of Powder Recycling, *J. Therm. Spray Technol.*, Springer US, 2019, **28**(1–2), p 144–160, doi:10.1007/s11666-018-0758-3.
24. S.H. Zahiri, W. Yang, and M. Jahedi, Characterization of Cold Spray Titanium Supersonic Jet, *J. Therm. Spray Technol.*, Springer US, 2009, **18**(1), p 110–117, doi:10.1007/s11666-008-9278-x.
25. S.P. Mates, D. Basak, F.S. Biancaniello, S.D. Ridder, and J. Geist, Calibration of a Two-Color Imaging Pyrometer and Its Use for Particle Measurements in Controlled Air Plasma Spray Experiments, *J. Therm. Spray Technol.*, 2002, **11**(2), p 195–205.
26. J. Mishin, M. Vardelle, J. Lesinski, and P. Fauchais, Two-Colour Pyrometer for the Statistical Measurement of the Surface Temperature of Particles under Thermal Plasma Conditions, *J. Phys. E.*, 1987, **20**(6), p 620–625.
27. S. Yin, M. Meyer, W. Li, H. Liao, and R. Lupoi, Gas Flow, Particle Acceleration, and Heat Transfer in Cold Spray: A Review, *J. Therm. Spray Technol.*, 2016, **25**(5), p 874–896.
28. M. Faizan-Ur-Rab, S.H. Zahiri, S.H. Masood, T.D. Phan, M. Jahedi, and R. Nagarajah, Application of a Holistic 3D Model to Estimate State of Cold Spray Titanium Particles, *Mater. Des.*, 2016, **89**, p 1227–1241.
29. X.-J. Ning, Q.-S. Wang, Z. Ma, and H.-J. Kim, Numerical Study of In-Flight Particle Parameters in Low-Pressure Cold Spray Process, *J. Therm. Spray Technol.*, 2010, **19**(6), p 1211–1217.
30. T. Mashimo, A. Nakamura, M. Kodama, K. Kusaba, K. Fukuoka, and Y. Syono, Yielding and Phase Transition under Shock Compression of Yttria-doped Cubic Zirconia Single Crystal and Polycrystal, *J. Appl. Phys.*, American Institute of Physics, 1995, **77**(10), p 5060–5068, doi:10.1063/1.359314.
31. R. Singh, K.H. Rauwald, E. Wessel, G. Mauer, S. Schruefer, A. Barth, S. Wilson, and R. Vassen, Effects of Substrate Roughness and Spray-Angle on Deposition Behavior of Cold-Sprayed Inconel 718, *Surf. Coatings Technol.*, Elsevier B.V., 2017, **319**, p 249–259.
32. M.P. Dewar, A.G. McDonald, and A.P. Gerlich, Interfacial Heating during Low-Pressure Cold-Gas Dynamic Spraying of Aluminum Coatings, *J. Mater. Sci.*, Springer, 2012, **47**(1), p 184–198, doi:10.1007/s10853-011-5786-z.
33. S. Suresh, S.-W. Lee, M. Aindow, H.D. Brody, V.K. Champagne, and A.M. Dongare,

Unraveling the Mesoscale Evolution of Microstructure during Supersonic Impact of Aluminum Powder Particles, *Sci. Rep.*, Nature Publishing Group, 2018, **8**(1), p 10075, doi:10.1038/s41598-018-28437-3.

34. B. Jodoin, L. Ajdelsztajn, E. Sansoucy, A. Zúñiga, P. Richer, and E.J. Lavernia, Effect of Particle Size, Morphology, and Hardness on Cold Gas Dynamic Sprayed Aluminum Alloy Coatings, *Surf. Coatings Technol.*, Elsevier, 2006, **201**(6), p 3422–3429, doi:10.1016/J.SURFCOAT.2006.07.232.
35. W.Y. Li, C.J. Li, and H. Liao, Significant Influence of Particle Surface Oxidation on Deposition Efficiency, Interface Microstructure and Adhesive Strength of Cold-Sprayed Copper Coatings, *Appl. Surf. Sci.*, Elsevier B.V., 2010, **256**(16), p 4953–4958.
36. N. Sanpo, M.L. Tan, P. Cheang, and K.A. Khor, Antibacterial Property of Cold-Sprayed HA-Ag/PEEK Coating, *J. Therm. Spray Technol.*, Springer US, 2009, **18**(1), p 10–15, doi:10.1007/s11666-008-9283-0.
37. J.H. Lee, H.L. Jang, K.M. Lee, H.-R. Baek, K. Jin, K.S. Hong, J.H. Noh, and H.-K. Lee, In Vitro and in Vivo Evaluation of the Bioactivity of Hydroxyapatite-Coated Polyetheretherketone Biocomposites Created by Cold Spray Technology, *Acta Biomater.*, Elsevier, 2013, **9**(4), p 6177–6187, doi:10.1016/J.ACTBIO.2012.11.030.
38. H. Che, P. Vo, and S. Yue, Metallization of Carbon Fibre Reinforced Polymers by Cold Spray, *Surf. Coatings Technol.*, 2017, **313**, p 236–247, doi:10.1016/j.surfcoat.2017.01.083.
39. H.Q. Che, A. Liberati, P. Vo, and S. Yue, Cold Spray of Mixed Sn-Zn and Sn-Al Powders on Carbon Fiber Reinforced Polymers, *Mater. Sci. Forum*, Trans Tech Publications Ltd, 2018, **941**, p 1892–1897, doi:10.4028/www.scientific.net/MSF.941.1892.
40. G. Archambault, B. Jodoin, S. Gaydos, and M. Yandouzi, Metallization of Carbon Fiber Reinforced Polymer Composite by Cold Spray and Lay-up Molding Processes, *Surf. Coatings Technol.*, 2016, **300**, p 78–86, doi:10.1016/j.surfcoat.2016.05.008.
41. C. Chen, X. Xie, Y. Xie, X. Yan, C. Huang, S. Deng, Z. Ren, and H. Liao, Metallization of Polyether Ether Ketone (PEEK) by Copper Coating via Cold Spray, *Surf. Coatings Technol.*, 2018, **342**, p 209–219, doi:10.1016/j.surfcoat.2018.02.087.
42. H. Ye and J. Wang, Preparation of Aluminum Coating on Lexan by Cold Spray, *Mater. Lett.*, North-Holland, 2014, **137**, p 21–24, doi:10.1016/J.MATLET.2014.08.119.
43. A. Małachowska, M. Winnicki, M. Stachowicz, and M. Korzeniowski, Metallisation of Polycarbonates Using a Low Pressure Cold Spray Method, *Surf. Eng.*, Taylor & Francis, 2018, **34**(3), p 251–258, doi:10.1080/02670844.2016.1277843.
44. H. Che, X. Chu, P. Vo, and S. Yue, Cold Spray of Mixed Metal Powders on Carbon Fibre

Reinforced Polymers, *Surf. Coatings Technol.*, 2017, **329**, p 232–243, doi:10.1016/j.surfcoat.2017.09.052.

45. A. Ganesan, M. Yamada, and M. Fukumoto, Cold Spray Coating Deposition Mechanism on the Thermoplastic and Thermosetting Polymer Substrates, *J. Therm. Spray Technol.*, Springer US, 2013, **22**(8), p 1275–1282, doi:10.1007/s11666-013-9984-x.
46. H. Che, X. Chu, P. Vo, and S. Yue, Metallization of Various Polymers by Cold Spray, *J. Therm. Spray Technol.*, Springer US, 2018, **27**(1–2), p 169–178, doi:10.1007/s11666-017-0663-1.
47. P.G. Keech, P. Vo, S. Ramamurthy, J. Chen, R. Jacklin, and D.W. Shoesmith, Design and Development of Copper Coatings for Long Term Storage of Used Nuclear Fuel, *Corros. Eng. Sci. Technol.*, Taylor & Francis, 2014, **49**(6), p 425–430, doi:10.1179/1743278214Y.0000000206.
48. P. Jakupi, P.G. Keech, I. Barker, S. Ramamurthy, R.L. Jacklin, D.W. Shoesmith, and D.E. Moser, Characterization of Commercially Cold Sprayed Copper Coatings and Determination of the Effects of Impacting Copper Powder Velocities, *J. Nucl. Mater.*, 2015, **466**, p 1–11, doi:10.1016/j.jnucmat.2015.07.001.
49. R. Fernández, D. MacDonald, A. Nastić, B. Jodoin, A. Tieu, and M. Vijay, Enhancement and Prediction of Adhesion Strength of Copper Cold Spray Coatings on Steel Substrates for Nuclear Fuel Repository, *J. Therm. Spray Technol.*, 2016, **25**(8), p 1577–1587, doi:10.1007/s11666-016-0467-8.
50. D.S. Hall and P.G. Keech, An Overview of the Canadian Corrosion Program for the Long-Term Management of Nuclear Waste, *Corros. Eng. Sci. Technol.*, Taylor & Francis, 2017, **52**(sup1), p 2–5, doi:10.1080/1478422X.2016.1275419.
51. C.H. Boyle and S.A. Meguid, Mechanical Performance of Integrally Bonded Copper Coatings for the Long Term Disposal of Used Nuclear Fuel, *Nucl. Eng. Des.*, North-Holland, 2015, **293**, p 403–412, doi:10.1016/J.NUCENGDES.2015.08.011.
52. M. Ševeček, A. Gurgen, A. Seshadri, Y. Che, M. Wagih, B. Phillips, V. Champagne, and K. Shirvan, Development of Cr Cold Spray–Coated Fuel Cladding with Enhanced Accident Tolerance, *Nucl. Eng. Technol.*, Elsevier, 2018, **50**(2), p 229–236, doi:10.1016/J.NET.2017.12.011.
53. N. Bala, H. Singh, J. Karthikeyan, and S. Prakash, Cold Spray Coating Process for Corrosion Protection: A Review, *Surf. Eng.*, Taylor & Francis, 2014, **30**(6), p 414–421, doi:10.1179/1743294413Y.0000000148.
54. H. Bu, M. Yandouzi, C. Lu, D. MacDonald, and B. Jodoin, Cold Spray Blended

Al + Mg17Al12 Coating for Corrosion Protection of AZ91D Magnesium Alloy, *Surf. Coatings Technol.*, Elsevier, 2012, **207**, p 155–162, doi:10.1016/J.SURFCOAT.2012.06.050.

55. B.S. DeForce, T.J. Eden, and J.K. Potter, Cold Spray Al-5% Mg Coatings for the Corrosion Protection of Magnesium Alloys, *J. Therm. Spray Technol.*, Springer US, 2011, **20**(6), p 1352–1358, doi:10.1007/s11666-011-9675-4.
56. S.M. Hassani-Gangaraj, A. Moridi, and M. Guagliano, Critical Review of Corrosion Protection by Cold Spray Coatings, *Surf. Eng.*, Taylor & FrancisSuite 1C, Joseph's Well, Hanover Walk, Leeds LS3 1AB, UK, 2015, **31**(11), p 803–815, doi:10.1179/1743294415Y.0000000018.
57. G. Archambault, B. Jodoin, S. Gaydos, and M. Yandouzi, Metallization of Carbon Fiber Reinforced Polymer Composite by Cold Spray and Lay-up Molding Processes, *Surf. Coatings Technol.*, Elsevier, 2016, **300**, p 78–86, doi:10.1016/J.SURFCOAT.2016.05.008.
58. O. Stier, Fundamental Cost Analysis of Cold Spray, *J. Therm. Spray Technol.*, Springer US, 2014, **23**(1–2), p 131–139, doi:10.1007/s11666-013-9972-1.
59. O. Nooririnah, A.Y. Khalil, M.S. Aludin, A. Rohana, and R.R. Zuraidah, Overview Potential Applications of Cold Spray Process for Aviation Industry in Malaysia, *Adv. Mater. Res.*, Trans Tech Publications Ltd, 2013, **701**, p 375–377, doi:10.4028/www.scientific.net/AMR.701.375.
60. V. Champagne and D. Helfritch, Critical Assessment 11: Structural Repairs by Cold Spray, *Mater. Sci. Technol.*, Taylor & Francis, 2015, **31**(6), p 627–634, doi:10.1179/1743284714Y.0000000723.
61. C. Chen, S. Gojon, Y. Xie, S. Yin, C. Verdy, Z. Ren, H. Liao, and S. Deng, A Novel Spiral Trajectory for Damage Component Recovery with Cold Spray, *Surf. Coatings Technol.*, Elsevier, 2017, **309**, p 719–728, doi:10.1016/J.SURFCOAT.2016.10.096.
62. S. Yin, P. Cavaliere, B. Aldwell, R. Jenkins, H. Liao, W. Li, and R. Lupoi, Cold Spray Additive Manufacturing and Repair: Fundamentals and Applications, *Addit. Manuf.*, Elsevier, 2018, **21**, p 628–650, doi:10.1016/J.ADDMA.2018.04.017.
63. C. Velotti, A. Astarita, C. Leone, S. Genna, F.M.C. Minutolo, and A. Squillace, Laser Marking of Titanium Coating for Aerospace Applications, *Procedia CIRP*, Elsevier, 2016, **41**, p 975–980, doi:10.1016/J.PROCIR.2016.01.006.
64. P. Cavaliere and A. Silvello, Crack Repair in Aerospace Aluminum Alloy Panels by Cold Spray, *J. Therm. Spray Technol.*, Springer US, 2017, **26**(4), p 661–670, doi:10.1007/s11666-017-0534-9.

65. E. Irissou, J.-G. Legoux, A.N. Ryabinin, B. Jodoin, and C. Moreau, Review on Cold Spray Process and Technology: Part I—Intellectual Property, *J. Therm. Spray Technol.*, Springer US, 2008, **17**(4), p 495–516, doi:10.1007/s11666-008-9203-3.

66. V.K. Champagne, The Repair of Magnesium Rotorcraft Components by Cold Spray, *J. Fail. Anal. Prev.*, Springer US, 2008, **8**(2), p 164–175, doi:10.1007/s11668-008-9116-y.

67. H. Singh, T.S. Sidhu, and S.B.S. Kalsi, Cold Spray Technology: Future of Coating Deposition Processes, *Frat. ed Integrità Strutt.*, 2012, **6**(22), p 69–84, doi:10.3221/IGF-ESIS.22.08.

68. A. Bacciochini, S. Bourdon-Lafleur, C. Poupart, M. Radulescu, and B. Jodoin, Ni-Al Nanoscale Energetic Materials: Phenomena Involved During the Manufacturing of Bulk Samples by Cold Spray, *J. Therm. Spray Technol.*, Springer US, 2014, **23**(7), p 1142–1148, doi:10.1007/s11666-014-0078-1.

69. S.W. Dean, J.K. Potter, R.A. Yetter, T.J. Eden, V. Champagne, and M. Trexler, Energetic Intermetallic Materials Formed by Cold Spray, *Intermetallics*, Elsevier, 2013, **43**, p 121–130, doi:10.1016/J.INTERMET.2013.07.019.

70. R. Vaßen, Z. Yi, H. Kaßner, and D. Stöver, Suspension Plasma Spraying of TiO2 for the Manufacture of Photovoltaic Cells, *Surf. Coatings Technol.*, Elsevier, 2009, **203**(15), p 2146–2149, doi:10.1016/J.SURFCOAT.2008.10.021.

71. M. Yamada, H. Isago, H. Nakano, and M. Fukumoto, Cold Spraying of TiO2 Photocatalyst Coating With Nitrogen Process Gas, *J. Therm. Spray Technol.*, Springer US, 2010, **19**(6), p 1218–1223, doi:10.1007/s11666-010-9520-1.

72. J. Henao, A. Concustell, I. G.Cano, S. Dosta, N. Cinca, J.M. Guilemany, and T. Suhonen, Novel Al-Based Metallic Glass Coatings by Cold Gas Spray, *Mater. Des.*, Elsevier, 2016, **94**, p 253–261, doi:10.1016/J.MATDES.2016.01.040.

73. K. Spencer, D.M. Fabijanic, and M.-X. Zhang, The Use of Al–Al2O3 Cold Spray Coatings to Improve the Surface Properties of Magnesium Alloys, *Surf. Coatings Technol.*, Elsevier, 2009, **204**(3), p 336–344, doi:10.1016/J.SURFCOAT.2009.07.032.

74. R.N. Raoelison, C. Verdy, and H. Liao, Cold Gas Dynamic Spray Additive Manufacturing Today: Deposit Possibilities, Technological Solutions and Viable Applications, *Mater. Des.*, Elsevier, 2017, **133**, p 266–287, doi:10.1016/J.MATDES.2017.07.067.

75. D. MacDonald, R. Fernández, F. Delloro, and B. Jodoin, Cold Spraying of Armstrong Process Titanium Powder for Additive Manufacturing, *J. Therm. Spray Technol.*, Springer US, 2017, **26**(4), p 598–609, doi:10.1007/s11666-016-0489-2.

76. S. Pathak and G. Saha, Development of Sustainable Cold Spray Coatings and 3D Additive

Manufacturing Components for Repair/Manufacturing Applications: A Critical Review, *Coatings*, Multidisciplinary Digital Publishing Institute, 2017, **7**(8), p 122, doi:10.3390/coatings7080122.

77. P. Dupuis, Y. Cormier, M. Fenech, A. Corbeil, and B. Jodoin, Flow Structure Identification and Analysis in Fin Arrays Produced by Cold Spray Additive Manufacturing, *Int. J. Heat Mass Transf.*, Pergamon, 2016, **93**, p 301–313, doi:10.1016/J.IJHEATMASSTRANSFER.2015.10.019.
78. R.N. Raoelison, C. Verdy, and H. Liao, Cold Gas Dynamic Spray Additive Manufacturing Today: Deposit Possibilities, Technological Solutions and Viable Applications, *Mater. Des.*, Elsevier, 2017, **133**, p 266–287, doi:10.1016/J.MATDES.2017.07.067.
79. A. Sova, S. Grigoriev, A. Okunkova, and I. Smurov, Potential of Cold Gas Dynamic Spray as Additive Manufacturing Technology, *Int. J. Adv. Manuf. Technol.*, Springer London, 2013, **69**(9–12), p 2269–2278, doi:10.1007/s00170-013-5166-8.
80. X. Wang, F. Feng, M.A. Klecka, M.D. Mordasky, J.K. Garofano, T. El-Wardany, A. Nardi, and V.K. Champagne, Characterization and Modeling of the Bonding Process in Cold Spray Additive Manufacturing, *Addit. Manuf.*, Elsevier, 2015, **8**, p 149–162, doi:10.1016/J.ADDMA.2015.03.006.
81. "NRC Canada to Advance Adoption of Cold Spray Additive Manufacturing - 3D Printing Industry," n.d., https://3dprintingindustry.com/news/nrc-canada-to-advance-adoption-of-cold-spray-additive-manufacturing-158862/. Accessed 8 September 2019.
82. T. Pelsoci, "Benefit Cost Analysis: ESTCP Funded Cold Spray Technology for DOD Applications," 2015.
83. A. Papyrin, The Development of the Cold Spray Process, *The Cold Spray Materials Deposition Process: Fundamentals and Applications*, Elsevier Ltd., 2007, p 11–42.
84. S. Kumar, M. Kumar, and N. Jindal, Overview of Cold Spray Coatings Applications and Comparisons: A Critical Review, *World J. Eng.*, Emerald Group Publishing Ltd., 2020, **17**(1), p 27–51.
85. A. Alkhimov, A. Papyrin, and V. Kosarev, "Gas-Dynamic Spraying Method for Applying a Coating," *US Patent 5,302,414*, (United States), United States, 1994.
86. R. Fernández, D. MacDonald, A. Nastić, B. Jodoin, A. Tieu, and M. Vijay, Enhancement and Prediction of Adhesion Strength of Copper Cold Spray Coatings on Steel Substrates for Nuclear Fuel Repository, *J. Therm. Spray Technol.*, 2016, **25**(8).
87. A. Nastic, "Repair of Aluminum Alloy Aerospace Components and Cold Gas Dynamic Spray Flow Distribution Study," Univeristy of Ottawa, 2015,

https://ruor.uottawa.ca/handle/10393/32998.

88. H. Assadi, H. Kreye, F. Gärtner, and T. Klassen, Cold Spraying – A Materials Perspective, *Acta Mater.*, 2016, **116**, p 382–407.
89. M. Grujicic, C.. Zhao, C. Tong, W.. DeRosset, and D. Helfritch, Analysis of the Impact Velocity of Powder Particles in the Cold-Gas Dynamic-Spray Process, *Mater. Sci. Eng. A*, Elsevier, 2004, **368**(1–2), p 222–230, doi:10.1016/J.MSEA.2003.10.312.
90. M.R. Rokni, S.R. Nutt, C.A. Widener, V.K. Champagne, and R.H. Hrabe, Review of Relationship Between Particle Deformation, Coating Microstructure, and Properties in High-Pressure Cold Spray, *J. Therm. Spray Technol.*, Springer New York LLC, 2017, **26**(6), p 1308–1355.
91. T.C. Hanson, C.M. Hackett, and G.S. Settles, Independent Control of HVOF Particle Velocity and Temperature, *J. Therm. Spray Technol.*, 2002, **11**(1), p 75–85.
92. P. Fauchais, G. Montavon, and G. Bertrand, From Powders to Thermally Sprayed Coatings, *J. Therm. Spray Technol.*, 2010, **19**(1–2), p 56–80.
93. P. King, M. Yandouzi, and B. Jodoin, The Physics of Cold Spray, *Modern Cold Spray: Materials, Process, and Applications*, Springer International Publishing, 2015, p 31–72, doi:10.1007/978-3-319-16772-5_2.
94. Compressible Flow, *Fluid Mechanics*, Elsevier, 2012, p 729–778, doi:10.1016/B978-0-12-382100-3.10015-0.
95. J. Pattison, S. Celotto, A. Khan, and W. O'Neill, Standoff Distance and Bow Shock Phenomena in the Cold Spray Process, *Surf. Coatings Technol.*, 2008, **202**(8), p 1443–1454.
96. J.C. Carling and B.L. Hunt, The near Wall Jet of a Normally Impinging, Uniform, Axisymmetric, Supersonic Jet, *J. Fluid Mech.*, Cambridge University Press, 1974, **66**(1), p 159–176.
97. A.P. Alkhimov, V.F. Kosarev, and S. V. Klinkov, The Features of Cold Spray Nozzle Design, *J. Therm. Spray Technol.*, Springer, 2001, **10**(2), p 375–381, doi:10.1361/105996301770349466.
98. C.B. Henderson, Drag Coefficients of Spheres in Continuum and Rarefied Flows, *AIAA J.*, 1976, **14**(6), p 707–708.
99. C.T. Crowe, Drag Coefficient of Particles in a Rocket Nozzle., *AIAA J.*, 1967, **5**(5), p 1021–1022.
100. V.K. Champagne and D.J. Helfritch, "Comparison of Empirical and Theoretical Computations of Velocity for a Cold Spray Nozzle," n.d.
101. S. Chadha, R. Jefferson-Loveday, and T. Hussain, Modelling Knudsen Number Effects in

Suspension High Velocity Oxy Fuel Thermal Spray, *Int. J. Heat Mass Transf.*, Elsevier Ltd, 2020, **152**, p 119454.

102. A. Aissa, M. Abdelouahab, A. Noureddine, M. El Ganaoui, and B. Pateyron, Ranz and Marshall Correlations Limits on Heat Flow Between a Sphere and Its Surrounding Gas at High Temperature, *Therm. Sci.*, 2015, **19**(5), p 1521–1528.
103. E. Loth, Compressibility and Rarefaction Effects on Drag of a Spherical Particle, *AIAA J.*, 2008, **46**, p 2219–2228.
104. I.A. Bedarev, A. V. Fedorov, and V.M. Fomin, Numerical Analysis of the Flow around a System of Bodies behind the Shock Wave, *Combust. Explos. Shock Waves*, Springer, 2012, **48**(4), p 446–454, doi:10.1134/S0010508212040119.
105. M. Meyer, F. Caruso, and R. Lupoi, Particle Velocity and Dispersion of High Stokes Number Particles by PTV Measurements inside a Transparent Supersonic Cold Spray Nozzle, *Int. J. Multiph. Flow*, Pergamon, 2018, **106**, p 296–310, doi:10.1016/J.IJMULTIPHASEFLOW.2018.05.018.
106. H. Tabbara, S. Gu, D.G. McCartney, T.S. Price, and P.H. Shipway, "Study on Process Optimization of Cold Gas Spraying," *Journal of Thermal Spray Technology*, Springer, 2011, p 608–620.
107. O.C. Ozdemir and C.A. Widener, Influence of Powder Injection Parameters in High-Pressure Cold Spray, *J. Therm. Spray Technol.*, Springer New York LLC, 2017, **26**(7), p 1411–1422.
108. A. Nastic and B. Jodoin, Evaluation of Heat Transfer Transport Coefficient for Cold Spray Through Computational Fluid Dynamics and Particle In-Flight Temperature Measurement Using a High-Speed IR Camera, *J. Therm. Spray Technol.*, Springer US, 2018, **27**(8), p 1491–1517, doi:10.1007/s11666-018-0787-y.
109. W.-Y. Li, H. Liao, G. Douchy, and C. Coddet, Optimal Design of a Cold Spray Nozzle by Numerical Analysis of Particle Velocity and Experimental Validation with 316L Stainless Steel Powder, *Mater. Des.*, Elsevier, 2007, **28**(7), p 2129–2137, doi:10.1016/J.MATDES.2006.05.016.
110. J.-O. Kliemann, H. Gutzmann, F. Gärtner, H. Hübner, C. Borchers, and T. Klassen, Formation of Cold-Sprayed Ceramic Titanium Dioxide Layers on Metal Surfaces, *J. Therm. Spray Technol.*, Springer US, 2011, **20**(1–2), p 292–298, doi:10.1007/s11666-010-9563-3.
111. R. Fernandez and B. Jodoin, Effect of Particle Morphology on Cold Spray Deposition of Chromium Carbide-Nickel Chromium Cermet Powders, *J. Therm. Spray Technol.*, Springer US, 2017, **26**(6), p 1356–1380, doi:10.1007/s11666-017-0580-3.

112. V.K. Champagne, D.J. Helfritch, S.P.G. Dinavahi, and P.F. Leyman, "Theoretical and Experimental Particle Velocity in Cold Spray," *Journal of Thermal Spray Technology*, 2011, p 425–431.

113. M. Bray, A. Cockburn, and W. O'Neill, The Laser-Assisted Cold Spray Process and Deposit Characterisation, *Surf. Coatings Technol.*, Elsevier, 2009, **203**(19), p 2851–2857.

114. T. Schmidt, H. Assadi, F. Gärtner, H. Richter, T. Stoltenhoff, H. Kreye, and T. Klassen, From Particle Acceleration to Impact and Bonding in Cold Spraying, *J. Therm. Spray Technol.*, Springer New York LLC, 2009, **18**(5–6), p 794–808, doi:10.1007/s11666-009-9357-7.

115. B. Samareh, O. Stier, V. Lüthen, and A. Dolatabadi, Assessment of CFD Modeling via Flow Visualization in Cold Spray Process, *J. Therm. Spray Technol.*, 2009, **18**(5–6), p 934–943.

116. B. Samareh and A. Dolatabadi, A Three-Dimensional Analysis of the Cold Spray Process: The Effects of Substrate Location and Shape, *J. Therm. Spray Technol.*, Springer US, 2007, **16**(5–6), p 634–642, doi:10.1007/s11666-007-9082-z.

117. S.A. Morsi and A.J. Alexander, An Investigation of Particle Trajectories in Two-Phase Flow Systems, *J. Fluid Mech.*, Cambridge University Press, 1972, **55**(2), p 193–208, doi:10.1017/S0022112072001806.

118. A. Sova, M. Doubenskaia, S. Grigoriev, A. Okunkova, and I. Smurov, Parameters of the Gas-Powder Supersonic Jet in Cold Spraying Using a Mask, *J. Therm. Spray Technol.*, 2013, **22**(4), p 551–556.

119. S.H. Zahiri, T.D. Phan, S.H. Masood, and M. Jahedi, Development of Holistic Three-Dimensional Models for Cold Spray Supersonic Jet, *J. Therm. Spray Technol.*, 2014, **23**(6), p 919–933.

120. J.R.G.M.E.W. R. Clift, "Bubbles, Drops, and Particles - Roland Clift, John R. Grace, Martin E. Weber, Martin F. Weber - Google Books," *Academic Press, New Yrok*, 1978, https://books.google.ca/books/about/Bubbles_Drops_and_Particles.html?id=n8gRAQAAIAAJ. Accessed 12 September 2020.

121. M. Karimi, A. Fartaj, G. Rankin, D. Vanderzwet, W. Birtch, and J. Villafuerte, Numerical Simulation of the Cold Gas Dynamic Spray Process, *J. Therm. Spray Technol.*, 2006, **15**(4), p 518–523.

122. S. Yin, M. Zhang, Z. Guo, H. Liao, and X. Wang, Numerical Investigations on the Effect of Total Pressure and Nozzle Divergent Length on the Flow Character and Particle Impact Velocity in Cold Spraying, *Surf. Coatings Technol.*, 2013, **232**, p 290–297.

123. T. Han, Z. Zhao, B.A. Gillispie, and J.R. Smith, Effects of Spray Conditions on Coating

Formation by the Kinetic Spray Process, *J. Therm. Spray Technol.*, 2005, **14**(3), p 373–383.

124. S. Yoon, Y. Xiong, H. Kim, and C. Lee, Dependence of Initial Powder Temperature on Impact Behaviour of Bulk Metallic Glass in a Kinetic Spray Process, *J. Phys. D Appl. Phys*, 2009, **42**, p 5, doi:10.1088/0022-3727/42/8/082004.
125. W.E. Ranz and W.R.M. Jr., Evaporation from Drops Part I, *Chem. Eng. Prog.*, 1952, **48**, p 141–146.
126. L.L. KAVANAU and J. DRAKE, R. M., "Heat Transfer from Spheres to a Rarefied Gas in Subsonic Flow," 1977, https://apps.dtic.mil/sti/citations/AD0001911. Accessed 12 September 2020.
127. T. Stoltenhoff, H. Kreye, and H.J. Richter, An Analysis of the Cold Spray Process and Its Coatings, *J. Therm. Spray Technol.*, 2002, **11**(4), p 542–550.
128. S. Whitaker, Forced Convection Heat Transfer Correlations for Flow in Pipes, Past Flat Plates, Single Cylinders, Single Spheres, and for Flow in Packed Beds and Tube Bundles, *AIChE J.*, John Wiley & Sons, Ltd, 1972, **18**(2), p 361–371, doi:10.1002/aic.690180219.
129. N. Ellendt, A.M. Lumanglas, S.I. Moqadam, and L. Mädler, A Model for the Drag and Heat Transfer of Spheres in the Laminar Regime at High Temperature Differences, *Int. J. Therm. Sci.*, Elsevier Masson SAS, 2018, **133**, p 98–105.
130. J.K. Fiszdon, Melting of Powder Grains in a Plasma Flame, *Int. J. Heat Mass Transf.*, Pergamon, 1979, **22**(5), p 749–761.
131. I. and T.A. of Thermal and S.P. and F.-D.C. of H.S. Devices, "No Title," Thayer School of Engineering, Dartmouth College, and RWTH Aachen, 1997.
132. O.C. Ozdemir, Q. Chen, S. Muftu, and V.K. Champagne, Modeling the Continuous Heat Generation in the Cold Spray Coating Process, *J. Therm. Spray Technol.*, Springer New York LLC, 2019, **28**(1–2), p 108–123.
133. I.E. Beckwith and J.J. Gallagher, "Heat Transfer and Recovery Temperature on a Sphere with Laminar, Transitional and Turbulent Boundary Layers at Mach Numbers of 2.00 and 4.15," (Washington), 1957.
134. S. Forrest L., "Survey of Literature on Convective Heat Transfer Coefficients and Recovery Factors for High Atmosphere Thermometry," (Utah, USA), 1973.
135. T.L. Bergman, F.P. Incropera, D.P. DeWitt, and A.S. Lavine, "Fundamentals of Heat and Mass Transfer," (Hoboken, NJ), John Wiley & Sons, 2011.
136. J. Vattulainen, E. Hämäläinen, R. Hernberg, P. Vuoristo, and T. Mäntylä, Novel Method for In-Flight Particle Temperature and Velocity Measurements in Plasma Spraying Using a Single CCD Camera, *J. Therm. Spray Technol.*, 2001, **10**(1), p 94–104.

137. B.H. Wang, B.Q. Li, H. Yang, and Y. Bai, Radiation Spectral Analysis and Particle Temperature/Velocity Measurement in Plasma Spray with One-Color Camera, *J. Therm. Spray Technol.*, 2017, **26**(7), p 1632–1640.

138. H. Fukanuma, N. Ohno, B. Sun, and R. Huang, In-Flight Particle Velocity Measurements with DPV-2000 in Cold Spray, *Surf. Coatings Technol.*, Elsevier, 2006, **201**(5), p 1935–1941.

139. G. Mauer, R. Vaßen, and D. Stöver, "Comparison and Applications of DPV-2000 and Accuraspray-G3 Diagnostic Systems," *Journal of Thermal Spray Technology*, Springer, 2007, p 414–424, doi:10.1007/s11666-007-9047-2.

140. J.F. Bisson, B. Gauthier, and C. Moreau, "Effect of Plasma Fluctuations on In-Flight Particle Parameters," *Journal of Thermal Spray Technology*, Springer, 2003, p 38–43, doi:10.1361/105996303770348483.

141. "In-Flight Particle Pyrometer for Thermal Spray Processes. Final Report, October 1, 1992--December 31, 1994," (Idaho Falls, ID), 1995, doi:10.2172/656793.

142. G. Mauer, R. Vaßen, and D. Stöver, Plasma and Particle Temperature Measurements in Thermal Spray: Approaches and Applications, *J. Therm. Spray Technol.*, 2011, **20**(3), p 391–406.

143. Y. Bai, K. Liu, Z.H. Wen, J.J. Tang, L. Zhao, and Z.H. Han, The Influence of Particle In-Flight Properties on the Microstructure of Coatings Deposited by the Supersonic Atmospheric Plasma Spraying, *Ceram. Int.*, Elsevier, 2013, **39**(7), p 8549–8553.

144. M. Jalali Azizpour and M. Tolouei-Rad, The Effect of Spraying Temperature on the Corrosion and Wear Behavior of HVOF Thermal Sprayed WC-Co Coatings, *Ceram. Int.*, Elsevier Ltd, 2019, **45**(11), p 13934–13941.

145. A. Ianiro and G. Cardone, Measurement of Surface Temperature and Emissivity with Stereo Dual-Wavelength IR Thermography, *J. Mod. Opt.*, 2010, **57**(18), p 1708–1715.

146. J. Mishin, M. Vardelle, J. Lesinski, and P. Fauchais, Two-Colour Pyrometer for the Statistical Measurement of the Surface Temperature of Particles under Thermal Plasma Conditions, *J. Phys. E.*, IOP Publishing, 1987, **20**(6), p 620–625, doi:10.1088/0022-3735/20/6/008.

147. P. Gougeon and C. Moreau, "In-Flight Particle Surface Temperature Measurement: Influence of the Plasma Light Scattered by the Particles," *Journal of Thermal Spray Technology*, Springer-Verlag, 1993, p 229–233, doi:10.1007/BF02650470.

148. G. Mauer, R. Vaen, and D. Stöver, "Plasma and Particle Temperature Measurements in Thermal Spray: Approaches and Applications," *Journal of Thermal Spray Technology*,

Springer, 2011, p 391–406, doi:10.1007/s11666-010-9603-z.

149. J. Mishin, M. Vardelle, J. Lesinski, and P. Fauchais, "Related Content," *Journal of Physics E: Scientific Instruments*, IOP Publishing, 1987, doi:10.1088/0022-3735/20/6/008.

150. B. Müller and U. Renz, Development of a Fast Fiber-Optic Two-Color Pyrometer for the Temperature Measurement of Surfaces with Varying Emissivities, *Rev. Sci. Instrum.*, American Institute of PhysicsAIP, 2001, **72**(8), p 3366–3374, doi:10.1063/1.1384448.

151. M.W. Lee, J.J. Park, D.Y. Kim, S.S. Yoon, H.Y. Kim, S.C. James, S. Chandra, and T. Coyle, "Numerical Studies on the Effects of Stagnation Pressure and Temperature on Supersonic Flow Characteristics in Cold Spray Applications," *Journal of Thermal Spray Technology*, Springer, 2011, p 1085–1097, doi:10.1007/s11666-011-9641-1.

152. X. Wang, B. Zhang, J. Lv, and S. Yin, Investigation on the Clogging Behavior and Additional Wall Cooling for the Axial-Injection Cold Spray Nozzle, *J. Therm. Spray Technol.*, Springer New York LLC, 2015, **24**(4), p 696–701.

153. D. Adebiyi, A. Popoola, I. Botef, D.I. Adebiyi, A.P. Popoola, and I. Botef, Experimental Verification of Statistically Optimized Parameters for Low-Pressure Cold Spray Coating of Titanium, *Metals (Basel).*, Multidisciplinary Digital Publishing Institute, 2016, **6**(6), p 135, doi:10.3390/met6060135.

154. M. Rab, S. Zahiri, S. Masood, M. Jahedi, and R. Nagarajah, Development of 3D Multicomponent Model for Cold Spray Process Using Nitrogen and Air, *Coatings*, MDPI AG, 2015, **5**(4), p 688–708, doi:10.3390/coatings5040688.

155. Y. Yu, M. Shademan, R.M. Barron, and R. Balachandar, Cfd Study of Effects of Geometry Variations on Flow in a Nozzle, *Eng. Appl. Comput. Fluid Mech.*, Taylor & Francis, 2012, **6**(3), p 412–425, doi:10.1080/19942060.2012.11015432.

156. T. Raja jayasingh, T. Raja jeyaseelan, C. Kannan, and M. Ganesh Karthikeyan, "Numerical (CFD) Analysis of Thermal Spray Coating Process," n.d., www.ijmer.com. Accessed 24 July 2020.

157. S. Yin, Q. Liu, H. Liao, and X. Wang, Effect of Injection Pressure on Particle Acceleration, Dispersion and Deposition in Cold Spray, *Comput. Mater. Sci.*, Elsevier, 2014, **90**, p 7–15.

158. S. Rajkumar Vadla and J. Doom, Analysis of Jet Characteristics Among Various Cold Spray Nozzles, *J. Therm. Spray Eng.*, 2018, **1**(1), p 24–31, doi:10.jtse/xxxx-xxxx/1-1.5.

159. M.C. Meyer, S. Yin, K.A. McDonnell, O. Stier, and R. Lupoi, Feed Rate Effect on Particulate Acceleration in Cold Spray under Low Stagnation Pressure Conditions, *Surf. Coatings Technol.*, Elsevier B.V., 2016, **304**, p 237–245.

160. B. Samareh and A. Dolatabadi, A Three-Dimensional Analysis of the Cold Spray Process:

The Effects of Substrate Location and Shape, n.d.

161. A.A. Mofakham and G. Ahmadi, On Random Walk Models for Simulation of Particle-Laden Turbulent Flows, *Int. J. Multiph. Flow*, Elsevier Ltd, 2020, **122**, p 103157.
162. M. Meyer and R. Lupoi, An Analysis of the Particulate Flow in Cold Spray Nozzles, *Mech. Sci*, 2015, **6**, p 127–136, doi:10.5194/ms-6-127-2015.
163. B. Samareh and A. Dolatabadi, Dense Particulate Flow in a Cold Gas Dynamic Spray System, *J. Fluids Eng.*, 2008, **130**(8), p 1–11.
164. A.B. Bailey and J. Hiatt, Sphere Drag Coefficients for a Broad Range of Mach and Reynolds Numbers, *AIAA J.*, 1972, **10**(11), p 1436–1440.
165. H. Assadi, T. Schmidt, H. Richter, J.-O. Kliemann, K. Binder, F. Gärtner, T. Klassen, and H. Kreye, On Parameter Selection in Cold Spraying, *J. Therm. Spray Technol.*, 2011, **20**(6), p 1161–1176.
166. P.C. King, C. Busch, T. Kittel-Sherri, M. Jahedi, and S. Gulizia, Interface Melding in Cold Spray Titanium Particle Impact, *Surf. Coatings Technol.*, Elsevier, 2014, **239**, p 191–199.
167. G. Bae, S. Kumar, S. Yoon, K. Kang, H. Na, H.J. Kim, and C. Lee, Bonding Features and Associated Mechanisms in Kinetic Sprayed Titanium Coatings, *Acta Mater.*, Pergamon, 2009, **57**(19), p 5654–5666.
168. S. Guetta, M.H. Berger, F. Borit, V. Guipont, M. Jeandin, M. Boustie, Y. Ichikawa, K. Sakaguchi, and K. Ogawa, Influence of Particle Velocity on Adhesion of Cold-Sprayed Splats, n.d.
169. P.C. King, S.H. Zahiri, and M. Jahedi, Microstructural Refinement within a Cold-Sprayed Copper Particle, n.d.
170. H. Koivuluoto, M. Honkanen, and P. Vuoristo, Cold-Sprayed Copper and Tantalum Coatings - Detailed FESEM and TEM Analysis, *Surf. Coatings Technol.*, Elsevier, 2010, **204**(15), p 2353–2361.
171. Y. Zou, W. Qin, E. Irissou, J.G. Legoux, S. Yue, and J.A. Szpunar, Dynamic Recrystallization in the Particle/Particle Interfacial Region of Cold-Sprayed Nickel Coating: Electron Backscatter Diffraction Characterization, *Scr. Mater.*, Pergamon, 2009, **61**(9), p 899–902.
172. M. Hassani-Gangaraj, D. Veysset, V.K. Champagne, K.A. Nelson, and C.A. Schuh, Adiabatic Shear Instability Is Not Necessary for Adhesion in Cold Spray, *Scr. Mater.*, Elsevier Ltd, 2018, **158**, p 430–439.
173. M. Grujicic, C.L. Zhao, W.S. DeRosset, and D. Helfritch, Adiabatic Shear Instability Based Mechanism for Particles/Substrate Bonding in the Cold-Gas Dynamic-Spray Process,

Mater. Des., Elsevier Ltd, 2004, **25**(8), p 681–688.

174. V.K. Champagne, D. Helfritch, P. Leyman, S. Grendahl, and B. Klotz, "Interface Material Mixing Formed by the Deposition of Copper on Aluminum by Means of the Cold Spray Process," *Journal of Thermal Spray Technology*, Springer, 2005, p 330–334, doi:10.1361/105996305X59332.
175. C. Chen, Y. Xie, R. Huang, S. Deng, Z. Ren, and H. Liao, On the Role of Oxide Film's Cleaning Effect into the Metallurgical Bonding during Cold Spray, *Mater. Lett.*, North-Holland, 2018, **210**, p 199–202, doi:10.1016/J.MATLET.2017.09.024.
176. Y. Watanabe, C. Yoshida, K. Atsumi, M. Yamada, and M. Fukumoto, Influence of Substrate Temperature on Adhesion Strength of Cold-Sprayed Coatings, *J. Therm. Spray Technol.*, 2014, **24**(1–2), p 86–91.
177. D.K. Christoulis, S. Guetta, E. Irissou, V. Guipont, M.H. Berger, M. Jeandin, J.G. Legoux, C. Moreau, S. Costil, M. Boustie, Y. Ichikawa, and K. Ogawa, Cold-Spraying Coupled to Nano-Pulsed Nd-YaG Laser Surface Pre-Treatment, *J. Therm. Spray Technol.*, Springer, 2010, **19**(5), p 1062–1073.
178. S. Yin, X. Wang, W. Li, H. Liao, and H. Jie, Deformation Behavior of the Oxide Film on the Surface of Cold Sprayed Powder Particle, *Appl. Surf. Sci.*, Elsevier B.V., 2012, **259**, p 294–300.
179. "Deformation Behavior of the Oxide Film on the Surface of Cold Sprayed Powder Particle | Elsevier Enhanced Reader," n.d., https://reader.elsevier.com/reader/sd/pii/S016943321201210X?token=58FB9614B4425A412A2BD537C190328468CABB4ABAB9F201FD22127F0FDC035FD1BE793DA09216F6333D99F2F6C196CF. Accessed 9 August 2020.
180. Y. Xie, S. Yin, C. Chen, M.P. Planche, H. Liao, and R. Lupoi, New Insights into the Coating/Substrate Interfacial Bonding Mechanism in Cold Spray, *Scr. Mater.*, Elsevier Ltd, 2016, **125**, p 1–4.
181. M. Hassani-Gangaraj, D. Veysset, K.A. Nelson, and C.A. Schuh, Impact-Bonding with Aluminum, Silver, and Gold Microparticles: Toward Understanding the Role of Native Oxide Layer, *Appl. Surf. Sci.*, North-Holland, 2019, **476**, p 528–532, doi:10.1016/J.APSUSC.2019.01.111.
182. M. Hassani-Gangaraj, D. Veysset, K.A. Nelson, and C.A. Schuh, In-Situ Observations of Single Micro-Particle Impact Bonding, *Scr. Mater.*, Acta Materialia Inc., 2018, **145**, p 9–13.
183. G. Bae, Y. Xiong, S. Kumar, K. Kang, and C. Lee, General Aspects of Interface Bonding

in Kinetic Sprayed Coatings, *Acta Mater.*, Pergamon, 2008, **56**(17), p 4858–4868.

184. S. Kumar, M. Ramakrishna, N.M. Chavan, and S. V. Joshi, Correlation of Splat State with Deposition Characteristics of Cold Sprayed Niobium Coatings, *Acta Mater.*, Elsevier Ltd, 2017, **130**, p 177–195.
185. Y. Xiong, G. Bae, X. Xiong, and C. Lee, "The Effects of Successive Impacts and Cold Welds on the Deposition Onset of Cold Spray Coatings," *Journal of Thermal Spray Technology*, Springer, 2010, p 575–585, doi:10.1007/s11666-009-9455-6.
186. J. Wu, J. Yang, H. Fang, S. Yoon, and C. Lee, The Bond Strength of Al-Si Coating on Mild Steel by Kinetic Spraying Deposition, *Appl. Surf. Sci.*, Elsevier, 2006, **252**(22), p 7809–7814.
187. J. Wu, H. Fang, S. Yoon, H. Kim, and C. Lee, The Rebound Phenomenon in Kinetic Spraying Deposition, *Scr. Mater.*, Elsevier Ltd, 2006, **54**(4 SPEC. ISS.), p 665–669.
188. T. Schmidt, F. Gaertner, and H. Kreye, New Developments in Cold Spray Based on Higher Gas and Particle Temperatures, *J. Therm. Spray Technol.*, Springer-Verlag, 2006, **15**(4), p 488–494, doi:10.1361/105996306X147144.
189. A. Viscusi, A. Astarita, S. Genna, and C. Leone, On the Influence of Different Superficial Laser Texturing on the Deposition of Powders through Cold Spray Process, *Trans. IMF*, Taylor and Francis Ltd., 2018, **96**(1), p 34–40, doi:10.1080/00202967.2018.1403096.
190. S. Kumar, G. Bae, and C. Lee, Influence of Substrate Roughness on Bonding Mechanism in Cold Spray, *Surf. Coatings Technol.*, Elsevier B.V., 2016, **304**, p 592–605.
191. M. Perton, S. Costil, W. Wong, D. Poirier, E. Irissou, J.G. Legoux, A. Blouin, and S. Yue, "Effect of Pulsed Laser Ablation and Continuous Laser Heating on the Adhesion and Cohesion of Cold Sprayed Ti-6Al-4V Coatings," *Journal of Thermal Spray Technology*, Springer, 2012, p 1322–1333.
192. T. Samson, D. MacDonald, R. Fernández, and B. Jodoin, Effect of Pulsed Waterjet Surface Preparation on the Adhesion Strength of Cold Gas Dynamic Sprayed Aluminum Coatings, *J. Therm. Spray Technol.*, 2015, **24**(6), p 984–993.
193. M. Perton, S. Costil, W. Wong, D. Poirier, E. Irissou, J.G. Legoux, A. Blouin, and S. Yue, "Effect of Pulsed Laser Ablation and Continuous Laser Heating on the Adhesion and Cohesion of Cold Sprayed Ti-6Al-4V Coatings," *Journal of Thermal Spray Technology*, Springer, 2012, p 1322–1333, doi:10.1007/s11666-012-9812-8.
194. H. Couque, The Use of the Direct Impact Hopkinson Pressure Bar Technique to Describe Thermally Activated and Viscous Regimes of Metallic Materials, *Philos. Trans. R. Soc. A Math. Phys. Eng. Sci.*, The Royal Society Publishing, 2014, **372**(2023), p 20130218,

doi:10.1098/rsta.2013.0218.

195. S. Rahmati and A. Ghaei, "The Use of Particle/Substrate Material Models in Simulation of Cold-Gas Dynamic-Spray Process," *Journal of Thermal Spray Technology*, 2014, p 530–540.

196. L.N. Brewer, J.F. Schiel, E.S.K. Menon, and D.J. Woo, The Connections between Powder Variability and Coating Microstructures for Cold Spray Deposition of Austenitic Stainless Steel, *Surf. Coatings Technol.*, Elsevier, 2018, **334**, p 50–60, doi:10.1016/J.SURFCOAT.2017.10.082.

197. T. Liu, J.D. Leazer, S.K. Menon, and L.N. Brewer, Microstructural Analysis of Gas Atomized Al-Cu Alloy Feedstock Powders for Cold Spray Deposition, *Surf. Coatings Technol.*, Elsevier, 2018, **350**, p 621–632, doi:10.1016/J.SURFCOAT.2018.07.006.

198. P. Coddet, C. Verdy, C. Coddet, and F. Debray, Effect of Cold Work, Second Phase Precipitation and Heat Treatments on the Mechanical Properties of Copper–Silver Alloys Manufactured by Cold Spray, *Mater. Sci. Eng. A*, Elsevier, 2015, **637**, p 40–47, doi:10.1016/J.MSEA.2015.04.008.

199. W.A. Story and L.N. Brewer, Heat Treatment of Gas-Atomized Powders for Cold Spray Deposition, *Metall. Mater. Trans. A*, Springer US, 2018, **49**(2), p 446–449, doi:10.1007/s11661-017-4428-8.

200. S. Kumar, G. Bae, and C. Lee, Deposition Characteristics of Copper Particles on Roughened Substrates through Kinetic Spraying, *Appl. Surf. Sci.*, Elsevier B.V., 2009, **255**(6), p 3472–3479.

201. Y. Zou, W. Qin, E. Irissou, J.-G. Legoux, S. Yue, and J.A. Szpunar, Dynamic Recrystallization in the Particle/Particle Interfacial Region of Cold-Sprayed Nickel Coating: Electron Backscatter Diffraction Characterization, *Scr. Mater.*, Pergamon, 2009, **61**(9), p 899–902, doi:10.1016/J.SCRIPTAMAT.2009.07.020.

202. K. Araci, D. Mangabhai, and K. Akhtar, Production of Titanium by the Armstrong Process®, *Titanium Powder Metallurgy*, Elsevier Inc., 2015, p 149–162.

203. A. Nastic, D. MacDonald, and B. Jodoin, The Influence of Feedstock Powder, 2020, p 33–85.

204. B. Daneshian and H. Assadi, Impact Behavior of Intrinsically Brittle Nanoparticles: A Molecular Dynamics Perspective, *J. Therm. Spray Technol.*, Springer US, 2014, **23**(3), p 541–550, doi:10.1007/s11666-013-0019-4.

205. P. Zhao, Q. Zhang, Y. Guo, H. Liu, and Z. Deng, Atomic Simulation of Crystal Orientation Effect on Coating Surface Generation Mechanisms in Cold Spray, *Comput. Mater. Sci.*,

Elsevier B.V., 2020, **184**, p 109859.

206. T. Malama, A. Hamweendo, and I. Botef, Molecular Dynamics Simulation of Ti and Ni Particles on Ti Substrate in the Cold Gas Dynamic Spray (CGDS) Process, *Mater. Sci. Forum*, Trans Tech Publications Ltd, 2015, **828–829**, p 453–460, doi:10.4028/www.scientific.net/MSF.828-829.453.
207. F. Yuan and X. Wu, Size Effect and Boundary Type on the Strengthening of Nanoscale Domains in Pure Nickel, *Mater. Sci. Eng. A*, 2015, **648**, p 243–251, doi:10.1016/j.msea.2015.09.071.
208. T. Chen and C. Zhou, Effect of the Grain Size and Distribution of Nanograins on the Deformation of Nanodomained Heterogeneous Nickel, *Mater. Lett.*, North-Holland, 2019, **236**, p 661–664, doi:10.1016/J.MATLET.2018.11.045.
209. M.A. Meyers, A. Mishra, and D.J. Benson, Mechanical Properties of Nanocrystalline Materials, *Prog. Mater. Sci.*, 2006, **51**(4), p 427–556, doi:10.1016/j.pmatsci.2005.08.003.
210. Y.M. Wang and E. Ma, Three Strategies to Achieve Uniform Tensile Deformation in a Nanostructured Metal, *Acta Mater.*, 2004, **52**(6), p 1699–1709, doi:10.1016/j.actamat.2003.12.022.
211. Q.X. Pei, C. Lu, F.Z. Fang, and H. Wu, Nanometric Cutting of Copper: A Molecular Dynamics Study, *Comput. Mater. Sci.*, Elsevier, 2006, **37**(4), p 434–441, doi:10.1016/J.COMMATSCI.2005.10.006.
212. F. Yang and Z. Zhong, On the Energy Conservation during the Active Deformation in Molecular Dynamics Simulations, *J. Mech. Phys. Solids*, Pergamon, 2015, **77**, p 146–157, doi:10.1016/J.JMPS.2015.01.012.
213. Z. El-Bayyari and Ş. Erkoç, Bulk and Surface Properties of Aluminum: A Molecular-Dynamics Simulation, *Mater. Chem. Phys.*, 1994, **37**(4), p 382–388, doi:10.1016/0254-0584(94)90179-1.
214. S.A. Adcock and J.A. McCammon, Molecular Dynamics: Survey of Methods for Simulating the Activity of Proteins., *Chem. Rev.*, Howard Hughes Medical Institute, 2006, **106**(5), p 1589–615, doi:10.1021/cr040426m.
215. T. Hussain, D.G. Mccartney, P.H. Shipway, and D. Zhang, Bonding Mechanisms in Cold Spraying: The Contributions of Metallurgical and Mechanical Components, n.d.
216. W. Sun, A.W.Y. Tan, N.W. Khun, I. Marinescu, and E. Liu, Effect of Substrate Surface Condition on Fatigue Behavior of Cold Sprayed Ti6Al4V Coatings, *Surf. Coatings Technol.*, Elsevier B.V., 2017, **320**, p 452–457.
217. A. International, “Standard Test Method for Adhesion or Cohesion Strength of Thermal

Spray Coatings, C633 - 13(2017)," (West Conshohocken), 2017.

218. Y. Xie, C. Chen, M.P. Planche, S. Deng, R. Huang, Z. Ren, and H. Liao, Strengthened Peening Effect on Metallurgical Bonding Formation in Cold Spray Additive Manufacturing, *J. Therm. Spray Technol.*, Springer, 2019, **28**(4), p 769–779, doi:10.1007/s11666-019-00854-4.

219. R. Fernández, D. MacDonald, A. Nastić, B. Jodoin, A. Tieu, and M. Vijay, Enhancement and Prediction of Adhesion Strength of Copper Cold Spray Coatings on Steel Substrates for Nuclear Fuel Repository, *J. Therm. Spray Technol.*, Springer New York LLC, 2016, **25**(8), p 1577–1587, doi:10.1007/s11666-016-0467-8.

220. M. Liu, C. Lu, K.A. Tieu, C.-T. Peng, and C. Kong, A Combined Experimental-Numerical Approach for Determining Mechanical Properties of Aluminum Subjects to Nanoindentation, *Sci. Rep.*, Nature Publishing Group, 2015, **5**(1), p 15072, doi:10.1038/srep15072.

221. P. Tremblay, L. Belhumeur, M. Chamberland, A. Villemaire, P. Dubois, F. Marcotte, C. Belzile, V. Farley, and P. Lagueux, "Pixel-Wise Real-Time Advanced Calibration Method for Thermal Infrared Cameras," *Proceedings Volume 7662, Infrared Imaging Systems: Design, Analysis, Modeling, and Testing XXI*, G.C. Holst and K.A. Krapels, Eds., (Orlando), 2010, p 766212.

222. "ASTM D4145 - 10(2018) Standard Test Method for Coating Flexibility of Prepainted Sheet," n.d., https://www.astm.org/Standards/D4145.htm. Accessed 2 September 2020.

APPENDIX A- Hugoniot Energy

The Hugoniot energy, E_H, pressure, P_H, and the Mie-Gruneisen equation expressed in the linear equation of state from, described in section 4.6.2.2 are demonstrated in the following appendices.

Starting from the energy conservation equation given in Eq. 91;

$$\frac{\dot{M}}{A}\cdot\left[h_1 - h_0 + \frac{1}{2}(u_s - u_m)^2 - \frac{1}{2}(u_s)^2\right] = 0 \qquad \textbf{A. 1}$$

The enthalpy, *h*, can be replaced by:

$$h = e + \frac{P}{\rho}, \qquad \textbf{A. 2}$$

which provides:

$$\frac{\dot{M}}{A}\cdot\left[e_1 + \frac{P_1}{\rho_1} - e_0 + \frac{P_0}{\rho_0} + \frac{1}{2}(u_s - u_m)^2 - \frac{1}{2}(u_s)^2\right] = 0. \qquad \textbf{A. 3}$$

Using the mass conservation, presented in Eq. 89 and developing the expression $(u_s - u_m)^2$the above equation becomes;

$$\rho_1(u_s - u_m)\frac{P_1}{\rho_1} - \rho_0 u_s\frac{P_0}{\rho_0} + \rho_0 u_s\left(e_1 - e_0 - u_s u_m + \frac{1}{2}u_m^2\right) = 0 \qquad \textbf{A. 4}$$

$$P_0 u_s - P_1(u_s - u_m) = \rho_0 u_s\left(e_1 - e_0 - u_s u_m + \tfrac{1}{2}u_m^2\right). \qquad \textbf{A. 5}$$

Using the momentum conservation, given in Eq. 90, and the mass conservation;

$$P_0 u_s - (\rho_0 u_s u_m + P_0)(u_s - u_m) = \rho_0 u_s\left(e_1 - e_0 - u_s u_m + \frac{1}{2}u_m^2\right) \qquad \textbf{A. 6}$$

$$(\rho_0 u_s u_m^2 + P_0 u_m - \rho_0 u_s^2 u_m) = \rho_0 u_s\left(e_1 - e_0 - u_s u_m + \frac{1}{2}u_m^2\right) \qquad \textbf{A. 7}$$

$$(P_0 u_m) = \rho_0 u_s\left(e_1 - e_0 - \tfrac{1}{2}u_m^2\right). \qquad \textbf{A. 8}$$

Assuming that in the above developed equation, the P_0 is negligible compared to P_1, e_0 is negligible compared to e_1, and using the mass conservation (Eq. 89);

$$0 = \rho_0 u_s\left(e_1 - \tfrac{1}{2}u_m^2\right), \qquad \textbf{A. 9}$$

$$0 = \rho_0 u_s e_1 - \frac{1}{2}\rho_0 u_s u_m^2 \qquad \textbf{A. 10}$$

From the momentum equation, the term $\rho_0 u_s u_m$ is equal to P_1;

$$0 = \rho_0 u_s e_1 - \frac{1}{2} P_1 u_m. \qquad \textbf{A. 11}$$

The mass equation can be rewritten as, using $\eta = 1 - \rho_0/\rho_1$

$$u_m = \eta u_s. \qquad \textbf{A. 12}$$

Using this equality in A. 11;

$$\rho_0 u_s e_1 = \frac{1}{2} P_1 \eta u_s. \qquad \textbf{A. 13}$$

$$\rho_0 e_1 = \frac{1}{2} P_1 \eta. \qquad \textbf{A. 14}$$

$$e_1 = e_H = \frac{1}{2}\frac{P_1}{\rho_0}\eta. \qquad \textbf{A. 15}$$

APPENDIX B- Hugoniot Pressure

The Hugoniot pressure, P_H, is developed by starting from the momentum conservation while considering that P_0 (state 0) is assumed negligeable compared to P_1 (state 1);

$$P_1 = \rho_0 u_s u_m \quad \textbf{B. 1}$$

and using the relation between η, u_s and u_m given by $u_m = \eta u_s$, the following is obtained;

$$P_1 = \rho_0 u_s^2 \eta. \quad \textbf{B. 2}$$

Using the linear relation between speed and material velocity, given in Eq. 92 and the relation provided in A. 12;

$$u_s = c_0 + s \cdot \eta u_s \quad \textbf{B. 3}$$

$$u_s(1 - s\eta) = c_0 \quad \textbf{B. 4}$$

$$u_s = \frac{c_0}{(1 - s\eta)}. \quad \textbf{B. 5}$$

Finally, combining B. 2 and B. 5 and recognizing that stage 1 refers to shock Hugoniot (thermodynamic state behind a traveling shock), the equation of Hugoniot pressure is given by;

$$P_1 = P_H = \frac{\rho_0 c_0^2 \eta}{(1 - s\eta)^2}. \quad \textbf{B. 6}$$